

Issue: 32

SCOPUS

UNIVERSIDAD POLITÉCNICA SALESIANA ECUADOR

pISSN: 1390-650X

eISSN: 1390-860X

july / december 2024

INGENIUS

Revista de Ciencia y Tecnología



Q4
SJIR Journal
Rank

SUBJECT AREA AND CATEGORY
Engineering
(miscellaneous)

- Structural evaluation of a three-wheeler vehicle using simulation tools: a case study in Mexico.

Pag. 18

- Optimization of the VARTM process for prototyping a bumper using hybrid composite.

Pag. 48

- Diagnosis of oral cancer using deep learning.

Pag. 58

- Storytelling based on generative AI to promote the inclusion of people with disabilities.

Pag. 101

Indexed in: **SCOPUS**

INGENIUS

INGENIUS • Issue 32 • july/december 2024. Journal of Science and Tecnology of the Universidad Politécnica Salesiana of Ecuador. Publication dedicated to studies related to the Sciences of Mechanical Engineering, Electrical Engineering, Electronic Engineering, Mechatronic Engineering, Systems Engineering and Industrial Engineering.

Editors Board

RAFAEL ANTONIO BALART GIMENO, PhD, Universidad Politécnica de Valencia, España – Editor-in-chief.
JOHN IGNACIO CALLE SIGÜENCIA, PhD, Universidad Politécnica Salesiana, Ecuador – Editor-in-chief.

ESTEBAN MAURICIO INGA ORTEGA, PhD, Universidad Politécnica Salesiana, Ecuador – Associate Editor.
MARLON XAVIER QUINDE ABRIL, MSc, Universidad Politécnica Salesiana, Ecuador – Associate Editor.

TEODIANO FREIRE BASTOS FILHO, PhD, (Universidade Federal do Espírito Santo, Brasil – Associate Editor.

Scientific board

JUAN LÓPEZ MARTÍNEZ, PhD, Universidad Politécnica de Valencia, España.

ELENA FORTUNATI, PhD, Universidad de Perugia, Italia.

GUSTAVO ROVELO RUIZ, PhD, Hasselt University, Diepenbeek, Bélgica.

FRANKLIN GAVILANEZ ALVAREZ, PhD, American University, Estados Unidos.

PIEDAD GAÑAN ROJO, PhD, Universidad Pontificia Bolivariana, Colombia.

JOSÉ ALEX RESTREPO, PhD, Universidad Simón Bolívar, Venezuela.

SERGIO LUJAN MORA, PhD, Universidad de Alicante, España.

MARTHA ZEQUERA DÍAZ, PhD, Pontificia Universidad Javeriana, Colombia.

GROVER ZURITA, PhD, Universidad Privada Boliviana, Bolivia.

VLADIMIR ROBLES, PhD, Universidad Politécnica Salesiana, Ecuador.

GERMÁN ARÉVALO, PhD, Universidad Politécnica Salesiana, Ecuador.

WILBERT AGUILAR, PhD, Universidad de las Fuerzas Armadas, ESPE, Ecuador.

JACK BRAVO TORRES, PhD, Universidad Politécnica Salesiana, Ecuador.

WALTER OROZCO, PhD, Universidad Politécnica Salesiana, Ecuador.

MARIELA CERRADA, PhD, Universidad Politécnica Salesiana, Ecuador.

JULIO CÉSAR VIOLA, PhD, Universidad Politécnica Salesiana, Ecuador.

SERGIO GAMBOA SÁNCHEZ, PhD, Universidad Nacional Autónoma de México, México.

ROGER ABDÓN BUSTAMANTE PLAZA, PhD, Universidad de Chile, Chile.

CHRISTIAN BLUM, PhD, Consejo Superior de Investigaciones Científicas, España.

SILVIA NOEMI SCHIAFFINO, PhD, Universidad Nacional del Centro de la Provincia de Buenos Aires, Argentina.

ANALÍA ADRIANA AMANDI, PhD, Universidad Nacional del Centro de la Provincia de Buenos Aires, Argentina.

RUBÉN DE JESÚS MEDINA MOLINA, PhD,

Universidad de Los Andes, Venezuela.

JOHNNY JOSUÉ BULLÓN TORREALBA, PhD, Universidad de Los Andes, Venezuela.

RODRIGO PALMA HILLERNS, PhD, Universidad de Chile, Chile.

GERARDO ESPINOZA PÉREZ, PhD, Universidad Nacional Autónoma de México, México.

ALEXANDRE MENDES ABRÃO, PhD, Universidad Federal de Minas Gerais, Brasil.

KAMLA ABDEL RADI ISMAIL, PhD, Universidad Estatal de Campinas Unicamp, Brasil.

ARNALDO DA SILVA, PhD, Universidad Estatal de Campinas Unicamp, Brasil.

ÁLVARO ROCHA, PhD, Universidad de Coimbra, Portugal.

JOSÉ ANTENOR POMILIO, PhD, Universidad Estatal de Campinas Unicamp, Brasil.

LUIS PAULO REIS, PhD, Universidad de Minho, Portugal.

LUÍS FERNANDES, PhD, Escuela Superior Náutica Infante d. Henrique, Portugal.

ANÍBAL TRAÇA DE ALMEIDA, PhD, Universidad de Coimbra, Portugal.

JORGE SÁ SILVA, PhD, Universidad de Coimbra, Portugal.

PEDRO MANUEL SOARES MOURA, PhD, Universidad de Coimbra, Portugal.

SÉRGIO MANUEL RODRIGUES LOPES, PhD, Universidad de Coimbra, Portugal.

RICARDO MADEIRA SOARES BRANCO, PhD, Universidad de Coimbra, Portugal.

CARLOS ALEXANDRE BENTO CAPELA, PhD, Universidad de Coimbra, Portugal.

FILIPPE ARAUJO, PhD, Universidad de Coimbra, Portugal.

LUIS MANUEL GUERRA SILVA ROSA, PhD, Universidad de Lisboa, Portugal.

HÉLDER DE JESUS FERNANDES, PUGA, PhD, Universidad de Minho, Portugal.

FILIPPE SAMUEL, PEREIRA DA SILVA, PhD, Universidad de Minho, Portugal.

CÉSAR SEQUEIRA, PhD, Universidad de Lisboa, Portugal.

JOSÉ TEIXEIRA ESTÊVÃO FERREIRA, PhD,

Universidad de Coimbra, Portugal.

NUNO LARANJEIRO, PhD, Universidad de Coimbra, Portugal.

LUÍS AMARAL, PhD, Universidad de Lisboa, Portugal.

JORGE HENRIQUES, PhD, Universidad de Coimbra, Portugal.

WILLIAM IPANAQUE, PhD, Universidad de Piura, Perú.

LORENZO LEIJA SALAS, PhD, Centro de Investigación y Estudios Avanzados del Instituto Politécnico Nacional, México.

VALERI KONTOROVICH MAZOVER, PhD, Centro de Investigación y de Estudios Avanzados del Instituto Politécnico Nacional, México.

ALEJANDRO ÁVILA GARCÍA, PhD, Centro de Investigación y de Estudios Avanzados del Instituto Politécnico Nacional, México.

PAOLO BELLAVISTA, PhD, Universidad de Bologna, Italia.

CARLOS RUBIO, PhD, Centro de Ingeniería y Desarrollo Industrial, México.

FERNANDO HERNÁNDEZ SÁNCHEZ, PhD, Centro de Investigación Científica de Yucatán, México.

EMILIO MUÑOZ SANDOVAL, PhD, Instituto Potosino de Investigación Científica y Tecnológica, México.

YASUHIRO MATSUMOTO KUWABARA, PhD, Centro de Investigación y de Estudios Avanzados del Instituto Politécnico Nacional, México.

DAVID ZUMOFFEN, PhD, Centro Internacional Franco Argentino de Ciencias de la Información y de Sistemas, Argentina.

VICENTE RODRÍGUEZ GONZÁLEZ, PhD, Instituto Potosino de Investigación Científica y Tecnológica, México.

ALEJANDRO RODRÍGUEZ ÁNGELES, PhD, Centro de Investigación y de Estudios Avanzados del Instituto Politécnico Nacional, México.

ALISTAIR BORTHWICK, PhD, Universidad de Edimburgo, Reino Unido.

Reviewers board

FEDERICO DOMINGUEZ, PhD, Escuela Superior Politécnica del Litoral, Ecuador.

ENRIQUE CARRERA, PhD, Universidad de las Fuerzas Armadas, ESPE, Ecuador.

ANDRÉS TELLO, MSc, Universidad de Cuenca, Ecuador.

CRISTIAN GARCÍA BAUZA, PhD, Universidad Nacional del Centro de la Provincia de Buenos Aires, Argentina.

OSVALDO AÑÓ, PhD, Universidad Nacional de San Juan, Argentina.

THALÍA SAN ANTONIO, PhD, Universidad Técnica de Ambato, Ecuador.

VICTOR SAQUICELA, PhD, Universidad de Cuenca, Ecuador.

GONZALO OLMEDO, PhD, Universidad de las Fuerzas Armadas, ESPE, Ecuador.

ROMÁN LARA, PhD, Universidad de las Fuerzas Armadas, ESPE, Ecuador.

GUILLERMO SORIANO, PhD, Escuela Superior Politécnica del Litoral, Ecuador.

MARÍA FERNANDA GRANDA, PhD, Universidad de Cuenca, Ecuador.

RICARDO CAYSSIALS, PhD, Universidad Tecnológica Nacional, Argentina.

LEONARDO SOLAQUE GUZMAN, PhD, Universidad Militar Nueva Granada, Colombia.

JOSÉ DI PAOLO, PhD, Universidad Nacional de Entre Ríos, Argentina.

ASTRID RUBIANO FONSECA, PhD, Universidad Militar Nueva Granada, Colombia.

ROBINSON JIMÉNEZ, PhD, Universidad Militar Nueva Granada, Colombia.

ALFONSO ZOZAYA, PhD, Universidad de Carabobo, Venezuela.

MAURICIO MAULEDOUX, PhD, Universidad Militar Nueva Granada, Colombia.

LUIS MEDINA, PhD, Universidad Simón Bolívar, Venezuela.

ERNESTO CUADROS-VARGAS, PhD, Universidad Católica San Pablo, Perú.

SAMUEL SEPÚLVEDA CUEVAS, PhD, Universidad de la Frontera, Chile.

CARLOS CARES, PhD, Universidad de la Frontera, Chile.

RAFAEL SOTELO, PhD, Universidad de Montevideo, Uruguay.

OMAR LOPEZ, PhD, Universidad de Los Andes, Colombia.

JOB FLORES-GODOY, PhD, Universidad Católica del Uruguay, Uruguay.

LUIS MARIO MATEUS, PhD, Universidad de los Andes, Colombia.

AMADEO ARGÜELLES CRUZ, PhD, Instituto Politécnico Nacional, México.

SANTIAGO BENTANCOURT PARRA, PhD, Universidad Pontificia Bolivariana, Colombia.

GERMÁN ZAPATA, PhD, Universidad Nacio-

nal de Colombia, Colombia.

PEDRO GARCÍA, PhD, Universidad Autónoma de Barcelona, España.

ARTURO CONDE ENRÍQUEZ, PhD, Universidad Autónoma de Nuevo León, México.

ALBERTO CAVAZOS GONZÁLEZ, PhD, Universidad Autónoma de Nuevo León, México.

ERNESTO VÁZQUEZ MARTÍNEZ, PhD, Universidad Autónoma de Nuevo León, México.

MIGUEL DÍAZ RODRIGUEZ, PhD, Universidad de Los Andes, Venezuela.

EFRAÍN ALCORTA GARCÍA, PhD, Universidad Autónoma de Nuevo León, México.

LUIS CHIRINOS GARCIA, PhD, Pontificia Universidad Católica de Perú, Perú.

OSCAR AVILÉS, PhD, Universidad Militar Nueva Granada, Colombia.

DORA MARTÍNEZ DELGADO, PhD, Universidad Autónoma de Nuevo León, México.

DAVID OJEDA, PhD, Universidad Técnica del Norte, Ecuador.

IRENE BEATRÍZ STEINMANN, PhD, Universidad Tecnológica Nacional, Argentina.

MARIO SERRANO, Universidad Nacional de San Juan, Argentina.

CORNELIO POSADAS CASTILLO, PhD, Universidad Autónoma Nuevo León, México.

MARIO ALBERTO RIOS MESIAS, PhD, Universidad de Los Andes, Colombia.

YUDITH CARDINALE VILLARREAL, PhD, Universidad Simón Bolívar, Venezuela.

JOSE EDUARDO OCHOA LUNA, PhD, Universidad Católica San Pablo, Perú.

DANTE ANGEL ELIAS GIORDANO, PhD, Pontificia Universidad Católica de Perú, Perú.

MANUEL PELAEZ SAMANIEGO, PhD, Universidad de Cuenca, Ecuador.

JUAN ESPINOZA ABAD, PhD, Universidad de Cuenca, Ecuador.

PIETRO CODARA, PhD, Universidad de Milan, Italia.

ALBERTO SORIA, PhD, Centro de Investigación y de Estudios Avanzados del Instituto Politécnico Nacional, México.

JOSÉ M. ALLER, PhD, Universidad Politécnica Salesiana, Ecuador.

FERNEY AMAYA F., PhD, Universidad Pontificia Bolivariana, Medellín, Colombia.

SANTIAGO ARANGO ARAMBURO, PhD, Universidad Nacional de Colombia, Colombia.

DIEGO ARCOS-AVILÉS, PhD, Universidad de las Fuerzas Armadas, ESPE, Ecuador.

PABLO AREVALO, PhD, Universidad Politécnica Salesiana, Ecuador.

ROBERTO BELTRAN, MSc, Universidad de las Fuerzas Armadas, ESPE, Ecuador.

LEONARDO BETANCUR, PhD, Universidad Pontificia Bolivariana, Medellín, Colombia.

ROBERTO GAMBOA, PhD, Universidad de Lisboa, Portugal.

PAULO LOPES DOS SANTOS, PhD, Universidad do Porto, Portugal.

PEDRO ANDRÉ DIAS PRATES, PhD, Universidad de Coimbra, Portugal.

JOSÉ MANUEL TORRES FARINHA, PhD, Universidad de Coimbra, Portugal.

CELSE DE ALMEIDA, PhD, Universidad Estatal de Campinas Unicamp, Brasil.

RAMON MOLINA VALLE, PhD, Universidad Federal de Minas Gerais, Brasil.

CRISTINA NADER VASCONCELOS, PhD, Universidad Federal Fluminense, Brasil.

JOÃO M. FERREIRA CALADO, PhD, Universidad de Lisboa, Portugal.

GUILHERME LUZ TORTORELLA, PhD, Universidad Federal de Santa Catarina, Brasil.

MAURO E. BENEDET, PhD, Universidad Federal de Santa Catarina, Brasil.

ARTEMIS MARTI CESCHIN, PhD, Universidade de Brasília, Brasil.

GILMAR BARRETO, PhD, Universidad Estatal de Campinas Unicamp, Brasil.

RICARDO EMILIO F. QUEVEDO NOGUEIRA, PhD, Universidad Federal de Ceará, Brasil.

WESLEY LUIZ DA SILVA ASSIS, PhD, Universidad Federal Fluminense, Brasil.

ANA P. MARTINAZZO, PhD, Universidad Federal Fluminense, Brasil.

JORGE BERNARDINO, PhD, Universidad de Coimbra, Portugal.

LUIS GERALDO PEDROSO MELONI, PhD, Universidad Estatal de Campinas Unicamp, Brasil.

FACUNDO ALMERAYA CALDERÓN, PhD, Universidad Autónoma de Nuevo León, México.

FREDDY VILLAO QUEZADA, PhD, Escuela Superior Politécnica del Litoral, Ecuador.

JOSE MANRIQUE SILUPU, MSc, Universidad de Piura, Perú.

GERMÁN ARIEL SALAZAR, PhD, Instituto de Investigaciones en Energía no Convencional, Argentina.

JOSÉ MAHOMAR JANANÍAS, PhD, Universidad del BIOBIO, Chile.

ARNALDO JÉLVEZ CAAMAÑO, PhD, Universidad del BIOBIO, Chile.

JORGE ANDRÉS URIBE, MSc, Centro de Ingeniería y Desarrollo Industrial, México.

RICARDO BELTRAN, PhD, Centro de Investigación en Materiales Avanzados, México.

ADI CORRALES, MSc, Centro de Ingeniería y Desarrollo Industrial, México.

JORGE URIBE CALDERÓN, PhD, Centro de Investigación Científica de Yucatán, México.

JOSÉ TRINIDAD HOLGUÍN MOMACA, MSc, Centro de Investigación en Materiales Avan-

zados, México.

JUAN MANUEL ALVARADO OROZCO, PhD, Centro de Ingeniería y Desarrollo Industrial, México.

ARNALDO JÉLVEZ CAAMAÑO, PhD, Universidad del BIOBIO, Chile.

JAVIER MURILLO, PhD, Centro Internacional Franco Argentino de Ciencias de la Información y de Sistemas, Argentina.

LUCAS DANIEL TERISSI, PhD, Universidad Nacional de Rosario, Argentina.

RENE VINICIO SANCHEZ LOJA, MSC, Universidad Politécnica Salesiana, Ecuador.

FREDDY LEONARDO BUENO PALOMEQUE, MSC, Universidad Politécnica Salesiana, Ecuador.

DIEGO CABRERA MENDIETA, MSC, Universidad Politécnica Salesiana, Ecuador.

EDWUIN JESUS CARRASQUERO, PhD, Universidad Técnica de Machala, Ecuador.

CARLOS MAURICIO CARRILLO ROSERO, MSC, Universidad Técnica de Ambato, Ecuador.

DIEGO CARRION GALARZA, MSC, Universidad Politécnica Salesiana, Ecuador.

CARMEN CELI SANCHEZ, MSC, Universidad Politécnica Salesiana, Ecuador.

DIEGO CHACON TROYA, MSC, Universidad Politécnica Salesiana, Ecuador.

PAUL CHASI, MSC, Universidad Politécnica Salesiana, Ecuador.

JUAN CHICA, MSC, Universidad Politécnica Salesiana, Ecuador.

DIEGO MARCELO CORDERO GUZMÁN, MSC, Universidad Católica de Cuenca, Ecuador.

LUIS JAVIER CRUZ, PhD, Universidad Pontificia Bolivariana, Medellín, Colombia.

FABRICIO ESTEBAN ESPINOZA MOLINA, MSC, Universidad Politécnica Salesiana, Ecuador.

JORGE FAJARDO SEMINARIO, MSC, Universidad Politécnica Salesiana, Ecuador.

PATRICIA FERNANDEZ MORALES, PhD, Universidad Pontificia Bolivariana, Medellín, Colombia.

MARCELO FLORES VAZQUEZ, MSC, Universidad Politécnica Salesiana, Ecuador.

CARLOS FLORES VÁZQUEZ, MSC, Universidad Católica de Cuenca, Ecuador.

CARLOS FRANCO CARDONA, PhD, Universidad Nacional de Colombia, Colombia.

CRISTIAN GARCÍA GARCÍA, MSC, Universidad Politécnica Salesiana, Ecuador.

TEONILA GARCÍA ZAPATA, PhD, Universidad Nacional Mayor de San Marcos, Perú.

LUIS GARZÓN MÑOZ, PhD, Universidad Politécnica Salesiana, Ecuador.

NATALIA GONZALEZ ALVAREZ, MSC, Universidad Politécnica Salesiana, Ecuador.

ERNESTO GRANADO, PhD, Universidad Simón Bolívar, Venezuela.

ADRIANA DEL PILAR GUAMAN, MSC, Univer-

sidad Politécnica Salesiana, Ecuador.

JUAN INGA ORTEGA, MSC, Universidad Politécnica Salesiana, Ecuador.

ESTEBAN INGA ORTEGA, PhD, Universidad Politécnica Salesiana, Ecuador.

PAOLA INGAVÉLEZ, MSC, Universidad Politécnica Salesiana, Ecuador.

CESAR ISAZA ROLDAN, PhD, Universidad Pontificia Bolivariana.

NELSON JARA COBOS, MSC, Universidad Politécnica Salesiana, Ecuador.

RUBEN JERVES, MSC, Universidad Politécnica Salesiana, Ecuador.

VICTOR RAMON LEAL, PhD, Investigador de PDVSA, Venezuela

GABRIEL LEON, MSC, Universidad Politécnica Salesiana, Ecuador.

EDILBERTO LLANES, PhD, Universidad Internacional SEK, Ecuador.

LUIS LÓPEZ, MSC, Universidad Politécnica Salesiana, Ecuador.

CARLOS MAFLA YÉPEZ, MSC, Universidad Técnica del Norte, Ecuador.

HADER MARTÍNEZ, PhD, Universidad Pontificia Bolivariana, Medellín, Colombia

JAVIER MARTÍNEZ, PhD, Instituto Nacional de Eficiencia Energética y Energías Renovables, Ecuador.

ALEX MAYORGA, MSC, Universidad Técnica de Ambato, Ecuador.

JIMMY MOLINA, MSC, Universidad Técnica de Machala, Ecuador.

ANDRES MONTERO, PhD, Universidad de Cuenca, Ecuador.

VICENTE MORALES, MSC, Universidad Técnica de Ambato, Ecuador.

FABIÁN MORALES, MSC, Universidad Técnica de Ambato, Ecuador.

DIEGO MORALES, MSC, Ministerio de Electricidad y Energías Renovables del Ecuador.

YOANDRYS MORALES TAMAYO, PhD, Universidad Técnica de Cotopaxi, Cotopaxi

OLENA LEONIDIVNA NAIDIUK, MSC, Universidad Politécnica Salesiana, Ecuador.

OSCAR NARANJO, MSC, Universidad del Azuay, Ecuador.

PAUL NARVAEZ, MSC, Universidad Politécnica Salesiana, Ecuador.

HERNÁN NAVAS OLMEDO, MSC, Universidad Técnica de Cotopaxi, Ecuador.

CESAR NIETO, PhD, Universidad Pontificia Bolivariana, Medellín, Colombia

FABIO OBANDO, MSC, Universidad Politécnica Salesiana, Ecuador.

LUIS ORTIZ FERNANDEZ, MSC, Universidade Federal de Rio Grande del Norte, Brasil

PABLO PARRA, MSC, Universidad Politécnica Salesiana, Ecuador.

PAULO PEÑA TORO, PhD, Ministerio de

Productividad, Ecuador.

PATSY PRIETO VELEZ, MSC, Universidad Politécnica Salesiana, Ecuador.

DIEGO QUINDE FALCONI, MSC, Universidad Politécnica Salesiana, Ecuador.

DIANA QUINTANA ESPINOZA, MSC, Universidad Politécnica Salesiana, Ecuador.

WILLIAM QUITIAQUEZ SARZOSA, MSC, Universidad Politécnica Salesiana, Ecuador.

FLAVIO QUIZHPI PALOMEQUE, MSC, Universidad Politécnica Salesiana, Ecuador.

WASHINGTON RAMIREZ MONTALVAN, MSC, Universidad Politécnica Salesiana, Ecuador.

FRAN REINOSO AVECILLAS, MSC, Universidad Politécnica Salesiana, Ecuador.

NÉSTOR RIVERA CAMPOVERDE, MSC, Universidad Politécnica Salesiana, Ecuador.

JORGE ROMERO CONTRERAS, MSC, Universidad de Carabobo, Venezuela

FABIAN SAENZ ENDERICA, MSC, Universidad de las Fuerzas Armadas, ESPE, Ecuador.

LUISA SALAZAR GIL, PhD, Universidad Simón Bolívar, Venezuela

GUSTAVO SALGADO ENRÍQUEZ, MSC, Universidad Central del Ecuador., Ecuador.

JUAN CARLOS SANTILLÁN LIMA, MSC, Universidad Nacional de Chimborazo

JONNATHAN SANTOS BENÍTEZ, MSC, Universidad Politécnica Salesiana, Ecuador.

ANDRÉS SARMIENTO CAJAMARCA, MSC, Universidad Federal de Santa Catarina, Brasil

LUIS SERPA ANDRADE, MSC, Universidad Politécnica Salesiana, Ecuador.

CRISTIAN TIMBI SISALIMA, MSC, Universidad Politécnica Salesiana, Ecuador.

MILTON TIPAN SIMBAÑA, MSC, Universidad Politécnica Salesiana, Ecuador.

PAUL TORRES JARA, MSC, Universidad Politécnica Salesiana, Ecuador.

RODRIGO TUFÍÑO CÁRDENAS, MSC, Universidad Politécnica Salesiana, Ecuador.

FERNANDO URGILES ORTÍZ, MSC, Universidad Politécnica Salesiana, Ecuador.

JUAN VALLADOLID QUITOISACA, MSC, Universidad Politécnica Salesiana, Ecuador.

EFREN VÁZQUEZ SILVA, PhD, Universidad Politécnica Salesiana, Ecuador.

JULIO VERDUGO, MSC, Universidad Politécnica Salesiana, Ecuador.

MARY VERGARA PAREDES, PhD, Universidad de los Andes, Merida, Venezuela

JENNIFER YEPEZ ALULEMA, MSC, Universidad Politécnica Salesiana, Ecuador.

JULIO ZAMBRANO ABAD, MSC, Universidad Politécnica Salesiana, Ecuador.

PATRICIA ZAPATA MOLINA, MSC, Universidad Politécnica Salesiana, Ecuador.

Publications board

JUAN CÁRDENAS TAPIA, SDB, PhD
JOSÉ JUNCOSA BLASCO, PhD
ESTEBAN MAURICIO INGA ORTEGA, PhD
ANGLE TORRES TOUKOUMIDIS, PhD
JAIME PADILLA VERDUGO, PhD
SHEILA SERRANO VINCENTI, MSc
JORGE CUEVA ESTRADA, MSc
JOHN CALLE SIGÜENCIA, PhD
FLORALBA AGUILAR GORDÓN, PhD
BETTY RODAS SOTO, MSc
MÓNICA RUIZ VÁSQUEZ, MSc
JORGE ALTAMIRANO SÁNCHEZ, MSc
DAVID ARMENDÁRIZ GONZÁLEZ, MSc

General Editor

ANGEL TORRES TOUKOUMIDIS, PhD

Technical board

DRA. MARCIA PEÑA, Style Reviewer,
Centro Gráfico Salesiano - Editorial Don Bosco
MSc. MARLON QUINDE ABRIL, Diagramming and layout
BSc. ANDRES LOPEZ, Community Manager - Diagramming and layout
BSc. MARÍA JOSÉ CABRERA, Marcalyc Support
BSc. CHRISTIAN ARPI, Community Managers Coordinator's team

Publications Service

HERNÁN HERMOSA (General Coordination)
MARCO GUTIÉRREZ (OJS Layout)
PAULINA TORRES (Style Editing)
RAYSA ANDRADE (Layout)
MARTHA VINUEZA (Layout)
YIXI GONZALEZ, (Style Reviewer)

Editorial

Editorial Abya Yala (Quito-Ecuador),
Av. 12 de octubre N422 y Wilson,
Bloque A, UPS Quito, Ecuador.
Casilla 17-12-719 Teléfonos: (593-2) 3962800 ext. 2638
email: editorial@abyayala.org

Printing: 800 copies

Typographic system used in the composition of this document L^AT_EX.

INGENIUS

REVISTA DE CIENCIA Y TECNOLOGIA

Issue 32

july – december 2024

ISSN impreso 1390-650X / ISSN electrónico 1390-860X

The administration of the journal is done through the following parameters:

The journal uses the academic anti-plagiarism system



The articles have an identification code (Digital Object Identifier)



The editorial process is managed through the Open Journal System



It is an open access publication (Open Access) licensed Creative Commons



The politics copyright of use postprint, are published in the Self-Archive Policy Repository

Sherpa/Romeo.



The articles of the present edition can be consulted in

<http://revistas.upse.edu.ec/index.php/ingenius>



UNIVERSIDAD POLITÉCNICA SALESIANA DEL ECUADOR

INGENIUS Journal, is indexed in the following Databases and scientific information systems:

SELECTIVE DATABASES



Scopus



Scientific Indexing Services



REVIEWS EVALUATION PLATFORMS



SELECTIVE DIRECTORIES



ULRICHSWEB™
GLOBAL SERIALS DIRECTORY

SELECTIVE SERIAL LIBRARY



SCIENTIFIC LITERATURE SEARCHERS OPEN ACCESS



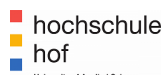
DIRECTORY OF
OPEN ACCESS
JOURNALS



OTHER BIBLIOGRAPHICAL DATABASES



CATALOG OF INTERNATIONAL UNIVERSITY LIBRARIES



UNIVERSITÄT BAMBERG



Dear readers,

Currently, scientific research in science and technology is at a crucial moment of global expansion and collaboration, as reflected in the articles presented in this issue. Coming from diverse academic and geographical backgrounds, these contributions stand out not only for their rigor and relevance, but also for the variety of topics they address, providing a broad and enriching panorama for our scientific community.

From the Universidad Estatal Península de Santa Elena in Ecuador, the work of Torres Guin, Sánchez Aquino, Bustos Gaibor, and Coronel Suárez on IoT architecture for monitoring vehicle emissions using Machine Learning is notable for its innovation in mitigating pollutants, a critical issue for global sustainable development.

On the other hand, from Mexico, the Universidad Popular Autónoma del Estado de Puebla and the Benemérita Universidad Autónoma de Puebla contribute with advanced structural evaluation of mototaxis using simulation tools, led by Cuautle-Gutiérrez, Cordero Guridi, Olivares Rojas, and Pena Preza. This study not only enhances vehicle safety but also demonstrates the potential of simulation tools in automotive applications.

In the energy field, the impact of electric vehicles on electrical distribution systems is explored by Zavala-Tubay, Pico-Mera, and Pico-Mera from Ecuador, offering crucial insights for the transition towards cleaner and more efficient energy.

From the University of Guanajuato, Mexico, Camaraza-Medina investigates radiant heat transfer in H_2O and CO_2 mixtures, contributing to the fundamental understanding of key physical processes with implications across various industries, from environmental to industrial sectors.

In the realm of composite materials, Jiménez-Pereira and Picoita-Camacho, from the Instituto Superior Tecnológico Loja in Ecuador, optimize the VARTM process for prototyping bumpers, highlighting its practical application and relevance in the

automotive industry.

The inclusion of artificial intelligence in medical diagnosis is a crucial topic, as demonstrated by the work of Dávila Olivos, Herrera Del Águila, and Santos López from the National University of San Marcos in Peru, who develop deep learning algorithms for oral cancer diagnosis, improving the accuracy and speed of medical diagnostics.

The experimental analysis of kinematics in elastic collisions, investigated by Arcos Villagómez, Píllalaza, Rivera Gálvez, Michelena Rosero, and Camacho Cañar from the Pontificia Universidad Católica del Ecuador, stands out for its interdisciplinary approach that bridges experimental physics with systems engineering.

From the University of Guanajuato, Trujillo-Romero explores robot localization based on neural networks and visual features, advancing the automation and precision of robotic systems.

From Pakistan, Haider from the Air University Islamabad investigates the structural integrity of combat aircraft wing stations, applying finite element analysis to enhance the safety and performance of critical aircraft components.

Finally, from the Autonomous University of the State of Mexico, Ramírez Vergara, López-Chau, and Rojas Hernández present the design and evaluation of an innovative storytelling system based on Generative Artificial Intelligence (GAI). This system is aimed at children aged 4 to 6 and aims to promote the inclusion of people with disabilities.

Each article reflects not only a commitment to academic excellence but also the diversity of approaches and international collaborations that characterize contemporary research. In our role as editors, it is crucial to promote and celebrate this diversity, ensuring that the voices and perspectives of researchers worldwide are heard and valued. We hope that this special issue inspires new collaborations and scientific advances that benefit global society.

John Calle-Sigüencia, PhD
Editor in Chief

TABLE OF CONTENTS

IoT Architecture for Vehicle Pollutant Gas Emission Monitoring and Validation through Machine Learning	9
Arquitectura de IoT para el monitoreo de emisiones de gases contaminantes de vehículos y su validación a través de Machine Learning	
Washington Torres Guin, José Sánchez Aquino, Samuel Bustos Gaibor, Marjorie Coronel Suárez	
Structural Evaluation of a Three-Wheeler Vehicle Using Simulation Tools: A Case Study in Mexico	18
Evaluación estructural de un vehículo tipo mototaxi usando herramientas de simulación: caso México	
Luis Cuautle-Gutiérrez, José de Jesús Cordero Guridi, Jesús Eduardo Olivares Rojas, Marjorie Nashira Pena Preza	
Electric Vehicles and Their Impact on the Electric Distribution System: A Case Study of the Urban Feeder in Portoviejo	27
Los vehículos eléctricos y su impacto en el sistema eléctrico de distribución: Caso de estudio “Alimentador urbano de la ciudad de Portoviejo”	
Arturo Zavala-Tubay, Hugo Pico-Mera, Gabriel Pico-Mera	
Radiative heat transfer in H₂O and CO₂ mixtures	36
Intercambio térmico radiante en mezclas de H ₂ O y CO ₂	
Yanan Camaraza-Medina	
Optimization of the VARTM Process for Prototyping a Bumper Using Hybrid Composite Materials	48
Optimización del proceso VARTM, para el prototipado de un guardachoque, utilizando materiales compuestos híbridos	
Diego Javier Jiménez-Pereira, Christian Augusto Picoita-Camacho	
Diagnosis of oral cancer using deep learning algorithms	58
Diagnóstico de cáncer oral mediante algoritmos de aprendizaje profundo	
Mayra Alejandra Dávila Olivos, Henry Miguel Herrera Del Águila, Félix Melchor Santos López	
Experimental analysis of the kinematics in the elastic collision between two bodies during the contact time	69
Análisis experimental de la cinemática en la colisión elástica entre dos cuerpos durante el tiempo de contacto	
Suyana Arcos Villagómez, Santiago Álvaro Pillalaza, Xavier Rivera Gálvez,	
César Michelena Rosero, Emilse Camacho Cañar	
Neural network-based robot localization using visual features	77
Localización de robots basada en red neural utilizando características visuales	
Felipe Trujillo-Romero	
Optimizing Structural Integrity of Fighter Aircraft Wing Stations: a Finite Element Analysis Approach	90
Optimización de la integridad estructural de las estaciones de ala de aeronaves de combate: un enfoque de análisis de elementos finitos	
Aun Haider Bhutta	
Storytelling Utilizing Generative AI to Foster Inclusion of Individuals with Disabilities	101
Cuentacuentos basado en IA generativa para promover la inclusión de personas con discapacidades	
Keren Mitsue Ramírez Vergara, Asdrúbal López-Chau, Rafael Rojas Hernández	
Guidelines	114
Normas editoriales	



IoT ARCHITECTURE FOR VEHICLE POLLUTANT GAS EMISSION MONITORING AND VALIDATION THROUGH MACHINE LEARNING

ARQUITECTURA DE IoT PARA EL MONITOREO DE EMISIONES DE GASES CONTAMINANTES DE VEHÍCULOS Y SU VALIDACIÓN A TRAVÉS DE MACHINE LEARNING

Washington Torres Guin^{1,*} , José Sánchez Aquino¹ ,
 Samuel Bustos Gaibor¹ , Marjorie Coronel Suárez¹

Received: 16-11-2023, Received after review: 12-12-2023, Accepted: 16-02-2024, Published: 01-07-2024

Abstract

This study proposes an IoT architecture for monitoring vehicle pollutant gas emissions in response to increasing concerns about air pollution and global warming. The architecture is based on a node equipped with DHT22, MQ9, and MQ135 sensors to capture temperature, humidity, and gas emissions. This node effectively communicates through the LTE network to send the data to the ThingSpeak platform. An analysis of CO_2 , CO, and CH_4 pollution levels is conducted using the collected data. This data is validated through the technical review of a test vehicle. Subsequently, an Artificial Neural Network (ANN) is trained using a specific database of CO_2 emissions from cars in Canada. As a result, a high coefficient of determination (R^2) of 99.2 % is achieved, along with low values of Root Mean Square Error (RMSE) and Mean Squared Error (MSE), indicating that the model makes accurate predictions and fits well with the training data. The ANN aims to predict CO_2 emissions and verify CO_2 data from the IoT network. The architecture demonstrates its capability for real-time monitoring and its potential to contribute to pollution reduction.

Keywords: Vehicle pollution, pollutant gases, IoT, LTE, sensors.

Resumen

Este estudio propone una arquitectura IoT para el monitoreo de emisiones de gases contaminantes en vehículos, en respuesta a la creciente preocupación por la contaminación del aire y el calentamiento global. La arquitectura se basa en un nodo equipado con sensores DHT22, MQ9 y MQ135 para capturar la temperatura, humedad y emisiones de gases, mismo que se comunica de manera efectiva a través de la red LTE para enviar los datos a la plataforma *ThingSpeak*. Se lleva a cabo un análisis de los niveles de contaminación de CO_2 , CO y CH_4 mediante los datos recopilados. Estos datos se validan mediante la revisión técnica de un vehículo de prueba. Posterior, se entrena una red neuronal artificial (ANN) utilizando una base de datos específica de emisiones de CO_2 de vehículos en Canadá, como resultado se obtiene un R^2 alto de 99,2 % y los valores de RMSE y MSE bajos, esto indican que el modelo está haciendo predicciones precisas y se ajusta bien a los datos de entrenamiento. La ANN tiene como objetivo predecir las emisiones de CO_2 y verificar los datos de CO_2 provenientes de la red IoT. La arquitectura demuestra su capacidad para el monitoreo en tiempo real y su potencial para contribuir a la reducción de la contaminación.

Palabras clave: contaminación vehicular, gases contaminantes, IoT, LTE, sensores

^{1,*}Facultad de Sistemas y Telecomunicaciones, Universidad Estatal Península de Santa Elena, Santa Elena, Ecuador.
 Corresponding author ✉: wtorres@upse.edu.ec.

Suggested citation: Torres Guin, W.; Sánchez Aquino, J.; Bustos Gaibor, S.; Coronel Suárez, M. "IoT Architecture for Vehicle Pollutant Gas Emission Monitoring and Validation through Machine Learning," *Ingenius, Revista de Ciencia y Tecnología*, N.º 32, pp. 9-17, 2024, DOI: <https://doi.org/10.17163/ings.n32.2024.01>.

1. Introduction

Accelerated urbanization and increased demand for transportation have exacerbated the environmental issues associated with road transport [1]. Despite a temporary reduction in emissions during 2020 due to the COVID-19 pandemic, global warming continues, accompanied by rising atmospheric pollution [2]. The challenges posed by climate change are global, transcending national borders. Emissions of greenhouse gases such as methane (CH_4), hydrofluorocarbons (HFCs), and carbon dioxide (CO_2) disrupt the balance between the Earth and its atmosphere. Specifically, CO_2 emissions, releasing approximately eight billion tons annually from the combustion of fossil fuels in transportation, heating, and energy production, have become a critical factor in worsening global warming [3]. These emissions primarily originate from industrial and vehicular sources, with passenger cars accounting for 75% of the carbon dioxide emissions [4].

Heavy vehicles, including buses and trucks are responsible for approximately 25% of road emissions. This contribution could increase unless appropriate measures are implemented. Despite stricter regulations to enhance fuel efficiency and reduce greenhouse gas emissions, the number of vehicles on the road has significantly increased. This surge has led to a marked rise in the kilometers these vehicles travel, further exacerbating their impact on atmospheric pollution [5].

Monitoring pollution in the vehicular sector is crucial for several reasons [6,7]. It provides vital data on the sources and intensity of air pollution across public, private, and freight transportation environments. This information is essential for developing policies and strategies to reduce exposure and enhance air quality. Furthermore, such surveillance helps identify practical approaches to address this problem, including the implementation of cleaner fuels and the adoption of advanced technologies. These measures play a critical role in fostering sustainable solutions and promoting healthier urban environments for travelers and the population in general.

The challenge in vehicular transportation arises from the lack of precise and reliable air quality data. This deficiency drives the need to design and test a mobile measurement system capable of addressing these gaps [8]. The capture, processing, and analysis of pollution data in urban transportation are crucial. These processes improve the understanding of air pollution sources and subsequently encourage the development of targeted policies and interventions to address this issue.

Below, we review various IoT proposals for emission monitoring. Senthilkumar et al. [9] describe an integrated system where sensors collect air quality data and transmit it to fog nodes. Moses [10] proposes a cloud-based scheme to monitor air quality using sen-

sors that measure pollutant levels such as NO_x , CO , O_3 , PM_{10} , $PM_{2.5}$, and SO_2 , along with environmental data like humidity and temperature. The collected data is updated in the cloud via a LoRa Gateway infrastructure and LoRa nodes. Time series analysis, support vector regression models, and multilayer perceptron neural networks are used to predict pollutant concentrations. Behal and Singh [11] use the ANFIS method to predict air quality based on pollutant levels and a modified air quality index (m-AQI). A support vector regression model is employed to forecast values, which involves determining a best-fit line that is robust to outliers.

Shetty et al. [12] apply IoT methods to monitor vehicular emission rates and use real-world data on a global scale to forecast carbon monoxide levels. Wei et al. [13] utilize vehicular monitoring to provide owners with details about current pollution levels at their location and their vehicles emission rates, using machine learning techniques to predict pollution based on historical and current data collected by sensors. Mumtaz et al. [14] offer a solution that combines advanced IoT sensors with machine learning capabilities to monitor and predict indoor air quality, thus enabling the measurement of various pollutants. In Mohamed's study [15], an IoT sensor network is employed to detect eight types of pollutants through machine learning techniques, achieving a high accuracy rate of 99.1% in classifying indoor air quality.

Therefore, in a world increasingly aware of the importance of sustainability and reducing environmental pollution, monitoring vehicular emissions has become a critical challenge. The rapid urbanization and expansion of the vehicle fleet have intensified the urgent need to control and mitigate air pollution to preserve environmental quality and safeguard public health. In this context, the Internet of Things (IoT) emerges as a powerful tool that enables real-time data collection and analysis, thus allowing the efficient and effective monitoring and management of vehicular emissions.

This project focuses on developing an IoT architecture for monitoring vehicular emissions of polluting gases, supported by machine learning techniques. This architecture will enable the real-time collection of accurate data on emissions from operating vehicles, along with subsequent analysis and validation of this data using machine learning algorithms. The implementation of this proposal is critically important for several reasons.

- **Emission Control:** Real-time monitoring of vehicle emissions enables identifying and proactively managing pollution sources, which is crucial for achieving air quality objectives and reducing environmental impact.
- **Technology and Sustainability:** The combination of IoT and Machine Learning constitutes an

advanced technological approach that enhances sustainability and illustrates how innovation can drive positive change in society.

2. Materials and Methods

The proposed architecture and its constituent elements for constructing the sensor node for gas acquisition in a test vehicle, specifically a 2012 Kia Sportage, are presented in the following section.

2.1. Proposed IoT Architecture

In this Internet of Things (IoT) architecture (see Figure 1), a complete system is designed to monitor vehicle emissions of polluting gases, referencing the proposals in [16, 17]. The architecture comprises several layers that work together to collect, store, and validate emission data.

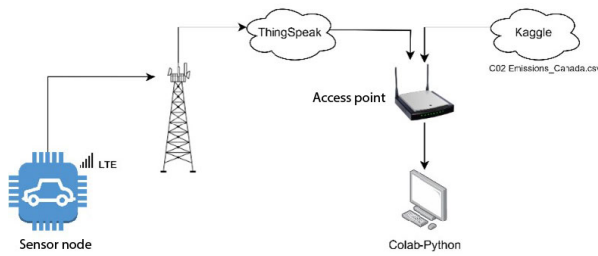


Figure 1. IoT Architecture for Pollutant Gas Monitoring.

Below, the architecture is described considering its layers and functionality:

- **Perception Layer:** In the perception layer, a node equipped with a DHT22 temperature sensor along with MQ-135 and MQ-9 gas sensors, is utilized for gas detection. This node captures real-time temperature, humidity, and air pollutant concentration data.
- **Network Layer:** The network or communication layer is essential for transmitting the data captured by the sensor node. The LTE network has been selected as the communication medium, offering reliable connectivity, wide coverage for the sensor node, and potential network scalability.
- **Application Layer:** In the application layer, the IoT platform ThingSpeak has been integrated to store and manage the data collected by the sensors. ThingSpeak provides a user-friendly interface and enables secure data storage via the HTTP protocol, thus facilitating subsequent access and analysis.

- **Data Analysis:** Once the data has been uploaded to ThingSpeak, a more detailed analysis is conducted to verify the distribution of carbon dioxide (CO_2), carbon monoxide (CO), and methane (CH_4) emission data. Colab, a Python programming collaboration platform, is utilized for this purpose.

- **Data Validation:** A comprehensive verification process is conducted to ensure the accuracy of the data captured by the sensors, including tests based on the technical inspection of a test vehicle. Additionally, regression analysis is performed using a Canadian-origin CO_2 emissions database as a reference point to verify the data received from the IoT platform. This procedure facilitates comparison, validation, and prediction.

2.2. Design of the Sensor Node

The sensor node design (Figure 2) incorporates the LILYGO® TTGO T-Call V1.4 controller, which features a variety of essential functionalities. This device provides LTE network connectivity via a SIM800L module and leverages the ESP32 for wireless capabilities, including Wi-Fi and Bluetooth. Additionally, the sensor node includes a built-in GPS positioning system, enabling precise geolocation of measurements. The sensors, carefully chosen for their accuracy, include the DHT22 sensor for measuring environmental temperature and humidity. Meanwhile, the MQ135 and MQ9 sensors detect concentrations of CO, CO_2 , and methane (CH_4). It should be noted that the DHT22 sensor is connected to a digital port on the controller, whereas the MQ135 and MQ9 sensors are connected to analog ports, offering a versatile interface for data acquisition. This comprehensive configuration allows for precise measurement and collection of critical data necessary for monitoring vehicular pollutant gas emissions.

The DHT22 sensor operates within a voltage range of 3.3–5 VDC and can measure relative air humidity from 0 to 99% RH with an accuracy of $\pm 2\%$ (at $25^\circ C$) and a resolution of up to 0.1%. It measures temperature within a range of $-40^\circ C$ to $80^\circ C$, with an accuracy of $\pm 0.5^\circ C$ and a resolution of $0.1^\circ C$. The sensor refreshes at a rate of 1 Hz (reporting every 1 second) and employs the Wire protocol for its operation. Its functionality is supported by the DHT.h library.

The MQ-135 sensor operates through a specific detection mechanism involving gas interactions, which result in variations in its electrical resistance. Although the sensor does not inherently discriminate between gases, it can be calibrated and configured to detect specific gases based on their unique response patterns. By precisely adjusting the sensor parameters and applying advanced signal processing techniques, it becomes

possible to distinguish between various gases and their concentrations, thereby enabling effective differentiation between gases such as CO and CO_2 . According to the technical information provided by the sensor, the load resistance is $20.1\text{ k}\Omega$, and the resistance in clean air conditions is $10\text{ k}\Omega$. Considering this data, Figure 3 illustrates the sensor calibration curve along with the model equation, where R_0 is defined as the constant representing the sensor resistance in response to a concentration of 0.4 mg/L , and R_s denotes the sensor resistance in another context.

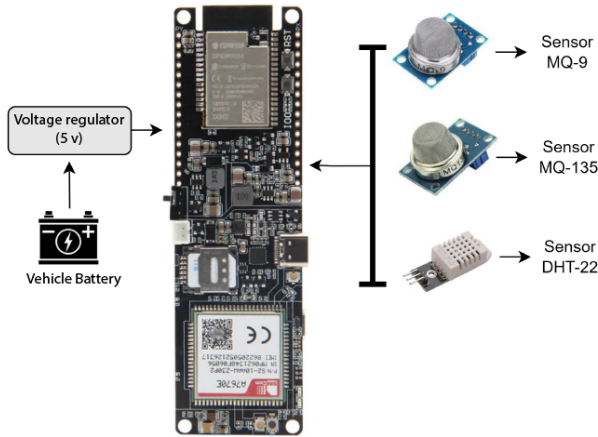


Figure 2. IoT Sensor Node.

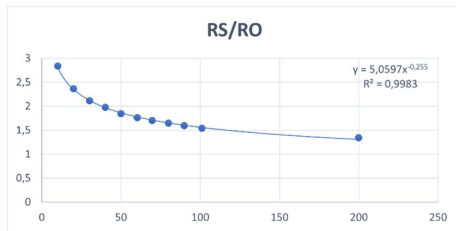


Figure 3. Calibration Curve of the MQ-135 Sensor.

The MQ-9 sensor was used to determine methane concentration (CH_4). The sensor's analog output data is transmitted to the controller's analog input. The conversion of this data by the analog-to-digital converter (ADC) occurs within a range of 0 to 3.3 V. The characteristics and specifications, such as load and resistance in fresh air, are similar to those of the MQ-135, as both sensors originate from the same manufacturer and share identical values. Consequently, the same configurations are utilized.

2.3. Implementation of the Sensor Node into the Vehicle

The IoT sensor node is positioned following the indications provided in Figure 4, allowing for strategic placement of the sensors directly at the vehicle's exhaust

pipe outlet. The controller in contrast, is securely installed inside the car, establishing a direct connection with the onboard computer. This connection facilitates real-time visualization of the data captured by the sensor. Moreover, the sensor is connected to the ThingSpeak platform via LTE technology, utilizing the HTTP protocol for efficient data transmission and storage. This comprehensive design allows for effective monitoring of vehicle pollutant gas emissions, thereby providing valuable real-time information. For power supply, the device is connected to the vehicle's battery.

In Figure 5, the physical sensor node installed in the vehicle is depicted for sample collection.

In Figure 6, the placement of sensors on the vehicle's exhaust pipe is visible.

It is essential to highlight that GPS is used to visualize the precise position of the vehicle and obtain a detailed record of its path.

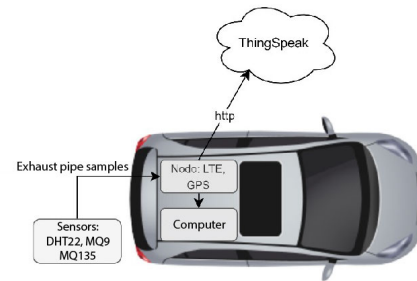


Figure 4. Arrangement of the IoT Sensor Node in the Vehicle.

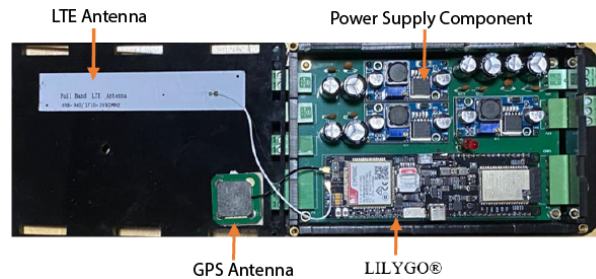


Figure 5. IoT Sensor Node Installed.

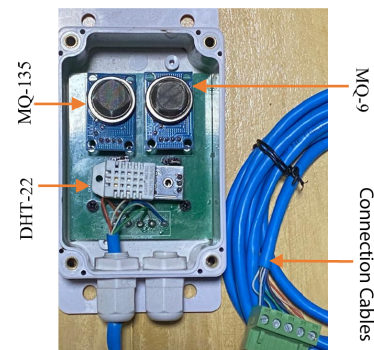


Figure 6. Sensors for Data Collection.

3. Results and Discussion

Firstly, the results obtained from the 50 samples collected from the exhaust pipe with the engine idling and undergoing specific changes in revolutions, are presented to illustrate the variability in data collection. These samples reveal the levels of pollutants, specifically CH_4 (methane), CO_2 , and CO. The data from sensors, expressed in parts per million (ppm), provide detailed insight into the emissions.

Upon analysis, it is observed that the concentration of CH_4 (see Figure 7) varies approximately between 45 and 65 ppm, reflecting the data distribution. Additionally, Figure 8 highlights that CO oscillations range from 26,000 to 38,000 ppm, while CO_2 levels fluctuate between 121,000 and 140,000 ppm.

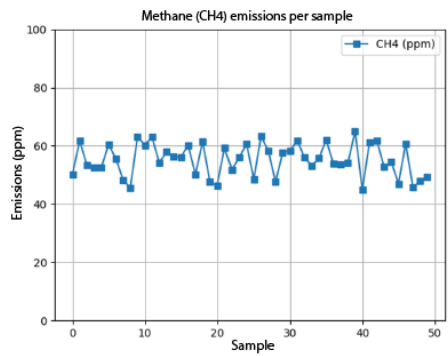


Figure 7. Graph of the data for CH_4 .

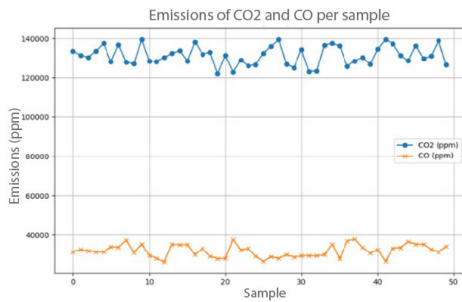


Figure 8. Graph of the data for CO and CO_2 .

It is worth noting that these values fall within the specified ranges, as mentioned in the study [17]. These findings emphasize the importance of closely monitoring vehicle emissions to gain a clear understanding of engine pollutant variability. Importantly, the samples are collected approximately every 3 to 4 minutes, reflecting the time required for the controller to process and upload the data to the ThingSpeak platform.

The graphical representation of temperature and humidity data was not performed because these parameters do not vary abruptly according to the sensor position in the exhaust pipe. During measurements,

the temperature displayed minimal oscillations, consistently ranging from approximately 30 to 37°C. Simultaneously, humidity exhibited a similar stability, fluctuating between 80% and 99%.

The data capture validation was performed through a comprehensive technical inspection of a 2012 Kia Sportage SUV used as the test vehicle. This evaluation yielded CO_2 concentrations ranging from 12% to 14%, with the engine idling and CO concentrations ranging from 2.6% to 3.8%. According to Segura [18], this information can be utilized to estimate emissions in ppm, assigning CO_2 an estimated maximum level of 140,000 ppm and CO a maximum of 38,000 ppm.

This information supports the reliability of the collected data, as the vehicle technical inspection as the results from the vehicle technical inspection are consistent with the measurements obtained by the sensors. The precise calibration of the sensors for capturing these gases improves the accuracy of the estimations, thereby confirming that the concentration of CH_4 is also accurate and reliable.

To evaluate the vehicle's pollution level, focusing on CO_2 as a crucial reference variable due to its significant contribution to vehicle emissions, a conversion is performed to calculate the units in grams of pollution per kilometer traveled (g/km). The importance of this data is underscored by its verification against the vehicle's technical specifications, which specify a pollution level of 158 g/km of CO_2 in urban environments.

Therefore, to calculate the amount of carbon dioxide (CO_2) released per kilometer traveled, if the vehicle exhibits a CO_2 concentration of 14%, this percentage indicates that 14% of the gas volume in the vehicle's exhaust pipe consists of CO_2 . The remaining 86% comprises other types of exhaust gases, such as nitrogen, oxygen, and unburned hydrocarbons (HC), among others.

To accurately calculate the amount of CO_2 emitted, several factors must be considered, including the vehicle's efficiency, the volume of fuel consumed, and the amount of CO_2 generated per liter of fuel burned.

Vehicle efficiency: This parameter is derived from the vehicle's technical specifications, which indicate a fuel consumption rate of 5.7 liters per 100 kilometers.

Amount of CO_2 per liter of fuel: The amount of CO_2 produced by burning one liter of gasoline varies depending on the fuel's exact composition. In this case, it amounts to approximately 2.8 kg of CO_2 per liter of gasoline. Using these parameters, we then apply the following equation (1) to calculate the CO_2 emissions in g/km.

$$\begin{aligned} CO_2 \left(\frac{g}{km} \right) &= C_{l/km} * CO_{2kg/l} * 100_{g/kg} \\ CO_2 \left(\frac{g}{km} \right) &= 0.057_{l/km} * 2,8_{\frac{kg}{l}} * 100_{\frac{g}{kg}} \\ &= 159,6 \text{ g/km} \end{aligned} \quad (1)$$

This calculation provides a close approximation to the vehicle's technical specifications, which estimate CO_2 emissions at 158 g/km.

With this established conversion data, an Artificial Neural Network (ANN) model is developed to predict potential emissions of pollutant gases in the automotive fleet. For this purpose, a dataset from Kaggle [19] that contains information on vehicle pollutant gas emissions in Canada is utilized. This dataset was selected because it includes information about the vehicle used in our sensor tests. Consequently, a learning model is tailored to our specific scenario, enabling the prediction of CO_2 pollution levels.

The database includes essential parameters such as make, model, vehicle class, engine size, number of cylinders, transmission type, fuel type, fuel consumption in the city (L/100 km), fuel consumption on highways (L/100 km), as well as CO_2 emissions measured in grams per kilometer (g/km). During the analysis, correlations between these parameters and CO_2 emissions are evaluated to identify the variables that have the most significant relationships. Variables demonstrating notable correlations are selected for training the Artificial Neural Network (ANN) model, thereby focusing the model on the features that most significantly influence CO_2 emissions and improving its predictive capability.

This correlation is illustrated in Figure 9, which shows that the variables engine size, number of cylinders, fuel consumption in the city, and fuel consumption on highways exert the most significant influence on CO_2 emissions.

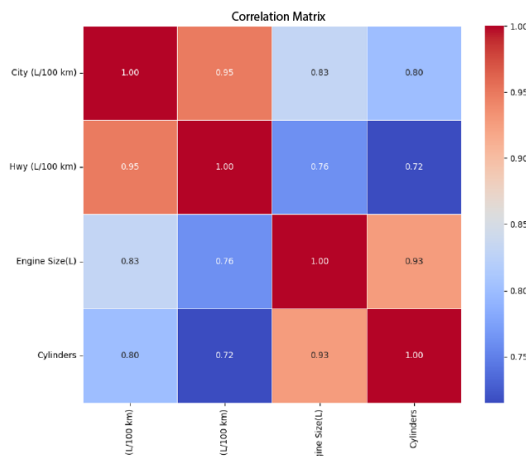


Figure 9. Correlation of Variables Influencing CO_2 Emissions.

Progress is made in developing a machine learning model using an Artificial Neural Network (ANN) based on the information obtained from the correlation analysis. This model is configured using the TensorFlow library in Python, as outlined in the following structure (see Figure 10).

Model: "sequential"

Layer (type)	Output Shape	Param #
dense (Dense)	(None, 64)	6464
dense_1 (Dense)	(None, 32)	2080
dense_2 (Dense)	(None, 16)	528
dense_3 (Dense)	(None, 1)	17
Total params: 9,089		
Trainable params: 9,089		
Non-trainable params: 0		

Figure 10. Structure of the ANN.

The model structure is defined as sequential, indicating a neural network architecture where the layers are arranged in sequence. It comprises four densely connected layers (Dense), labeled $dense_1$, $dense_2$, and $dense_3$. The first layer contains 64 neurons, the second 32, the third 16, and the output layer includes a single neuron. Each layer utilizes the 'relu' (Rectified Linear Unit) activation function, except for the output layer, which employs the 'linear' activation function suitable for CO_2 emissions. The parameters are automatically calculated and detailed in Figure 10, which displays the number of trainable parameters and the total sum of parameters, amounting to 9,089. These parameters represent the weights and biases of the neural network that are adjusted during the training process to optimize the model's performance.

Following the model training, Figure 11 illustrates the model's loss over the training sessions. It shows that as the epochs progress, there is a predictable decrease in loss and an increase in accuracy, suggesting that the model is successfully learning and improving its ability to make accurate predictions. Therefore, Figure 11 confirms that the model is appropriately trained.

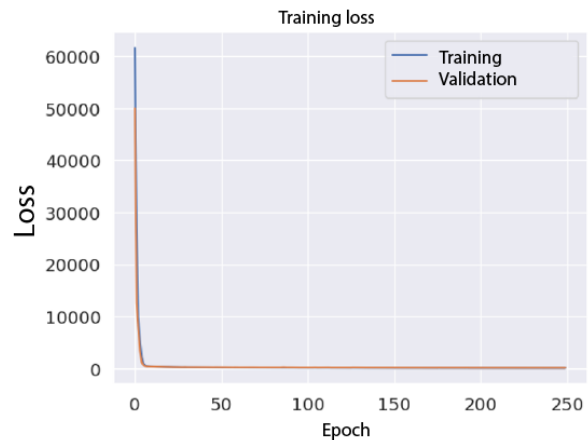


Figure 11. Loss During Training.

Then, to assess the performance of a machine learning model in its predictions, it is essential to measure its accuracy. It is achieved through the use of performance metrics such as the root mean square error

(RMSE), the mean square error (MSE), and the coefficient of determination (R squared). These metrics help confirm the accuracy of regression models [19] and play a crucial role in evaluating and refining learning models, enabling a deeper understanding of their ability to explain and predict data. These metrics are presented below in equation (2):

To assess the predictive performance of a machine learning model, it is crucial to measure its accuracy. This is accomplished by employing performance metrics such as the root mean square error (RMSE), the mean square error (MSE), and the coefficient of determination (R-squared). These metrics are instrumental in verifying the accuracy of regression models [19] and play an essential role in evaluating and refining learning models. They enable a deeper understanding of the models' capabilities to explain and predict data. These metrics are presented below in Equation (2):

$$\begin{aligned} MSE &= \frac{1}{n} \sum_{i=1}^n \left(y_{real}^{(i)} - y_{pred}^{(i)} \right)^2 \\ RMSE &= \sqrt{\frac{1}{n} \sum_{i=1}^n \left(y_{real}^{(i)} - y_{pred}^{(i)} \right)^2} \\ R^2 &= 1 - \frac{SS_{res}}{SS_{tot}} \end{aligned} \quad (2)$$

Where SS_{res} is the sum of the squares of the discrepancies between the observed and predicted values. SS_{tot} represents the sum of the squares of the differences between the observed values and their mean. An R^2 value close to 1 indicates a good fit of the model, whereas a value close to 0 suggests that the model does not adequately explain the data's variability.

The results of the model metrics are auspicious: the coefficient of determination (R^2) reaches an outstanding 0.992, indicating an exceptional ability to explain the variability in the data. The mean squared error (MSE) is at 20.59, demonstrating a reasonably low average magnitude of squared errors, meanwhile, the root mean squared error (RMSE) stands at 4.53, confirming significant accuracy in the model's predictions. These results underscore the model's robust capability to forecast emissions of pollutant gases in the automotive fleet, affirming its suitability for predictive applications. These values are illustrated in Figure 12.

Coefficient of determination (R^2): 0.9922332006414919
Mean Squared Error (MSE): 20.59925370801521
Root Mean Squared Error (RMSE): 4.538640072534416

Figure 12. Results of the model metrics.

To evaluate the effectiveness of the developed model, a test comparing the actual values of pollutant gas emissions with the predictions generated by the neural network was conducted (Figure 13). This visual analysis sought the proximity of the points to an ideal diagonal line, representing perfect prediction. The dispersion and distribution of points on the graph

facilitate a quick assessment of the model's ability to capture variability in the actual data. Alignment close to the diagonal indicates precise predictions, while significant dispersion suggests areas for improvement in the model's predictive accuracy. This approach provides an intuitive and visual assessment of the quality of the model's predictions relative to the actual data.

Therefore, implementing an Artificial Neural Network (ANN) to monitor vehicle pollutant gas emissions significantly enhances and effectively complements conventional monitoring methods. Unlike simpler, linear approaches, ANNs can capture complex nonlinear relationships in the data, thereby offering improved prediction accuracy. They dynamically adapt to changes, providing more robust and flexible monitoring. Furthermore, ANNs efficiently process multidimensional and complex data, simultaneously handling multiple inputs such as temperature, humidity, and various gas emissions. The potential for machine learning and continuous improvement enables ongoing enhancements in accuracy as more data on vehicle emissions are collected.

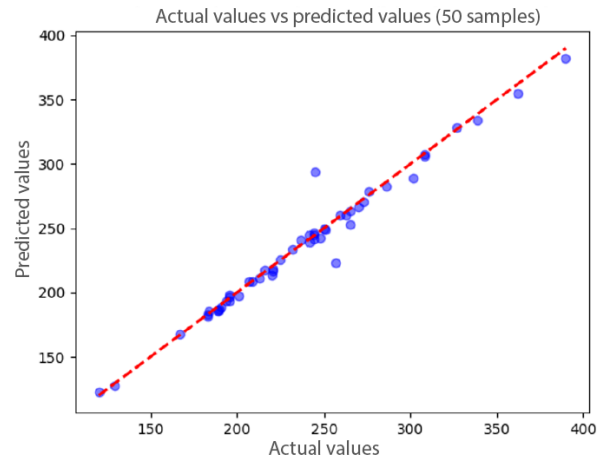


Figure 13. Model Testing.

4. Conclusions

This article thoroughly examines the monitoring of pollutant gas emissions in vehicles, from the construction of a dedicated sensor node for data collection to the development of an Artificial Neural Network (ANN) model for predicting CO_2 emissions. The implementation of the sensor node, equipped with DHT22, MQ9, and MQ135 sensors, has proven effective in capturing critical data such as temperature, humidity, and gas concentrations during tests on a 2012 Kia Sportage SUV. The validation of these data, conducted through a technical vehicle review, confirms the accuracy and reliability of the measurements.

Subsequently, an ANN model was utilized, leveraging vehicle emissions data from Canada and focusing

on key variables identified through correlation analysis. The model results, boasting a remarkable coefficient of determination (R^2) of 99.2%, underscore its ability to predict CO_2 emissions accurately. These findings demonstrate the effectiveness of integrating advanced sensor technologies with machine learning models, providing a robust approach for monitoring and predicting vehicle emissions, thereby contributing to the management and mitigation of environmental pollution.

For future work, the proposed architecture will be implemented in urban buses, where the Artificial Neural Network (ANN) is expected to significantly enhance air quality control and vehicle condition monitoring. This implementation will facilitate more effective management of circulation policies and planning.

References

- [1] J. Krause, C. Thiel, D. Tsokolis, Z. Samaras, C. Rota, A. Ward, P. Prenninger, T. Coosemans, S. Neugebauer, and W. Verhoeve, "EU road vehicle energy consumption and CO_2 emissions by 2050 – Expert-based scenarios," *Energy Policy*, vol. 138, p. 111224, 2020. [Online]. Available: <https://doi.org/10.1016/j.enpol.2019.111224>
- [2] M. M. Ajmal, M. Khan, M. K. Shad, H. AlKatheeri, and F. Jabeen, "Empirical examination of societal, financial and technology-related challenges amid COVID-19 in service supply chains: evidence from emerging market," *The International Journal of Logistics Management*, vol. 34, no. 4, pp. 994–1019, Jan 2023. [Online]. Available: <https://doi.org/10.1108/IJLM-04-2021-0220>
- [3] J. Lynn and N. Peeva, "Communications in the IPCC's Sixth Assessment Report cycle," *Climatic Change*, vol. 169, no. 1, p. 18, Nov 2021. [Online]. Available: <https://doi.org/10.1007/s10584-021-03233-7>
- [4] Z. Yang and A. Bandivadekar, *Light-duty vehicle greenhouse gas and fuel economy standards*. The International Council on clean Transportation, 2017. [Online]. Available: <https://bit.ly/4anzh8u>
- [5] R. Guensler, "Data needs for evolving motor vehicle emission modeling approaches," *The University of California, Transportation Center*, 1993. [Online]. Available: <https://bit.ly/3THURO5>
- [6] Y. Lu, *Traffic-Related PM_{2.5} Air Pollution and Schools in Proximity to Major Roadways in Shanghai, China*. University of Washington, Department of Urban Design and Planning, 2016. [Online]. Available: <https://bit.ly/43KjOgq>
- [7] N. Kozarev and N. Ilieva, "Plume rise in particular meteorological conditions," *Journal of the University of Chemical Technology and Metallurgy*, vol. 46, pp. 305–308, 01 2011. [Online]. Available: <https://bit.ly/3VLqMQ3>
- [8] N. Barmpareos, V. D. Assimakopoulos, M. N. Assimakopoulos, and E. Tsairidi, "Particulate matter levels and comfort conditions in the trains and platforms of the Athens underground metro," *AIMS Environmental Science*, vol. 3, no. 2, pp. 199–219, 2016. [Online]. Available: <https://doi.org/10.3934/environsci.2016.2.199>
- [9] R. Senthilkumar, P. Venkatakrishnan, and N. Balaji, "Intelligent based novel embedded system based IoT enabled air pollution monitoring system," *Microprocessors and Microsystems*, vol. 77, p. 103172, 2020. [Online]. Available: <https://doi.org/10.1016/j.micpro.2020.103172>
- [10] L. Moses, Tamilselvan, Raju, and Karthikeyan, "IoT enabled Environmental Air Pollution Monitoring and Rerouting system using Machine learning algorithms," *IOP Conference Series: Materials Science and Engineering*, vol. 955, no. 1, p. 012005, nov 2020. [Online]. Available: <https://dx.doi.org/10.1088/1757-899X/955/1/012005>
- [11] V. Behal and R. Singh, "Personalised healthcare model for monitoring and prediction of airpollution: machine learning approach," *Journal of Experimental & Theoretical Artificial Intelligence*, vol. 33, no. 3, pp. 425–449, 2021. [Online]. Available: <https://doi.org/10.1080/0952813X.2020.1744197>
- [12] C. Shetty, B. Sowmya, S. Seema, and K. Srinivasa, "Chapter eight - air pollution control model using machine learning and IoT techniques," in *The Digital Twin Paradigm for Smarter Systems and Environments: The Industry Use Cases*, ser. Advances in Computers, P. Raj and P. Evangeline, Eds. Elsevier, 2020, vol. 117, no. 1, pp. 187–218. [Online]. Available: <https://doi.org/10.1016/bs.adcom.2019.10.006>
- [13] "Guest Editorial: Special Section on Integration of Big Data and Artificial Intelligence for Internet of Things," *IEEE Transactions on Industrial Informatics*, vol. 16, no. 4, pp. 2562–2565, 2020. [Online]. Available: <https://doi.org/10.1109/TII.2019.2958638>
- [14] R. Mumtaz, S. M. H. Zaidi, M. Z. Shakir, U. Shafi, M. M. Malik, A. Haque, S. Mumtaz, and S. A. R. Zaidi, "Internet of Things (IoT) Based Indoor Air Quality Sensing and Predictive

- Analytic—A COVID-19 Perspective,” *Electronics*, vol. 10, no. 2, 2021. [Online]. Available: <https://doi.org/10.3390/electronics10020184>
- [15] M. Abdel-Basset, G. Manogaran, M. Mohamed, and E. Rushdy, “Internet of things in smart education environment: Supportive framework in the decision-making process,” *Concurrency and Computation: Practice and Experience*, vol. 31, no. 10, p. e4515, 2019. [Online]. Available: <https://doi.org/10.1002/cpe.4515>
- [16] M. Montaña Blacio, J. González-Escarabay, O. Jiménez-Sarango, L. Mingo-Morocho, and C. Carrión-Aguirre, “Design and deployment of an IoT-based monitoring system for hydroponic crops,” *Ingenius. Revista de Ciencia y Tecnología*, no. 30, pp. 9–18, 2023. [Online]. Available: <https://doi.org/10.17163/ings.n30.2023.01>
- [17] M. Montaña Blacio, V. García Santos, D. Jaramillo Chamba, W. Torres Guin, and L. Chuquimarca Jiménez, “Empowering Low-Power Wide-Area Networks: Unlocking the Potential of Sigfox in Local Transmission,” in *Advanced Research in Technologies, Information, Innovation and Sustainability*, T. Guarda, F. Portela, and J. M. Diaz-Nafria, Eds. Cham: Springer Nature Switzerland, 2024, pp. 417–429. [Online]. Available: https://doi.org/10.1007/978-3-031-48930-3_32
- [18] J. K. Segura Gómez, *Prototipo de un sistema IoT para medición de gases de efecto invernadero*. Universidad Santo Tomás. Colombia, 2021. [Online]. Available: <https://bit.ly/3J4OvDl>
- [19] Kaggle. (2020) CO₂ Emission by Vehicles. Kaggle. [Online]. Available: <https://bit.ly/3J7Navw>



STRUCTURAL EVALUATION OF A THREE-WHEELER VEHICLE USING SIMULATION TOOLS: A CASE STUDY IN MEXICO

EVALUACIÓN ESTRUCTURAL DE UN VEHÍCULO TIPO MOTOTAXI USANDO HERRAMIENTAS DE SIMULACIÓN: CASO MÉXICO

Luis Cuautle Gutiérrez¹ , José de Jesús Cordero Guridi^{1,*} ,
 Jesús Eduardo Olivares Rojas¹ , Nashira Pena Preza²

Received: 14-05-2023, Received after review: 28-03-2024, Accepted: 23-04-2024, Published: 01-07-2024

Abstract

The mototaxi, a three-wheeled vehicle equipped with a roof, is a widely utilized mode of transportation in Mexico. Typically, it is employed for short-distance journeys in exchange for payment, similar to the operation of a conventional taxi. This study conducts a structural analysis of a mototaxi-type vehicle utilized in Mexico to assess its performance and safety. It underscores the significance of this mode of transportation, widely relied upon by numerous individuals. A product design and development methodology was employed, utilizing torsional deformation simulations to validate the new geometry. The objective was to minimize torsions as much as possible, thereby enhancing the motorcycle taxi's safety and ensuring the vehicle's correct positioning. Through computer-aided design, the prevailing torsions within the casing were assessed, establishing the operating conditions to which the system is commonly subjected. The findings from the chosen vehicular structure reveal a flexural rigidity of 6,508.15 N/mm, torsional rigidity of 27.35 KNm/°, and a range of natural frequencies between 8-21 Hz. These values indicate favorable resistance against bending forces and operational frequency. However, the torsional results exhibit deficiencies, suggesting an unsafe structure for all motorcycle taxi occupants. Consequently, technology developers and national legislators should prioritize enhancing the structural integrity of such vehicles.

Keywords: Structural, Mototaxi, Safety, ANSYS, CAE, Simulation

Resumen

El mototaxi es un vehículo de tres ruedas y con techo que se usa como medio de transporte popular en México, generalmente para recorrer caminos cortos a cambio de dinero, de la misma forma que opera un taxi. Esta investigación presenta el análisis estructural de un vehículo tipo mototaxi empleado en México, para evaluar su desempeño y seguridad, teniendo en cuenta que es un medio de transporte utilizado por muchas personas. Se empleó una metodología de diseño y desarrollo de producto, utilizando simulaciones de deformación torsionales para validar la nueva geometría, minimizando las torsiones en lo posible, tratando de mejorar la seguridad del mototaxi, así como la posición correcta del vehículo. Mediante el diseño asistido por computadora se probaron las torsiones existentes en la carcasa, determinando las condiciones de operación por las que generalmente es sometido el sistema. Los resultados obtenidos en la estructura vehicular seleccionada son para la rigidez por flexión de 6508,15 N/mm, la rigidez torsional de 27,35 KNm/° y el rango de frecuencias naturales en 8-21 Hz, valores que muestran que la estructura presenta condiciones favorables mediante esfuerzos de resistencia por flexión y la frecuencia de operación de la estructura, pero carencias en los resultados torsionales, generando así una estructura insegura para los ocupantes del mototaxi. Es necesario que los desarrolladores de tecnología como los legisladores nacionales actúen en favor de mejorar sus condiciones estructurales.

Palabras clave: estructural, mototaxi, seguridad, ANSYS, CAE, simulación

^{1,*}Facultad de Ingeniería Industrial, Logística, Manufactura y Automotriz, Universidad Popular Autónoma del Estado de Puebla, México. Corresponding author ✉: josejesus.cordero@upaep.mx.

²Benemérita Universidad Autónoma de Puebla – México.

Suggested citation: Cuautle Gutiérrez, L.; Cordero Guridi, J. J.; Olivares Rojas, J. E. and Pena Preza, N. "Structural Evaluation of a Three-Wheeler Vehicle Using Simulation Tools: A Case Study in Mexico," *Ingenius, Revista de Ciencia y Tecnología*, N.º 32, pp. 18-26, 2024, DOI: <https://doi.org/10.17163/ings.n32.2024.02>.

1. Introduction

The insufficient supply and restricted public transportation coverage in developing countries have prompted the emergence of mototaxism in numerous cities worldwide, wherein motorcycles are utilized as a form of public transportation.

A mototaxi, characterized by its three-wheeled structure and roof, is a cost-effective means for individuals to fulfill their mobility requirements, akin to traditional taxis. It fills a unique niche in transportation services, catering to entire journeys and the initial and final segments of trips in densely populated, congested, or otherwise inaccessible areas. These trips are often too lengthy and challenging to traverse by foot yet fall short of commercial viability for conventional public transportation modes.

The inception of the mototaxi occurred in Paris in 1999, representing an innovative and efficient transportation solution aimed at addressing the travel requirements of passengers commuting between the city's two airports [1].

For approximately two decades, this mode of transportation has been present in Mexico City and various states of the Republic, predominantly in the form of motorcycles equipped with a canopy and cabin-incorporated motocarros [2].

The mototaxi caters to particular yet unfulfilled transportation demands and functions more as a supplementary service than a direct competitor to other public transportation modes. Its primary advantage lies in its lightweight construction, speed, and ease of parking, enabling users to traverse short distances more efficiently. According to the National Institute of Statistics and Geography, over 273,000 mototaxi trips occur daily in Mexico City and its metropolitan region, constituting 3.7% of all public transportation journeys [3].

In Juchitán de Zaragoza, Oaxaca, Mexico, the King model is frequently employed as a mototaxi owing to its versatile chassis, instrumentation, engine, power, and torque capabilities. This model achieves a maximum speed of 56 kilometers per hour and has a curb weight of 300 kilograms [4].

Mototaxis belong to the classification of small motor vehicles, alongside mopeds, scooters, motorcycles, motorized tricycles, quad bikes, and analogous vehicles [5].

The mototaxi industry grapples with numerous challenges, encompassing congestion, road infrastructure, regulatory standards, and safety considerations [6].

On a global scale, the utilization of mototaxis has adversely affected the environment, social dynamics, and road safety.

The adverse environmental impacts primarily stem from pollutant emissions resulting from inadequate

vehicle maintenance and the use of low-quality fuel [7].

In the State of Mexico, mototaxis serve as sources of informal employment for both men and women, offering an average weekly income of \$1236 to drivers. These drivers typically possess a secondary or high school education, with common-law marriage being the most prevalent marital status [8]. Puebla has over ten thousand estimated mototaxi drivers across over sixty municipalities [9].

Regarding road safety issues, mototaxis are responsible for numerous severe traffic accidents.

Table 1 presents some characteristics of these vehicles that highlight the safety issues associated with them.

Table 1. Characteristics of Mototaxis

Characteristic	Description
Availability	High (general community)
Capacity	Six occupants (6), plus luggage
Comfort	Low
Safety	Low (traffic accidents)
Cabin Space	Limited
Traffic Accidents	Severe due to lack of safety equipment (helmet, seat belts, airbags).
Noise	High. This can cause hearing damage due to high decibel levels.

Moreover, the chassis is commonly regarded as the vehicle's skeleton, as it accommodates the components necessary for proper operation. The chassis must possess sufficient strength to withstand impacts, torsion, vibrations, and other stresses encountered during operational activities.

Another crucial aspect concerns legislation, as all vehicles operating on public roads must adhere to specific regulations established by some institutions and laws. In numerous Mexican states, mototaxis remain largely unregulated. However, in the state of Puebla, guidelines governing mototaxis are outlined in the transportation law, particularly in articles 12 and 37 [10].

Hence, this study aims to assess the structural integrity of this mode of transportation to ascertain the level of safety provided by service providers to their users.

2. Materials and method

A product design and development methodology was employed to assess the performance and safety of the mototaxi-type vehicle, utilizing a digital model of the three-wheeled vehicle structure. The study proceeded through the following phases: benchmarking, technical characterization, development of the analysis model, and structural evaluation.

Four prominent brands in Mexico, including TSV, ATUL, KingWay, and Bajaj and their primary models

were examined during the benchmarking phase. Eight key characteristics were analyzed, including maximum power, maximum torque, fuel consumption, load capacity, brakes, chassis, and stabilizer bar, as detailed in Table 2.

Table 2. Evaluation of Mototaxi Brands

Characteristic	TSV	ATUL	KingWay	Bajaj
Suspension	4	4	3	4
Load Capacity	5	3	4	3
Fuel Consum.	2	3	4	2
Brake System	3	3	3	3
Transmission	3	3	4	3
Dimensions	3	4	3	3
Chassis	4	3	2	5
Cooling System	5	4	3	4
Maintenance	5	4	4	4

Using the acquired data, each vehicle underwent an evaluation to ascertain the one possessing superior attributes. In this subsequent phase, nine characteristics were considered as delineated by the authors. Ratings were assigned on a 5-point scale, with 1 representing deficiency and 5 indicating optimal performance, as outlined in Table 2. The TSV brand, specifically the King Duramax model, attained the highest score.

The ratings were determined through consensus among the authors. Based on the averaged scores, the King Duramax was selected with a rating of 3.71. It is noteworthy that the results were closely aligned, as the four models under scrutiny exhibited very comparable characteristics and performance, thereby sharing similar attributes.

In the technical characterization, the TVS Group, an Indian company ranking third globally, is India's largest manufacturer of two-wheeled vehicles, with its products being exported to over sixty countries. Renowned for delivering high-quality vehicles that cater to customer requirements, TVS has established Motocarros TVS in Mexico. This branch, dedicated to the distribution of three-wheeled vehicles, operates under Kawasaki with the backing of Grupo Motomex.

The selected unit was the King Duramax 2020, shown in Figure 1. Based on the obtained data, each vehicle was rated to determine the one with the best qualities. For this new stage, nine characteristics defined by the authors were considered. The ratings were on a 5-point scale where 1 is deficient and 5 is optimal, as presented in Table 2. The highest score was obtained by the TSV brand, with the King Duramax model.

The ratings were assigned by consensus among the authors. According to the averages obtained, the King Duramax was chosen with a score of 3.71. It is important to mention that the results were very close because the four analyzed models have very similar

characteristics and performance, thus having similar elements.

In the technical characterization, the TVS Group, an Indian company that ranks third, is the largest manufacturer of two-wheeled vehicles in India, currently exporting to more than sixty countries. It is a company known for offering quality vehicles that anticipate customer needs. In Mexico, Motocarros TVS, the branch dedicated to the commercialization of three-wheeled vehicles, is part of Kawasaki with the support of Grupo Motomex.

The chosen unit was the King Duramax 2020, as illustrated in Figure 1.



Figure 1. King Duramax 2020 [11].

Table 3 presents some of its technical features.

Table 3. Technical Characteristics of the King Duramax 2020

Property	Value
Maximum Power	10 Hp @ 4750 RPM
Maximum Torque	18 Nm @ 2750 RPM
Displacement	225 cc
Maximum Speed	63 km/h
Brake Type	Hydraulic drum
Structure Type	Semi-monocoque formed by longitudinal and transverse pressed elements
Structure Material	Metal
Curb Weight	399 kg
Ground Clearance (loaded)	169 mm
Dimensions	Length: 2647 mm Width: 1329 mm Height: 1740 mm

During the development stage of the CAD analysis model, CAD and CAE software, including CATIA V5 2020 and Ansys 2020, were utilized.

A similar configuration model was proposed using the data collected from the mototaxi benchmarking. It comprised a semi-monocoque structure constructed from longitudinal and transverse pressed elements, commonly referred to as a ladder frame or chassis-type structure, as depicted in Figure 2.

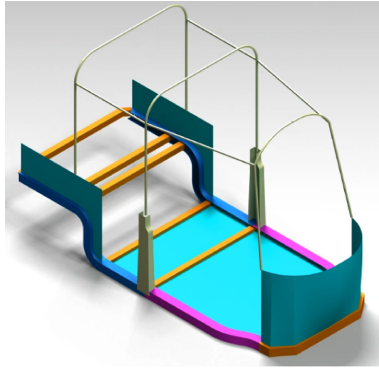


Figure 2. Ladder or Chassis Type Automotive Structure

Considering the information from the TVS manufacturer, a model comprising 30 components was developed. These components primarily encapsulate those pertinent and indispensable for analysing the vehicle's structure, including chassis elements, lower panels, and select exterior panels, as depicted in Figure 3.

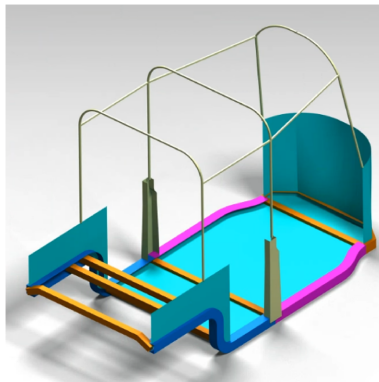


Figure 3. CAD Model of the Structure

Figure 4 depicts the structure's frontal components, featuring the removal of the front panel to expose the chassis components and panels.

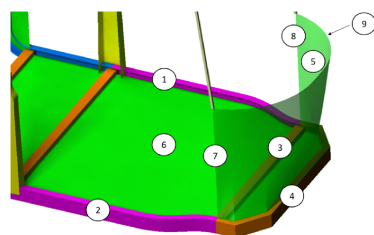


Figure 4. Front Chassis Elements

Figure 5 illustrates the intermediate elements of the vehicle, highlighting the "posts" and components responsible for supporting the passengers.

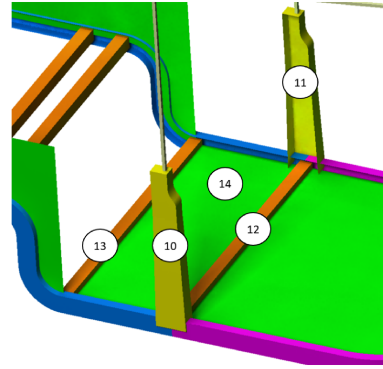


Figure 5. Intermediate Chassis Elements

Figure 6 illustrates the rear section of the structure with the components that accommodate mechanical elements like the engine system and rear suspension, along with the rear panels and the rear impact bar.

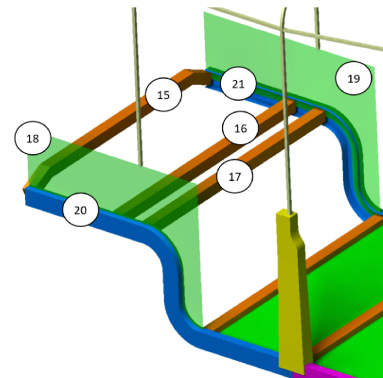


Figure 6. Rear Chassis Elements

Furthermore, additional minor pertinent elements were included in the vehicle evaluation, characterized by a roof structure possessing the following properties, as illustrated in Figure 7.

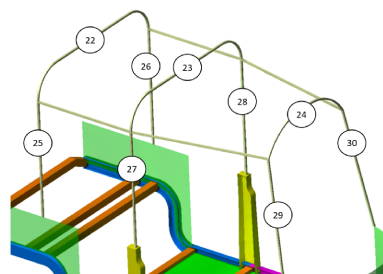


Figure 7. Estructura superior del techo

Ultimately, Figure 8 displays the final model intended for structural analysis. This model exclusively incorporates the elements utilized in the CAE evaluation of the vehicle.

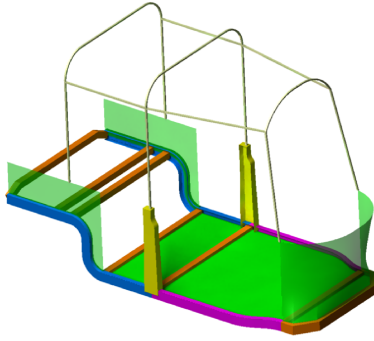


Figure 8. Global View of the Mototaxi Model for Structural Evaluation

Table 4 presents the various components utilized along with their descriptions, particularly regarding the type of profile employed for structural evaluation.

For the vehicle evaluation, several materials were initially explored for the modeled elements to ensure optimal outcomes. ASTM A36 steel and 6063-T83 aluminum alloy were chosen for their established applications in automotive structures and panels [12].

Table 4. Specification of Selected Components in the Mototaxi Structure

Section	Number	Specification	Material
Front Element	1,2	C-profile 3 in \times 1,498 in \times 0,258 in	ASTM A36
Front Element	3, 4, 7, 8	Square profile 2 in \times 2 in \times 0,25 in	ASTM A36
Front Element	5	Fiberglass panel thickness 0,109 in	6063-T83
Front Element	6	Aluminum sheet gauge 12	6063-T83
Front Element	9	Square profile 0,5 in \times 0,5 in \times 1,10 in	ASTM A36
Intermediate Element	10, 11, 14	Aluminum sheet gauge 12	6063-T83
Intermediate Element	12, 13	Square profile 2 in \times 2 in \times 0,25 in	ASTM A36
Rear Element	18, 19	Aluminum sheet gauge 12	6063-T83
Rear Element	15, 16, 17	Square profile 2 in \times 2 in \times 0,25 in	ASTM A36
Rear Element	20,21	C-profile 3 in \times 1,498 in \times 0,258 in	ASTM A36
Other Elements	22-30	Square profile 0,5 in \times 0,5 in \times 0,110 in	ASTM A36

Considering this, three studies were proposed using ANSYS software to assess torsional rigidity, flexural rigidity, and natural vibration modes. The pertinent global variables are outlined in Table 5.

Table 5. Technical Specification of Considered Global Variables

Study	Geometry Type	Study Type	Number of Mesh Elements
Torsion	Chassis 1D Panels Midsurface 2D	Static linear	Elements: 26616
Flexion	Chassis 1D Panels Midsurface 2D	Static linear	Elements: 26616
Natural Vibration Modes	Chassis 1D Panels Midsurface 2D	Modal	Elements: 26616

Figure 9 illustrates the applied constraints (depicted by stars labeled with the letter F) and the utilized loads (vectors identified with annotations B and C inside circles) for the torsion analysis of the structure, along with the obtained deformation values. The load values were determined by prioritizing loads that closely mimic real-world conditions, as specified in Table 6.

Table 6. Specification of Load Locations on the Primary Structure of the Mototaxi for Study

Load type	Value	Ubication
Axial	2354,4 N	Lateral
Axial	-2354,4 N	Lateral

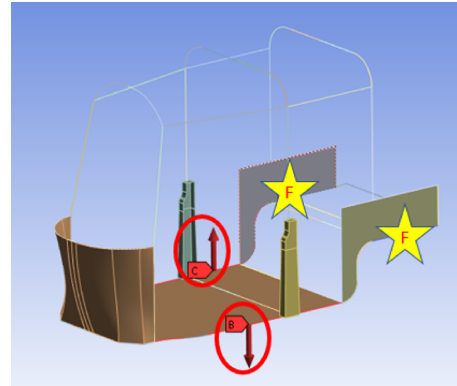


Figure 9. Global View of the Mototaxi Model Representing Applied Loads for Study

Given the possibility of mototaxi operators occasionally overloading the structure, it is imperative to ascertain its resistance to torsional forces. Consequently, investigations were conducted using a maximum load capacity of six individuals, each weighing an average of eighty kilograms, resulting in a total of 4708 N, distributed in two sections. These revised values were then applied to the lateral areas of the mototaxi structure in opposite directions to assess and validate the newly acquired results.

Figure 10 illustrates the applied constraints (depicted by stars labeled with the letter F) and the utilized loads (directional vectors annotated with B,

C, and D enclosed in circles) for the flexural analysis of the structure, from which deformation values are derived.

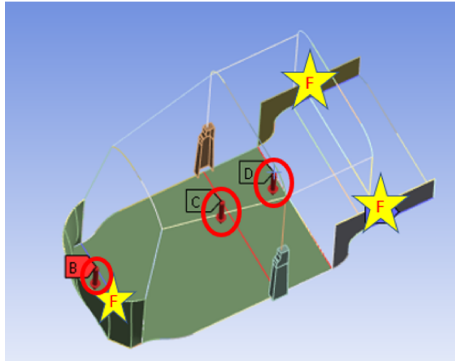


Figure 10. Constraints in the Flexural Analysis

For the flexural analysis, the maximum load capacity that the primary structure can sustain was considered, amounting to seven individuals, each averaging eighty kilograms. Consequently, with a total load of 560 kilograms, this value is distributed among the three beams depicted in the figure, resulting in a distribution of 5494 N among the three beams represented.

For the modal study, the analysis focused on examining the six natural vibration modes of the model. Figure 11 illustrates the positional constraints applied to the vehicle structure for this analysis. Table 7 specifies the type of restraints employed in the study.

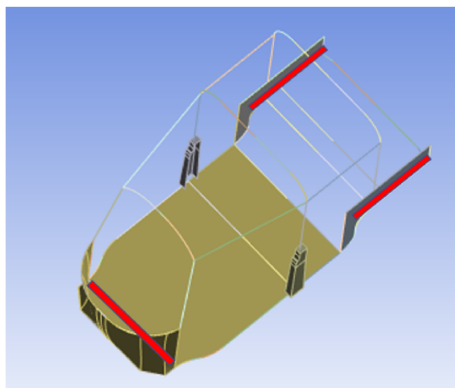


Figure 11. Positional Constraints

Table 7. Specification of Load Locations on the Primary Structure of the Mototaxi for Study

Restraint Type	Number of Restraints	Location
Fixed Support	3	Internal lower beams

3. Results and Discussion

Figure 12 illustrates the torsional deformation induced by the previously described loads.

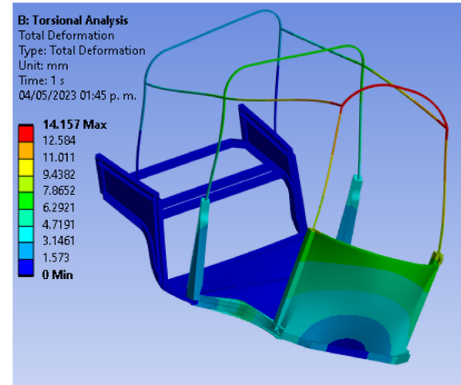


Figure 12. Global View of the Mototaxi Model Representing the Results of Torsional Loads

As depicted in Table 8, a torsional rigidity value of 27.35 KNm/° was derived from the applied torsional load and a measured structural torsion angle of 0.27251°. Furthermore, the maximum observed deformation amounts to 14.157 mm.

Table 8. Torsional Evaluation Results

Torsion results	
Maximum	(Angle)
14,157 mm	0,27251°

For flexural rigidity, Figure 13 depicts the observed deformation in the mototaxi structure.

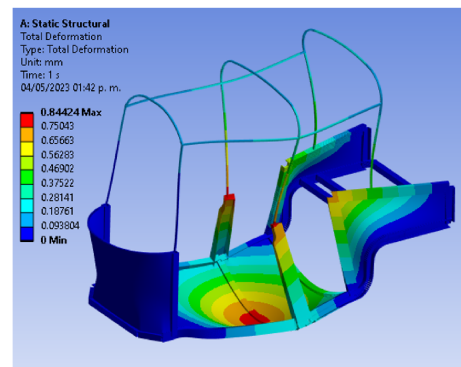


Figure 13. Global View of the Mototaxi Model Representing the Results of Flexural Loads

The maximum observed deformation is 0.84424 mm, leading to a flexural rigidity value of 6508.15 N/mm. As for the modal analysis of the mototaxi structure, Figure 14 illustrates the various vibration modes of the analyzed structure. As part of this assessment, the typical engine operating revolutions of the

vehicle were identified, with an operational frequency determined to be 88 Hz.

In Table 9, the numerical values found in the vibration modes of the structure are described.

Table 9. Modal Evaluation Results

Operating Revolutions of the Mototaxi Engine	Vibration Modes Results	Numerical Values in Hertz
5250 rpm→88 Hz	1	8.01
	2	10.335
	3	15.211
	4	26.205
	5	20.592
	6	21.3

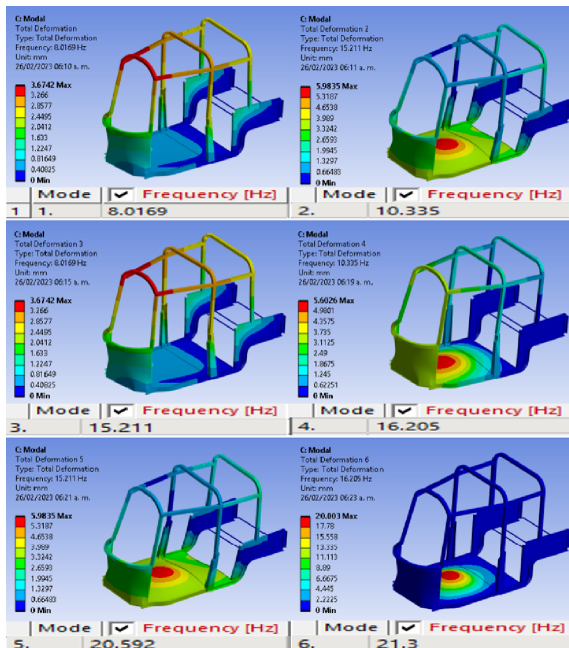


Figure 14. Global View of the Mototaxi Model Representing the Results of Applied Loads for Study

To ascertain the suitability of the acquired torsion and flexion values for the analyzed structure, the comparison by Hirz was employed as a reference. This comparison encompasses nine distinct categories, detailing specific ranges of torsional stresses for each category [13].

In the analysis of the mototaxi, the categories primarily considered were "mini car," "compact car," and "convertible," facilitating a comparable assessment. Particular emphasis was placed on the "convertible" category due to the mototaxi's configuration. Given its structural design primarily in the lower part, it bears a strong resemblance to the "convertible" category.

Based on the analysis depicted in Figure 15, it is evident that the structure exhibits greater torsional

rigidity compared to the "convertible" category, which typically ranges from 10 to 17 KNm/°, while the mototaxi demonstrates a value of 27.35 KNm/°. As for flexural rigidity, a similar comparison was conducted with analogous structures from diverse studies, and Figure 16 displays six different studies [14–19] along with their respective values.

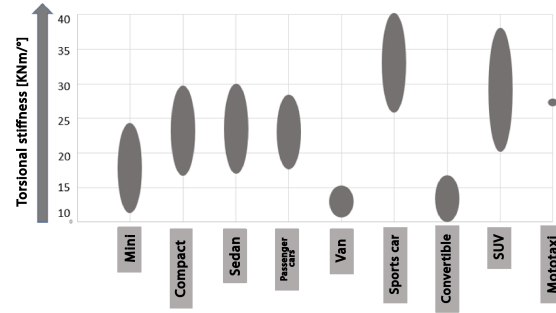


Figure 15. Comparison of Structural Torsion Resistance Results

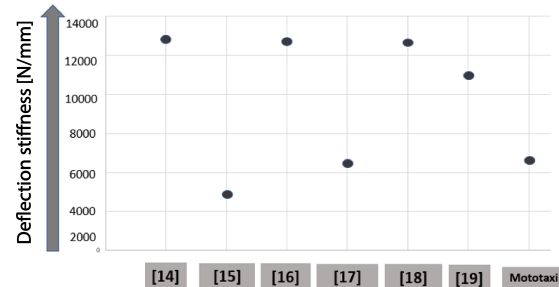


Figure 16. Comparison of Flexural Rigidity Results

When comparing flexural stresses, it is evident that the mototaxi structure exhibits a value of 6508.15 N/mm. The reviewed studies reveal comparable values, suggesting that the structure behaves similarly (with values ranging from 5 to 13 KN/mm) to other studies evaluating flexural rigidity.

4. Conclusions

The conducted studies comprehensively assessed the performance of the vehicle structure across three primary criteria: flexural rigidity, torsional rigidity, and modal evaluation. The meticulous analysis of the calculated values and comparisons revealed that the mototaxi-type structure exhibits notable concerns regarding structural integrity. These concerns were underscored by observable deviations compared to similar structures in the vehicle's torsional studies. This discrepancy hints at potential structural behavioral issues during operation, possibly stemming from the absence of an integrated structure, including the roof.

Consequently, this deficiency impairs the structure's performance efficiency, diminishing energy absorption and dissipation capacity. Notably, the flexural studies of the structure yielded values closely aligned with those of comparable structures. In contrast, the modal evaluation revealed a lack of alignment between the natural frequencies and the operational frequency of the vehicle's components, thus indicating inadequacies under these criteria.

Similarly, A. Rodríguez [20] analyzed a tricycle structure under defined parameters and specified load cases. Unlike the aforementioned studies, which primarily focused on assessing the structure's failure and fatigue criteria, this investigation focused on evaluating the vehicle's response under static working conditions. Future work could encompass evaluations incorporating relevant failure criteria and dynamic behavior analyses, thereby addressing potential hazards associated with frontal and lateral collisions or rollovers.

While vehicles of this class were primarily developed to provide an economical mobility option for both users and operators, the structure of mototaxis poses risks to the safety of passengers. It is imperative for local and national legislation, as well as developers of this vehicle technology, to enhance its structural and dynamic conditions.

References

- [1] B. A. Arvizu López, N. D. Lora Ledón, J. A. González, and J. E. Duarte Reinoso, "Mototaxis como medio de transporte público en el municipio de San Blas, Nayarit," *Universo de la Tecnología*, vol. 1, no. 43, pp. 25–31, 2023. [Online]. Available: <https://bit.ly/3UoAe9Q>
- [2] N. Ortuya. (2023) Mototaxi en México: ¿Una buena alternativa de transporte? Autofact. [Online]. Available: <https://bit.ly/3QoFold>
- [3] M. Sánchez. (2019) Están prohibidos, pero los mototaxis llevan a la gente a donde tiene que ir. Global Press Journal. [Online]. Available: <https://bit.ly/3JGoRFi>
- [4] M. J. Solís, C. A. López, and R. Gómez, "El mototaxi como medio de transporte público en Juchitán de Zaragoza, Oaxaca," *Centro Educativo Cruz Azul*, 2016. [Online]. Available: <https://bit.ly/3WghKuR>
- [5] DRTCSanMartin, *Manual del conductor, Capítulo 6: El Vehículo*. Dirección Regional de Transportes y Comunicaciones de San Martín. Perú, 2021. [Online]. Available: <https://bit.ly/4aUO9vz>
- [6] Z. J. Chan, V. Hung, and F. Kallmyer, *Inclusión social y movilidad: el sector del mototaxi en Tarapoto (Perú)*, 2019. [Online]. Available: <https://bit.ly/44mbsvA>
- [7] L. Díaz Olvera, D. Plat, P. Pochet, and M. Sahabana, "Un transporte urbano no convencional en África Subsahariana: el mototaxi," *Revista VIAL*, pp. 52–54, 01 2011. [Online]. Available: <https://bit.ly/3QCLgr8>
- [8] J. L. Bernal López, "El autoempleo en el transporte informal como forma de exclusión social: el caso de los mototaxistas del municipio de Chimalhuacán," *Análisis económico*, vol. 36, no. 93, pp. 141–158, 2021. [Online]. Available: <https://doi.org/10.24275/uam/azc/dcsh/ae/2021v36n93/Bernal>
- [9] B. Barrios Hernández and P. F. Coutiño Osorio, "El servicio de mototaxis: una fuente alternativa de trabajo en Puebla," *DIKE*, no. 15, pp. 157–171, 2014. [Online]. Available: <http://dx.doi.org/10.32399/fder.rdk.2594-0708.2014.15.168>
- [10] Congreso de Puebla, *Ley de movilidad y transporte del Estado de Puebla*. Honorable Congreso del Estado de Puebla, 2021. [Online]. Available: <https://bit.ly/4a5ZxDn>
- [11] MSM, *Ficha técnica: Motor de encendido por chispa de 4 tiempos, refrigerado por líquido*. Moto Soluciones México, 2023. [Online]. Available: <https://bit.ly/3JQSAvI>
- [12] C. Okpala, T. Nwokeocha, L. Ofuoku, A. Akajiuo, and J. Adonu, "Design and analysis of chassis and spring of a load-bearing tricycle," *International Journal of Advanced Engineering Technology*, vol. 8, no. 3, pp. 10–15, 2017. [Online]. Available: <https://bit.ly/3WxEbMi>
- [13] M. Hirz. (2016) What are the typical stiffness values while designing car chassis?. ReserachGate. ReserachGate. [Online]. Available: <https://bit.ly/4bgYOLu>
- [14] D. Fang and W. Kefei, "Simulation analysis and experimental verification on body-in-white static stiffness of a certain commercial vehicle," *Vibroengineering PROCEDIA*, vol. 29, pp. 141–147, nov 2019. [Online]. Available: <https://doi.org/10.21595/vp.2019.21171>
- [15] H. J. Yan, X. Liu, G. Q. Zhao, N. Tian, and S. K. Zhang, "Analysis and Research of Stiffness Based on Body-in-White NVH," *Journal of Physics: Conference Series*, vol. 1087, no. 4, p. 042078, sep 2018. [Online]. Available: <https://dx.doi.org/10.1088/1742-6596/1087/4/042078>

-
- [16] Z. Wentao, W. Zhenhu, F. Xiangdong, Y. Xuyue, L. Luoxing, and W. Wanlin, “A calculation method of car body in white’s static stiffness based on modal theory,” *China Mechanical Engineering*, vol. 29, no. 5, pp. 511–518, 2018. [Online]. Available: <https://bit.ly/4a7wkYN>
- [17] C. Hartmann, M. Welm, S. Schreyer, C. Hartmann, and W. Volk, “A modular car body for sustainable, cost-effective, and versatile vehicle development,” *Technologies*, vol. 9, no. 1, 2021. [Online]. Available: <https://doi.org/10.3390/technologies9010013>
- [18] M. H. Shojaeefard, A. Khalkhali, M. Sarmadi, and N. Hamzehi, “Investigation on the optimal simplified model of BIW structure using FEM,” *Latin American Journal of Solids and Structures*, vol. 12, no. 10, pp. 1972–1990, Oct 2015. [Online]. Available: <https://doi.org/10.1590/1679-78251923>
- [19] M. M. Shivakumar and L. Nirmala, “Fatigue life estimation of chassis frame FESM bracket for commercial vehicle,” *International Journal of Science and Research (IJSR)*, vol. 3, no. 8, pp. 441–447, 2014. [Online]. Available: <https://bit.ly/4brALP9>
- [20] A. Rodríguez, B. Chiné, J. A. Ramírez, and Costa, “Finite element modeling of an aluminum tricycle frame,” 2016. [Online]. Available: <https://bit.ly/4aqmFwR>



ELECTRIC VEHICLES AND THEIR IMPACT ON THE ELECTRIC DISTRIBUTION SYSTEM: A CASE STUDY OF THE URBAN FEEDER IN PORTOVIEJO

LOS VEHÍCULOS ELÉCTRICOS Y SU IMPACTO EN EL SISTEMA ELÉCTRICO DE DISTRIBUCIÓN: CASO DE ESTUDIO “ALIMENTADOR URBANO DE LA CIUDAD DE PORTOVIEJO”

Arturo Zavala-Tubay^{1,*} , Hugo Pico-Mera¹ , Gabriel Pico-Mera²

Received: 16-06-2023, Received after review: 05-04-2024, Accepted: 30-04-2024, Published: 01-07-2024

Abstract

In Portoviejo, the current use of electric vehicles (EVs) is limited compared to conventional vehicles. However, due to the implementation of laws, regulations, and policies promoting electric mobility in Ecuador, a significant increase in the integration of EVs into the city's electrical system is anticipated in the coming years. To anticipate the impact on the electrical infrastructure, a simulation is conducted using CYMDIST software on an electrical distribution feeder operated by the Public Company Corporación Nacional de Electricidad (CNEL EP), Manabí Business Unit (Portoviejo). The simulation considers three scenarios projected for 2030: 1. Baseline scenario without EV integration, 2. Unrestrained EV integration, and 3. Managed EV integration. This research aims to simulate the integration of up to 230 EVs into the network to provide benchmark data for understanding the potential impacts on the feeder as EV adoption increases, with vehicles being charged over extended periods. The investigation will highlight the importance of demand management with EV integration, demonstrating significant effects on the demand curve, voltage profile, and total harmonic distortion rate (THD%) of a 13.8 kV distribution feeder.

Keywords: EV, Electric Vehicle, Harmonics, Technical Losses, Electrical Planning, CYMDIST, Distribution, CNEL

Resumen

En la ciudad de Portoviejo, actualmente el uso de vehículos eléctricos (VE) es limitado en comparación con el uso de los convencionales. Sin embargo, debido a la implementación de leyes, reglamentos y regulaciones que impulsan la movilidad eléctrica en el Ecuador, se espera que en los próximos años se produzca un ingreso considerable de esta carga (VE) en el sistema eléctrico de la ciudad. En este sentido, para determinar probables afectaciones a producirse en el sistema eléctrico en el futuro, se realiza la simulación en el software CYMDIST de un alimentador de distribución eléctrico de la Empresa Pública Corporación Nacional de Electricidad CNEL EP Unidad de Negocio Manabí (Portoviejo), considerando tres escenarios de análisis proyectados al año 2030 como son: 1. Caso base sin ingreso de VE, 2. Ingreso no controlado de VE y 3. Ingreso controlado de VE. El presente trabajo simula el ingreso de hasta 230 vehículos en la red, puesto que, el objetivo del estudio es tomar datos referenciales para conocer la posible afectación en el alimentador cuando los VE se conecten de forma masiva y se carguen prolongadamente. Al final del estudio se comprobará la importancia de la gestión de la demanda cuando se produzca el ingreso de vehículos eléctricos, el cual refleja resultados importantes en la curva de demanda, perfil de voltaje y tasa de distorsión armónica THD % de un alimentador de distribución a 13,8 kV.

Palabras clave: VE, vehículo eléctrico, armónicos, pérdidas técnicas, planificación eléctrica, CYMDIST, distribución, CNEL

^{1,*}Departamento de Planificación, Corporación Nacional de Electricidad (CNEL EP UN MAN), Ecuador.

Corresponding Author✉: arturo.zavala@cnel.gob.ec.

²Facultad de Ciencias Matemáticas, Físicas y Químicas, Universidad Técnica de Manabí, Ecuador.

Suggested citation: Zavala-Tubay, A.; Pico-Mera, H. and Pico-Mera, G. “Electric Vehicles and Their Impact on the Electric Distribution System: A Case Study of the Urban Feeder in Portoviejo,” *Ingenius, Revista de Ciencia y Tecnología*, N.º 32, pp. 27-35, 2024, DOI: <https://doi.org/10.17163/ings.n32.2024.03>.

1. Introduction

The global commitment to significantly reduce carbon emissions in the short term has driven the development of environmentally sustainable technologies, such as electric vehicles (EVs) [1]. Consequently, in recent years, the adoption of this technology has spread worldwide in response to the urgent need to reduce environmental pollutant emissions [2].

Considering that the use of electric vehicles contributes to environmental conservation, it is necessary to analyze the impact that charging this new technology may have on electrical distribution networks. According to [3] and [4], since these loads are modeled and behave as nonlinear, they could have a considerable negative impact on power quality (including voltage, imbalance levels, and harmonics), altering these electrical parameters under different load conditions.

Moreover, it is anticipated that the uncontrolled increase in loads due to the integration of EVs will directly impact the electrical infrastructure of the distribution company, owing to the potential rise in demand [5].

Electric vehicles (EVs) are characterized by the use of an electric traction motor for vehicle propulsion [6]. The energy required to drive this motor is stored in batteries, which are typically charged from an external power source [7].

Typically, EVs use lithium-ion batteries due to their advantages over other technologies, including higher efficiency, low maintenance costs, and lightweight properties. These characteristics make them particularly attractive for use in electric vehicles [8].

While batteries are considered the primary energy source for EVs, this study will focus on the impact these devices will have on electrical networks rather than on the batteries themselves.

The introduction of electric vehicles into the market will result in significant variations in energy and power demand [9]. This will impact electrical networks, presenting a major challenge for distribution companies. They must ensure the continuity of service to their customers while accommodating the increasing power and energy demand.

Anastasiadis et al. [10] emphasize the necessity of anticipating suitable solutions to potential issues within the electrical system. As the popularity of electric traction vehicles continues to grow, the increased demand significantly impacts the network.

Negative effects include impacts on voltage profiles, saturation of electrical system components, voltage imbalances, harmonic distortion, and increased technical energy losses. Conversely, positive effects encompass improved energy management techniques, commonly referred to as demand management strategies [11].

To determine the impact of integrating electric vehicles (EVs) into the system, it is essential to analyze

various involved variables. These include network demand, electrical system loadability, load profiles of different customer types, and the characteristics of electric vehicles [12].

The impact on the network is closely linked to the type of charging applied to electric vehicles. According to [13], charging can be classified into three levels: Level 1 (slow charging), Level 2 (semi-fast charging), and Level 3 (fast charging at charging stations). The type of charging corresponds to the battery charging speed. Levels 2 and 3 are typically used in public and private settings, while Level 1 is primarily designated for domestic or garage charging.

Table 1 presents the classification of battery recharge types according to EV characteristics [14].

Table 1. Battery charging levels for EVs

Charging type	Charging Level	Typical use	Maximum expected current	Charging time
Level I	Slow	Home	12 A	6 a 24 hours
Level II	Semi-fast	Private or public sector	32 A	2-6 hours
Level III	Fast	C.Satations	250 A CA 400 A CC	0,5 hours

The fast charging process can be completed in approximately 30 minutes, allowing the battery to reach 80% of its nominal capacity [15].

Although the impact of EVs on the grid is directly related to the charging performed (slow, semi-fast, or fast), the current analysis will focus solely on slow charging. This type of charging is expected to be prevalent in residential settings among consumers or clients of electric distribution companies.

Due to the challenges posed by the nonlinear loads of electric vehicles, it is essential to conduct a study to estimate their impact on the grid. This research will analyze the effects of electric vehicle charging on the demand curve of a feeder, as well as the impact on voltage profiles, harmonics, and practical technical losses.

This study will be conducted through a simulation using CYMDIST software, based on a real feeder from the electrical distribution system of Corporación Nacional de Electricidad CNEL EP, Manabí Business Unit, projected up to 2030. The program modules will encompass load distribution, load flow, harmonics, and long-term dynamics.

Data derived from readings of the electrical system under analysis will be utilized for the network simulation. An urban feeder from Portoviejo, Manabí, has been selected for this study. The electric vehicle load, designed for simulation in the CYMDIST software, will be modeled as an unbalanced multifrequency current source. The data for this modeling will be obtained

from readings taken while charging electric vehicle batteries using type I (slow) charging, with measurement intervals of 10 minutes.

This study explores simulated scenarios involving the integration of 160 and 230 electric vehicles into the electrical grid. These figures are referential and can be adjusted according to the projected EV integration estimates published in Panorama Eléctrico magazine [16].

Considering that electric vehicles (EVs) contribute to various quality issues within the distribution network, notably voltage imbalance, alterations to voltage profiles, electrical infrastructure saturation, and deviations from nominal frequency [17], this article presents real-world data collected during the low-voltage charging process of an electric vehicle.

In Ecuador, the Energy and Non-Renewable Natural Resources Regulation and Control Agency (ARCERNNR) oversees the strategic sectors of electricity, hydrocarbons, and mines. This agency establishes directives and guidelines for the Electric Energy Distribution Company through corresponding regulations. Specifically, Resolution No. ARCERNNR 017/2020 enacts Regulation No. ARCERNNR 002/20 "Quality of Distribution and Commercialization of Electric Energy Service" [18], which comprehensively addresses product quality in its second chapter.

The referenced regulation delineates the permissible ranges for electrical variables, which are commonly influenced by integrating electric vehicles into the networks, as detailed below:

1.1. Product Quality

1.1.1. Voltage Level

Table 2 displays the voltage ranges mandated by the regulatory authority ARCERNNR for distribution companies in Ecuador, as stipulated by the regulation [18].

Table 2. Acceptable Voltage Level Ranges

Voltage Level	Acceptable Range
High Voltage (Group 1 and Group 2)	$\pm 5,0 \%$
Medium Voltage	$\pm 6,0 \%$
Low Voltage	$\pm 8,0 \%$

For this research, the values corresponding to medium voltage will be examined, and compliance with the regulations will be assessed, as outlined in Table 2.

1.1.2. Harmonic Distortion of Voltage

The individual harmonic distortion factor of voltage (%) and the total harmonic distortion factor of voltage (THD %) adhere to the ranges specified in ARCERNNR Regulation 002-20, as detailed in Table 3. The analysis will reference values corresponding to both medium and low voltage levels.

Table 3. Maximum Voltage Harmonic Limits (% of nominal voltage)

Voltage Level	Individual Harmonic Distortion Factor (%)	THD (%)
Low Voltage	5	8
Medium Voltage	3	5
High Voltage (Group 1)	1.5	2.5
High Voltage (Group 2)	1	1.5

2. Materials and Methods

This research aims to establish a foundational baseline for subsequent demand studies to be undertaken by the Strategic Public Company Corporación Nacional de Electricidad CNEL EP, Manabí Business Unit, concerning electromobility. This initiative will equip the distribution company with an enhanced tool for long-term planning of the electrical system, considering the potential impacts of electric vehicle integration across various load scenarios.

To analyze the impact on the electrical grid, this study references a case in which a specific number of electric vehicles (EVs) were randomly integrated into the system. Their incorporation was simulated using CYMDIST software, an advanced engineering tool for electrical planning, operation, and optimization studies [19].

The materials employed for the simulation are outlined as follows:

- Georeferenced electrical network, considering loads according to user type.
- Primary measurements or readings from the existing 13.8 kV feeder.
- Measurements or readings conducted on an electric vehicle by CNEL EP.

2.1. Methodology

The methodology employed aligns with the diagram depicted in Figure 1.

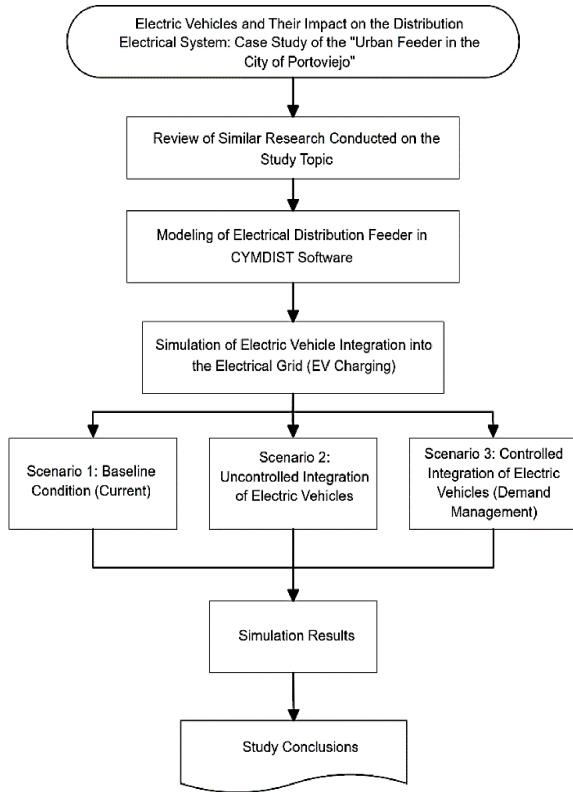


Figure 1. Flowchart of the Methodology Applied in the Study

2.1.1. Determination of Scenarios

To elucidate the impact on the electrical grid stemming from the integration of electric vehicle (EV) charging, three simulation scenarios projected up to the year 2030 have been delineated. These scenarios aim to assess the influence of EVs on various parameters, including demand, voltage drop, harmonics, and technical losses.

A) Scenario 1: Baseline Scenario, Feeder Projected to 2030.

The operational dynamics of the feeder under study are meticulously analyzed. For the projection to the year 2030, a vegetative annual growth rate of 3.5% for the feeder is considered. EV charging is not included in this scenario.

B) Scenario 2: Unrestricted EV Charging (Year 2030).

In this scenario, the projected situation is analyzed by simulating that EVs will be charged when their owners return home after work. Consequently, vehicle charging is expected to start shortly after 6:00 PM.

C) Scenario 3: Controlled EV Charging (Year 2030).

This scenario anticipates the year 2030, analyzing electric vehicle (EV) charging initiation post-10:00 PM to prevent its peak from coinciding with the system's maximum demand period. It also explores strategic demand management approaches, including the staggered charging of vehicles at times that do not overlap with peak demand. This involves implementing public policies to facilitate EV charging management. One such strategy is developing charging infrastructure in public and private parking areas at workplaces, enabling vehicles to charge throughout the day and thus mitigating peak demand impacts [20]. The aim is to model a controlled charging environment for residential and commercial users. EVs are progressively connected to the distribution grid post-workday, with charging activities extending overnight into the early morning.

2.1.2. Information on the Feeder under Study

The feeder chosen for this study is part of the electrical distribution system of Portoviejo, located in the province of Manabí. According to the projection for the year 2030, the pertinent data for this feeder are detailed in Table 4.

Table 4. Characteristics of the Feeder

Substation	Customers	Voltage (kV)	Main conductor	Main Line Length (km)	Active power (MW)	Reactive power (MVAR)
Portoviejo 2	2612	13.8	ACSR 3/0	2.1	4.77	1.1

As delineated in Table 4, the network comprises 2.10 km of ACSR 3/0 conductor along the main line. The base voltage is 13.8 kV, the projected active power load is 4.77 MW, and the reactive power load is 1.10 MVAR. The network serves a total of 2612 customers, including 954 residential users.

3. Results and discussion

This section presents the results of the scenarios described in section 2.1.1, which were simulated using CYMDIST software:

- Scenario 1: Baseline scenario, feeder projected to 2030.
- Scenario 2: Unrestricted EV charging (year 2030).
- Scenario 3: Controlled EV charging (year 2030).

3.1. Demand

Figure 2 illustrates the results of the three scenarios analyzed for 2030, comparing the impact of electric vehicles on demand within the simulated electrical system.

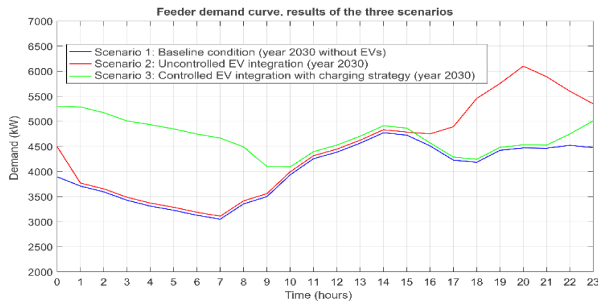


Figure 2. Demand Curve, Results Obtained in the Three Analyzed Scenarios (Consolidated)

According to Figure 2, Scenario 2, which features uncontrolled EV charging, exhibits a peak demand of approximately 6.1 MW. In contrast, Scenario 3, which implements controlled EV charging with demand management strategies, records a peak demand of approximately 4.5 MW during the same demand period.

This result underscores the positive impact of implementing demand management mechanisms on the feeder, significantly reducing peak loads during periods of maximum demand. Consequently, this enhances the network's efficiency and increases the feeder's available transport capacity.

This result aligns with the findings documented in [3], which assert that an uncontrolled charging strategy represents the worst scenario for demand control and distribution network imbalances.

3.2. Voltage Drop

3.2.1. Voltage Profile

Figure 3 displays the voltage profile results for the simulated feeder for 2030, illustrating its behavior across the three proposed scenarios.

The detailed results depicted in Figure 3 elucidate the positive impact of employing demand management techniques in the EV charging process. Specifically, the voltage level along the simulated feeder in Scenario 3, which incorporates EV charging with load management strategies, is comparatively higher than that observed in Scenario 2, where EV charging is uncontrolled.

As illustrated in Figure 3, it is noteworthy that the implementation of charging strategies plays a crucial role in adhering to the ARCERNR 002-20 regulations concerning the acceptable voltage range in the feeder, which is established at $\pm 6\%$.

This result aligns with the findings of Lascano et al. [21], who report that integrating each electric vehicle (EV) leads to a progressive voltage drop, resulting in values that eventually exceed the limits prescribed by the referenced regulations.

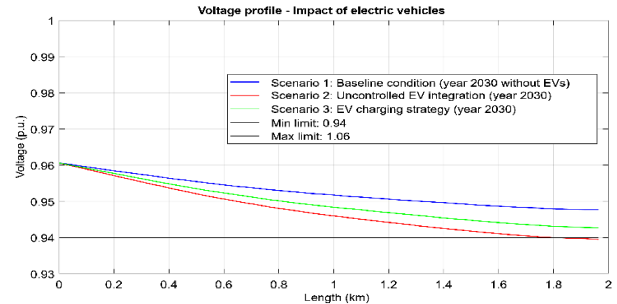


Figure 3. Voltage Profile, Results Obtained in the Three Analyzed Scenarios (Consolidated)

3.2.2. Voltage at the Farthest Node of the Feeder

Figure 4 illustrates the voltage behavior at the most distant node of the feeder across the three scenarios proposed in this study. As detailed in Section 3.2.1, the figure demonstrates that voltage levels at the farthest point of the feeder are higher when a demand management system for EV charging is implemented.

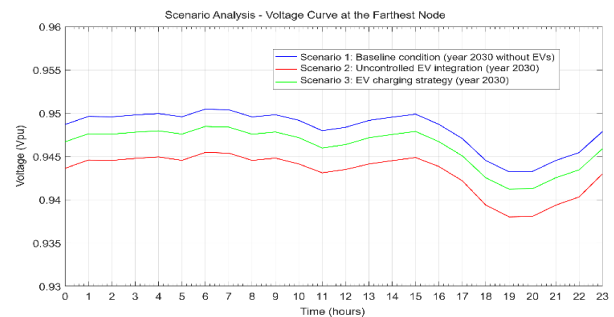


Figure 4. Voltage Profiles at the Farthest Node, Results in Three Scenarios

From Figure 4, it is evident that the voltage at the farthest point will be affected by the integration of EVs if strategies to mitigate this impact are not implemented. This result aligns with the findings of [21].

3.3. Total Harmonic Distortion Rate (THD %)

Table 5 presents the projected total harmonic distortion factor of voltage (THD %) for the year 2030, reflecting the impact of integrating 230 electric vehicles into the simulated feeder.

Table 5. Total Harmonic Distortion of Voltage in Medium Voltage (THD %)

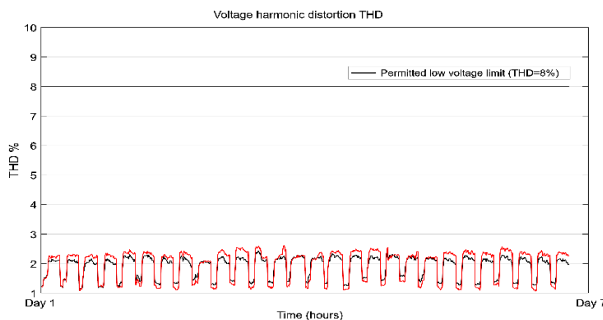
NODE	kV L-N	180,00 Hz IHD (%)	300,00 Hz IHD (%)	420,00 Hz IHD (%)	THD (%)
Main Feeder Output (Phase A)	7.58	0.019	0.008	0.007	0.023
Main Feeder Output (Phase B)	7.67	0.023	0.011	0.009	0.027
Main Feeder Output (Phase C)	7.71	0.013	0.007	0.005	0.016

As depicted in Table 5, the integration of electric vehicle (EV) loads, as simulated in the study, ensures that the total harmonic distortion of voltage (THD%) remains within the 5% threshold established by the ARCERNNR 002-20 regulation for medium voltage.

For simulation purposes, EV loads were gradually introduced using CYMDIST software. Even when the number of connected EVs reached 230, no significant levels of harmonic distortion were observed at medium voltage. Consequently, it is anticipated that the total harmonic distortion percentage (THD%) at this voltage level will not be substantially impacted when slow-charging EVs (Type I) are charged with the simulated number of EVs.

On the other hand, readings obtained using a power quality analyzer during the electric vehicle (EV) charging process at low voltage levels indicate that the total harmonic distortion of voltage (THD%) remains within limits prescribed by the ARCERNNR 002-20 regulation. However, there is a notable presence of the third and fifth current harmonics, suggesting that the total harmonic distortion of current includes significant values that must be considered when multiple EVs are connected to the same circuit.

Figures 5, 6, and 7 depict the curves for the total harmonic distortion of voltage (THD%) at low voltage and those for the third and fifth harmonics, respectively, at the same voltage level (real data measured at low voltage).

**Figure 5.** Total Harmonic Distortion of Voltage THD % Curve (Real Data from EV Charging Readings at Low Voltage)

The data depicted in Figure 5 indicate that the

harmonic distortion rate during the low-voltage charging process of an electric vehicle remains within the parameters set forth by current quality regulations.

Figure 6 presents the third harmonic current for phases 1 (IhL1) and 2 (IhL2). When correlated with the data in Figure 5, these currents fall within the permissible values specified by current regulations. Notably, the harmonics illustrated in Figure 6 were observed exclusively during the EV charging process.

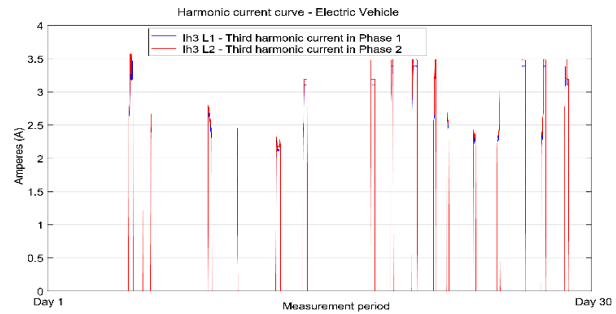
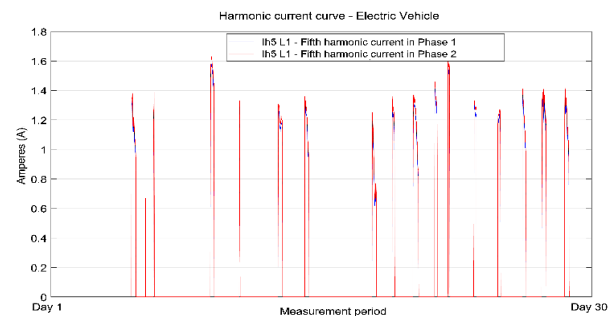
**Figure 6.** Third Harmonic Current Curve (Measured in EV, Low Voltage)

Figure 7 illustrates the fifth harmonic currents for phases 1 (IhL1) and 2 (IhL2). When compared with the data in Figure 5, these currents remain within the values allowed by current regulations for this parameter.

**Figure 7.** Fifth Harmonic Current Curve (Measured in EV, Low Voltage)

It is important to note that, despite the significant contributions of harmonics at low voltage (specifically, the third and fifth harmonic currents) during electric vehicle (EV) charging, these levels do not exceed the limits established by the ARCERNNR 002-20 regulation. However, these values will probably increase with the number of connected chargers. Consequently, the electric distribution utility should consider implementing preventive measures as necessary.

The case presented in this section aligns with the findings of [3], where the authors indicate that an increase in EV load can lead to harmonic distortion issues due to the heightened injection of the third harmonic.

3.4. Technical Losses

Table 6 presents the projected contribution of technical losses in power and energy for 2030, with detailed identification according to the analyzed scenario. The final projection for 2030 includes the integration of 230 electric vehicles.

Table 6. Projected Technical Losses for the Year 2030

Technical Losses	Year 2030 (baseline without EV load)	Year 2030 (uncontrolled EV load)	Year 2030 (controlled EV load)
Power (kW)	151.51	265.21	200.87
Energy (MWh/year)	790.68	1333.95	1026.49

As indicated in Table 6, integrating electric vehicles into the grid will substantially increase the system's technical power and energy losses. Specifically, when comparing the baseline scenario (Scenario 1, projected for 2030 without EVs) to the scenario where EVs are charged uncontrollably (Scenario 2), technical losses increase by 113 kW. In contrast, if EVs are charged using demand management strategies (Scenario 3), the increase in technical losses is limited to 49.36 kW compared to the baseline scenario.

These results demonstrate the positive impact of implementing demand management methods to reduce operational losses within the system.

4. Conclusions

This study has successfully established a baseline that will inform future demand studies conducted by the Strategic Public Company Corporación Nacional de Electricidad CNEL EP, Manabí Business Unit, focusing on electromobility.

The analysis has confirmed the effects on a feeder's demand curve due to controlled and uncontrolled electric vehicle (EV) charging. In scenarios where residential EV charging is concentrated at a specific hour of the day (uncontrolled charging), demand can increase by up to 1 MW for every 160 vehicles. Conversely, when EVs are charged in a controlled manner, the demand increase is estimated to be around 0.1 MW for the same number of electric vehicles connected to the grid.

Based on the cases studied, it is clear that the controlled scenario is the most suitable for implementing EV charging within a distribution feeder. Although voltage drops are inherent to the load characteristics in this scenario, they are considerably less severe compared to the uncontrolled charging scenario. In the latter, there is a significant deterioration in the voltage profile, potentially degrading to levels below those permitted by the quality regulations cited in this document.

Incorporating EV charging introduces an additional load on the electrical system. To mitigate the risk of high demand peaks that could lead to grid instability, component overloading, and reduced lifespan of infrastructure, it is advisable to manage this load through effective electric demand management mechanisms.

The implementation of electric demand management mechanisms to regulate EV charging (controlled demand) has effectively flattened the feeder's demand curve by reducing peak demands. This strategic control enhances the network's efficiency and, consequently, increases the available transport capacity within the feeder. In the cases examined, this approach resulted in a favorable reduction of 1.6 MW in peak demand when comparing Scenario 2 with Scenario 3 during the same demand period.

An additional positive impact on the system is the enhancement of voltage levels along the feeder, as evidenced by the improved voltage profile. This observation confirms that the voltage level at the most distant point of the feeder remains elevated when EV charging is controlled.

With the integration of an average of 230 electric vehicles utilizing Type I charging, the harmonic distortion rate does not compromise compliance with the Total Harmonic Distortion (THD%) standards for medium voltage in the analyzed feeder. Specifically, the feeder exhibits an approximate average harmonic distortion rate of 0.02% at its output. However, it is essential to note that the harmonic distortion rate (THD) may escalate with the increase in connected chargers, necessitating careful monitoring and management to maintain regulatory compliance and system integrity.

Data collected from an electric vehicle have shown that at low voltage, the third and fifth current harmonics make significant contributions. This finding indicates that the total harmonic distortion of current encompasses considerable values, which should be carefully considered by the distribution company.

The gradual integration of electric vehicles (EVs) into the electrical distribution system will considerably increase technical power losses. Specifically, for the feeder under study, technical losses may increase by approximately 113 kW when EV charging is uncontrolled. In contrast, adopting demand management methods and controlled EV charging can significantly mitigate these losses, limiting the increase to just 49.36 kW.

References

- [1] H. Pico, I. Pazmiño, and B. Ponce, "Análisis de los factores que intervienen en el envejecimiento prematuro de las baterías de ion-litio mediante modelo teórico validado en laboratorio,"

- Revista Técnica Energía*, vol. 17, no. 2, pp. 83–91, 2021. [Online]. Available: <https://doi.org/10.37116/revistaenergia.v17.n2.2021.432>.
- [2] CEPAL, *Propuesta de marco regulatorio para acelerar la inversión en electromovilidad mediante la reconversión de vehículos que usan combustibles fósiles*. Comisión Económica para América Latina y el Caribe, 2021. [Online]. Available: <https://bit.ly/3QBManI>
 - [3] P. Rodríguez-Pajarón, A. Hernández, and J. V. Milanović, “Probabilistic assessment of the impact of electric vehicles and nonlinear loads on power quality in residential networks,” *International Journal of Electrical Power & Energy Systems*, vol. 129, p. 106807, 2021. [Online]. Available: <https://doi.org/10.1016/j.ijepes.2021.106807>
 - [4] A. A. Ismail, N. T. Mbungu, A. Elnady, R. C. Bansal, A. Kadir Hamid, and M. AlShabi, “Impact of electric vehicles on smart grid and future predictions: a survey,” *International Journal of Modelling and Simulation*, vol. 43, no. 6, pp. 1041–1057, 2023. [Online]. Available: <https://doi.org/10.1080/02286203.2022.2148180>
 - [5] A. Jenn and J. Highleyman, “Distribution grid impacts of electric vehicles: A California case study,” *iScience*, vol. 25, no. 1, p. 103686, 2022. [Online]. Available: <https://doi.org/10.1016/j.isci.2021.103686>
 - [6] A. Ibrahim and F. Jiang, “The electric vehicle energy management: An overview of the energy system and related modeling and simulation,” *Renewable and Sustainable Energy Reviews*, vol. 144, p. 111049, 2021. [Online]. Available: <https://doi.org/10.1016/j.rser.2021.111049>
 - [7] Y. Sáez, E. Collado, and M. Serrano, “Modelado de estaciones de recarga lenta para vehículos eléctricos mediante software: revisión del estado del arte,” *Revista de Iniciación Científica*, vol. 7, no. 2, pp. 9–19, 2021. [Online]. Available: <https://doi.org/10.33412/rev-ric.v7.2.3334>
 - [8] S. Goel, R. Sharma, and A. K. Rathore, “A review on barrier and challenges of electric vehicle in India and vehicle to grid optimisation,” *Transportation Engineering*, vol. 4, p. 100057, 2021. [Online]. Available: <https://doi.org/10.1016/j.treng.2021.100057>
 - [9] D. T. Sandoval and E. G. Torres, “Res-puesta de demanda de energía por intro-ducción de vehículos eléctricos: estado del arte,” *Revista de I+D Tecnológico*, vol. 16, no. 1, pp. 5–11, 2020. [Online]. Available: <https://doi.org/10.33412/idt.v16.1.2433>
 - [10] A. G. Anastasiadis, G. P. Kondylis, A. Polyzakis, and G. Vokas, “Effects of increased electric vehicles into a distribution network,” *Energy Procedia*, vol. 157, pp. 586–593, 2019. [Online]. Available: <https://doi.org/10.1016/j.egypro.2018.11.223>
 - [11] H. Das, M. Rahman, S. Li, and C. Tan, “Electric vehicles standards, charging infrastructure, and impact on grid integration: A technological re-view,” *Renewable and Sustainable Energy Reviews*, vol. 120, p. 109618, 2020. [Online]. Available: <https://doi.org/10.1016/j.rser.2019.109618>
 - [12] A. K. Karmaker, S. Roy, and M. R. Ahmed, “Analysis of the impact of electric vehicle charging station on power quality issues,” in *2019 International Conference on Electrical, Computer and Communication Engineering (ECCE)*, 2019, pp. 1–6. [Online]. Available: <https://doi.org/10.1109/ECACE.2019.8679164>
 - [13] S. Habib, M. M. Khan, F. Abbas, L. Sang, M. U. Shahid, and H. Tang, “A comprehensive study of implemented international standards, technical challenges, impacts and prospects for electric vehicles,” *IEEE Access*, vol. 6, pp. 13 866–13 890, 2018. [Online]. Available: <https://doi.org/10.1109/ACCESS.2018.2812303>
 - [14] S. Sharma, A. K. Panwar, and M. Tri-pathi, “Storage technologies for electric ve-hicles,” *Journal of Traffic and Transportation Engineering (English Edition)*, vol. 7, no. 3, pp. 340–361, 2020. [Online]. Available: <https://doi.org/10.1016/j.jtte.2020.04.004>
 - [15] L. González, E. Siavichay, and J. Espinoza, “Impact of EV fast charging stations on the power distribution network of a Latin American inter-mediate city,” *Renewable and Sustainable Energy Re-views*, vol. 107, pp. 309–318, 2019. [Online]. Avail-able: <https://doi.org/10.1016/j.rser.2019.03.017>
 - [16] ARCERNNR, *Panorama Eléctrico*. Agencia de Regulación y Control de Energía y Recursos Naturales No Renovables, 2022. [Online]. Available: <https://acortar.link/jikL6I>
 - [17] A. Mohammad, R. Zamora, and T. T. Lie, “Inte-gration of electric vehicles in the distribution net-work: A review of PV based electric vehicle mod-elling,” *Energies*, vol. 13, no. 17, 2020. [Online]. Available: <https://doi.org/10.3390/en13174541>
 - [18] AECERNNR, *Regulación Nro. ARCERNNR - 002/20, Calidad del servicio de distribución y comercialización de energía eléctrica*. Agencia de Regulación y Control de Energía y Recursos Naturales No Renovables, 2020. [Online]. Available: <https://bit.ly/44vx74C>

- [19] EATON. (2024) Análisis de sistemas de distribución CYMDIST. EATOn Power Business World Wide. [Online]. Available: <https://bit.ly/3Uu3L1T>
- [20] A. A. Navarro Espinosa, M. A. Díaz Verriera, and J. M. Yáñez Castro, “Vehículos eléctricos y el impacto en el sistema de potencia. Análisis de la operación y emisiones,” *Revista de energía de Latinoamérica y el Caribe ENERLAC*, vol. 5, no. 2, pp. 14–39, 2021. [Online]. Available: <https://bit.ly/44zJXiw>
- [21] J. Lascano, L. Chiza, R. Saraguro, C. Quinatoa, and J. Tapia, “Estimación de la demanda de una estación de carga para vehículos eléctricos mediante la aplicación de métodos probabilísticos,” *Revista Técnica Energía*, vol. 20, no. 1, pp. 52–64, 2023. [Online]. Available: <https://doi.org/10.37116/revistaenergia.v20.n1.2023.569>



RADIATIVE HEAT TRANSFER IN H_2O AND CO_2 MIXTURES

INTERCAMBIO TÉRMICO RADIANTE EN MEZCLAS DE H_2O Y CO_2

Yanan Camaraza-Medina^{1,*}

Received: 27-11-2023, Received after review: 07-05-2024, Accepted: 13-05-2024, Published: 01-07-2024

Abstract

This study presents an approximate solution for assessing radiation heat exchange within a gaseous participating medium consisting of H_2O and CO_2 . This solution is applicable for values of the product of the total pressure and the mean beam length (PL), ranging from 0.06 to 20 $atm \cdot m$, and temperatures (T) ranging from 300 K to 2100 K. To approximate the exact solutions, the Spence root weighting method is employed. The exact spectral emissivity and absorptivity ε_λ and a_λ of the gas mixture for each set of PL and T values are calculated using the analytical solution (AS). Additionally, the values of the emissivity and absorptivity of the mixture ε_m and a_m are determined using the Hottel graphical method (HGM) and the proposed approximate solution. The HGM shows a weaker correlation, with mean errors of $\pm 15\%$ and $\pm 20\%$ for 54.2% and 75.3% of the evaluated data, respectively. In contrast, the proposed method yields the best fit, with mean errors of $\pm 10\%$ and $\pm 15\%$ for 79.4% and 98.6% of the evaluated data, respectively. In all cases, the agreement between the proposed model and the available experimental data is deemed sufficiently robust to warrant consideration for practical design applications.

Keywords: Participating media, emissivity, absorptivity, view factor, thermal radiation

Resumen

En este trabajo se presenta una solución aproximada para evaluar el intercambio de térmico por radiación a través de un medio participante gaseoso compuesto por H_2O y CO_2 , la cual es válida para valores del producto de la presión total y la longitud característica del haz de radiación (PL) desde 0,06 hasta 20 $atm \cdot m$ y temperaturas (T) desde 300 K a 2100 K. Para la aproximación de las SA disponibles es utilizado el método de ponderación de raíces de Spence. Para cada juego de valores PL ;T es calculado el valor de emisividad y absorptividad espectral exacta ε_λ y a_λ para la mezcla de gases mediante la solución analítica (SA) y el valor de la emisividad y absorptividad de la mezcla ε_m y a_m , usando el método gráfico de Hottel (MGH) y la solución aproximada propuesta. El peor ajuste de correlación se corresponde al MGH, con errores medios de $\pm 15\%$ y $\pm 20\%$ para el 54,2 % y 75,3 % de los datos evaluados, respectivamente, mientras que método propuesto proporciona el mejor ajuste, con errores medios de $\pm 10\%$ y $\pm 15\%$ para el 79,4 % y 98,6 % de los datos evaluados. En todos los casos, el acuerdo del modelo propuesto con los datos experimentales disponibles es lo suficientemente bueno como para ser considerado satisfactorio para el diseño práctico.

Palabras clave: medios participantes, emisividad, absorptividad, factor de visión, radiación térmica

^{1,*}Departamento de Ingeniería Mecánica, Universidad de Guanajuato, México.
 Corresponding author ✉: ycamaraza1980@yahoo.com.

Suggested citation: Camaraza-Medina, Y. "Radiative heat transfer in H_2O and CO_2 mixtures," *Ingenius, Revista de Ciencia y Tecnología*, N.º 32, pp. 36-47, 2024, DOI: <https://doi.org/10.17163/ings.n32.2024.04>.

1. Introduction

In the analysis of thermal radiation exchange between surfaces, it is frequently assumed for simplicity that both surfaces are separated by a non-participating medium. This assumption implies that the medium neither emits, scatters, nor absorbs radiation. Atmospheric air at common temperatures and pressures approximates a non-participating medium. Gases composed of monoatomic molecules, such as helium and argon, or symmetric diatomic molecules, such as O_2 and N_2 , exhibit behavior akin to that of a non-participating medium, except at extremely high temperatures where ionization occurs. For this reason, in practical radiation calculations, atmospheric air is regarded as a non-participating medium [1–3].

Gases with asymmetric molecules, such as SO_2 , CO , H_2O , CO_2 , and hydrocarbons C_mH_n , can absorb energy during radiative heat transfer processes at moderate temperatures. At high temperatures, such as those in combustion chambers, they can simultaneously emit and absorb radiation. Hence, in any medium containing these gases at adequate concentrations, the impact of the participating medium must be taken into account in radiation calculations. Combustion gases in a furnace or chamber contain significant quantities of H_2O and CO_2 consequently, the thermal assessment must incorporate the participating effect of these gases [4, 5].

The presence of a participating medium complicates the analysis of thermal radiation exchange. The participating medium absorbs and emits radiation throughout its volume, rendering gaseous radiation a volumetric phenomenon. This dependency on the size and shape of the body persists even if the temperature is uniform throughout the medium. Solids emit and absorb radiation across the entire spectrum; however, gases emit and absorb energy in multiple narrow wavelength bands. This suggests that assuming a grey body is not always suitable for gases, even when the surrounding surfaces are grey. The specific absorption and emission properties of gases within a mixture are also contingent on the pressure, temperature, and composition of the mixture. Hence, the radiation characteristics of a particular gas are affected by the presence of other participating gases, stemming from the overlap of emission bands from each component gas in the mixture [6–8].

In a gas, the distance between molecules and their mobility is greater than in solids, allowing a significant portion of radiation emitted from deeper layers to reach the boundary of the mass. Thick layers of gas absorb more energy and transmit less than thin layers. Therefore, in addition to specifying the properties determining the gas state (temperature and pressure), it is also necessary to define a characteristic length L of the gas mass to determine its radiative properties.

The emissive and absorptive powers are expressed as a function of this length L through which radiation must travel within the mass. Thus, in gases, the emissive power ε is a function of the product of the gas's partial pressure, denoted as P_x and the characteristic length of the radiation beam L [9–11].

The propagation of radiation through a participating medium can be complex due to the concurrent influence of aerosols, including dust, soot particles (unburnt carbon), liquid droplets, and ice particles, which scatter radiation. Scattering entails alterations in the radiation direction due to reflection, refraction, and diffraction. Rayleigh scattering, induced by gas molecules, typically exerts a minimal impact on heat transfer. Numerous researchers have undertaken advanced investigations into thermal radiation exchange within scattering media [12–14].

The investigation of thermal radiation exchange within participating media has been a research subject for several decades. Among the methodologies commonly employed and endorsed in specialized literature is the Hottel Graphical Method (HGM), renowned for yielding an average deviation of $\pm 25\%$. However, HGM requires reading and interpreting experimental nomograms, introducing additional errors stemming from visual graph interpretation. Consequently, in numerous instances, the actual deviation may surpass $\pm 35\%$, thus posing a notable limitation to its applicability [15, 16].

It initially entails establishing the analytical solution of the view factor, which is succeeded by volumetric integration, a process that can be streamlined by utilizing vector calculus advantages. The mathematical procedure involves managing an extensive array of primitive functions, often necessitating numerical methods to resolve special functions derived from cylindrical or spherical contours (such as Bessel, Spence, and Godunov functions). Consequently, an analytical solution (AS) for this problem category remains elusive, thus prompting reliance on approximate methods, predominantly derived from the Monte Carlo method, alongside numerical techniques and the finite element method [17–19].

While participating media can encompass liquid or semi-transparent solids, such as glass, water, and plastics, this study confines its scope to gases emitting and absorbing radiation. Specifically, the investigation will concentrate on the radiation emission and absorption properties of H_2O and CO_2 , given their prevalence as the predominant participating gases in practical applications. Notably, combustion products in furnaces and combustion chambers burning hydrocarbons contain these gases in elevated concentrations [20–22].

The study aims to procure an approximate solution for assessing thermal radiation exchange within a gaseous participating medium comprising H_2O and CO_2 . This solution aims to mitigate high mathemati-

cal intricacy while maintaining an acceptable margin of error compared to the analytical solution (within $\pm 15\%$), suitable for engineering applications. Additionally, this research endeavors to derive analytical solutions to determine the value of L across various geometric configurations of surfaces frequently used in engineering, alongside elucidating the emissivity and absorptivity characteristics of the participating gas mixture.

For comparative analysis, analytical solutions were computed for 355 permutations of thermodynamic temperature within the range $300\text{K} \leq T \leq 2100\text{K}$, and the product of the total pressure of the gas mixture and the characteristic length of the radiation beam (PL) within the range $0,06\text{ atm}\cdot\text{m} \leq PL \leq 20\text{ atm}\cdot\text{m}$. For each PL and T combination, the exact spectral emissivity and absorptivity ε_λ y α_λ for the gas mixture were determined using the analytical solution (AS). In contrast, the emissivity and absorptivity of the mixture ε_m y α_m were evaluated using the Hottel Graphical Method (HGM) and the proposed approximate solution.

Considering the pragmatic nature of the contribution and the favorable adjustment values obtained, the proposed method emerges as a fitting tool for implementation in thermal engineering and allied disciplines necessitating thermal radiation computations through participating media.

2. Materials and Methods

2.1. Radiative Properties in a Participating Medium

Consider a participating medium with a specified thickness. An incident spectral radiation beam of intensity $I_{\lambda(0)}$ impinges upon the medium and undergoes attenuation as it progresses, primarily due to absorption. The decrease in radiation intensity as it traverses a layer of thickness dx is directly proportional to both the intensity itself and the thickness dx . This phenomenon, known as Beer's Law, is mathematically expressed as [23]:

Where k_λ is the spectral absorption coefficient of the medium.

By separating variables in equation (1) and integrating within the limits $x=0$ to $x=L$, we obtain [13]:

$$dl_{\lambda(x)} = -k_\lambda I_{\lambda(x)} dx \quad (1)$$

In the derivation of equation (2) an assumption has been made that the absorptivity of the medium remains independent of x , based on its exponential decrease. The spectral transmissivity of a medium can be defined as the ratio of the intensity of radiation exiting the medium to that entering it, expressed as:

$$\frac{I_{\lambda(L)}}{I_{\lambda(0)}} = e^{-k_\lambda L} \quad (2)$$

The spectral transmissivity τ_λ of a medium represents the fraction of radiation transmitted through that medium at a specific wavelength. Radiation traversing a non-scattering (and consequently non-reflective) medium is either absorbed or transmitted. Hence, the following relationship holds [12]:

$$\tau_\lambda = \frac{I_{\lambda(L)}}{I_{\lambda(0)}} = e^{-k_\lambda L} \quad (3)$$

$$\alpha_\lambda + \tau_\lambda = 1 \quad (4)$$

By combining equations ((3) and (4) we derive the spectral absorptivity of a medium with thickness L , expressed as equation (5):

$$\alpha_\lambda = 1 - e^{-k_\lambda L} \quad (5)$$

Following Kirchhoff's law, the spectral emissivity is expressed as equation (6):

$$\varepsilon_\lambda = \alpha_\lambda = 1 - e^{-k_\lambda L} \quad (6)$$

Therefore, a medium's spectral absorptivity, transmissivity, and emissivity are dimensionless values equal to or less than one. The coefficients ε_λ , α_λ and τ_λ vary according to wavelength, temperature, pressure, and the composition of the mixture [12].

2.2. Mean beam length

The emissivity and absorptivity of a gas depend on the characteristic length, the shape and the size of the gaseous mass involved. In their experiments during the 1930s, Hottel and his colleagues postulated that radiation emission originates from a hemispherical gas mass directed towards a small surface element positioned at the center of the hemisphere's base. Hence, extending the emissivity data of gases examined by Hottel to gas masses with different geometric arrangements proves advantageous. This extension is accomplished by introducing the concept of characteristic or mean beam length L , which represents the radius of an equivalent hemisphere [24–26].

The analytical solution (AS) for deriving the spectral emissivity of the participating gas mixture is a function of the product of the length L , the partial pressure of the participating component, and the view factor between the emitting and receiving surfaces (see Figure 1. This is expressed by the following mathematical relationship (7), [27]:

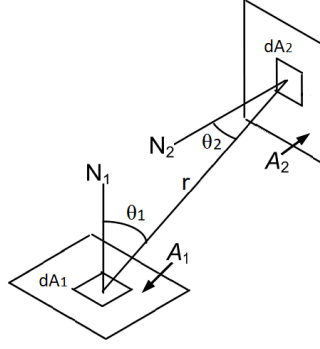


Figure 1. Basic geometry of the view factor

$$\varepsilon_\lambda = \frac{V_{gas}}{\pi A} \int_0^\infty P_P dP \int_0^\infty (1 - e^{-k_\lambda L}) d\lambda \quad (7)$$

$$\int_{A_1} \int_{A_2} \frac{\cos\theta_1 \cos\theta_2}{r^2} dA_1 dA_2$$

Where: A_1 and A_2 are the emitting and receiving surfaces, respectively θ_1, θ_2 : are the angles between the normal vector to the areas dA_1 and dA_2 and the line connecting the center of the surfaces A_1 y A_2 . V_{gas} represent the total area of the heating surfaces and the volume of the enclosure, respectively. R is the distance between the centers of the surfaces A_1 y A_2 .

Equation (7) is very complex for practical engineering calculations, which is why simplifications or approximations are often used [28].

Solving equation (7) is a complex task, largely owing to the multitude of primitive functions and immediate integrals involved in the integration process. Consequently, analytical solutions (AS) for specific cases exist in specialized literature to ascertain the values of L [29]. However, for other prevalent configurations, only experimentally derived approximate values are accessible [30].

2.3. Emissivity and absorptivity of participating gases and their mixtures

The radiative properties (RP) of an opaque solid are independent of its shape or configuration; however, the geometric shape of a gas does impact its RP. The spectral absorptivity of CO_2 consists of four absorption bands located at wavelengths of $1,9 \mu m$, $2,7 \mu m$, $4,3 \mu m$ and $15 \mu m$ [31].

The minima and maxima of this distribution and their discontinuities indicate notable distinctions between the absorption bands of a gas and those of a grey body. The width and shape of these absorption

bands exhibit variability in response to changes in pressure and temperature. Furthermore, the thickness of the gas layer exerts a significant influence. Hence, accurate estimation of the Radiative Properties (RP) of a gas necessitates the consideration of these three parameters [32].

Absorption and emission in gases exhibit discontinuities across the spectrum. Radiative Properties (RP) are notably pronounced within specific bands at various wavelengths while diminishing towards zero in adjacent bands. The complexity increases in gaseous mixtures due to the overlapping spectral bands of constituent gases. Consequently, this fundamental challenge stems from the absence of analytical solutions for predicting RP [33].

In thermal engineering, a method proposed by Hottel has been widely applied to estimate the RP in gaseous mixtures. This approach entails the separate assessment of each gaseous component within the mixture, followed by adjustments to account for factors such as partial pressure, temperature variations, and the spectral band overlap among mixture constituents [29].

This principle allows for predicting the emissivity or absorptivity of a gas mixture with a maximum deviation of $\pm 25\%$. However, the Hottel method has the disadvantage of relying on the reading and interpretation of the graphical results, which leads to additional errors. Consequently, the estimated RP values may exhibit an average deviation of $\pm 35\%$ or even higher [34].

The partial pressure P_x of each component in a gas mixture is expressed by the following relationship [34]:

$$P_x = P \cdot (\%_x) \quad (8)$$

Where: P is the total pressure of the gas mixture. $\%_c$ is the percentage fraction of each gas in the total composition. Note that $1 \text{ atm} = 10^5 \text{ N/m}^2$.

Hereafter, the subscripts w and c be employed to denote H_2O and CO_2 , respectively. The reduced partial pressures for H_2O and CO_2 are given by:

$$P_{WL} = \frac{P_W \cdot L}{0,3048} \quad (9)$$

$$P_{CL} = \frac{P_C \cdot L}{0,3048} \quad (10)$$

Where: P_W and P_C are the partial pressures of H_2O and CO_2 respectively; L is the characteristic length of the radiation beam.

For a unit pressure of 1 atm, the basic emissivities of H_2O and CO_2 are given by equation (11) and (12):

$$e_{W1} = \sqrt{P_{WL}} \left\{ \sqrt[4]{T} (0,078 - 0,003 \sqrt[4]{T}) - 0,41 \right\} + \sqrt[4]{P_{WL}} \left\{ \sqrt[4]{T} \cdot (0,032 - 0,018 \sqrt[4]{T}) + 0,88 \right\} + \sqrt[4]{T} (0,007 \sqrt[4]{T} - 0,03) - 0,24 \quad (11)$$

$$\begin{aligned}
e_{C1} = & \left\{ \sqrt{P_{CL}} \left\{ \sqrt[4]{T} \left(0.024 \sqrt[4]{T} - 0.264 \right) + 0.5 \right\} + \right. \\
& \sqrt[4]{P_{CL}} \left\{ \sqrt[4]{T} \left(0.484 - 0.042 \sqrt[4]{T} \right) - 0.0774 \right\} + \\
& \left. \sqrt[4]{T} \left(0.158 - 0.019 \sqrt[4]{T} \right) - 0.051 \right\}^4
\end{aligned} \tag{12}$$

In equations (11) and (12), the gas temperature T and (12) must be corrected. These correction factors are expressed in K. If $P \neq 1$ atm, then the basic emissivities of H_2O and CO_2 computed using equations (11)

$$\begin{aligned}
C_W = & \left\{ \sqrt[4]{P_{WL}} \cdot (0.137 \sqrt[4]{P_{WL}} - 0.047 \sqrt{P_{WL}} - 0.003) - 0.597 \right\} \cdot \left(\frac{P_W + P}{2} \right)^2 \\
& + \left\{ \sqrt[4]{P_{WL}} \cdot (0.685 \sqrt{P_{WL}} - 2.033 \sqrt[4]{P_{WL}} + 0.945) + 1.963 \right\} \cdot \left(\frac{P_W + P}{2} \right) \\
& + \sqrt[4]{P_{WL}} (0.982 \sqrt[4]{P_{WL}} - 0.33 \sqrt{P_{WL}} - 0.472) + 0.168
\end{aligned} \tag{13}$$

$$\begin{aligned}
C_c = & \left\{ \sqrt[4]{P_{CL}} (0.332 - 0.0442 \sqrt[4]{P_{CL}}) - 0.61 \right\} \cdot \\
& \sqrt{P} + \left\{ \sqrt[4]{P_{CL}} (0.44 \sqrt[4]{P_{CL}} - 1.993) + 2.862 \right\} \cdot \\
& \sqrt[4]{P} + \sqrt[4]{P_{CL}} (1.594 - 0.362 \sqrt[4]{P_{CL}}) - 1.171
\end{aligned} \tag{14}$$

Therefore, when $P \neq 1$ atm, the emissivities of H_2O and CO_2 are given by:

$$e_W = e_{W1} \cdot C_W \tag{15}$$

$$e_C = e_{C1} \cdot C_C \tag{16}$$

The emissivities derived from equations (15) and (16) correspond to the respective individual fractions of H_2O and CO_2 within the gas mixture.

To determine the total emissivity, it is necessary to determine a correction coefficient that considers the effect of the overlap of the emission bands. This correction factor depends on the temperature and the partial pressures of H_2O and CO_2 . To define the correction factor, two combinations involving the partial

pressures are established: the sum of the partial pressures and the deviation of the partial pressures, as determined by the following relationships:

$$P_1 = P_{WL} + P_{CL} \tag{17}$$

$$P_2 = P_W / (P_W + P_C) \tag{18}$$

The correction factor is obtained through the direct integration of equation (17). Due to the complexity of the mathematical process, only the correction factors for three predetermined temperature values will be presented here: $T=400$ K, $T=800$ K, and $T \geq 1200$ K. These correction factors are expressed as follows:

$$\begin{aligned}
C_{r(T=400K)} = & \left\{ \sqrt[4]{P_1} \cdot \left(1.841 \sqrt[4]{P_1} - 0.807 \sqrt{P_1} - 2.282 \right) + 1.059 \right\} \cdot (P_2)^4 \\
& + \left\{ \sqrt[4]{P_1} \cdot \left(3.067 \sqrt{P_1} - 9.259 \sqrt[4]{P_1} + 11.07 \right) - 4.585 \right\} \cdot (P_2)^3 \\
& + \left\{ \sqrt[4]{P_1} \cdot \left(11.79 \sqrt[4]{P_1} - 3.491 \sqrt{P_1} - 14.15 \right) + 5.678 \right\} \cdot (P_2)^2 \\
& + \left\{ \sqrt[4]{P_1} \cdot \left(1.332 \sqrt{P_1} - 4.685 \sqrt[4]{P_1} + 5.667 \right) - 2.249 \right\} \cdot P_2
\end{aligned} \tag{19}$$

$$\begin{aligned}
C_{r(T=800K)} = & \left\{ \sqrt[4]{P_1} \cdot \left(3.277 \sqrt{P_1} - 10.46 \sqrt[4]{P_1} + 9.524 \right) - 2.387 \right\} \cdot (P_2)^4 \\
& + \left\{ \sqrt[4]{P_1} \cdot \left(22 \sqrt[4]{P_1} - 6.7 \sqrt{P_1} - 21.12 \right) + 5.889 \right\} \cdot (P_2)^3 \\
& + \left\{ \sqrt[4]{P_1} \cdot \left(4.237 \sqrt{P_1} - 14.2 \sqrt[4]{P_1} + 14.02 \right) - 4.133 \right\} \cdot (P_2)^2 \\
& + \left\{ \sqrt[4]{P_1} \cdot \left(2.91 \sqrt[4]{P_1} - 0.869 \sqrt{P_1} - 2.782 \right) + 0.801 \right\} \cdot P_2
\end{aligned} \tag{20}$$

$$\begin{aligned}
C_{r(T \geq 1200K)} = & \left\{ \sqrt[4]{P_1} \cdot \left(9.731\sqrt{P_1} - 32.35\sqrt[4]{P_1} + 33.49 \right) - 10.83 \right\} \cdot (P_2)^4 \\
& + \left\{ \sqrt[4]{P_1} \cdot \left(63.03\sqrt[4]{P_1} - 18.69\sqrt{P_1} - 66.09 \right) + 21.64 \right\} \cdot (P_2)^3 \\
& + \left\{ \sqrt[4]{P_1} \cdot \left(10.49\sqrt{P_1} - 35.51\sqrt[4]{P_1} + 36.98 \right) - 12.04 \right\} \cdot (P_2)^2 \\
& + \left\{ \sqrt[4]{P_1} \cdot \left(4.939\sqrt[4]{P_1} - 1.533\sqrt{P_1} - 4.589 \right) + 1.335 \right\} \cdot P_2
\end{aligned} \tag{21}$$

For temperature values in the ranges $400K < T < 800K$ and $800K < T < 1200K$, the correction factor $C_{r(T)}$ will be determined through Newton's linear interpolation, using the following relationships:

$$400K < T < 800K \quad C_{r(T)} = C_{r(T=400K)} + \frac{C_{r(T=800K)} - C_{r(T=400K)}}{400} \cdot (T - 400) \tag{22}$$

$$800K < T < 1200K \quad C_{r(T)} = C_{r(T=800K)} + \frac{C_{r(T \geq 1200K)} - C_{r(T=800K)}}{400} \cdot (T - 800) \tag{23}$$

With the correction factor $C_{r(T)}$ for the mixture established, the effective emissivity of the mixture, denoted e_m is determined by the following equation:

$$e_m = e_W + e_C - C_{r(T)} \tag{24}$$

To determine the absorptivity of the gases, it is necessary to adjust the reduced partial pressures, as the reference temperature in this case corresponds to the source (emitter or wall). Consequently, equations (9) and (10) are transformed as follows:

$$P_{WLL} = \frac{P_W \cdot L \cdot T}{0.3048 \cdot T_s} \tag{25}$$

$$P_{CLL} = \frac{P_C \cdot L \cdot T}{0.3048 \cdot T_s} \tag{26}$$

Where: T_s corresponds to the temperatures of the emitting surfaces.

For a unit pressure of 1 atm, the basic absorptivities of H_2O and CO_2 are given by:

$$\begin{aligned}
a_{W1} = & \sqrt{P_{WLL}} \left\{ \sqrt[4]{T_s} \left(0.078 - 0.003\sqrt[4]{T_s} \right) - 0.41 \right\} \\
& + \sqrt[4]{P_{WLL}} \left\{ \sqrt[4]{T_s} \cdot \left(0.032 - 0.018\sqrt[4]{T_s} \right) + 0.88 \right\} \\
& + \sqrt[4]{T_s} \left(0.007\sqrt[4]{T_s} - 0.03 \right) - 0.24
\end{aligned} \tag{27}$$

$$\begin{aligned}
a_{C1} = & \left\{ \sqrt{P_{CLL}} \left\{ \sqrt[4]{T_s} \left(0.024\sqrt[4]{T_s} - 0.264 \right) + 0.5 \right\} \right. \\
& + \sqrt[4]{P_{CLL}} \left\{ \sqrt[4]{T_s} \cdot \left(0.484 - 0.042\sqrt[4]{T_s} \right) - 0.774 \right\} \\
& \left. + \sqrt[4]{T_s} \left(0.158 - 0.019\sqrt[4]{T_s} \right) - 0.051 \right\}^4
\end{aligned} \tag{28}$$

In equations (27) and (28), the temperature of the emitting surface T_s is given in K.

If $P \neq 1$ atm, then the basic absorptivity values for H_2O and CO_2 need adjustment by incorporating the correction factors calculated with equations (13) and (14) and a thermodynamic factor that addresses the non-uniformity of the temperature distribution on the emitting surface and within the gas. Mathematically, this is expressed as follows:

$$C_{Wa} = C_W \cdot \left(\frac{T}{T_s} \right)^{0.45} \tag{29}$$

$$C_{Ca} = C_C \cdot \left(\frac{T}{T_s} \right)^{0.65} \tag{30}$$

Therefore, when $P \neq 1$ atm, the absorptivities of H_2O and CO_2 are given by:

$$a_W = a_{W1} \cdot C_{Wa} \tag{31}$$

$$a_C = a_{C1} \cdot C_{Ca} \tag{32}$$

The absorptivities calculated using equations (31) and (32) correspond to the individual gaseous fractions of H_2O and CO_2 , respectively.

To calculate the total absorptivity, it is necessary to determine a correction coefficient that considers the effect of the overlap of the absorption bands. This correction factor depends on the sum of the reduced partial pressures of H_2O and CO_2 , which is obtained using the following relationship:

$$P_3 = P_{WLL} + P_{CLL} \tag{33}$$

The correction factor is obtained through the direct integration of equation (7). Due to the complexity of this integration process, only the correction factors for three predetermined temperature values will be provided here: $T = 400K$, $T = 800K$ and $T \geq 1200K$. These correction factors are expressed as follows:

$$\begin{aligned}
C_{ra(T=400\text{ K})} = & \left\{ \sqrt[4]{P_3} \cdot \left(1.841 \sqrt[4]{P_3} - 0.807 \sqrt{P_3} - 2.282 \right) + 1.059 \right\} \cdot (P_2)^4 \\
& + \left\{ \sqrt[4]{P_3} \left(3.067 \sqrt{P_3} - 9.259 \sqrt[4]{P_3} + 11.07 \right) - 4.585 \right\} \cdot (P_2)^3 \\
& + \left\{ \sqrt[4]{P_3} \left(11.79 \sqrt[4]{P_3} - 3.491 \sqrt{P_3} - 14.15 \right) + 5.678 \right\} \cdot (P_2)^2 \\
& + \left\{ \sqrt[4]{P_3} \cdot \left(1.332 \sqrt{P_3} - 4.685 \sqrt[4]{P_3} + 5.667 \right) - 2.249 \right\} \cdot P_2
\end{aligned} \tag{34}$$

$$\begin{aligned}
C_{ra(T=800\text{ K})} = & \left\{ \sqrt[4]{P_3} \cdot \left(3.277 \sqrt{P_3} - 10.46 \sqrt[4]{P_3} + 9.524 \right) - 2.387 \right\} \cdot (P_2)^4 \\
& + \left\{ \sqrt[4]{P_3} \cdot \left(22 \sqrt[4]{P_3} - 6.7 \sqrt{P_3} - 21.12 \right) + 5.889 \right\} \cdot (P_2)^3 \\
& + \left\{ \sqrt[4]{P_3} \left(4.237 \sqrt{P_3} - 14.2 \sqrt[4]{P_3} + 14.02 \right) - 4.133 \right\} \cdot (P_2)^2 \\
& + \left\{ \sqrt[4]{P_3} \cdot \left(2.91 \sqrt[4]{P_3} - 0.869 \sqrt{P_3} - 2.782 \right) + 0.801 \right\} \cdot P_2
\end{aligned} \tag{35}$$

$$\begin{aligned}
C_{ra(T \geq 1200\text{ K})} = & \left\{ \sqrt[4]{P_3} \cdot \left(9.731 \sqrt{P_3} - 32.35 \sqrt[4]{P_3} + 33.49 \right) - 10.83 \right\} \cdot (P_2)^4 \\
& + \left\{ \sqrt[4]{P_3} \cdot \left(63.03 \sqrt[4]{P_3} - 18.69 \sqrt{P_3} - 66.09 \right) + 21.64 \right\} \cdot (P_2)^3 \\
& + \left\{ \sqrt[4]{P_3} \cdot \left(10.49 \sqrt{P_3} - 35.51 \sqrt[4]{P_3} + 36.98 \right) - 12.04 \right\} \cdot (P_2)^2 \\
& + \left\{ \sqrt[4]{P_3} \cdot \left(4.939 \sqrt[4]{P_1} - 1.533 \sqrt{P_3} - 4.589 \right) + 1.335 \right\} \cdot P_2
\end{aligned} \tag{36}$$

In equations (34) to (36) the deviation of partial pressures P_2 is calculated using equation (18). For temperature values in the ranges $400\text{ K} < T < 800\text{ K}$

and $800\text{ K} < T < 1200\text{ K}$, the correction factor $C_{ra(T)}$ will be determined using Newton's linear interpolation, utilizing the following relationships:

$$400\text{ K} < T < 800\text{ K} \quad C_{ra}(T) = C_{ra}(T = 400\text{ K}) + \frac{C_{ra}(T = 800\text{ K}) - C_{ra}(T = 400\text{ K})}{400} \cdot (T - 400) \tag{37}$$

$$800\text{ K} < T < 1200\text{ K} \quad C_{ra}(T) = C_{ra}(T = 800\text{ K}) + \frac{C_{ra}(T \geq 1200\text{ K}) - C_{ra}(T = 800\text{ K})}{400} \cdot (T - 800) \tag{38}$$

Given the correction factor $C_{ra(T)}$ of the mixture, the effective absorptivity of the mixture a_m is defined by the following equation:

$$a_m = a_W + a_C - C_{ra(T)} \tag{39}$$

3. Results and Discussion

3.1. Validation of the Proposed Model

For the validation of the proposed model, random temperature values in the range $300\text{ K} \leq T \leq 2100\text{ K}$ are employed, alongside six predetermined values of the product PL (0.06, 0.6, 3, 5, 10, 20 atm · m), with 55, 55, 45, 55, 45, and 80 data points for each PL interval, respectively. For each combination of PL and T, the exact spectral emissivity ε_λ is determined using the analytical solution (AS), while the emissivity of the mixture e_m is calculated using the Hottel Graphical Method (HGM) and equation (24).

In Figure 2, the ratio ε_λ/e_m is correlated with temperature T, adjusted within error bands of $\pm 15\%$ and $\pm 20\%$, using the e_m values obtained through HGM. In Figure 3, the ratio ε_λ/e_m is correlated with temperature T, adjusted within error bands of $\pm 10\%$ and $\pm 15\%$, using the e_m values calculated through equation (24).

The percentage deviation (error) is computed relative to the AS and is determined using the following relationship [35]:

$$D\% = E\% = 100 \cdot \left(\frac{\varepsilon_\lambda - e_m}{\varepsilon_\lambda} \right) \tag{40}$$

Figure 2 illustrates that the HGM yields the poorest fit compared to the AS, with mean errors of $\pm 15\%$ and $\pm 20\%$ for 54.2% and 75.3% of the evaluated (PL; T) points. For the HGM, the optimal fit is achieved for PL = 3.0, with mean errors of $\pm 15\%$ and $\pm 20\%$ for 63.2% and 84.2% of the evaluated data, respectively, while the least favorable fit is obtained for PL = 10,

with mean errors of $\pm 15\%$ and $\pm 20\%$ for 42.7% and 57.1% of the evaluated data.

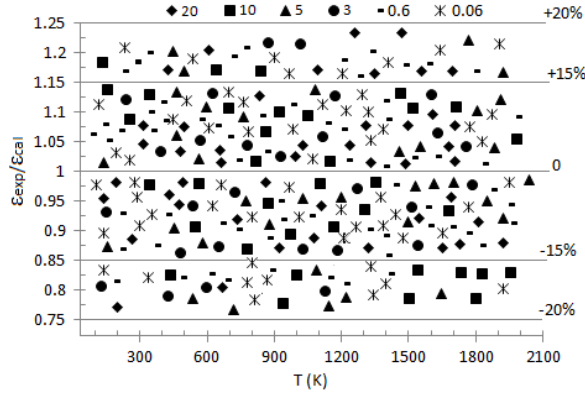


Figure 2. Correlation between temperature T and the ratio $\varepsilon_\lambda/\varepsilon_m$ using the HGM

Figure 3 illustrates that equation (24) yields superior fitting performance compared to the AS, with mean errors of $\pm 10\%$ and $\pm 15\%$ for 79.4% and 94.9% of the evaluated (PL; T) points. For equation (24), the best fit is obtained for $PL = 20$, with mean errors of $\pm 10\%$ and $\pm 15\%$ for 83.2% and 98.6% of the evaluated data, respectively. Conversely, the least favorable fitting occurs at $PL = 0.6$, where mean errors of $\pm 10\%$ and $\pm 15\%$ are registered for 75.1% and 91.9% of the evaluated data.

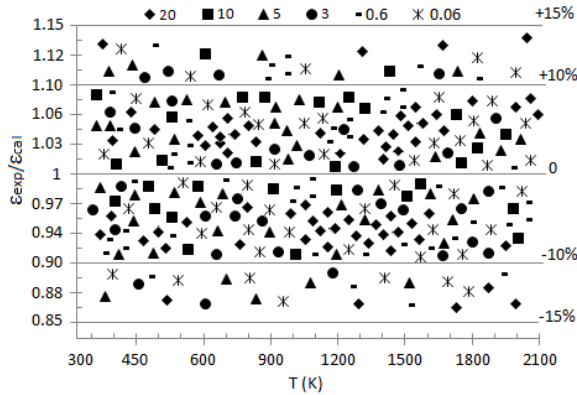


Figure 3. Correlation between temperature T and the ratio $\varepsilon_\lambda/\varepsilon_m$ using equation (24).

3.2. Application to a Case Study

A pressurized furnace, measuring (length \times width \times height) $3m \times 4m \times 5m$, contains combustion gases at $T=1200K$ and a pressure $P=2$ atm. In contrast, the surface temperature of the furnace walls, T_S , is maintained at $1100K$. Volumetric analysis reveals that the composition of the combustion gases comprises 87% N_2 , 8% of H_2O , and 5% of CO_2 . The task at hand is

to compute the heat transfer between the combustion gases and the furnace walls, consisting of bricks with a grey, satin finish surface.

Using the relationships given in [29], it is determined that $L = 3,04m \approx 3m$. Using equation (8), the partial pressures of H_2O and CO_2 are computed, yielding $P_W = 0,16$ y $P_C = 0,1$, respectively. Subsequently, the reduced partial pressures are determined utilizing equations (9) and (10), resulting in $P_{WL} = 1,575atm \cdot m$ y $P_{CL} = 0,984atm \cdot m$. The fundamental emissivities for H_2O and CO_2 are acquired through equations (11) and (12) correspondingly, yielding $e_{W1} = 0,255$ y $e_{C1} = 0,135$.

Since $P \neq 1atm$, the basic emissivities of H_2O and CO_2 must be corrected using equations (13) and (14), respectively, yielding $C_W = 1,379$ and $C_C = 1$. The actual emissivities of H_2O and CO_2 are determined through equations (15), and (16), resulting in $e_W = 0,3524$ and $e_C = 0,157$. The sum P_1 and deviation P_2 of partial pressures are calculated using relationships (17) and (18), obtaining $P_1 = 2,559atm \cdot m$ and $P_2 = 0,615atm \cdot m$.

The gas mixture temperature is maintained at 1200 K; hence, the correction coefficient $C_{r(T=1200K)}$ is determined utilizing equation (21), resulting in $C_{r(T=1200K)} = 0,052atm \cdot m$. The effective emissivity of the mixture e_m is given by equation (24), resulting in $e_m = 0,458$. Subsequently, employing equation (7) and undergoing a meticulous integration process, the precise value of $\varepsilon_\lambda = 0,463$ is obtained, whereas the HGM provides a value of $e_m = 0,43$. Using equation (40), the error with respect to the AS is determined, yielding $D\% = 1,08\%$ y $D\% = 7.13\%$, for equation (24) and the HGM, respectively.

The modified reduced pressures are obtained using equations (25) and (26), yielding $P_{WLL} = 1,718atm \cdot m$ y $P_{CLL} = 1,073atm \cdot m$. The basic absorptivities for H_2O and CO_2 are calculated using equations (27) and (28) respectively, resulting in $a_{W1} = 0,275$ and $a_{C1} = 0,144$.

Since $P \neq 1atm$, the basic absorptivities of H_2O and CO_2 must be corrected using equations (29) y (30), respectively, yielding $C_{Wa} = 1,434$ and $C_{Ca} = 1,234$. The absorptivities of the fractions of H_2O and CO_2 are determined using equations (31) and (32), resulting in $a_W = 0,394$ and $a_C = 0,178$. The sum of partial pressures P_3 is calculated using equation (33), obtaining $P_3 = 2,791atm \cdot m$.

The temperature of the gas mixture is 1200 K; therefore, the correction coefficient $C_{ra(T=1200K)}$ is estimated using equation (36), $C_{ra(T=1200K)} = 0,053atm \cdot m$. The effective absorptivity of the mixture a_m is given by equation (39), resulting in $a_m = 0,519$. Using equations (6) and (7) and undergoing a meticulous handling of immediate integrals, the precise value of $a_{\neq} = 0,525$ is obtained, while the HGM provides a value of $a_m = 0,449$. Using equation (40), the com-

puted error with respect to the AS is determined, yielding $D\% = 1,14\%$ y $D\% = 14,48\%$, for equation (24) and the HGM, respectively.

The furnace walls consist of brick, featuring a grey surface with a satin finish, maintaining an average temperature of $T_s = 1100K$. With these specifications, the surface's normal emissivity is $e_s = 0,75$.

The heat flux exchanged between the gases and the furnace wall is given by:

$$Q_n = \frac{\varepsilon_s + 1}{2} A_s \sigma (\varepsilon_m T^4 - a_m (T_s)^4) \quad (41)$$

The heat flux values exchanged (in kW) are obtained using the AS, the HGM, and equation (24), with the computed error relative to the AS also determined. Table 1 summarizes the obtained heat flux values (in kW) and the corresponding error $E\%$ in each case relative to the AS.

Table 1. Obtained Values Q_n and $E\%$ for the Case Study

Methods	$Q_n(kW)$	$E\%(%)$
AS	56.822	-
HGM	697.354	-22,4
Proposed method	565.108	0.82

4. Conclusions

Upon comparison with the AS, an approximate method was developed to estimate thermal radiation exchange through participating media. The proposed models were validated by comparing them with the existing AS.

The derived models correlate with all experimental data for both the HGM and the proposed method, exhibiting a mean deviation of $\pm 20\%$ and $\pm 10\%$, respectively.

For the HGM, the least favorable fitting compared to the AS is achieved for $PL=10$, exhibiting a mean error of $\pm 20\%$ for 57.1% of the assessed data. In contrast, the optimal fitting occurs for $PL=3.0$, displaying a mean error of $\pm 15\%$ for 63.2% of the evaluated data. Conversely, for the proposed method, the poorest fitting compared to the AS is observed for $PL=0.6$, with a mean error of $\pm 15\%$ for 91.9% of the analyzed data. In contrast, the most accurate fitting is achieved for $PL=20$, with a mean error of $\pm 10\%$ for 83.2% of the evaluated data.

In all instances, the alignment of the proposed model with the available experimental data is sufficiently robust to be deemed satisfactory for practical design purposes.

Acknowledgements

The author extends gratitude for the recommendations provided by Professor Dr. John R. Howell from the Department of Mechanical Engineering at the University of Texas at Austin.

References

- [1] M. H. Bordbar, G. Węcel, and T. Hyppänen, "A line by line based weighted sum of gray gases model for inhomogeneous CO_2-H_2O mixture in oxy-fired combustion," *Combustion and Flame*, vol. 161, no. 9, pp. 2435–2445, 2014. [Online]. Available: <https://doi.org/10.1016/j.combustflame.2014.03.013>
- [2] M. F. Modest and R. J. Riazzi, "Assembly of full-spectrum k-distributions from a narrow-band database; effects of mixing gases, gases and nongray absorbing particles, and mixtures with nongray scatterers in nongray enclosures," *Journal of Quantitative Spectroscopy and Radiative Transfer*, vol. 90, no. 2, pp. 169–189, 2005. [Online]. Available: <https://doi.org/10.1016/j.jqsrt.2004.03.007>
- [3] M. Cui, X. Gao, and H. Chen, "Inverse radiation analysis in an absorbing, emitting and non-gray participating medium," *International Journal of Thermal Sciences*, vol. 50, no. 6, pp. 898–905, 2011. [Online]. Available: <https://doi.org/10.1016/j.ijthermalsci.2011.01.018>
- [4] T. J. Moore and M. R. Jones, "Analysis of the conduction–radiation problem in absorbing, emitting, non-gray planar media using an exact method," *International Journal of Heat and Mass Transfer*, vol. 73, pp. 804–809, 2014. [Online]. Available: <https://doi.org/10.1016/j.ijheatmasstransfer.2014.02.029>
- [5] L. J. Dorigon, G. Duciak, R. Brittes, F. Cassol, M. Galarça, and F. H. França, "WSGG correlations based on HITEMP2010 for computation of thermal radiation in non-isothermal, non-homogeneous H_2O/CO_2 mixtures," *International Journal of Heat and Mass Transfer*, vol. 64, pp. 863–873, 2013. [Online]. Available: <https://doi.org/10.1016/j.ijheatmasstransfer.2013.05.010>
- [6] F. Cassol, R. Brittes, F. H. França, and O. A. Ezekoye, "Application of the weighted-sum-of-gray-gases model for media composed of arbitrary concentrations of H_2O , CO_2 and soot," *International Journal of Heat and Mass Transfer*, vol. 79, pp. 796–806, 2014. [Online]. Available: <https://doi.org/10.1016/j.ijheatmasstransfer.2014.08.032>

- [7] F. R. Centeno, R. Brittes, F. H. França, and O. A. Ezekoye, "Evaluation of gas radiation heat transfer in a 2D axisymmetric geometry using the line-by-line integration and WSGG models," *Journal of Quantitative Spectroscopy and Radiative Transfer*, vol. 156, pp. 1–11, 2015. [Online]. Available: <https://doi.org/10.1016/j.jqsrt.2015.01.015>
- [8] Y. Camaraza-Medina, "Polynomial cross-roots application for the exchange of radiant energy between two triangular geometries," *Ingenius, Revista de Ciencia y Tecnología*, no. 30, pp. 29–41, 2023. [Online]. Available: <https://doi.org/10.17163/ings.n30.2023.03>
- [9] M. Alberti, R. Weber, and M. Mancini, "Re-creating Hottel's emissivity charts for water vapor and extending them to 40 bar pressure using HITEMP-2010 data base," *Combustion and Flame*, vol. 169, pp. 141–153, 2016. [Online]. Available: <https://doi.org/10.1016/j.combustflame.2016.04.013>
- [10] —, "Gray gas emissivities for H_2O - CO_2 - CO - N_2 mixtures," *Journal of Quantitative Spectroscopy and Radiative Transfer*, vol. 219, pp. 274–291, 2018. [Online]. Available: <https://doi.org/10.1016/j.jqsrt.2018.08.008>
- [11] S. Khivisara, M. U. M. Reddy, K. Reddy, and P. Dutta, "Measurement of radiation heat transfer in supercritical carbon dioxide medium," *Measurement*, vol. 139, pp. 40–48, 2019. [Online]. Available: <https://doi.org/10.1016/j.measurement.2019.03.012>
- [12] M. F. Modest and S. Mazumder, "Chapter 4 - view factors," in *Radiative Heat Transfer (Fourth Edition)*, fourth edition ed., M. F. Modest and S. Mazumder, Eds. Academic Press, 2022, pp. 127–159. [Online]. Available: <https://doi.org/10.1016/B978-0-12-818143-0.00012-2>
- [13] Y. Camaraza-Medina, A. Hernández-Guerrero, and J. L. Luviano-Ortiz, "Experimental study on influence of the temperature and composition in the steels thermo physical properties for heat transfer applications," *Journal of Thermal Analysis and Calorimetry*, vol. 147, no. 21, pp. 11 805–11 821, Nov 2022. [Online]. Available: <https://doi.org/10.1007/s10973-022-11410-8>
- [14] J. Howell, M. Meng"u, K. Daun, and R. Siegel, *Thermal Radiation Heat Transfer*. CRC Press, 2021. [Online]. Available: <https://lc.cx/2KIpyY>
- [15] J. Farmer and S. Roy, "A quasi-Monte Carlo solver for thermal radiation in participating media," *Journal of Quantitative Spectroscopy and Radiative Transfer*, vol. 242, p. 106753, 2020. [Online]. Available: <https://doi.org/10.1016/j.jqsrt.2019.106753>
- [16] T. Li, X. Lin, Y. Yuan, D. Liu, Y. Shuai, and H. Tan, "Effects of flame temperature and radiation properties on infrared light field imaging," *Case Studies in Thermal Engineering*, vol. 36, p. 102215, 2022. [Online]. Available: <https://doi.org/10.1016/j.csite.2022.102215>
- [17] S. Li, Y. Sun, J. Ma, and R. Zhou, "Angular-spatial discontinuous galerkin method for radiative heat transfer with a participating medium in complex three-dimensional geometries," *International Communications in Heat and Mass Transfer*, vol. 145, p. 106836, 2023. [Online]. Available: <https://doi.org/10.1016/j.icheatmasstransfer.2023.106836>
- [18] J. Ávalos Patiño, S. Dargaville, S. Neethling, and M. Piggott, "Impact of inhomogeneous unsteady participating media in a coupled convection–radiation system using finite element based methods," *International Journal of Heat and Mass Transfer*, vol. 176, p. 121452, 2021. [Online]. Available: <https://doi.org/10.1016/j.ijheatmasstransfer.2021.121452>
- [19] Y. Camaraza-Medina, A. Hernández-Guerrero, and J. L. Luviano-Ortiz, "Analytical view factor solution for radiant heat transfer between two arbitrary rectangular surfaces," *Journal of Thermal Analysis and Calorimetry*, vol. 147, no. 24, pp. 14 999–15 016, Dec 2022. [Online]. Available: <https://doi.org/10.1007/s10973-022-11646-4>
- [20] B.-H. Gao, H. Qi, J.-W. Shi, J.-Q. Zhang, Y.-T. Ren, and M.-J. He, "An equation-solving method based on radiation distribution factor for radiative transfer in participating media with diffuse boundaries," *Results in Physics*, vol. 36, p. 105418, 2022. [Online]. Available: <https://doi.org/10.1016/j.rinp.2022.105418>
- [21] S. Sun, "Simultaneous reconstruction of thermal boundary condition and physical properties of participating medium," *International Journal of Thermal Sciences*, vol. 163, p. 106853, 2021. [Online]. Available: <https://doi.org/10.1016/j.ijthermalsci.2021.106853>
- [22] B.-H. Gao, H. Qi, A.-T. Sun, J.-W. Shi, and Y.-T. Ren, "Effective solution of three-dimensional inverse radiation problem in participating medium based on RDFIEM," *International Journal of Thermal Sciences*, vol. 156, p. 106462, 2020. [Online]. Available: <https://doi.org/10.1016/j.ijthermalsci.2020.106462>

- [23] E. Gümücşsu and H. I. Tarman, “Numerical simulation of duct flow in the presence of participating media radiation with total energy based entropic lattice Boltzmann method,” *International Journal of Thermofluids*, vol. 20, p. 100516, 2023. [Online]. Available: <https://doi.org/10.1016/j.ijft.2023.100516>
- [24] Y. Camaraza-Medina, A. M. Rubio-Gonzales, O. M. Cruz-Fonticiella, and O. F. Garcia-Morales, “Analysis of pressure influence over heat transfer coefficient on air cooled condenser,” *Journal Européen des Systèmes Automatisés*, vol. 50, no. 3, pp. 213–226, 2017. [Online]. Available: <https://doi.org/10.3166/JESA.50.213-226>
- [25] P. Sadeghi and A. Safavinejad, “Radiative entropy generation in a gray absorbing, emitting, and scattering planar medium at radiative equilibrium,” *Journal of Quantitative Spectroscopy and Radiative Transfer*, vol. 201, pp. 17–29, 2017. [Online]. Available: <https://doi.org/10.1016/j.jqsrt.2017.06.023>
- [26] Y. Wang, A. Sergeant, D. Saury, D. Lemonnier, and P. Joubert, “Numerical study of an unsteady confined thermal plume under the influence of gas radiation,” *International Journal of Thermal Sciences*, vol. 156, p. 106474, 2020. [Online]. Available: <https://doi.org/10.1016/j.ijthermalsci.2020.106474>
- [27] Y. Camaraza-Medina, Y. Retirado-Mediceja, A. Hernández-Guerrero, and J. Luis Luviano-Ortiz, “Energy efficiency indicators of the steam boiler in a power plant of Cuba,” *Thermal Science and Engineering Progress*, vol. 23, p. 100880, 2021. [Online]. Available: <https://doi.org/10.1016/j.tsep.2021.100880>
- [28] Y. Camaraza-Medina, A. Hernández-Guerrero, and J. L. Luviano-Ortiz, “Contour integration for the view factor calculation between two rectangular surfaces,” *Heat Transfer*, vol. 53, no. 1, pp. 225–243, 2024. [Online]. Available: <https://doi.org/10.1002/htj.22950>
- [29] Y. Camaraza-Medina, A. Hernandez-Guerrero, and J. L. Luviano-Ortiz, “Radiant energy exchange through participating media composed of arbitrary concentrations of H_2O , CO_2 , and CO ,” *Heat Transfer*, vol. 53, no. 4, pp. 2073–2094, 2024. [Online]. Available: <https://doi.org/10.1002/htj.23026>
- [30] X. Liu, S. Kelm, M. Kampili, G. V. Kumar, and H.-J. Allelein, “Monte Carlo method with SNBCK nongray gas model for thermal radiation in containment flows,” *Nuclear Engineering and Design*, vol. 390, p. 111689, 2022. [Online]. Available: <https://doi.org/10.1016/j.nucengdes.2022.111689>
- [31] Y. Camaraza-Medina, A. Hernández-Guerrero, and J. Luis Luviano-Ortiz, “Contour integration for the exchange of radiant energy between diffuse rectangular geometries,” *Thermal Science and Engineering Progress*, vol. 47, p. 102289, 2024. [Online]. Available: <https://doi.org/10.1016/j.tsep.2023.102289>
- [32] A. Mukherjee, V. Chandrakar, and J. R. Senapati, “New correlations for infrared suppression devices having louvered diabatic tubes with surface radiation,” *Thermal Science and Engineering Progress*, vol. 44, p. 102011, 2023. [Online]. Available: <https://doi.org/10.1016/j.tsep.2023.102011>
- [33] V. Chandrakar, A. Mukherjee, and J. R. Senapati, “Free convection heat transfer with surface radiation from infrared suppression system and estimation of cooling time,” *Thermal Science and Engineering Progress*, vol. 33, p. 101369, 2022. [Online]. Available: <https://doi.org/10.1016/j.tsep.2022.101369>
- [34] F. Asllanaj, S. Contassot-Vivier, G. C. Fraga, F. H. França, and R. J. da Fonseca, “New gas radiation model of high accuracy based on the principle of weighted sum of gray gases,” *Journal of Quantitative Spectroscopy and Radiative Transfer*, vol. 315, p. 108887, 2024. [Online]. Available: <https://doi.org/10.1016/j.jqsrt.2023.108887>
- [35] Y. Camaraza-Medina, A. A. Sánchez Escalona, O. Miguel Cruz-Fonticiella, and O. F. García-Morales, “Method for heat transfer calculation on fluid flow in single-phase inside rough pipes,” *Thermal Science and Engineering Progress*, vol. 14, p. 100436, 2019. [Online]. Available: <https://doi.org/10.1016/j.tsep.2019.100436>



OPTIMIZATION OF THE VARTM PROCESS FOR PROTOTYPING A BUMPER USING HYBRID COMPOSITE MATERIALS

OPTIMIZACIÓN DEL PROCESO VARTM, PARA EL PROTOTIPADO DE UN GUARDACHOQUE, UTILIZANDO MATERIALES COMPUESTOS HÍBRIDOS

Diego Javier Jiménez-Pereira^{1,*} , Christian Augusto Picoita-Camacho² 

Received: 30-09-2023, Received after review: 30-04-2024, Accepted: 20-05-2024, Published: 01-07-2024

Abstract

To provide an alternative for manufacturing auto parts using composite materials, the Vacuum Assisted Resin Transfer Molding (VARTM) process was utilized to prototype the bumper for the Chevrolet Aveo vehicle. This technique emerges as an alternative for composite material manufacturing, allowing for rapid and high-quality production of advanced composites. In this study, a hybrid composite material reinforced with fiberglass, cabuya fiber, IN2 epoxy resin, an infusion mesh, peel ply, and a vacuum bag was employed. To optimize the VARTM process in bumper prototyping, several simulations of resin flow were conducted with different locations of resin injection and vacuum entry points. Autodesk Moldflow Insight software facilitated the modification and addition of resin injection points to observe the flow evolution, thus determining the filling time for each proposed design. Six different designs were applied for the bumper mold filling. The proposed linear flow design reduced the total filling time of the bumper mold by 81.56% compared to the other five designs analyzed. The result of the numerical simulation was validated through the experimental process, where a high degree of concordance in the mold filling time was achieved between both methods.

Keywords: bumper, cabuya fiber, fiberglass, optimization, resin, simulation, VARTM

Resumen

Con el fin de brindar una alternativa para la manufactura de autopartes utilizando materiales compuestos, se aplicó el proceso VARTM en el prototipado del guardachoque del vehículo Chevrolet Aveo. Esta técnica surge como una alternativa para la fabricación de materiales compuestos, ya que permite realizar una producción rápida y de alta calidad de compuestos avanzados. En el presente estudio, se utilizó un material compuesto híbrido reforzado con fibra de vidrio, cabuya, resina epóxica IN2, una malla de infusión, peel ply y una bolsa de vacío. Para la optimización del proceso VARTM en el prototipado del guardachoque, se llevaron a cabo varias simulaciones de flujo de resina con distintas ubicaciones de los puntos de entrada de resina y de vacío. El software Autodesk Moldflow Insight permitió modificar y agregar puntos de entrada de resina con el fin de observar la evolución del flujo y de esta forma llegar a determinar el tiempo de llenado para cada diseño planteado. Se aplicaron seis diseños diferentes para el llenado del molde del guardachoque. El diseño propuesto de flujo lineal reduce un 81,56 % el tiempo total de llenado del molde del guardachoque en comparación con los otros 5 diseños analizados. El resultado de la simulación numérica fue validado mediante la experimentación del proceso, donde se obtuvo una gran concordancia del tiempo de llenado del molde entre ambos métodos.

Palabras clave: fibra de cabuya, fibra de vidrio, guardachoque, optimización, resina, simulación, VARTM

^{1,*}Carrera de Tecnología Superior en Mecánica Automotriz, Instituto Superior Tecnológico Loja, Ecuador.
 Corresponding author ✉: djjimenez@tecnologicoloja.edu.ec.

²Carrera de Tecnología Superior en Electricidad, Instituto Superior Tecnológico Loja, Ecuador.

Suggested citation: Jiménez-Pereira, D.J. and Picoita-Camacho, C.A. "Optimization of the VARTM Process for Prototyping a Bumper Using Hybrid Composite Materials," *Ingenius, Revista de Ciencia y Tecnología*, N.º 32, pp. 48-57, 2024, DOI: <https://doi.org/10.17163/ings.n32.2024.05>.

1. Introduction

The manufacturing process predominantly employed for producing bumpers is plastic injection molding. This method involves injecting molten plastic under high pressure into a mold, forming the bumper into the desired shape. Despite necessitating costly tooling and substantial capital investment, this process is preferred due to its capacity to consistently produce parts of excellent quality with high reproducibility [1].

As an alternative for manufacturing auto parts, fiber-reinforced composite materials (FRCM) have gained widespread adoption in the automotive industry, particularly for constructing body components. Employing these materials facilitates a reduction in vehicle weight by up to 25%, consequently achieving fuel savings of approximately 5% [2]. One notable technique for fabricating components from FRCM is the Vacuum Assisted Resin Transfer Molding (VARTM). This method utilizes a flexible material known as a vacuum bag to serve as the counter-mold, enabling precise and efficient production processes [3].

In this process, the reinforcing material, typically fibers, is arranged within a mold and encased by a vacuum bag. Vacuum pressure is applied, reducing the internal pressure of the bag, which in turn minimizes air content and enhances the flow of resin through strategically placed pipes within the mold to thoroughly impregnate the fibers. A resin distribution mesh is commonly employed to expedite the resin flow, along with a peel ply that remains unimpregnated by the resin. This methodology enables using cost-effective tools to fabricate high-quality composite parts, thereby establishing it as a favored manufacturing technique across various industries [4]. Figure 1 illustrates the described process.

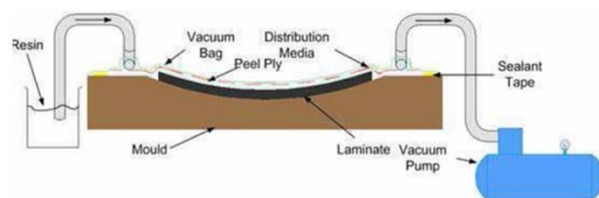


Figure 1. Resin Infusion Process [5]

This process has been widely used for manufacturing different components. Khan et al. [2] manufactured a car body to participate in the Shell Eco-marathon in Malaysia, using the VARTM process. The fibers used for reinforcement were 92110 glass fabric and 260G non-crimp carbon fabric. The epoxy resin LY 5052/Aradur 5052 served as the matrix. In the manufacturing process, a layer of randomly arranged nylon filaments was used to distribute and accelerate resin infusion. Vinyl spiral tubes were used as vacuum and

supply conduits. Finally, an Accutrak VPE-1000 device was used to detect leaks. The infusion process began from the innermost central part of the mold and extended to its perimeter, resulting in a car body that weighed 14.5 kg, including the metal structure.

The researchers [6] used Resin Transfer Molding (RTM) to manufacture a tire cover, utilizing polyester resin as the base and fiberglass as the reinforcing material with a volume fraction of 14% (equivalent to two layers of fiberglass mats). Mechanical tests conducted on samples of the final product using the RTM process revealed a significant increase of 185% in the elastic modulus and 97% in maximum tensile stress. However, achieving the final product required three unsuccessful attempts to adequately fill the mold. The issues identified included insufficient resin entry in certain reinforcement areas, attributable to mold design flaws, and elevated viscosities in the resin mixture caused by additives.

In 2016, Pachón and Orozco [7] explored the feasibility of using release wax as peel ply in the VARTM process to fabricate an air filter cover for a carbureted vehicle. The final product was obtained after six failed attempts, ultimately determining that release wax was unsuitable as a release agent.

As evidenced in previous projects, the VARTM process requires several trial and error tests during the manufacturing stage, demanding excessive use of resources and time. Additionally, it is essential to ensure that the resin fully impregnates the reinforcing material within the mold when applying the VARTM technique [8]. Air leaks during the infusion process can result in manufactured components having void-rich areas, reducing their mechanical properties [9]. Moreover, the resin infusion process becomes slow for large parts, rendering the method economically unfeasible for large-scale production. According to Reference [10], to perform a proper resin infusion process, the locations of resin entry and air exit points in the mold must be carefully considered.

As evidenced in previous projects, the VARTM process requires several trial and error tests during the manufacturing stage, demanding excessive use of resources and time. Additionally, it is essential to ensure that the resin fully impregnates the reinforcing material within the mold when applying the VARTM technique [8]. Air leaks during the infusion process can result in manufactured components having void-rich areas, reducing their mechanical properties [9]. Moreover, the resin infusion process becomes slow for large parts, rendering the method economically unfeasible for large-scale production. According to Reference [10], to perform a proper resin infusion process, the locations of resin entry and air exit points in the mold must be carefully considered.

To mitigate these issues, numerical simulation of the resin flow front has become an essential tool for

optimizing the process. According to Simacek and Advani [11], simulation packages based on RTM molding process models are the only viable option for practical VARTM process simulation and, consequently, its optimization. Below, some studies conducted by various researchers aimed at simulating and optimizing the VARTM process are discussed.

Du et al. [4] determined the optimal positions for resin entry and air extraction points using RTM-Worx software, which simulates the resin flow process. Employing design criteria for placing resin entry and extraction ports in the Vacuum Assisted Resin Transfer Molding (VARTM) process, they found that the entry ports should be located in the central part and along the curves. In contrast, the extraction ports should be positioned at the bumper corners to achieve a shorter filling time.

In 2014, Poorzeinolabedin et al. [10] used PAM-RTM software to conduct several simulations aimed at identifying the most suitable locations for resin entry ports and vents in the manufacturing of an exterior part of the Samand Sarir vehicle body. Eight case studies were conducted, each proposing different locations for entry and extraction points to observe the resin flow pattern and filling time. The placement of resin entry points on the right side and extraction points on the left side yielded a simulated filling time of 1203 s, compared to the experimental filling time was 1350 s.

In 2013, Li et al. [12] conducted simulations of the Resin Transfer Molding (RTM) process for manufacturing a wind turbine blade using Moldflow software. These simulations encompassed various parameters, including filling time, temperature, buckling deformation, and pressure evolution, comparing scenarios with and without cooling. The analysis revealed that air bubble formation predominantly occurs at the blade roots and edges. Additionally, it was determined that the filling time is longer when the cooling process is implemented than when it is omitted.

Laurenzi et al. [13] presented the analysis of the numerical process and experimental research for manufacturing a carbon fiber-reinforced beam for an aircraft turbine using resin transfer molding. Initially, they experimentally characterized the permeability value. Subsequently, they conducted process simulations using a modified control volume through the finite element method (FEM-CV). This approach enabled them to explore resin flow front patterns and determine the injection scheme that ensures proper preform impregnation and a filling time compatible with the hardener gelation time.

In Ecuador, bumpers are imported from countries like China, Brazil, and Colombia due to the absence of local companies dedicated to their manufacture. This lack of investment and innovation in manufacturing processes has positioned the country as an importer of this automotive component. Domestic production is

confined to manufacturing rear bumpers for pickups and buses, utilizing fiberglass and resins [14].

Academic innovation projects have utilized natural fibers for manufacturing auto parts. One such fiber is cabuya, naturally found throughout the Ecuadorian highlands. This fiber exhibits good mechanical strength (305.15 MPa), high durability, light weight, and other properties that make it suitable for composite materials [15]. Examples of these projects are detailed in [14], where a hybrid composite material (fiberglass + cabuya fiber + fiberglass) was employed to manufacture a bus bumper. The resin deposition was performed manually using brushes and rollers, resulting in favorable mechanical properties. Similarly, Pachacama [16] utilized a composition of 70% resin and 30% cabuya fiber to manufacture a Mazda BT50 pickup hood through Hand-Lay Up and compression molding techniques. This prototype achieved a tensile strength of 85.92 MPa and a maximum flexural stress of 13.72 MPa.

This study introduces an alternative manufacturing process using innovative techniques for producing front bumpers. A prototype front bumper for the Chevrolet Aveo vehicle is fabricated using FRCM with epoxy resin as the matrix, reinforced with mat fiberglass and cabuya fiber, through the VARTM process.

The process simulation was conducted using Autodesk Moldflow Insight software to identify the optimal location of resin entry and exit points within the mold for manufacturing the prototype. For the final production, the assembly of materials and equipment on the prototype mold was carried out considering the information obtained from the simulations to optimize the VARTM process. The following section provides a detailed description of the methodology used to create the bumper prototype.

2. Materials and Methods

2.1. Materials

The properties of IN2 resin with AT30 SLOW hardener used in the fabrication of the bumper prototype are presented in Tables 1 and 2, respectively. These components are manufactured by Easy Composites Ltd.

Table 1. Properties of IN2 Epoxy Resin

Characteristic	Unit	Resin	Hardener	Combined
Appearance	-	Clear liquid	Clear liquid	Clear liquid
Viscosity (25°)	mPa.s	500-800	10-20	200-450
Density	g/cm3	1,08-1,18	1,07-1,13	1,12-1,18

Table 2. Curing Properties of the Hardener

Trade name	Pot Life at 25 °C	Gel Time at 25 °C	Demold Time	Curing Time at 25 °C
AT 30 SLOW	80-100 min	8-11 hours	18-24 hours	24 hours

Fine thread woven cabuya fiber, with a thickness of 0.9 mm, was sourced from a local producer in the province of Loja. For fiberglass, Chopped Strand Mat type distributed by Pinturas América was used. The prototype was fabricated using a combination of Glass + Cabuya + Glass to form the hybrid composite material. Additionally, an infusion mesh and peel ply were employed as optimization tools to fabricate the prototype. Figure 2 illustrates the fibers used in the project.

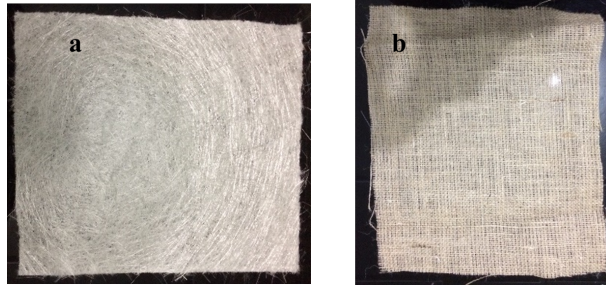


Figure 2. Types of Fibers Used: a) Chopped Strand Mat Fiberglass and b) Woven Cabuya Fiber

2.2. Numerical Simulation

Initially, a numerical simulation of the VARTM process was performed using Autodesk Moldflow Insight software. Six options for resin inlet points and vacuum points were proposed, following the methodology described by [4]. For each configuration, a mold filling time simulation was conducted to identify the option that yielded the shortest filling time.

For the prototype mold filling simulation, determining the permeability of the reinforcement is essential. Given that it comprises a hybrid material (glass + cabuya + glass) and utilizes an infusion mesh with peel ply, its permeability was established following the methods outlined in [17]. Several resin infusion tests were conducted on the hybrid material, with the radial movement of the resin flow front being recorded by filming the process. Figure 3 illustrates the scheme used.

Subsequently, data on the flow front advancement at time intervals of 20 s, 40 s, 80 s, 160 s, 320 s, 640 s, and 840 s were extracted from the tests and averaged. Equation (1) was then used to determine the permeability K in both directions $K11$ and $K22$. This equation describes Darcy's law applied to radial flows. The porosity data of the fibers were sourced from the

literature review, while the volume fraction was set to 40% fiberglass, 20% cabuya, and 40% epoxy resin.

$$K_{ij} = \frac{u\varepsilon}{4t\Delta P} \left\{ r_f^2 \left[2 \ln \left(\frac{r_f}{r_0} \right) - 1 \right] + (r_0^2) \right\} \quad (1)$$

Where:

- r_f = Radius of the flow front in direction 11 or 22
- r_0 = Radius of resin inlet
- μ = Viscosity
- ε = Porosity
- t = Time
- ΔP = Injection pressure

Table 3 indicates the properties of the hybrid material used in the simulation.

Table 3. Permeability Data of the Hybrid Material Used in the Simulation

Material	Volume fraction	Porosity	Permeability (m^2)		
			K11	K22	K33
Chopped Glass, Cabuya	40.2	0.4	3.7327×10^{10}	2.602×10^{10}	3.7327×10^{10}

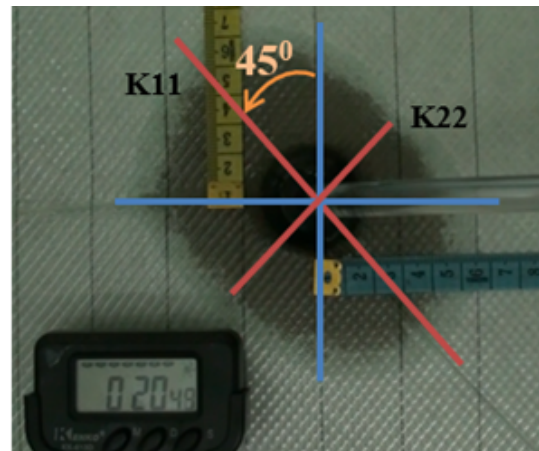


Figure 3. Scheme Used to Determine Permeability

Figures 4, 5, 6, 7 and 8 illustrate the various designs established for placing the resin and vacuum entry points in the mold filling of the Chevrolet Aveo bumper using VARTM.

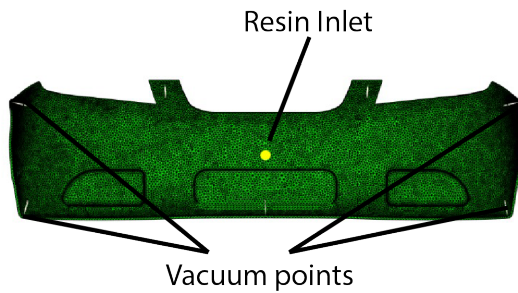


Figure 4. Design 1 (1 Resin Entry Point, 7 Vacuum Points)

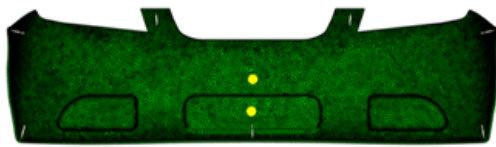


Figure 5. Design 2 (2 Resin Entry Points, 7 Vacuum Points)

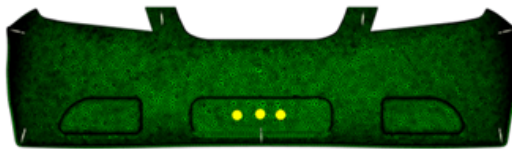


Figure 6. Design 3 (3 Resin Entry Points, 7 Vacuum Points)

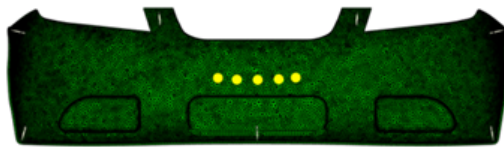


Figure 7. Design 4 (5 Resin Entry Points, 7 Vacuum Points)

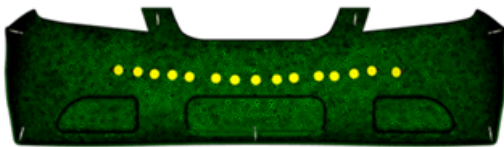


Figure 8. Design 5 (Multiple Resin Entry Points, 7 Vacuum Points)

Figure 9 depicts Design 6, which focuses on optimizing resource utilization and infusion time for the process application. This design strategy proposes multiple resin entry points along the upper edge of the bumper and a single vacuum point at the lower central part of the mold. This design aims to achieve a linear

flow from the upper to the lower part of the mold. According to [18], using the linear injection technique results in a shorter filling time compared to the convergent radial injection technique used in permeability characterization.

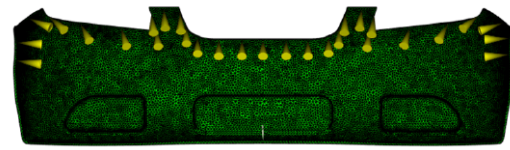


Figure 9. Design 6 (linear flow)

Finally, for each of the proposed designs, a VARTM process simulation is performed to determine which design minimizes the mold filling time. The validation of the selected design is conducted through the experimental process for manufacturing the bumper prototype.

2.3. Manufacturing the Bumper Prototype

First, a mold is constructed from the original bumper by molding its outer part and covering the holes for the headlights and grilles, as depicted in Figure 10. For this process, fiberglass and polyester resin are applied using the Hand Lay-Up method.



Figure 10. Bumper Manufacturing

Next, the mold is prepared by applying a chemical agent compatible with the IN2 epoxy resin to facilitate the demolding of the part. Sealant tape is placed around the mold, as depicted in Figure 11. This ensures that the vacuum bag can be securely sealed to the mold, compacting the fibers when applying vacuum pressure. The fiberglass and cabuya fibers are then positioned on the mold, as illustrated in Figure 12. Given the complexity of the mold, it is advisable to cut small layers of fibers and place them in the corners to ensure complete coverage of the surface.



Figure 11. Placement of Sealant Tape on the Mold



Figure 12. Arrangement of Fiberglass and Cabuya Fibers on the Mold

Peel ply and the distribution mesh are immediately placed over the fibers to accelerate the resin flow. Figure 13 illustrates the arrangement of these optimization aids.



Figure 13. Peel Ply and distribution mesh over the fibers used as reinforcement.

Next, based on the data derived from the VARTM process simulation, the resin and vacuum entry points

are strategically arranged for filling the bumper mold, selecting the configuration from Design 6. A spiral hose is installed to facilitate multiple resin entry points and optimize resources. This hose follows the mold's contour as indicated in the Design 6 simulation, while the vacuum point is situated in the lower central part of the mold. Figure 14 illustrates the placement of the spiral hose and the vacuum point.

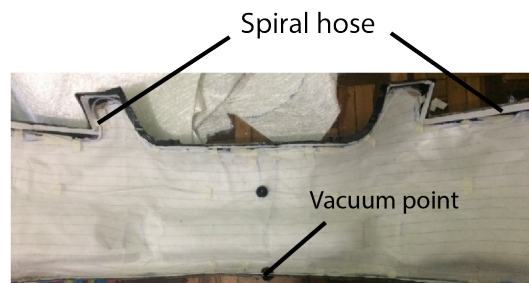


Figure 14. Placement of the spiral hose and vacuum point used for VARTM

After positioning the spiral hose and vacuum point, the vacuum bag is placed over the mold, applying pressure on the sealing tape. This step ensures a complete seal and prevents vacuum leaks. Figure 15 illustrates the placement of the vacuum bag over the mold.



Figure 15. Vacuum bag used for the VARTM process

Next, a vacuum is applied, allowing the resin to flow through the spiral hose to impregnate the fibers in the mold. The conditions under which the VARTM process was conducted for prototype manufacturing are detailed in Table 4. These data were sourced from the Composite Materials Manufacturing Guide by Easy Composites. Finally, the piece is allowed to cure for 24 hours following the infusion, after which demolding is performed to obtain the bumper prototype.

Table 4. Conditions used in the VARTM process

Injection Pressure (Pa)	Temperature (°C)	Resin Viscosity (Pa.s)
88 000	20-25	0.65

3. Results and Discussion

The process simulation was conducted, observing the advancement of the resin flow at various mold filling percentages (25%, 50%, 75%, and 100%). Figure 16 illustrates the progression of the resin flow, indicating that filling 25% of the mold requires 73 s, 50% takes 216 s, 75% is achieved in 432 s, and complete filling (100%) necessitates 865 s.

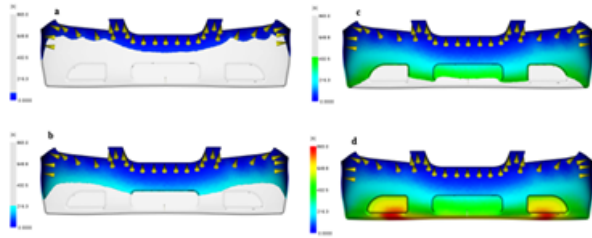


Figure 16. Simulation of the flow front advancement and filling time for design 6 of the VARTM process. a) 25%, b) 50%, c) 75%, d) 100%

The filling times corresponding to each of the previously proposed designs are specified in Table 5. These times were directly derived from the process simulations and serve as a guide for selecting the optimal positions for resin inlet and vacuum extraction points in the production of the bumper prototype.

For the validation of the performed simulation, Figure 17 compares the prototype fabrication using the VARTM process with the proposed Design 6 simulation, which requires the least time. It is observed that the progression of the resin flow front in the experimentation consistently matches the simulated process representation.

After curing the piece for 24 hours, the prototype is demolded. The initially applied chemical agent helps with the demolding of the piece. Figures 18 and 19 show the final piece obtained through the application of the VARTM process for the prototype fabrication.

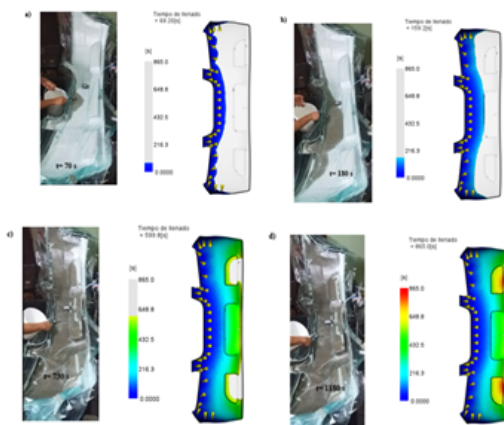


Figure 17. Comparison between the simulation and experimentation of the VARTM process for filling the bumper mold of the Chevrolet Aveo vehicle

Table 5. Filling time for each mold filling simulation design for the bumper

Design	Filling time (s)
1	4691.7
2	3025.4
3	2877
4	2237.7
5	870.7
6	865



Figure 18. Front view of the bumper prototype obtained through VARTM



Figure 19. Side view of the bumper prototype obtained through VARTM

3.1. Discussion

The results obtained from the simulations of the six proposed designs indicate that multiple resin entry points are necessary to improve the efficiency of the filling process. The analysis reveals that in Design 1, which features only one resin entry point located in the central part of the bumper mold, the infusion time is 4691.7 s. As the number of resin entry points increases, as observed in Design 6, which distributes these points along the central axis of the bumper, the infusion time is reduced to 870 s, which represents a decrease of 81.4% compared to the first option. In study [4], which focuses on the flow simulation and optimization of the VARTM process for bumper fabrication, increasing the resin entry points along the central axis of the bumper results in a reduction of 79.8% in infusion time.

To improve the efficiency of the bumper mold filling process, the configuration of Design 6 is proposed,

aiming for resource and time optimization. In this configuration, a single vacuum point is incorporated at the lower central part of the mold. In contrast, the resin entry points are positioned on the upper edge of the bumper mold. With this arrangement, the resin travels a shorter distance from the top to the bottom of the bumper mold. The time required to achieve complete mold filling is 865 s, resulting in a unidirectional and uniform resin flow front. Conversely, the optimization study presented by [4] arranged different resin flow fronts, which, upon meeting, can cause the formation of bubbles and dry spots. Additional vacuum points are strategically placed at the intersections of the resin flows to avoid this issue.

In this analysis, using a single vacuum point optimizes the mold filling time during implementation. Choosing to have multiple vacuum points, as in Designs 1-2-3-4-5, would require several vacuum pumps to meet the requirements. Ultimately, Design 6 allows for a notable reduction of 81.56% in infusion time compared to Design 1. It should be noted that although the simulation indicates a bumper mold filling time of 865 s, practical experimentation yielded a time of 1180 s, resulting in a margin of error of 36.41%. Figure 15 illustrates that at the beginning of the infusion, the configuration of the resin flow front in the experimentation differs from that in the simulation, primarily due to the use of the spiral hose. In the simulation, the resin is injected simultaneously through several entry points, while in the experimentation, the injection at the edges is carried out as the resin flows through the internal channel of the spiral hose. This results in a higher resin flow speed at the central point during the experimentation, altering the shape of the resin flow front.

Once the infusion begins, the resin flow front stabilizes, and the numerical simulation data align with the experimental results. When the central resin flow front reaches the vacuum point located in the mold, a specific amount of resin that does not impregnate the fibers arranged in the outer edges of the mold is removed. This discrepancy is why the experimentation requires more infusion time than initially calculated in the numerical simulation. This analysis is consistent with the study conducted by [19], which compared the simulation performed in LIMS software with the experimentation of the VARTM process for fabricating an airplane hatch. The time determined in the simulation was 3385 s, whereas it was 5940 s in the experimentation.

In the project presented by [20] for manufacturing a tricycle base using VARTM, some variations were observed between the process simulation and experimentation due to irregularities caused by the deformation of the vacuum bag. Despite these challenges, the cited authors emphasize and recognize the importance of numerical simulations in optimization processes.

During the demolding of the piece, a 15% increase in pressure inside the vacuum bag was noted, preventing the curing process from being conducted under adequate pressure. This pressure increase is attributed to small leaks detected after the infusion process, impacting the bumper's surface quality and generating areas with excess resin. The occurrence of leaks after infusion should be considered in future projects to ensure the production of high-quality parts.

It is worth noting that after the prototype was fabricated, tensile and flexural tests were conducted according to ASTM D3039-08 for tension and ASTM D7264M-07 for flexion on various specimens of the fiber-reinforced hybrid composite material. The results indicate that the material has an average maximum tensile stress of 86.74 MPa and an average maximum flexural stress of 128.73 MPa. When comparing these results with those from projects conducted Paredes [14] and Pachacama [16], it is evident that the tensile and flexural stresses are higher. This improvement is primarily attributed to the technique used for the bumper prototype fabrication, which is vacuum-assisted resin infusion. This method ensures uniform resin distribution and compaction at consistent vacuum pressure, yielding a higher-quality product. In contrast, the projects by [14] and [16] involve manual placement of the resin in the mold, resulting in uneven mold compaction.

4. Conclusions

The bumper prototype for the Chevrolet Aveo vehicle was produced using the VARTM process with hybrid materials. The process optimization was performed using Autodesk Moldflow software and was validated through practical experimentation. Incorporating distribution meshes and peel ply in molding processes with liquid composites is highlighted as a key method for optimization, resulting in a reduction of infusion times by up to 64.4%.

Simulations were conducted for six proposed designs regarding the placement of resin entry and vacuum points using Autodesk Moldflow. The choice of the optimization proposal was based on the filling time results. This proposal featured multiple resin entry points along the upper edge of the mold and a single vacuum point at the base, facilitating the observation of flow front progression. This setup acted as a guide to prevent areas of the fibers from lacking resin impregnation. The proposal emphasized resource optimization by utilizing practical and accessible tools for process experimentation. The simulation tool proved invaluable in minimizing the need for multiple trial and error tests, thereby enhancing the efficiency of producing a high-quality part.

The VARTM process is utilized in various automo-

tive applications and presents several critical aspects. Among these, the imperative to avoid air leaks during resin infusion is paramount to prevent defects in the component and ensure complete impregnation of the fibers used for reinforcement. Additionally, the material and economic resources required for applying VARTM in bumper manufacturing are more accessible than those required for other technologies dedicated to auto parts production.

References

- [1] P. Mitschang and K. Hildebrandt, “8 - polymer and composite moulding technologies for automotive applications,” in *Advanced Materials in Automotive Engineering*, J. Rowe, Ed. Woodhead Publishing, 2012, pp. 210–229. [Online]. Available: <https://doi.org/10.1533/9780857095466.210>
- [2] L. A. Khan, A. H. Mahmood, B. Hassan, T. Sharif, S. Khushnod, and Z. M. Khan, “Cost-effective manufacturing process for the development of automotive from energy efficient composite materials and sandwich structures,” *Polymer Composites*, vol. 35, no. 1, pp. 97–104, 2014. [Online]. Available: <https://doi.org/10.1002/pc.22638>
- [3] J. Summerscales, *Resin Infusion Under Flexible Tooling (RIFT)*. John Wiley & Sons, Ltd, 2012, pp. 1–11. [Online]. Available: <https://doi.org/10.1002/9781118097298.weoc216>
- [4] R. K. Du, F. F. Wang, X. H. Chen, Y. F. Zhang, G. Z. Zhao, and Y. Q. Liu, “Flow simulation and optimization of the car bumper beam by VARTM process,” in *Materials Processing and Manufacturing III*, ser. Advanced Materials Research, vol. 753. Trans Tech Publications Ltd, 10 2013, pp. 236–240. [Online]. Available: <https://doi.org/10.4028/www.scientific.net/AMR.753-755.236>
- [5] S. Sunaryo, G. L. Putra, and S. M. Lestari, “Thickness and fiber content optimization in VARTM method for high speed craft,” in *Advances in Materials, Processing and Manufacturing*, ser. Advanced Materials Research, vol. 789. Trans Tech Publications Ltd, 11 2013, pp. 412–416. [Online]. Available: <https://doi.org/10.4028/www.scientific.net/AMR.789.412>
- [6] J. G. Anchatuña León and V. H. Loachamín Navarrete, *Construcción de un prototipo de cubreneumático mediante moldeado por transferencia de resina de compuestos*. Tesis Maestría, 2015. [Online]. Available: <https://acortar.link/TfrUvy>
- [7] D. G. Chávez Pachón and E. R. Ledesma Orozco, “Fabricación en fibra de carbón de un accesorio automotriz utilizando el método de transferencia de resina,” *Jóvenes en la ciencia*, vol. 2, no. 1, pp. 1838–1842, 2017. [Online]. Available: <https://acortar.link/kKHR3L>
- [8] J. Porto, M. Letzow, E. dos Santos, S. Amico, J. Avila Souza, and L. Isoldi, “Computational modeling of RTM and LRTM processes applied to complex geometries,” *Revista de Engenharia Térmica*, vol. 11, pp. 93–99, 10 2018. [Online]. Available: <http://dx.doi.org/10.5380/reterm.v11i1-2.62007>
- [9] C. Wang, G. Yue, G. Bai, L. Pan, and B. Zhang, “Compaction behavior and permeability property tests of preforms in vacuum-assisted resin transfer molding using a combined device,” *Measurement*, vol. 90, pp. 357–364, 2016. [Online]. Available: <https://doi.org/10.1016/j.measurement.2016.04.058>
- [10] M. Poorzeinolabedin, L. Parnas, and S. H. Dashatan, “Resin infusion under flexible tooling process and structural design optimization of the complex composite part,” *Materials & Design*, vol. 64, pp. 450–455, 2014. [Online]. Available: <https://doi.org/10.1016/j.matdes.2014.08.008>
- [11] P. Simacek and S. G. Advani, “Resin flow modeling in compliant porous media: an efficient approach for liquid composite molding,” *International Journal of Material Forming*, vol. 11, no. 4, pp. 503–515, Jul 2018. [Online]. Available: <https://doi.org/10.1007/s12289-017-1360-9>
- [12] C. Li, M. Xu, and Y. Tie, “Simulation analysis of wind turbine blade during resin transfer molding process,” *Materials Physics and Mechanics*, vol. 18, pp. 127–134, 01 2013. [Online]. Available: <https://acortar.link/Kqm2K2>
- [13] S. Laurenzi, A. Grilli, M. Pinna, F. De Nicola, G. Cattaneo, and M. Marchetti, “Process simulation for a large composite aeronautic beam by resin transfer molding,” *Composites Part B: Engineering*, vol. 57, pp. 47–55, 2014. [Online]. Available: <https://doi.org/10.1016/j.compositesb.2013.09.039>
- [14] M. A. Córdova Suárez and J. G. Paredes Salinas, *Estudio de polímeros híbridos estratificados de matriz poliéster reforzada con fibra de vidrio y cabuya como material alternativo y su incidencia en las propiedades mecánicas en guardachoques para buses*. Tesis de Maestría, Universidad Técnica de Ambato, 2012. [Online]. Available: <https://acortar.link/BkoiLh>
- [15] J. M. Tixe Subina and J. D. Vistín Bastidas, *Aplicación de materiales compuestos para la fabricación de guardabarros y tapas laterales de una*

- moto de 125 cc, 4 tiempos*. Tesis de grado, Escuela Superior Politécnica del Chimborazo, 2015. [Online]. Available: <https://acortar.link/op1pAM>
- [16] V. Pachacama, *Diseño, caracterización y aplicación de un material compuesto con base de resina epoxi y refuerzo de fibras orgánicas para la aplicación en un prototipo de capot de la camioneta Mazda BT50*. Tesis de Grado, Universidad de las Fuerzas Armadas, 2015. [Online]. Available: <https://acortar.link/bbOfKF>
- [17] D. B. Peralta-Zurita, D. Jiménez-Pereira, J. V. Molina-Osejos, and G. A. Moreno-Jiménez, “Permeability characterization of a composite reinforced material with fiberglass and cabuya by VARTM process. case hybrid material,” in *Recent Advances in Electrical Engineering, Electronics and Energy*, M. Botto Tobar, H. Cruz, and A. Díaz Cadena, Eds. Cham: Springer International Publishing, 2021, pp. 16–30. [Online]. Available: https://doi.org/10.1007/978-3-030-72212-8_2
- [18] E. Ruiz and F. Trochu, “19 - flow modeling in composite reinforcements,” in *Composite Reinforcements for Optimum Performance*, ser. Woodhead Publishing Series in Composites Science and Engineering, P. Boisse, Ed. Woodhead Publishing, 2011, pp. 588–615. [Online]. Available: <https://doi.org/10.1533/9780857093714.4.588>
- [19] C. L. R. Polowick, *Optimizing vacuum assisted resin transfer moulding (VARTM) processing parameters to improve part quality*. PhD Thesis Carleton University, 2013. [Online]. Available: <https://acortar.link/WgvVAV>
- [20] E. Díaz Escriche, *Simulación y control de los procesos de transferencia de resina en moldes flexibles mediante modelos de permeabilidad equivalente*. PhD Tesis, Universidad Politécnica de Valencia, 2012. [Online]. Available: <https://doi.org/10.4995/Thesis/10251/17321>



DIAGNOSIS OF ORAL CANCER USING DEEP LEARNING ALGORITHMS

DIAGNÓSTICO DE CÁNCER ORAL MEDIANTE ALGORITMOS DE APRENDIZAJE PROFUNDO

Mayra Alejandra Dávila Olivos^{1,*} , Henry Miguel Herrera Del Águila¹ ,
 Félix Melchor Santos López¹

Received: 15-05-2023, Received after review: 20-05-2024, Accepted: 28-05-2024, Published: 01-07-2024

Abstract

Objective. The aim of this study was to use deep learning for the automatic diagnosis of oral cancer, employing images of the lips, mucosa, and oral cavity. A deep convolutional neural network (CNN) model, augmented with data, was proposed to enhance oral cancer diagnosis. **Materials and methods.** We developed a Mobile Net deep CNN designed to detect and classify oral cancer in the lip, mucosa, and oral cavity areas. The dataset comprised 131 images, including 87 positive and 44 negative cases. Additionally, we expanded the dataset by varying cropping, focus, rotation, brightness, and flipping. The diagnostic performance of the proposed CNN was evaluated by calculating accuracy, precision, recall, F1 score, and area under the curve (AUC) for oral cancer. **Results.** The CNN achieved an overall diagnostic accuracy of 90.9% and an AUC of 0.91 with the dataset for oral cancer. **Conclusion.** Despite the limited number of images of lips, mucosa, and oral cavity, the CNN method developed for the automatic diagnosis of oral cancer demonstrated high accuracy, precision, recall, F1 score, and AUC when augmented with data.

Keywords: Automatic diagnosis, convolutional neural network, data augmentation, dental health, oral cancer, oral disease

Resumen

Objetivo. El propósito de este estudio fue diagnosticar automáticamente el cáncer oral en imágenes de labios, mucosa y cavidad oral utilizando aprendizaje profundo. Se propuso un modelo de red neuronal convolucional (CNN) profunda con aumento de datos para el diagnóstico de enfermedades bucodentales. **Materiales y métodos.** Se desarrolló una CNN profunda de MobileNet para detectar y clasificar la enfermedad de cáncer oral en la zona de los labios, mucosa y cavidad oral. El conjunto de datos de 131 imágenes de labios, mucosa y cavidad oral estaba compuesto por 87 casos positivos y 44 casos negativos. Además, el número de imágenes se multiplicó mediante cambios de corte, enfoque, rotación, brillo y volteo. Se evaluó el rendimiento de diagnóstico de la CNN propuesta a través del cálculo de la exactitud, la precisión, la recuperación, la puntuación F1 y el AUC (Área bajo la curva) para la enfermedad de cáncer oral. **Resultados.** El rendimiento general del diagnóstico de la enfermedad de cáncer oral alcanzó el 90.9% de exactitud y 0.91 AUC usando la CNN con el conjunto de datos. **Conclusión.** El método CNN desarrollado para diagnosticar automáticamente el cáncer oral en imágenes de labios, mucosa y cavidad oral usando aumento de datos mostró una alta exactitud, precisión, recuperación, puntaje F1 y AUC a pesar del número limitado de imágenes de labios, mucosa y cavidad oral utilizadas.

Palabras clave: Diagnóstico automático, aumento de datos, cáncer oral, enfermedad bucodental, red neuronal convolucional, salud dental

^{1,*}Faculty of Systems Engineering and Informatics, National University of San Marcos, Perú.
 Corresponding author ✉: 12200133@unmsm.edu.pe.

Suggested citation: Dávila Olivos, M. A.; Herrera Del Águila, H.M. ; Santos López, F.M. "Diagnosis of oral cancer using deep learning algorithms," *Ingenius, Revista de Ciencia y Tecnología*, N.º 32, pp. 58-68, 2024, DOI: <https://doi.org/10.17163/ings.n32.2024.06>.

1. Introduction

Oral diseases pose a significant global public health challenge, particularly affecting less privileged populations due to their widespread occurrence. Treatment costs are often prohibitively high and remain unattainable in many low- and middle-income countries. According to the World Health Organization, managing oral diseases ranks as the fourth most expensive health condition in heavily urbanized nations. Given its profound impact on overall health, oral health is an essential determinant of human well-being and a critical component of healthcare. Furthermore, the presence of oral diseases increases the risk of chronic conditions such as diabetes, respiratory issues, and cardiovascular and cerebrovascular diseases [1].

Machine learning (ML), a subset of artificial intelligence (AI), employs statistical, probabilistic, and optimization techniques that enable machines to learn from historical data, acquire information, and make predictions regarding new data based on the learned information [2,3]. Within dental clinical decision-making, methods grounded in deep learning (DL), another subset of AI, streamline processes and address intricate challenges. Among these methods, a deep convolutional neural network (CNN), a well-defined algorithm in DL, has proven highly effective for organ segmentation and the classification and detection of organs and diseases within medical images [4–6].

ML has demonstrated remarkable accuracy and precision, surpassing human judgment in predicting medical outcomes [2]. DL techniques offer advantages over feature-based methods in medical image analysis, consistently outperforming healthcare professionals in disease identification [7].

In the field of oral cancer diagnosis, DL has yielded promising results in automated pathology analysis, oral cavity imaging, confocal laser endomicroscopy imaging, and fluorescence imaging. These advancements facilitate the prediction of cancer risk and patient diagnostic outcomes, enabling the identification of subtle patterns within large, noisy datasets. The ultimate goal is to develop tools to improve public dental health [2], [7,8].

This article aims to implement a model for diagnosing oral cancer using high-performance DL algorithms. The proposed model can potentially be an asset in the decision-making process for diagnosing this disease.

1.1. Literature review

The systematic review of the literature was conducted using the PRISMA methodology. This approach facilitated a comprehensive understanding of the research background, supported this work, and demonstrated proficiency in machine learning (ML) and deep learning (DL) approaches, thereby ensuring the study's relevance [9].

The study presented in [2] develops and validates four ML models to predict the occurrence of lymph node metastases in early-stage Oral Tongue Squamous Cell Cancer (OTSCC), both before and after surgery. The random forest and support vector machine models exhibit superior predictive performance compared to traditional methods based on the depth of invasion, neutrophil-to-lymphocyte ratio, or tumor budding.

Another study [7] explores an efficient imaging method utilizing smartphones and a DL algorithm for the automatic detection of oral diseases. The researchers introduce the HRNet DL network and assess its efficacy in detecting oral cancer. The proposed HRNet model demonstrates marginally improved performance over the VGG16, ResNet50, and DenseNet169 models across 455 test images based on sensitivity, specificity, precision, and F1-score metrics.

In a separate research endeavor [4], scientists automate the diagnosis of odontogenic cysts and tumors in both jaws using panoramic X-rays and. They enhance a modified deep CNN derived from YOLOv3 to detect and classify these conditions. The overall disease classification performance improves when using CNN with an augmented dataset compared to a non-augmented dataset.

1.2. MobileNet

MobileNet uses depth separable convolutions, a technique that significantly reduces the number of parameters compared to networks that use regular convolutions with the same depth. This reduction in parameters allows for the creation of lightweight deep neural networks. Developed by Google as an open-source CNN class, MobileNet is an excellent base for training classifiers. The classifiers generated using MobileNet are not only compact and fast, but also help minimize model size and computational requirements. This is accomplished by replacing standard convolution filters with deep and point convolutions [10].

1.3. Performance metrics

1. Receiver operating characteristic (ROC)

curves: ROC curves are graphical representations widely employed to assess and compare the performance of classifiers. These two-dimensional graphs illustrate the trade-off between sensitivity and specificity in a classifier's predictions. They visually demonstrate the classifier's performance across various discrimination thresholds, facilitating the classification and selection of classifiers according to specific user requirements. These requirements frequently encompass considerations of differential error costs and precision demands [11].

2. **Area under the curve (AUC):** AUC is a single scalar value that provides a comprehensive measure of the overall performance of a binary classifier. The AUC value ranges from 0.5 to 1.0, where the minimum value indicates the performance of a random classifier, and the maximum value corresponds to that of a perfect classifier. In Figure 1, the ROC curves for two scoring classifiers, A and B, are presented. In this example, classifier A has a higher AUC value than classifier B [12].

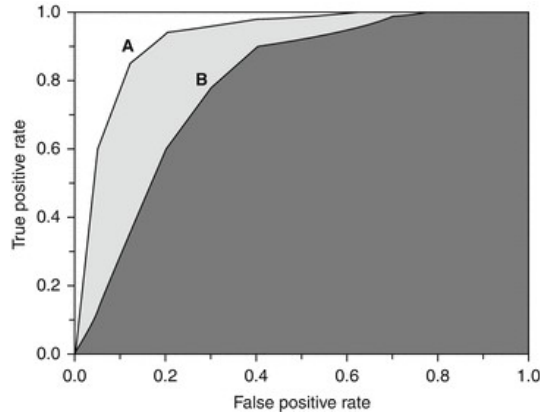


Figure 1. Area under the curve [11]

3. **Confusion matrix:** A confusion matrix is a table-like representation that shows the true and predicted class of each case in the test set. This matrix is essential for evaluating the performance of a model in a classification problem. By presenting a clear breakdown of true positives, true negatives, false positives, and false negatives, it enables a detailed understanding of the model's performance across different classes. Figure 2 provides a visual representation of the confusion matrix, specifically designed for a binary class classification problem [13].

		Current values	
		Positive	Negative
Predicted values	Positive	TP (True Positive)	FP (False Positive)
	Negative	FN (False Negative)	TN (True Negative)

Figure 2. Binary confusion matrix [12]

4. **Accuracy:** A test method is considered accurate when it precisely measures what it is intended

to measure. In other words, it can effectively determine a substance's accurate amount or concentration within a sample [14].

$$Accuracy = \frac{TP + TN}{TP + FP + FN + TN} \dots \quad (1)$$

5. **Precision:** Precision in a test method is achieved when repeated determinations or analyses on the same sample yield consistent results. In the context of accuracy, a precise test method exhibits minimal random variation, enhancing trust in its reliability. The ability of the test method to consistently reproduce results over time underscores its dependability [14].

$$Precision = \frac{TP}{TP + FP} \dots \quad (2)$$

6. **Recall:** Recall, also referred to as sensitivity, denotes the capability of a diagnostic test to correctly detect individuals afflicted with a particular disease or disorder. A test with high sensitivity minimizes instances of 'false negatives,' wherein the test fails to identify the presence of a disease despite its actual existence [14].

$$Recall = \frac{TN}{TN + FP} \dots \quad (3)$$

7. **F1 score:** The F1 score integrates accuracy and recall measurements into a unified metric, facilitating a comparative assessment of overall performance across diverse solutions. The F1 score operates under the assumption that both accuracy and recall hold equal significance [15].

$$F1Score = 2 * \frac{Precision * Recall}{Precision + Recall} \dots \quad (4)$$

1.4. Oral cancer

Oral cancer includes malignant tumors that affect the lip, different areas of the mouth, and the oropharynx, as shown in Figure 3. This form of cancer is more common in men and older individuals, with significant differences associated with socioeconomic status. Interestingly, in some countries in Asia and the Pacific, oral cancer is among the top three cancers with the highest occurrence [16].



Figure 3. Oral cancer sore [16]

2. Materials and methods

2.1. Data acquisition

The dataset used in this study was acquired from the Kaggle web platform [17], which offers open access to downloadable data. The original data format comprised jpg images. The dataset included 131 cases, with 87 featuring images of lips, mucous membranes, and the oral cavity indicative of oral cancer and the remaining 44 showcasing images without oral cancer. Figure 4 visually summarizes the research methodology, clearly outlining the phases. The implementation of this stage is detailed in Section 2.6.1.

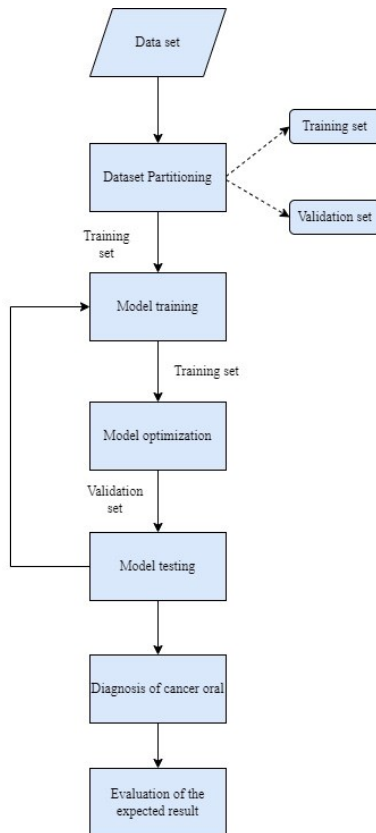


Figure 4. Model development methodology

2.2. Dataset partitioning

The partitioning of the dataset entails a non-overlapping division of the available data into two distinct subsets: the training dataset and the validation dataset. This separation provides one subset for analytical purposes and another for model verification.

1. **Training set:** The training dataset constitutes 90% of the total dataset, encompassing 118 images of lips, mucosa, and the oral cavity. This includes 78 images indicative of oral cancer and 40 images without signs of oral cancer.
2. **Validation set:** The validation dataset comprises 10% of the total dataset, featuring 13 images of lips, mucosa, and the oral cavity. This includes 9 images indicative of oral cancer and 4 images without signs of oral cancer.

The implementation of this stage is detailed in Section 2.6.2.

2.3. Model training, optimization, and tests

The CNN model proposed in this study was implemented and trained on the Kaggle platform, utilizing Python as the programming language due to its extensive capabilities in machine learning (ML) and deep learning (DL). These features make Python particularly well-suited for managing the complexities of the task. During this phase, the training dataset served not only for the initial training but also for the pre-validation of the model, thereby laying the groundwork for further optimization and testing.

When validating the developed model, which exhibits performance metrics ranging from 0.5 to 1.0, areas requiring improvement are identified to enhance its performance. Adjustments are made using the training dataset. Upon achieving satisfactory evaluation metrics, the model is subjected to testing to verify its effectiveness and reliability.

To evaluate the proposed model, the validation dataset is employed to confirm its high performance. If the outcomes differ from expectations, additional iterations of training, optimization, and testing are conducted until the desired results are achieved. This iterative process is documented in Sections 2.6.3 and 2.6.4.

2.4. Diagnosis of oral cancer disease

Based on the performance results obtained from the model tests, the capability for automatic diagnosis of oral cancer is determined. This diagnosis pertains to the images of the lips, mucosa, and oral cavity utilized in the model. The implementation of this stage is detailed in Section 2.6.5.

2.5. Evaluation of the expected result

Following the diagnosis of oral cancer, the results obtained are evaluated by comparing their accuracy, precision, recall, and F1 score. Through this comparison, it is determined that the diagnosis provided by the proposed model yields satisfactory results. The implementation of this stage is detailed in Section 2.6.6.

2.6. Implementation

2.6.1. Loading libraries and read in data

The development of the solution commences with the loading of essential libraries, such as matplotlib, NumPy, and pandas. Global parameters are defined, and images of the lips, mucosa, and oral cavity, whether indicative of the disease or not, are obtained. Key parameters include:

1. **Size:** Input size [18].
2. **Epochs:** The number of iterations over the entire dataset [19].
3. **Batch size:** Division of the dataset into multiple smaller batches [19].
4. **Fold:** The number of folds the dataset will be divided into [20].

2.6.2. Generating dataset

A dataset comprising images of lips, mucous membranes, and the oral cavity, with or without the disease, is created. The images are resized, and their quantity is augmented through various alterations, including cropping, focus adjustment, rotation, brightness modification, and flipping.

The dataset, initially unbalanced with 44 cases not presenting oral cancer and 87 cases that do, undergoes class balancing. Classes are determined to identify the presence or absence of disease, and the images are segmented based on whether they depict oral cancer.

2.6.3. Creating a model

The proposed CNN model is established using "MobileNet" as the chosen architecture. Additionally, the following attributes are employed:

1. **Early Stopping:** Configured with a patience of "10" training cycles, this attribute monitors a specified metric for any signs of improvement before concluding [21].
2. **Adam:** This optimizer implements Adam's algorithm, a stochastic gradient descent method based on the adaptive estimation of first- and second-order moments [22].

3. **Sequential:** This attribute provides training and inference functions for the model [23].
4. **Conv2D:** A 2D convolution layer that generates a convolution kernel rolled over input layers, producing an output tensor [24].
5. **Relu:** Applied to activate the rectified linear unit activation function [25].
6. **MaxPooling2D:** This attribute performs a maximum pooling operation for 2D spatial data [26].
7. **Flatten:** Used to flatten the input without affecting the batch size [27].
8. **Dense:** This layer applies weights to all nodes of the preceding layer [28].
9. **Dropout:** During training, this attribute randomly sets input units to 0 with a specified frequency at each step, helping to prevent overfitting [29].
10. **SoftMax:** It converts a vector of values into a probability distribution [25].
11. **Compile:** A method that accepts a metric argument and a list of metrics [30].
12. **Categorical cross entropy:** This attribute calculates the cross-entropy loss between labels and predictions [31].
13. **Accuracy:** It calculates the frequency with which predictions match [32] the labels.

2.6.4. Training with K-fold

Model training is executed utilizing the following attributes:

1. **K-fold:** The dataset is divided into K folds, with each fold serving as the test set while the remaining dataset is used as the training set [33, 34].
2. **Stratified Fold:** This attribute ensures further cross-validation by preserving the distribution of classes in the dataset across both training and validation splits [35].
3. **To categorical:** It converts a class vector (integers) into a binary class array [36].
4. **Image Data Generator:** This attribute facilitates the generation of training blocks and performs data augmentation by increasing the number of images through modifications such as zooming, scaling, horizontal flipping, etc [37].
5. **Fit:** This function is used to train the model for a fixed number of epochs (iterations on a dataset) [38].

6. **Model Checkpoint:** It serves as a callback to save the Kera's model or model weights at specified intervals [39].

7. **Create model:** This function is responsible for creating and training a new model instance [40].

Similarly, another CNN is proposed to create the model, utilizing "ResNet152V2," "DenseNet121," and "EfficientNetB6" as the chosen architectures. Table 1 illustrates a comparison of the model's performance using these deep learning architectures:

Table 1. Comparison of deep learning architectures

ResNet152V2	Precision (%)	Recall (%)	F1 Score (%)
With oral cancer	90	93	92
No oral cancer	85	80	82
Accuracy	0.8855		
AUC	0.863244514106583		
DenseNet121	Precision (%)	Recall (%)	F1 Score (%)
With oral cancer	85	94	90
No oral cancer	86	68	76
Accuracy	0.8550		
AUC	0.812173458725183		

Regarding the use of "Efficient Net B6", a memory problem arises at the beginning of fold 3 during model training, preventing the completion of the process.

Similarly, although the results of the model using the "ResNet152V2," "DenseNet121," and "MobileNet" architectures on the same dataset are comparable, the number of hyperparameters used in MobileNet is smaller. Figures 5, 6, and 7 illustrate the number of hyperparameters obtained for each architecture:

"ResNet152V2" used 76MM, as depicted in Figure 5.

Notebook	Input	Output	Logs	Comments (0)	Settings
*****Starting fold 1 of 4					
Downloading data from https://storage.googleapis.com/tensorflow/keras-applications/t152v2_weights_tf_dim_ordering_tf_kernels_notop.h5					
234553344/234545216 [*****] - 6s 0us/step					
234551536/234545216 [*****] - 6s 0us/step					
layers 564					
Model: 'sequential'					

Layer (type)	Output Shape	Param #			
resnet152v2 (Functional)	(None, 7, 7, 2048)	58331648			
conv2d (Conv2D)	(None, 5, 5, 64)	1179712			
conv2d_1 (Conv2D)	(None, 3, 3, 64)	36928			
max_pooling2d_3 (MaxPooling2D)	(None, 1, 1, 64)	0			
flatten (Flatten)	(None, 64)	0			
dense (Dense)	(None, 4096)	266240			
dropout (Dropout)	(None, 4096)	0			
dense_1 (Dense)	(None, 4096)	16781312			
dropout_1 (Dropout)	(None, 4096)	0			
dense_2 (Dense)	(None, 2)	8194			

Total params: 76,684,934					
Trainable params: 76,460,290					

Figure 5. ResNet152V2 hyperparameter number

"DenseNet121" used 24MM, as depicted in Figure 6.

Notebook	Input	Output	Logs	Comments (0)	Settings
*****Starting fold 1 of 4					
Downloading data from https://storage.googleapis.com/tensorflow/keras-applications/dense121_weights_tf_dim_ordering_tf_kernels_notop.h5					
2989792/2988484 [*****] - 0s 0us/step					
2989792/2988484 [*****] - 0s 0us/step					
Layers: 427					
Model: "sequential"					

Layer (type)	Output Shape	Param #			

dense121 (Functional)	(None, 7, 7, 1024)	7037584			
conv2d (Conv2D)	(None, 5, 5, 64)	589888			
conv2d_1 (Conv2D)	(None, 3, 3, 64)	36928			
max_pooling2d (MaxPooling2D)	(None, 1, 1, 64)	0			
flatten (Flatten)	(None, 64)	0			
dense (Dense)	(None, 4096)	266240			
dropout (Dropout)	(None, 4096)	0			
dense_1 (Dense)	(None, 4096)	16781312			
dropout_1 (Dropout)	(None, 4096)	0			
dense_2 (Dense)	(None, 2)	8194			

Total params: 24,728,866					
Trainable params: 24,636,418					

Figure 6. DenseNet121 hyperparameter number

"MobileNet" used 24MM, as depicted in Figure 7.

Notebook	Input	Output	Logs	Comments (0)	Settings
*****Starting fold 1 of 4					
layers 86					
Model: "sequential_29"					

layer (type)		Output Shape			Param #

mobilenet_1.00_224 (Function (None, 7, 7, 1024))					
					3228864

conv2d_52 (Conv2D)		(None, 5, 5, 64)			589888

conv2d_53 (Conv2D)		(None, 3, 3, 64)			36928

max_pooling2d_26 (MaxPooling)		(None, 1, 1, 64)			0

flatten_26 (Flatten)		(None, 64)			0

dense_84 (Dense)		(None, 4096)			266240

dropout_58 (Dropout)		(None, 4096)			0

dense_85 (Dense)		(None, 4096)			16781312

dropout_59 (Dropout)		(None, 4096)			0

dense_86 (Dense)		(None, 2)			8194

Total params: 20,911,426					
Trainable params: 20,889,538					

Figure 7. MobileNet hyperparameter number

2.6.5. Ground truth

The model verification process is conducted using the entire validation dataset, employing the following attributes:

1. **Evaluate:** This function returns the loss value and metric values of the model in test mode [38].
2. **Predict:** It generates output predictions for the input samples [38].
3. **Confusion matrix:** Calculating the confusion matrix is used to evaluate the accuracy of a classification [41].
4. **Subplot:** This attribute obtains the index position in a grid with "n" rows and "n" columns [42].

5. **Heatmap:** It is utilized to obtain a class activation heatmap for an image classification model [43].
6. **Set-ticklabels:** This function sets the target names for the confusion matrix.
7. **Roc curve:** This attribute calculates the ROC [44].
8. **Roc-auc-core:** It calculates the ROC AUC from the prediction scores [45].

2.6.6. Plotting AUC curves

Figure 8 depicts a plot of the true positive rate against the false positive rate, illustrating the AUC through lines. This visualization allows for the observation of the relationship between these two variables.

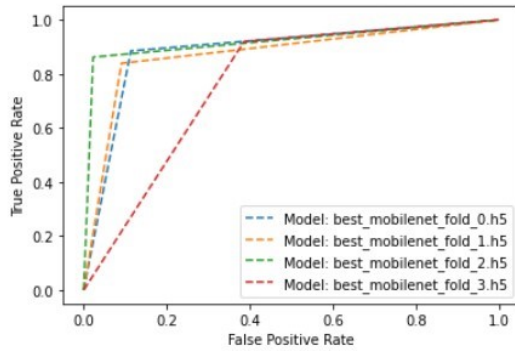


Figure 8. Plotting AUC curves

It is confirmed that the proposed CNN model demonstrates high performance in classifying the presence and absence of oral cancer.

3. Results and discussion

Figure 9 illustrates the plot of accuracy values against the number of epochs, using lines to visualize the relationship between these two variables.

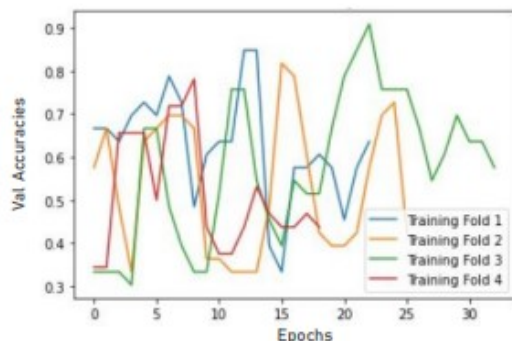


Figure 9. Plotting model accuracy per fold

When training the model, accuracy is obtained for each fold:

In the first training, with fold 1, a "value accuracy" of 0.84848 is achieved. In the second training, with fold 3, a "value accuracy" of 0.81818 is achieved. In the third training, with fold 3, a "value accuracy" of 0.90909 is achieved. In the fourth training, with fold 4, a "value accuracy" of 0.78125 is achieved.

It is observed that fold 1 attains a good "value accuracy", fold 2 decreases the "value accuracy", fold 3 achieves the highest "value accuracy" with a value of 0.90909, and fold 4 decreases the "value accuracy".

During the model validation, the following metrics are obtained for the model saved as "best mobilenet fold 0.h5," as illustrated in Table 2.

Table 2. Simple model performance metrics with fold 1

	Precision (%)	Recall (%)	F1 Score (%)
With oral cancer	80	89	84
No oral cancer	94	89	91
AUC	0.8857105538140021		

The "best mobilenet fold 1.h5" achieves the following rankings, as depicted in Table 3.

Table 3. Simple model performance metrics with fold 2

	Precision (%)	Recall (%)	F1 Score (%)
With oral cancer	74	91	82
No oral cancer	95	84	89
AUC	0.8740856844305119		

The "best mobilenet fold 2.h5" achieves the following rankings, as depicted in Table 4.

Table 4. Simple model performance metrics with fold 3

	Precision (%)	Recall (%)	F1 Score (%)
With oral cancer	78	98	87
No oral cancer	99	86	92
AUC	0.9196708463949843		

The "best mobilenet fold 3.h5" achieves the following rankings, as depicted in Table 5.

Table 5. Simple model performance metrics with fold 4

	Precision (%)	Recall (%)	F1 Score (%)
With oral cancer	79	61	69
No oral cancer	82	92	87
AUC	0.7665882967607105		

It is concluded that the "best mobilenet fold 2.h5" model stands out as the optimal choice, exhibiting the highest precision (78% and 99%), recall (98% and 86%), F1 score (87% and 92%), and AUC (0.9196708463949843) for both non-cancerous and cancerous cases, surpassing the performance of other models.

Comparatively, among the architectures "ResNet152V2," "DenseNet121," and "MobileNet," it is demonstrated that the "MobileNet" architecture is

optimal in terms of resource optimization, utilizing 20 million hyperparameters, whereas the "ResNet152V2" and "DenseNet121" architectures use a significantly greater number of hyperparameters.

In addition to the performance metrics of the "ResNet152V2", "DenseNet121" and "EfficientNetB6" architectures evaluated, the model featured in [7] demonstrated a precision of 84.3%, recall of 83.0%, F1 score of 83.6%, and AUC of 0.8974. In contrast, the model proposed in this study exhibited improvements, achieving a precision of 88.5%, recall of 92.0%, F1 score of 89.5%, and AUC of (0.9196708463949843). Thus, a noticeable enhancement in overall performance ranging between 2% and 9% is observed.

4. Conclusions

This study highlights the potential of AI in addressing oral health issues, particularly oral cancer, which affects a significant portion of the population. The research emphasizes the effectiveness of DL and concludes that CNNs are a suitable DL algorithm for processing images of the mucosa and the oral cavity. CNNs take these images as input and assign weights to specific elements to distinguish between them. The choice of the MobileNet CNN is justified due to its ability to reduce model size and computation by replacing standard convolution filters with deep, pointwise convolutions. The study utilizes the open-source Kaggle platform and implements the model using the Python programming language. The evaluation of various performance metrics yields an accuracy of 0.90909, confirming that the proposed CNN model demonstrates high diagnostic performance for oral cancer. Regarding image quantity, the study specifies that using more images enhances the proposed DL model's results. Additionally, evaluating different CNN architectures helps to understand their performance, facilitating the determination of the most optimal model. Ultimately, this research asserts that the developed model is ready for practical application, offering valuable support for dental decision-making in real-time diagnostic scenarios.

4.1. Future work

Continued efforts in collecting more images of lips, mucosa, and the oral cavity depicting various oral conditions, including oral cancer, will be a focal point for future studies. Augmenting the image dataset and collaborating with public or private clinical institutions for evaluation are believed to significantly improve the results and facilitate the practical application of the model. Recognizing the pivotal role of large datasets in optimizing DL algorithms, the current results are promising and serve as a first step to advance this line of research. Furthermore, upcoming research endeavors

will aim to evaluate the performance of the proposed CNN method in diagnosing a broader spectrum of oral diseases.

References

- [1] L. A. Zanella-Calzada, C. E. Galván-Tejada, N. M. Chávez-Lamas, J. Rivas-Gutiérrez, R. Magallanes-Quintanar, J. M. Celaya-Padilla, J. I. Galván-Tejada, and H. Gamboa-Rosales, "Deep artificial neural networks for the diagnostic of caries using socioeconomic and nutritional features as determinants: Data from NHANES 2013–2014," *Bioengineering*, vol. 5, no. 2, 2018. [Online]. Available: <https://doi.org/10.3390/bioengineering5020047>
- [2] J. Shan, R. Jiang, X. Chen, Y. Zhong, W. Zhang, L. Xie, J. Cheng, and H. Jiang, "Machine learning predicts lymph node metastasis in early-stage oral tongue squamous cell carcinoma," *Journal of Oral and Maxillofacial Surgery*, vol. 78, no. 12, pp. 2208–2218, 2020. [Online]. Available: <https://doi.org/10.1016/j.joms.2020.06.015>
- [3] A. M. Bur, A. Holcomb, S. Goodwin, J. Woodroof, O. Karadaghy, Y. Shnayder, K. Kakarala, J. Brant, and M. Shew, "Machine learning to predict occult nodal metastasis in early oral squamous cell carcinoma," *Oral Oncology*, vol. 92, pp. 20–25, 2019. [Online]. Available: <https://doi.org/10.1016/j.oraloncology.2019.03.011>
- [4] O. Kwon, T.-H. Yong, S.-R. Kang, J.-E. Kim, K.-H. Huh, M.-S. Heo, S.-S. Lee, S.-C. Choi, and W.-J. Yi, "Automatic diagnosis for cysts and tumors of both jaws on panoramic radiographs using a deep convolution neural network," *Dentomaxillofacial Radiology*, vol. 49, no. 8, p. 20200185, Dec 2020. [Online]. Available: <https://doi.org/10.1259/dmfr.20200185>
- [5] X. Zhang, Y. Liang, W. Li, C. Liu, D. Gu, W. Sun, and L. Miao, "Development and evaluation of deep learning for screening dental caries from oral photographs," *Oral Diseases*, vol. 28, no. 1, pp. 173–181, 2022. [Online]. Available: <https://doi.org/10.1111/odi.13735>
- [6] H.-J. Chang, S.-J. Lee, T.-H. Yong, N.-Y. Shin, B.-G. Jang, J.-E. Kim, K.-H. Huh, S.-S. Lee, M.-S. Heo, S.-C. Choi, T.-I. Kim, and W.-J. Yi, "Deep learning hybrid method to automatically diagnose periodontal bone loss and stage periodontitis," *Scientific Reports*, vol. 10, no. 1, p. 7531, May 2020. [Online]. Available: <https://doi.org/10.1038/s41598-020-64509-z>
- [7] H. Lin, H. Chen, L. Weng, J. Shao, and J. Lin, "Automatic detection of oral cancer in

- smartphone-based images using deep learning for early diagnosis,” *Journal of Biomedical Optics*, vol. 26, no. 8, p. 086007, 2021. [Online]. Available: <https://doi.org/10.1117/1.JBO.26.8.086007>
- [8] W. Li, Y. Liang, X. Zhang, C. Liu, L. He, L. Miao, and W. Sun, “A deep learning approach to automatic gingivitis screening based on classification and localization in RGB photos,” *Scientific Reports*, vol. 11, no. 1, p. 16831, Aug 2021. [Online]. Available: <https://doi.org/10.1038/s41598-021-96091-3>
- [9] M. A. Dávila Olivos and F. M. Santos López, “Prediction models of oral diseases: A systematic review of the literature,” in *Emerging Research in Intelligent Systems*, G. F. Olmedo Cifuentes, D. G. Arcos Avilés, and H. V. Lara Padilla, Eds. Cham: Springer Nature Switzerland, 2024, pp. 309–322. [Online]. Available: https://doi.org/10.1007/978-3-031-52255-0_22
- [10] A. Pujara, “Image classification with mobilenet,” *Analytics Vidhya*, 2020. [Online]. Available: <https://n9.cl/coutpg>
- [11] F. Melo, *Receiver Operating Characteristic (ROC) Curve*. New York, NY: Springer New York, 2013, pp. 1818–1823. [Online]. Available: https://doi.org/10.1007/978-1-4419-9863-7_242
- [12] —, *Area under the ROC Curve*. New York, NY: Springer New York, 2013, pp. 38–39. [Online]. Available: https://doi.org/10.1007/978-1-4419-9863-7_209
- [13] H. Rhys, *Machine Learning with R, the tidyverse, and mlr*. Manning Publications, 2020. [Online]. Available: <https://n9.cl/q3hijw>
- [14] LabTests Online UK. (2018) Accuracy, precision, specificity & sensitivity. Association for Laboratory Medicine. [Online]. Available: <https://n9.cl/8cvyq>
- [15] J. Martínez Heras. (2018) Machine learning lectures esa. GitHub, Inc. [Online]. Available: <https://n9.cl/7yim6>
- [16] OMS. (2021) Salud bucodental. Organización Mundial de la Salud. [Online]. Available: <https://n9.cl/zpz0f>
- [17] Kaggle. (2020) Oral cancer (lips and tongue) images. Kaggle. [Online]. Available: <https://n9.cl/7ftbq>
- [18] Keras. (2022) Mobilenet, mobilenetv2, and mobilenetv3. Keras. [Online]. Available: <https://n9.cl/dcv2s>
- [19] S. Sharma. (2022) Epoch vs batch size vs iterations. Medium. [Online]. Available: <https://n9.cl/wlxncj>
- [20] S. Manna. (2022) K-fold cross validation for deep learning models using keras. Medium. [Online]. Available: <https://n9.cl/hmyvr>
- [21] Keras. (2022) Earlystopping. Keras. [Online]. Available: <https://n9.cl/undx7>
- [22] —. (2022) Adam. Keras. [Online]. Available: <https://n9.cl/x9m53>
- [23] —. (2022) The sequential class. Keras. [Online]. Available: <https://n9.cl/yi56j>
- [24] GeeksforGeeks. (2022) Keras.conv2d class. Geeks for Geeks. [Online]. Available: <https://n9.cl/6bemi>
- [25] Keras. (2022) Layer activation functions. Keras. [Online]. Available: <https://n9.cl/d9yeb>
- [26] —. (2022) Maxpooling2d layer. Keras. [Online]. Available: <https://n9.cl/51sbk>
- [27] —. (2022) Flatten layer. Keras. [Online]. Available: <https://n9.cl/cufk4>
- [28] I. Hull, *Dense layers – Introduction to tensorflow in Python*. DataCamp. [Online]. Available: <https://n9.cl/hny28>
- [29] Keras. (2022) Dropout layer. Keras. [Online]. Available: <https://n9.cl/02hdv>
- [30] —. (2022) Metrics. Keras. [Online]. Available: <https://n9.cl/jmihj>
- [31] —. (2022) Probabilistic metrics. Keras. [Online]. Available: <https://n9.cl/b3w2a>
- [32] —. (2022) Accuracy metrics. Keras. [Online]. Available: <https://n9.cl/7l3dt>
- [33] Data Science Team. (2020) Validación cruzada k-fold. Data Science Team. [Online]. Available: <https://n9.cl/c2i0bp>
- [34] R. Delgado. (2018) Introducción a la validación cruzada (k-fold cross validation) en R. Amazon-aws. [Online]. Available: <https://n9.cl/ijyq>
- [35] S. Yildirim. (2020) How to train test split : Kfold vs stratifiedkfold. Medium. [Online]. Available: <https://n9.cl/ymp9q>
- [36] Keras. (2022) Python & numpy utilities. Keras. [Online]. Available: <https://n9.cl/zrhgh>
- [37] J. Utrera Burgal. (2019) Tratamiento de imágenes usando imagedatagenerator en keras. Knowmad mood. [Online]. Available: <https://n9.cl/5gobr>

-
- [38] Keras. (2022) Model training apis. Keras. [Online]. Available: <https://n9.cl/4gjr6>
- [39] —. (2022) Modelcheckpoint. Keras. [Online]. Available: <https://n9.cl/wvut7>
- [40] Tensorflow. (2022) Guardar y cargar modelos. TensorFlow. [Online]. Available: <https://n9.cl/cjflnu>
- [41] Scikit Learn. (2022) sklearn.metrics.confusion matrix. Scikit-learn developers. [Online]. Available: <https://n9.cl/ya6b1h>
- [42] Matplotlib. (2022) matplotlib.pyplot.subplot. Matplotlib. [Online]. Available: <https://n9.cl/vlv1fe>
- [43] Keras. (2022) Grad-cam class activation visualization. Keras. [Online]. Available: <https://n9.cl/r5l7k>
- [44] Scikitlearn. (2022) sklearn.metrics.roc curve. Scikitlearn. [Online]. Available: <https://n9.cl/qles5>
- [45] —. (2022) sklearn.metrics.roc auc score. Scikitlearn. [Online]. Available: <https://n9.cl/1zf6r>



EXPERIMENTAL ANALYSIS OF THE KINEMATICS IN THE ELASTIC COLLISION BETWEEN TWO BODIES DURING THE CONTACT TIME

ANÁLISIS EXPERIMENTAL DE LA CINEMÁTICA EN LA COLISIÓN ELÁSTICA ENTRE DOS CUERPOS DURANTE EL TIEMPO DE CONTACTO

Suyana Arcos Villagómez^{1,*} , Santiago Álvaro Pillalaza² ,
 Xavier Rivera Gálvez² , César Michelena Rosero² , Emilse Camacho Cañar²

Received: 25-03-2024, Received after review: 21-05-2024, Accepted: 06-06-2024, Published: 01-07-2024

Abstract

The elastic collision between two bodies is a fleeting event challenging to observe due to its infinitesimally short contact time, usually lasting mere hundredths or even thousandths of a second. This brief duration poses significant challenges for accurately measuring velocities and impulsive forces and establishing representative functions. Consequently, this study aims to address these challenges. Experimental measurements of velocity, acceleration, and force changes during the contact period are crucial for validating theoretical models and functions that accurately represent the dynamics of collisions under realistic conditions. These measurements are critical in optimizing the activation response of airbag and restraint systems in vehicles and are fundamental in reconstructing physical scenarios of accidents. The experiments were conducted in a practical computer-assisted laboratory, utilizing wireless sensors embedded within the test vehicles and positioned on a low-friction track. The collision setup was designed to be horizontal and frontal, ensuring that the bodies involved did not undergo permanent deformations. The primary methodology adopted in this analysis integrates both quantitative and qualitative approaches, focusing on collecting and analyzing numerical data to identify patterns and establish mathematical relationships between variables. This integrated approach offers a more comprehensive understanding of the kinematics of colliding vehicles during the contact period.

Keywords: elastic collision, two-body collision, contact time, two-body kinematics, coefficient of friction

Resumen

La colisión elástica entre dos cuerpos es un evento rápido y difícil de observar, dado que el tiempo de contacto es infinitesimal, del orden de centésimas o incluso milésimas de segundo, por lo que surge el desafío de medir con precisión las velocidades y fuerzas impulsivas, así como establecer funciones representativas. En este trabajo se propone abordar precisamente ese objetivo. Las mediciones experimentales de la variación de la velocidad, aceleración y fuerza, durante el tiempo de contacto, desempeñan un papel esencial en la validación de modelos teóricos y funciones que describen el comportamiento de las colisiones en situaciones del mundo real. Estas mediciones permiten optimizar la respuesta de activación de los airbags, sistemas de retención en los automóviles, hasta reconstruir accidentes desde el punto de vista de la Física. La experimentación se llevó a cabo en un laboratorio práctico asistido por computadora, empleando sensores inalámbricos incorporados en los carros de prueba y dispuestos sobre una pista de bajo coeficiente de rozamiento. El escenario de la colisión fue horizontal y frontal, sin que los cuerpos sufrieran deformaciones permanentes. La metodología principal utilizada en este análisis es cuantitativa y cualitativa, enfocándose en la recopilación y estudio de datos numéricos para identificar patrones y relaciones matemáticas entre las variables. Este enfoque combinado permite una comprensión más completa de la cinemática de los carros en colisión durante el tiempo de contacto.

Palabras clave: choque elástico, colisión de dos cuerpos, tiempo de contacto, cinemática de dos cuerpos, coeficiente de rozamiento.

^{1,*}Escuela de Ingeniería de Sistemas, Facultad de Ingeniería, Pontificia Universidad Católica del Ecuador, Ecuador.
 Corresponding author ✉: sfarcos@puce.edu.ec.

²Facultad de Ciencias Exactas y Naturales, Pontificia Universidad Católica del Ecuador, Ecuador.

Suggested citation: Arcos Villagómez, S.; Álvaro Pillalaza, S.; Rivera Gálvez, X.; Michelena Rosero, C. and Camacho Cañar, E. "Experimental analysis of the kinematics in the elastic collision between two bodies during the contact time," *Ingenius, Revista de Ciencia y Tecnología*, N.º 32, pp. 69-76, 2024, DOI: <https://doi.org/10.17163/ings.n32.2024.07>.

1. Introduction

In physics, conducting experiments is essential for understanding phenomena often assumed in theoretical contexts [1]. The study of frontal elastic collisions is particularly intriguing. In such collisions, the bodies involved do not undergo permanent deformations or exchange mass, fully separating after the impact [2]. The principles of conservation of kinetic energy and linear momentum are upheld both before and after the collision. Nonetheless, the dynamics occurring during the contact time between the colliding objects frequently remain underexplored.

Collisions between bodies are a fundamental focus within the field of physics, with the characterization of contact time during these collisions being particularly critical for this research. Contact time, the instantaneous interval during which the objects interact upon impact, is crucial in determining the forces exerted and the velocities of the colliding bodies. The inherent complexity of this phenomenon, especially in real-world settings, has substantially limited the ability to fully understand it.

Contact time during collisions can span mere hundredths or thousandths of a second, posing significant challenges for accurately collecting experimental data. The growing integration of technology in Physics laboratories enables the measurement of physical parameters over brief intervals, facilitating the documentation of rapid events that are imperceptible to the human observer and beyond the capabilities of traditional instruments [2]. In this context, the advancement of position and motion sensors is crucial. These technologies allow for the detailed capture of data on practically instantaneous processes during body collisions, providing valuable insights into their dynamics.

Contemporary physics laboratories are equipped with advanced data loggers, sophisticated digital devices that facilitate the connection of multiple sensors for comprehensive data collection. These tools play an integral role in conducting experiments, significantly enhancing the accuracy and efficiency of data acquisition.

Data loggers can be replaced by computers equipped with Bluetooth connectivity, enabling the receipt of sensor information. These sensors are transducers fitted with the technology to detect physical or chemical quantities, called instrumentation variables, and convert them into electrical signals [3].

In practical applications, physical quantities are inherently analog. To facilitate their processing and utilization in digital devices, an analog-to-digital converter (ADC) is employed. However, these quantities undergo a preliminary stage before digitization, known as sampling frequency. This characteristic dictates the number of samples collected per second. Properly adjusting the sampling frequency is crucial for effectively

capturing the analog information, thereby minimizing data loss and enhancing conversion accuracy during digitization.

Sampling, also known as signal discretization, represents the initial step in converting an analog signal, characterized by continuous time and amplitude, into a digital signal, which features discrete time and amplitude. This process is fundamental to the accurate digital representation of analog data [4].

From this perspective, implementing sensor-equipped vehicles is proposed as an innovative approach to recreate elastic collisions and meticulously examine the events transpiring during the contact time between bodies.

In real-world applications, sensors are crucial for activating passive safety systems in vehicles. During an impact, the seatbelt pre-tensioner and airbag are passive safety systems. Key components of the airbag system include the control unit, the safing safety sensor, and the impact sensor. The safing safety sensor, integral to the airbag module, is connected to the frontal impact sensors. The impact sensor is designed to respond to a combination of force, acceleration, and duration [5]. Specifically, the acceleration sensor monitors changes in the vehicle's speed, while the impact sensor detects the force of frontal impacts, contributing to timely and effective safety responses [6].

An electronic control unit activates the airbag system, which operates based on signals received from the system's sensor. This sensor is strategically positioned to detect sudden decelerations resulting from a collision.

The airbag deploys in response to a sudden change in the vehicle's overall inertia, typically triggered by a frontal impact with an obstacle or another vehicle [7].

Simulating a frontal impact for biomechanical assessment using finite elements elucidates the advantages of incorporating airbags as passive safety elements [8]. This approach enhances the quality of this research and facilitates the exploration and validation of theoretical models within a practical and dynamic context.

The emerging challenge for Physics laboratories involves effectively utilizing the extensive information generated by sensors for detailed interpretation and analysis [9]. Meticulous and comprehensive analysis of this data is crucial for elucidating the underlying physical phenomena, validating existing theories, or generating new hypotheses. Such experimental data offer a solid empirical foundation that underpins scientific conclusions and enables researchers to make well-informed decisions regarding advancing theories and models.

2. Materials and Methods

Figure 1 summarizes the research methodology and illustrates the most relevant stages of the experimentation.

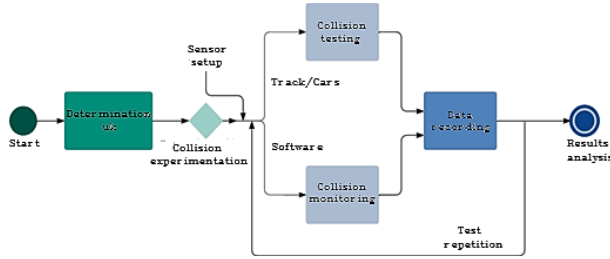


Figure 1. Diagram of the methodology used in the experimentation

To conduct the experimentation, the dynamic friction coefficient u_k between the thin plastic wheels of the cars and the aluminum track was determined. This was accomplished by positioning a car on the horizontal track and progressively increasing the inclination angle (θ) until the car began to move freely, reaching what is referred to as the kinetic friction angle (θ_k), [10].

The forces depicted in the free-body diagram [11] and the inclination angle were analyzed to derive the equation for determining the dynamic friction coefficient.

The mathematical formula used to calculate this coefficient is $u_k = \tan(\theta_k)$ [12], as sourced from Serway's Physics book. This approach yielded an experimental dynamic friction coefficient of $u_k = 0,009$.

Subsequently, test vehicles equipped with wireless sensors, maintained in optimal conditions and with nearly identical masses, were utilized. The masses were approximately ($m_1 = 0,5048kg$) and ($m_2 = 0,5022kg$), respectively.

The vehicles were positioned frontally on the aluminum track, spaced one meter apart. A connection was established between the computer's Bluetooth system and the sensors to facilitate data collection.

The track was meticulously installed to ensure it was level and free from obstructions, thereby minimizing the loss of kinetic energy, as illustrated in Figure 2.

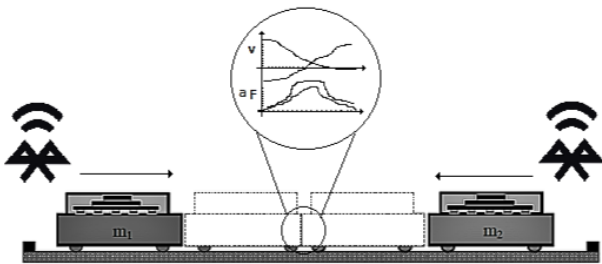


Figure 2. Schematic representation of the events occurring during the collision time

Similar springs exerting equivalent forces were used to initiate the cars' motion. These springs were integrated into the rear of each vehicle to provide the initial impulse. Upon release of the springs, the cars propelled in opposite directions, culminating in a collision.

The experiments confirmed that the contact time was 0.025 seconds, indicative of a rapid and potentially violent collision. During this brief interval, both the initial and final velocities were determined, representing the average values of the experimental data, as detailed in Table 1

Table 1. Car velocities during contact time

Time [s]	Car Velocity (1) [m/s]	Car Velocity (2) [m/s]
0.002	0.88	-0.88
0.024	-0.61	0.64

During this period, velocity changes occur rapidly. Consequently, if the sampling frequency falls below the required minimum, critical information can be lost, and the recorded signal may be distorted.

An adequate sampling frequency is crucial to accurately reconstruct the signal from sampled data. The Nyquist-Shannon theorem, applicable to various signals, including polynomial signals, mandates that the sampling frequency must be at least twice the highest frequency present in the signal to ensure accurate reconstruction [13]. For polynomial signals, which are not inherently periodic and thus lack an intrinsic frequency, the highest frequency corresponds to the maximum rate of oscillation of the polynomial function. This frequency can be determined by the function's maximum rate of change.

The maximum rate of change (T_{CM}) is determined by evaluating the velocity function during the collision interval using Equation (1).

$$T_{CM} = \frac{\Delta v}{\Delta t} = \frac{v_f - v_0}{t_f - t_0}$$

$$T_{CM}(v_1) = \frac{\Delta v_1}{\Delta t} = \frac{(-0.62 - 0.88)}{0.024 - 0.002} = -68.18 \quad (1)$$

$$T_{CM}(v_2) = \frac{\Delta v_2}{\Delta t} = \frac{(0.62 - (-0.87))}{0.024 - 0.002} = 67.72$$

The velocity functions' rate of change, with values of -68.18 and 67.72, indicates a rapid variation. Although the absolute values of these rates are similar, the highest rate of change is 68.18. This value is critical for applying the Nyquist-Shannon theorem (F_{NyS}), which dictates that the minimum sampling frequency should be twice the maximum rate of change to capture the signal accurately, (see equation (2)).

$$T_{cm}(v_1, v_2) = 68.18$$

$$F_{NyS} = 2 * T_{cm} = 136.36 \quad (2)$$

The minimum necessary sampling frequency is determined to be 136.36 Hz. However, to ensure optimal signal reconstruction, a sampling frequency exceeding this minimum requirement was utilized. Consequently, a sampling frequency (f_m) of 500 Hz was established for this study.

Over 0.024 seconds and at the defined sampling frequency, twelve data points were recorded, referred to as the number of data points (N_d), see equation (3).

$$\begin{aligned} N_d &= f_m * t \\ N_d &= 500 * 0.024 = 12 \end{aligned} \quad (3)$$

This number of data points is suitable for reconstructing the signals in question, given that the experimentation spans 0.024 seconds.

3. Results and Discussion

Within the framework of the analysis, multiple collisions were simulated. During these collisions, the test vehicles did not undergo permanent deformations or experience changes in mass. Velocities were continuously monitored, and data were systematically recorded within the designated time interval.

The multiple tests consistently demonstrated similar patterns and velocity values during the contact period, as illustrated in Figure 3.

As indicated in Figure 3, at the initial observation time, the vehicles exhibit average velocities of 0.88 m/s and -0.87 m/s, respectively. The opposite signs of these velocities indicate that the vehicles are moving in opposite directions. Over time, the velocities of both vehicles decrease.

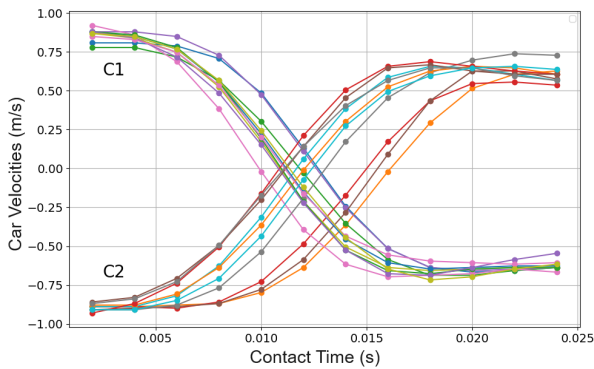


Figure 3. Car velocities during the contact time in the collision

This observation suggests that a braking force acts on the cars upon contact. At approximately 0.014 seconds, the velocities of both cars change signs, indicating a reversal in their directions of motion. From 0.014 seconds onward, the velocities of the vehicles continue to fluctuate, displaying different magnitudes

and directions; car 1 exhibits negative velocities, and car 2 exhibits positive velocities, showing that they are moving in directions opposite to their initial ones. By 0.024 seconds, it is evident that the velocities of both cars have diminished in magnitude, attributed to the presence of dissipative forces such as friction, which lead to energy loss.

A regression analysis was performed to determine the mathematical functions that most accurately fit the data. This analysis revealed that a fifth-degree polynomial function provides the most suitable model for the available data.

Experimentation in a controlled environment may be subject to inherent variations and errors, such as measurement inaccuracies or the physical conditions of the instruments used. Nonetheless, the replication of similar data across experiments indicates consistency in the findings. To mitigate the impact of these potential errors on the analysis, averaging the velocities during the contact period proves beneficial, as illustrated in Figure 4.

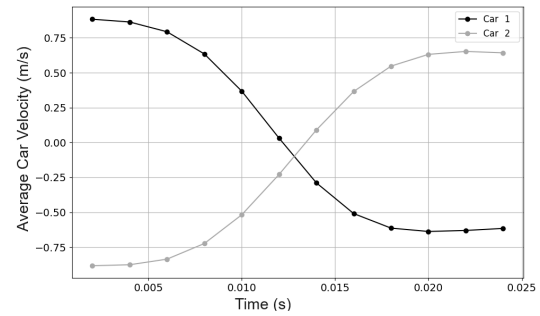


Figure 4. Average velocities of the cars during the contact time in the collision

3.1. Kinematics of Car 1

Figure 5 illustrates the variation of velocity during the contact time in the collision. The behavior of this variation is best modeled by a fifth-degree polynomial function, expressed as: $v(t) = -5E9t^5 + 3E8t^4 - 5E6t^3 + 28990t^2 - 66,985t + 0.9339$.

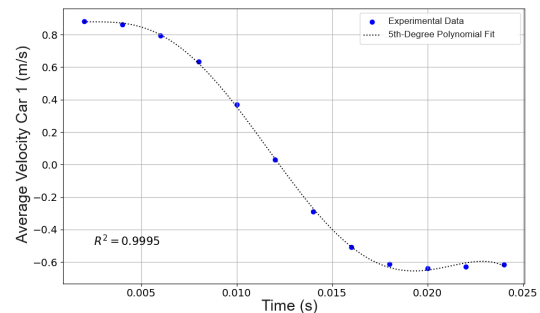


Figure 5. Variation of velocity as a function of time for Car 1 during the contact time in the collision

The curve fitting process yielded a coefficient of determination $R^2 = 0,9995$. A coefficient value close to 1 indicates a strong fit of the model to the data, meaning that 99.95% of the variability in the data is explained by the polynomial function.

At $t = 0,002[s]$ seconds, the initial velocity of the car is $0,88[m/s]$. From $t = 0,002[s]$ seconds to $t = 0,012[s]$ seconds, the velocity decreases from $0,88[m/s]$ to $0,03[m/s]$. From 0.012 seconds onward, the velocity changes from positive to negative, indicating a reversal in the direction of motion. Following this change, the velocity increases in magnitude, reaching $-0,64[m/s]$ at $t = 0,020[s]$ seconds. Beyond 0.020 seconds, the velocity tends to stabilize around $-0,64[m/s]$.

3.2. Kinematics of Car 2

The mathematical function that best describes the velocity variation of Car 2 is also a fifth-degree polynomial: $v(t) = 4E9t^5 - 3E8t^4 + 6E6t^3 - 43570t^2 + 135,4t - 1,023$, as illustrated in Figure 6.

The coefficient of determination R^2 for this curve fitting is 0.9999, indicating an excellent fit of the model to the data. This value signifies that 99.99% of the variability in the dependent variable is explained by the polynomial function.

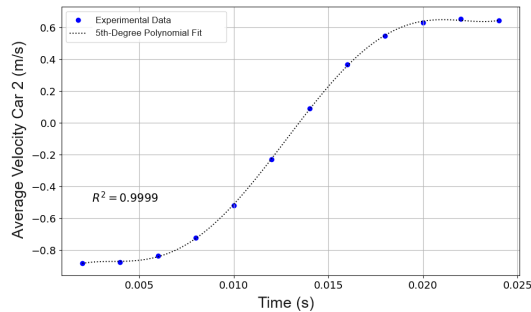


Figure 6. Variation of velocity as a function of time for Car 2 during the contact time in the collision

At $t = 0,002$ seconds, the initial velocity of the car is -0.87 m/s. The negative sign indicates that the vehicle is moving in the opposite direction to the chosen reference. The velocity decreases from -0.87 m/s to -0.22 m/s over the next 0.012 seconds. Subsequently, the velocity changes direction and begins to increase. At 0.014 seconds, the velocity is 0.09 m/s, indicating that the car has reversed direction. Following this change in direction, the velocity steadily increases, reaching 0.63 m/s at 0.024 seconds.

3.3. Coefficient of Restitution

For the analysis of the coefficient of restitution, Newton's kinematic impact law (ϵ_n) is applied as described by Equation (4), [14].

$$\epsilon_N = \frac{v^+}{u^-}, \quad 0 \leq \epsilon_N \leq 1 \quad (4)$$

Where the coefficient of restitution is the ratio of the relative velocities of the colliding bodies at the moments of contact and separation, as stated in the literature [15], (see Figure 7).

Consequently, the magnitude of the average velocity at the end of contact ($v_1 = 0,64$) for Car 2 decreased by 29.55% compared to the magnitude of the average velocity at the beginning of contact ($u_1 = -0,88$).

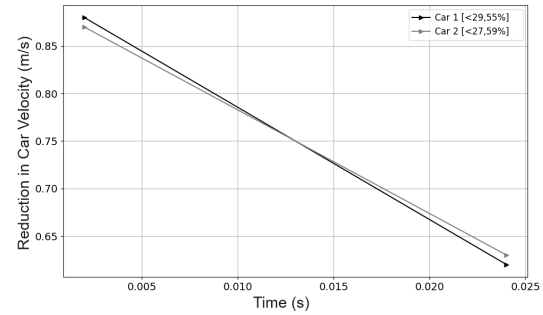


Figure 7. Variation in the magnitude of velocities during the contact time in the collision

The magnitude of the average velocity for Car 1 at the end of contact ($v_2 = -0,61$) decreased by 27.59% compared to the magnitude of the average velocity at the beginning of contact ($u_2 = 0,88$). Under these conditions, the coefficient of restitution calculated using Equation (4) is $\epsilon_N = 0,712$.

A coefficient of restitution between 0 and 1 indicates that the collision is partially elastic. This means that some of the kinetic energy is lost during the collision, manifesting as heat, sound, deformation, or other forms of non-kinetic energy.

3.4. Impulsive Forces

The variation in velocities during an impulse occurs over a very short interval (Δt), associated with a high-value impulsive force [16]. Impulse theory hypothesizes that the duration of the impulse interval is brief, allowing the phenomenon to be considered practically instantaneous. In physics, the impulse is defined as the change in the momentum of an object and is related to the force (F) and the differential time (dt) during which that force acts [16]. Refer to Equation (5).

$$I = \int_{t_1}^{t_2} F dt \quad (5)$$

Impulsive forces are responsible for changing the velocities of the cars during the collision. The experimentation enables the calculation of impulsive forces during contact time using Newton's second law without

assuming that the phenomenon is instantaneous. Figure 8 illustrates the impulsive forces acting at the moment of contact, which occurs at 0.022 seconds. These physical phenomena can be modeled using polynomial functions that accurately describe the system's behavior and predict its evolution during the contact time.

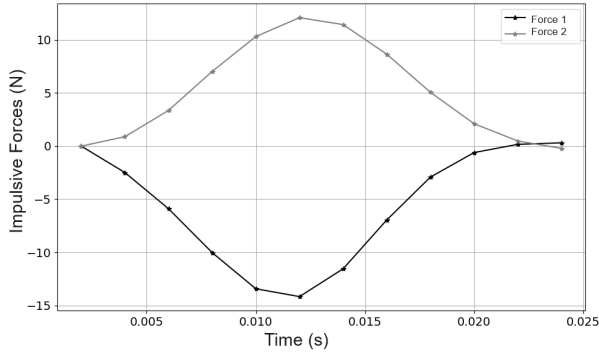


Figure 8. Impulsive forces during the contact time in the collision

The impulsive forces acting on Cars 1 and 2 exhibit different behaviors over time. Force 1 and 2 are oppositely directed, with the magnitude of Force 1 varying more significantly compared to Force 2.

The curve fitting for the impulsive forces of Cars 1 and 2 was performed using the coefficient of determination R^2 as the criterion, with a value close to 1 indicating a better fit.

The curve fitting for Impulsive Force 1 (Figure 9) and Impulsive Force 2 (Figure 10) was achieved using a fifth-degree polynomial function:

$$\begin{aligned}
 F_1(t) &= 9E10x^5 - 7E9x^4 + 2e8x^3 \\
 &\quad - 2e6x^2 + 7179,7x - 7,8949 \\
 R^2 &= 0,9901 \\
 F_2(t) &= -3e11x^5 + 3e10x^4 - 1e8x^3 \\
 &\quad + 1e6x^2 + 5414,2x + 6,4383 \\
 R^2 &= 0,9944
 \end{aligned} \tag{6}$$

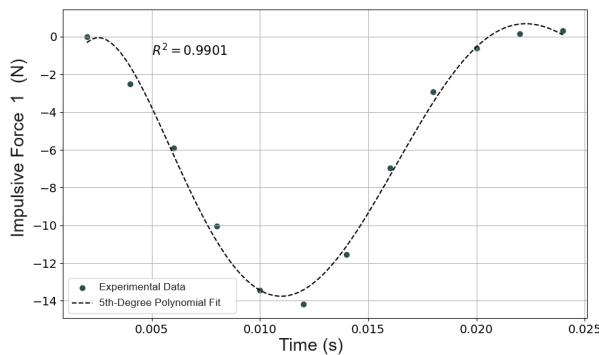


Figure 9. Curve fitting of impulsive force 1 during the contact time in the collision

Figure 9 illustrates that the impact force of Car 1 reached its maximum value $F_{I1} = -14,171[N]$ in a relatively short time $t_{I1} = 0,012[s]$, indicating a rapid transfer of energy between the colliding objects.

Figure 10 illustrates that the impact force of Car 2 reached its maximum value $F_{I2} = 12,097[N]$ in a relatively short time $t_{I2} = 0,012[s]$.

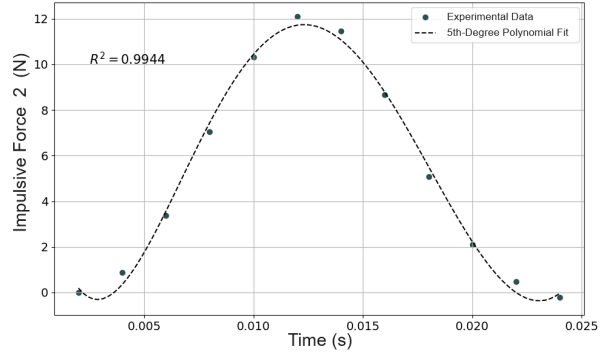


Figure 10. Curve fitting of impulsive force 2 during the contact time in the collision

The average time at which the impulsive forces reach their maximum value is 0.012 seconds. In a real impact scenario, this duration is critical, as the maximum magnitude of the force occurs within this interval. Therefore, establishing an airbag reaction time of less than 0.012 seconds in a real-world context becomes a crucial safety aspect. Implementing such a rapid reaction time in airbag systems would help mitigate the effects of impact forces, thereby reducing the risk of injury to vehicle occupants.

4. Conclusions

Understanding the variations in velocity, impulsive forces, and contact time during a collision is crucial for optimizing restraint systems such as seatbelts and airbags. This optimization ensures that these systems provide maximum protection at the critical moment of impact. As stated by Guazhambo and Larrea in their thesis from Universidad Politécnica Salesiana, titled "Database of Airbag Functionality in Vehicles Undergoing RTV in Cuenca, Determining Compliance with RTE INEN 034," this optimization is vital to enhancing vehicle safety.

Theoretical models may suggest perfectly elastic collisions with a restitution coefficient of 1. However, in practice, various real-world factors affect collisions, contributing to imperceptible deformations, friction, and energy loss. These factors make achieving a restitution coefficient of 1 in laboratory experiments challenging, if not impossible. Pursuing more realistic models and a deeper understanding of the sources of energy loss is essential for interpreting and applying experimental results effectively.

This research has modeled velocity-time and force-time functions as fifth-degree polynomial functions, capturing the variation of velocities and forces over 25 milliseconds. These models indicate nonlinear behavior with accelerated growth and decay. Understanding the kinematics of collisions at this scale, including relative velocity, impact force, and contact duration, can help detect the occurrence of a collision, determine when the peak value of impulsive forces is reached, and identify the optimal timing for activating passive safety systems.

Analyzing and understanding dynamic interaction processes can lead to exploring concepts in nanotechnology, where physical and chemical processes occur on infinitesimal scales. Therefore, future work should consider using mathematical models for simulating and analyzing physical processes at the nanoscale. This approach could help anticipate the behavior of velocity and force over extended periods and allow for comparisons with experimental data. Additionally, it would be valuable to explore which variables are represented by each of the coefficients in the velocity and force functions.

In the educational field, the experimental kinematics analysis in elastic collisions between two bodies during contact time allows students to apply theoretical concepts practically. This hands-on approach enhances their understanding and appreciation of Physics.

References

- [1] C. E. Donoso-León, M. M. Paredes-Godoy, M. M. Gallardo-Donoso, and A. F. Samaniego-Campoverde, "El laboratorio virtual en el aprendizaje procedimental de la asignatura de física," *Polo del Conocimiento*, vol. 6, no. 6, pp. 167–181, 2021. [Online]. Available: <https://doi.org/10.23857/pc.v6i6.2748>
- [2] P. M. Parra, *Uso de los Smartphones en los laboratorios de prácticas de física*. Universidad de Valladolid. España, 2017. [Online]. Available: <https://rb.gy/34xzk0>
- [3] P. Morcelle del Valle, *Transductores - instrumentación*. Universidad Nacional de la Plata, 2018. [Online]. Available: <https://rb.gy/iz42rz>
- [4] J. A. Osorio Cortéz, H. B. Cano Garzón, and J. A. Chaves Osorio, "Fundamentos y aplicación del muestreo en señales ubicadas en las bandas altas del espectro," *Scientia Et Technica*, 2008. [Online]. Available: <http://rb.gy/ctv6el>
- [5] B. I. Guazhambo Loja and D. J. Larrea Vásconez, *Base de datos del funcionamiento del airbag en los vehículos que realizan la RTV en la ciudad de Cuenca, determinando el cumplimiento de la RTE INEN 034*. Universidad Politécnica Salesiana, 2022. [Online]. Available: <http://rb.gy/qnnc4f>
- [6] A. González Mateo, *Sensores en los sistemas de seguridad del automóvil*. Universidad de Valladolid, 2019. [Online]. Available: <http://rb.gy/du99uh>
- [7] D. A. Jerez Mayorga, L. X. Orbea Hinojosa, E. P. Gualotuña Quishpe, J. A. Toapaxi Csanoba, and J. A. y Rodríguez Rodríguez, "Diseño de un protocolo de pruebas del sistema airbag mediante la interpretación de oscilogramas de operación," *INNOVA*, vol. 2, no. 9, pp. 135–146, 2017. [Online]. Available: <https://doi.org/10.33890/innova.v2.n9.2017.482>
- [8] E. I. Ayala Yunga and L. E. Tacuri Tacuri, *Análisis de la implementación de un sistema de airbag en autobuses en la seguridad del conductor durante un impacto frontal*. Universidad Politécnica Salesiana, 2021. [Online]. Available: <http://rb.gy/ui4ppl>
- [9] A. Cantero Díaz, M. M. Goire Castilla, and Y. Quintana Cassulo, "Sistema para la gestión y análisis de datos de una red de sensores inalámbricos basado en un almacén de datos." *Revista Cubana de Ciencias Informáticas*, 2019. [Online]. Available: <https://is.gd/C094kY>
- [10] R. Hibbeler, *Dinámica. Mecánica Vectorial Para Ingenieros*. Pearson Education, 2004. [Online]. Available: <https://n9.cl/o1itx>
- [11] J. González-Laprea and A. Santiago, "Sistema automatizado para medición del coeficiente de fricción estática. un dispositivo para actividades de docencia," *Revista Brasileira de Ensino de Física*, vol. 43, p. e20210056, 2021. [Online]. Available: <https://doi.org/10.1590/1806-9126-RBEF-2021-0056>
- [12] R. A. Serway and J. W. Jewett, *FÍSICA para ciencias e ingeniería*. CENGAGE Learning, 2005. [Online]. Available: <https://is.gd/LGiUOW>
- [13] M. Semeria, *Los tres teoremas: Fourier - Nyquist - Shannon*. ECONSTOR, 2015. [Online]. Available: <https://is.gd/t8NENE>
- [14] O. A. Rivera Ocampo, *Prototipo para el análisis dinámico del sistema leva-péndulo con impactos*. Universidad Nacional de Colombia, 2015. [Online]. Available: <https://is.gd/5aOWIx>
- [15] O. D. Pavioni and F. M. Ortega, "Obteniendo los coeficientes de restitución y arrastre en un solo experimento," *Revista Mexicana de Física E*, 2015.

[16] J. M. Goicolea Ruigómez, *Curso de mecánica, vol. I y II*. Universidad Politécnica de Madrid, 2010.

[Online]. Available: <https://is.gd/fzo4OI>



NEURAL NETWORK-BASED ROBOT LOCALIZATION USING VISUAL FEATURES

LOCALIZACIÓN DE ROBOTS BASADA EN RED NEURAL UTILIZANDO CARACTERÍSTICAS VISUALES

Felipe Trujillo-Romero¹

Received: 16-11-2023, Received after review: 29-05-2024, Accepted: 12-06-2024, Published: 01-07-2024

Abstract

This paper outlines the development of a module capable of constructing a map-building algorithm using inertial odometry and visual features. It incorporates an object recognition module that leverages local features and unsupervised artificial neural networks to identify non-dynamic elements in a room and assign them positions. The map is modeled using a neural network, where each neuron corresponds to an absolute position in the room. Once the map is constructed, capturing just a couple of images of the environment is sufficient to estimate the robot's location. The experiments were conducted using both simulation and a real robot. The Webots environment with the virtual humanoid robot NAO was used for the simulations. Concurrently, results were obtained using a real NAO robot in a setting with various objects. The results demonstrate notable precision in localization within the two-dimensional maps, achieving an accuracy of $\pm (0.06, 0.1)$ m in simulations contrasted with the natural environment, where the best value achieved was $\pm (0.25, 0.16)$ m.

Keywords: Visual Features, Bidimensional Maps, Inertial Odometry, Humanoid Robot NAO, A-KAZE descriptor, Growing Cell Structure

Resumen

Este artículo presenta el desarrollo de un módulo que puede desarrollar un algoritmo de construcción de mapas mediante odometría inercial y características visuales. Utiliza un módulo de reconocimiento de objetos basado en características locales y redes neuronales artificiales no supervisadas para conocer elementos no dinámicos en una habitación y asignarles una posición. El mapa está representado por una red neuronal donde cada neurona corresponde a una posición absoluta en la habitación. Una vez construido el mapa, basta con capturar un par de imágenes del entorno para estimar la ubicación del robot. Los experimentos se realizaron mediante simulación y utilizando un robot real. Se utilizó el entorno Webots con el robot humanoide virtual NAO para realizar las simulaciones. Al mismo tiempo, se obtuvieron resultados utilizando un robot NAO real en un escenario con diversos objetos. Los resultados muestran una buena precisión en la localización dentro de los mapas bidimensionales de $\pm(0,06, 0,1)$ m en simulación en contraste con el entorno natural; el mejor valor obtenido fue $\pm(0,25, 0,16)$ m.

Palabras clave: características visuales, mapas bidimensionales, odometría inercial, robot humanoide NAO, descriptor A-KAZE, estructura de crecimiento celular

^{1,*}Departamento de Ingeniería Electrónica, DICIS, Universidad de Guanajuato, México.
 Corresponding author ✉: fdj.trujillo@ugto.mx.

Suggested citation: Trujillo-Romero, F. "Neural network-based robot localization using visual features," *Ingenius, Revista de Ciencia y Tecnología*, N.º 32, pp. 77-89, 2024, DOI: <https://doi.org/10.17163/ings.n32.2024.08>.

1. Introduction

According to the International Federation of Robotics (IFR) [1], a service robot is a robotic system that operates wholly or partially autonomously to perform valuable services for the well-being of humans and equipment, excluding manufacturing operations. Service robots are specifically designed for human environments, such as homes, hospitals, and restaurants, requiring them to make complex decisions. These include identifying, detecting, recognizing, and manipulating various objects within their surroundings.

For a service robot to operate autonomously, it must be equipped with a control system that enables interaction with its environment to make the right decisions and achieve specific objectives. A critical component of this control system for service robots involves learning about the environment in which they will operate. Initially, the robot must familiarize itself with the location and the non-dynamic elements it will interact with. For instance, in some competitions, participants are given a period to acquaint themselves with the scenario interactions and perform the necessary calibrations to complete the tasks.

The ability to see enhances its interaction with people and the environment. For instance, in [2], vision sensors are used for localization and mapping. In [3], a stereovision system is developed to detect targets from the generated depth map. Additionally, Scona et al. [4] used a stereovision sensor to explore challenges such as motion blur, lack of visual features, illumination changes, and fast motion.

In environmental localization by mobile robots, in [5] a vision system was implemented to develop algorithms for simultaneous localization and mapping (SLAM). In [6], an application was developed for topological mapping and navigation using visual SLAM. Ovalle-Magallanes et al. [7] utilized visual information to create an appearance-based localization system for a humanoid robot. Lasguignes et al. [8] implemented an ICP-based localization system using visual information on the TALOS humanoid robot. Conversely, Wozniak et al. [9] proposed an algorithm for visual place recognition using images acquired by a humanoid robot, with a neural network as the recognizer. In [10], an augmented landmark vision-based ellipsoidal SLAM was developed on an NAO humanoid robot for indoor scenarios. Additionally, a method for efficient SLAM using a forward-viewing monocular vision sensor was implemented in [11].

In addition to RGB cameras, other sensors are employed, such as in [12], where an IMU sensor was utilized to locate a humanoid robot in the environment. In [13], a combination of 2D LiDAR and odometry was implemented to enable a robot to navigate and find itself. Wen et al. [14] presented an EKF-SLAM using camera and laser sensors for indoor localization and

mapping. In [15], a vision-based SLAM allows a mobile robot to navigate unknown environments. In [16], a SLAM system is proposed to estimate the robot's poses and build a 3D environment map. Furthermore, features-based tracking from a stereo vision sensor was combined to obtain a hybrid SLAM [17].

Meanwhile, Cheng, Sun, and Meng [18] utilized feature points to develop a method that integrates optical flow with ORB-SLAM to differentiate between dynamic and static elements. In [19], Ganesan et al. proposed a method to reduce the search space for the RRT* algorithm in path-planning tasks. Feature matching for map-building algorithms was explored using the distance from a point cloud obtained from a range finder sensor [20]. An environment map is built using a sensor fusion of odometry, 2D laser, and RGB-D [21]. A proposal where the environment is represented by 3D polygons that enable a robot to localize is presented in [22]. In contrast, a topological navigation system based on symbolic representation was proposed in [23] for a humanoid robot.

All the works mentioned above employ techniques to enhance localization, mapping, or object searching within a human environment, carried out by a mobile robot. For this reason, the humanoid robot NAO [24] is utilized as a platform for implementing localization and mapping in this study.

The remainder of this paper is structured as follows: Section 2 outlines the various methods and materials used in this study. Subsequently, Section 2.5 presents the implementation of the proposed system. The results obtained with both platforms are detailed in Section 3. Finally, Section 4 discusses the conclusions and directions for future research.

2. Materials and Methods

2.1. NAO robot

The NAO robot, as depicted in Figure 1 (a) is the pivotal robotic platform chosen to implement the developed system. NAO, a medium-height autonomous and programmable robot [24], is widely recognized as one of the market's most sophisticated and comprehensive robots. Over the years, five versions have been introduced, each incorporating specific enhancements, while the fundamental concept remains unaltered.

Figure 1 (b) presents a schematic of the robot, indicating its dimensions, including height, width, and arm length. The NAO robot is equipped with the embedded software NAOqi, which operates on the robot to provide autonomy. NAOqi is integrated into the robot's operating system, OpenNAO, an embedded GNU/Linux distribution based on Gentoo. This system includes numerous libraries and programs essential for NAOqi. A notable feature is the capability to run

copies of NAOqi on a computer, facilitating the use of virtual robots.

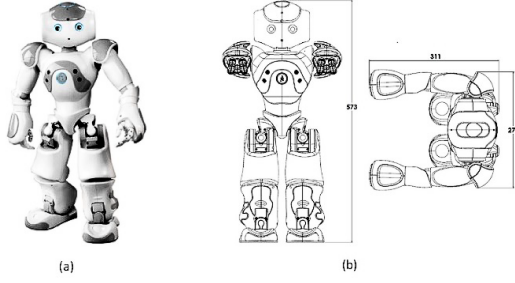


Figure 1. NAO (a) Robot, and (b) dimensions in mm [25]

2.2. A-KAZE descriptor

The A-KAZE [26] method, depicted in Figure 2, is divided into three main tasks: (1) construction of a nonlinear scale space, (2) feature detection, and (3) feature description. The construction of the nonlinear scale space involves processing an input image using the Fast Explicit Diffusion (FED) [25] numerical method, applied with a pyramidal approach.

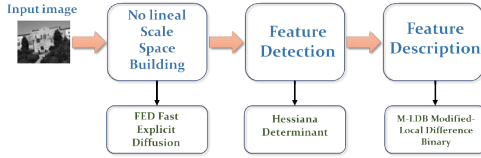


Figure 2. Overview of the A-KAZE algorithm

Initially, the scale space is discretized into a series of O octaves and S sublevels, identified by discrete indices (o and s , respectively). Subsequently, they are mapped to their corresponding scale, σ , using Equation (1).

$$\sigma(o, s) = 2^{\frac{o+s}{s}} \quad (1)$$

The input image is convolved with a Gaussian standard deviation σ 0 to reduce noise and potential artifacts, considering both the input image and a contrast factor λ , which is automatically calculated by the algorithm. Subsequently, 2D features of interest that exhibit a normalized scale determinant of the Hessian response are detected across the nonlinear scale space for each filtered image. Normalization is performed using a factor that accounts for the scale of each image in the nonlinear scale space, as illustrated in Equation (2).

$$L_{Hessiana}^i = \sigma_{i,norm}^2 (L_{xx}^i L_{yy}^i - L_{xy}^i L_{yx}^i) \quad (2)$$

The Scharr Concatenated Filter [27] calculates second-order derivatives to approximate rotation invariance. Initially, the maximum response of the detector at a specific spatial location is obtained to estimate

the 2D position of the key point. This is achieved by fitting a quadratic function to the maximum response of the Hessian determinant within a 3x3 neighborhood.

Finally, the principal orientation of the key point is calculated using the Modified-Local Difference Binary (M-LDB) descriptor [28]. This method utilizes information about gradients and intensity from the nonlinear scale space to generate a descriptor vector of length 64.

In the case of the descriptor used, its primary advantage is its superior performance in obtaining visual information when implementing the mapping system, owing to its invariance to scale and rotation changes. Additionally, it operates faster than other descriptors, and the algorithm's author provides the code. Among the disadvantages, it is necessary to mention that precise tuning of the threshold used to identify characteristic points is required, along with the adjustment of the number of levels and sublevels within the nonlinear scale space.

2.3. Growing Cell Structure

Growing Cell Structures (GCS) [29] are available in supervised and unsupervised variants. The variant of interest in this context is the unsupervised model, which offers the significant advantage of automatically determining an appropriate network structure and size. This capability is facilitated through controlled growth, which includes the periodic removal of units. This model builds upon Kohonen's [30] work on self-organizing maps. The pseudocode for GCS is presented in Algorithm 1 (see figure 3).

Algorithm 1: Growing Cell Structure [30].

Data: ϵ_b Best matching, ϵ_n neighboring and λ steps
1 Start: k -dimensional simplex $V = R^k$
2 **while** (\neq desired network size) **do**
3 **for** adaptation steps = 0 \rightarrow λ **do**
4 Choose an input signal ξ according to $P(\xi)$
5 Locate the best matching unit $s = \phi_w(\xi)$.
6 Increase matching:
7 $\Delta w_s = \epsilon_b(\xi - w_s)$
8 $\Delta w_c = \epsilon_n(\xi - w_c) (\forall c \in N_s)$
9 Increment the signal counter of s :
10 $\Delta \tau_s = 1$
11 Decrease all signal counters by a fraction α in the network A :
12 $\Delta \tau_c = -\alpha \tau_c (\forall c \in A)$
13 Determine $q : h_q \geq h_c (\forall c \in A)$
14 Look q largest distance neighbor $f : \|w_f - w_q\| \geq \|w_c - w_q\| (\forall c \in N_q)$
15 Insert cell r between q and f .
16 Initialize $r : w_r = 0 : 5(w_q + w_f)$
17 Redistribute counter:

$$\Delta \tau_c = \frac{|F_c^{new}| - |F_c^{old}|}{|F_c^{old}|} \tau_c$$

18 Initialize new cell:

$$\tau_r = - \sum_{c \in N_r} \Delta \tau_c$$

19 After insertion, check $\hat{p}_i < \eta$

20 Cells remove:

$$\hat{p} = \hat{p} - \sum_{c \in A} \hat{f}_c$$

Figure 3. Growing cell structure [30]

The Growing Cell Structure (GCS) algorithm offers several key advantages. It can autonomously adjust the number of neurons, adding or removing them as required. It operates as an unsupervised network, enabling it to form associations of input vectors independently of external input. Its simplicity of implementation is also a notable feature. However, a noted disadvantage is that the network may fail if the vectors to be associated are very close to each other.

2.4. WEBOTS robotic simulator

Webots [31] is an open-source, multi-platform desktop application for robot simulation. For this reason, Webots will be utilized to simulate the system and facilitate its respective validation.

This software simulator enables testing applications and algorithms for the NAO robot within a virtual environment. Figure 4 illustrates the software environment, a virtual world that simulates NAO movements while adhering to physical laws. This environment offers a secure setting for testing behaviors before they are implemented on a real robot.

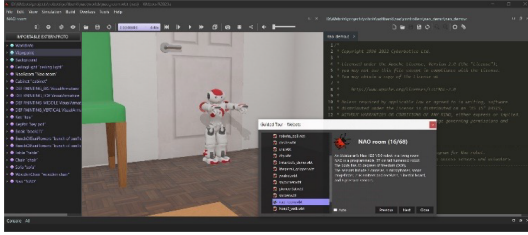


Figure 4. Webots environment [32]

2.5. Bidimensional map construction

As mentioned in the Introduction section, autonomy is achieved through a system of activity planning and control, designed to ensure the fulfillment of its objectives. One key feature of these systems is spatial navigation, which enables the calculation of a robot's pose (position and orientation) based on incremental, inertial, and visual measurements. This section presents the concepts of odometry, and visual features employed in the spatial navigation module. These tools enable the robot to construct a two-dimensional map and localize itself while navigating.

2.5.1. Odometry

Odometry facilitates estimating a mobile robot's relative position within an environment during navigation, starting from its initial location. Additionally, it records and tracks the robot's movement within a space to construct a two-dimensional map. The NAO robot has functions that address several challenges, including odometry. Algorithm 2 (see figure 5 displays

the pseudocode where functions from Aldebaran's inertial odometry [24] are utilized.

Algorithm 2: Pseudo code to store inertial odometry using Aldebaran functions [25].

```

1 //Store the initial position
2 AL::Math::Pose2D worldToRobotInit= Pose2D(getRobotPosition())
3 //Wait until it finishes scrolling
4 //Storing the final position
5 AL::Math::Pose2D worldToRobotAfter= Pose2D(getRobotPosition())
6 Pose2D robotMove = pose2DInverse(worldToRobotInit)+worldToRobotAfter //Movement
7 theta = modulo2PI(robotMove.theta)//Angle

```

Figure 5. Pseudo code to store inertial odometry using aldebaran functions [26]

In this implementation, the two-dimensional position of the robot is initialized with explicit values obtained from the initialized pose values, which are retrieved from the articulations' magnetic rotary encoders (MRE). Each time the robot is activated, it records an absolute position within the scenario world.

In constructing the two-dimensional map, the robot first saves its initial position. Then, the robot is instructed to follow a predetermined closed-circuit path within the room, advancing a specified distance while walking. As it moves, the robot's two-dimensional position is recorded periodically. Subsequently, the displacement and angle traversed by the robot are calculated. The two-dimensional position between consecutive points is then computed to accurately reflect the robot's movement.

Thus, the general implementation of odometry can be established as follows:

1. Capture the robot's position relative to the world before walking.
2. Detect when the robot starts walking.
3. Simultaneously begin collecting odometric data.
4. Process and accumulate odometric data.
5. Detect the completion of the robot's walk. If the walk is not completed, repeat steps 3 and 4.
6. Calculate the distance traveled by the robot.
7. Store the robot's distance and position data to construct the two-dimensional map.

Figure 6 presents the general flow diagram for generating the bidimensional map. In this diagram, the algorithm initiates with the capture of an image. Subsequently, visual features are extracted from this image; these features serve as inputs for the learning system, namely the neural network. Following this, the robot learns and records the spatial localization corresponding to its position. If the designated path is completed, the algorithm concludes. If not, the robot moves to the next position and the algorithm continues until the end of the path is reached.

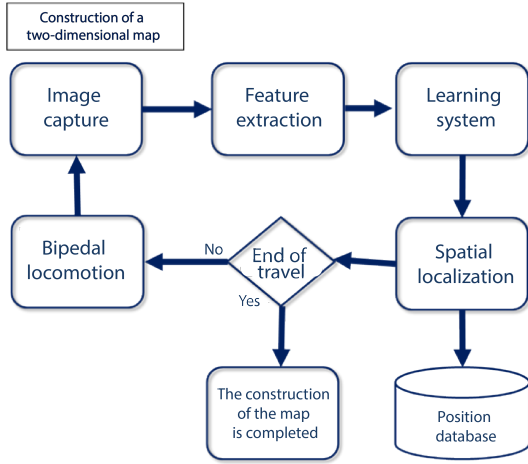


Figure 6. Dataflow diagram for the map reconstruction

2.6. Visual features

Visual elements are identified by analyzing and cataloging existing details in the environment, considering the robot's position when the image is captured. It is generally considered that the most significant visual elements for representing the environment are those located on or near the walls. A two-dimensional map of the room traversed by the robot can be constructed using these visual elements and the estimated location derived from odometry. For instance, figure 7 illustrates a virtual room with various everyday objects typically found in a home. These objects usually remain stationary. Therefore, the robot must navigate through this room following a closed, preferably quadrangular, circuit, capture images, and record the estimated position from where each image was taken.



Figure 7. Virtual room in Webots

Furthermore, the robot should focus on capturing images of the nearest wall to its path. Figure 8 illustrates three captures made by the robot at different points. During navigation, it will take a screenshot at

each step based on the number of images specified by the user for the room. For instance, if 20 images are required in a room where each wall is 4 meters long, one image will be taken every 20 cm. In addition to the number of captures and the dimensions of the room's walls, the tour frequency can also be determined. The more circuits completed, the more detailed the construction of the room map will be, and the easier it will be to localize the robot.

Once the circuits are completed, the robot uses the stored information to construct the two-dimensional map. The captured images will contain objects from which specific details must be extracted. The object recognition module [32] processes the images to obtain descriptors, which are then learned and linked to the robot's pose during capture. This information is integrated into a two-dimensional representation, forming the map of the room. Before initiating any room tour, the robot must identify the nearest wall to determine where it will focus its image captures by simply turning its head toward the visible wall. This wall detection is achieved by visually estimating distances. Before navigation, the robot should be positioned parallel to the selected wall and placed in a corner of the room. It then captures an image, which is subsequently analyzed by dividing it into two parts.

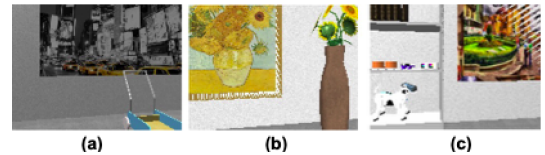


Figure 8. Images acquired by the NAO robot in a simulated room

For instance, Figure 9 displays three different captures of a room taken from various robot positions. In image 9(a), the nearest wall is to the left, while in images 9(b) and 9(c), it is on the right. For each image, interest points on each side are identified using the A-KAZE algorithm [26]. The image with the most salient points indicates the location of the nearest wall, assuming the room is free of obstacles.

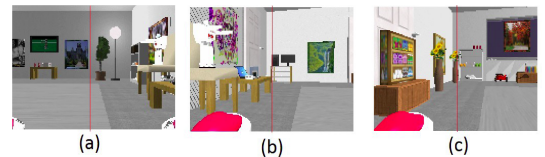


Figure 9. Images taken by the NAO robot before

Figure 10 displays the evaluation results for each image, with salient points indicated by small colored circles. In image 10(a), the right side contains the most salient points, numbering 108 compared to 36 on the left; in 10(b), the left side predominates with

128 points versus 50 on the right; and in 10(c), the left side again leads with 119 points compared to 53 on the right. Based on these observations, the robot then turns towards the side with more salient points to continue its exploration of the room.

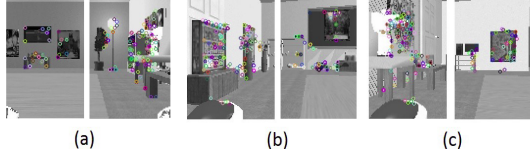


Figure 10. Wall detection using descriptors

2.7. Algorithm for the map construction

The construction of the two-dimensional map proceeds as follows: Initially, the robot performs a closed-loop circuit around a square room, capturing and recording images along with their respective poses. Knowledge of the wall dimensions, the step size during movement, and the number of iterations is essential. The robot enhances its understanding of the room with each additional circuit completed. At the commencement of Algorithm 3 (see figure 11), the robot executes an initial capture to detect the nearest wall and determine the angle for its subsequent turn.

Before commencing its movement, the robot records its current pose through odometry as the global reference point for the room. Subsequently, the distance traveled is logged, indicating both the length of the robot's journey and the total distance it needs to navigate within the room. This measurement is continually monitored by a work cycle, which persists until the traveled distance equals the combined length of the room's four walls.

Algorithm 3: Navigation Module. Execution of a closed lap.

Data: d dimensions of the room, p step size of the robot when walking, n number of paths
Result: $data$ images and poses

```

1 picture = TakePicture()
2 AngleYaw = DetectNearestWall(picture)
3 TurnHead(AngleYaw)
4  $O_n$  = CurrentPose()
5 TotalDistanceWalked = 0
6 for  $j = 1$  to  $n$  do
7   while TotalDistanceWalked  $\neq d \times 4$  do
8     DistanceWalked = 0
9     while DistanceWalked  $\neq d$  do
10      Walk( $p$ )
11      RP = CurrentPose()
12      picture = TakePicture()
13       $data = (P, I)$ 
14      DistanceWalked = DistanceWalked +  $p$ 
15      TurnBody(-AngleYaw)
16      TotalDistanceWalked = TotalDistanceWalked + DistanceWalked

```

Figure 11. Navigation module. Execution of a closed lap

After completing the circuit and storing the room database, Algorithm 4 (see figure 12), is initiated to learn from a new database that includes capture and pose information. All interest points are extracted, histograms are constructed, and a neural network

is trained using the Growing Cell Structures (GCS) method [32].

Algorithm 4: Navigation Module. Construction of two-dimensional map

Data: I images, P poses.
Result: $classes(N, P)$ classes of the two-dimensional map.

```

1 for  $i \leftarrow 1$  to  $I$  do
2   keypoints = AKAZE( $I(i)$ )
3    $H(i)$  = BuildHistos(keypoint)
4  $ANN\_trained$  = GCS( $H$ )
5  $classes(N)$  =  $ANN\_trained$ 
6 for  $i \leftarrow 1$  to  $N$  do
7    $NewPose(i)$  =  $\frac{1}{n} \sum_{j=1}^n P(classes(i))$ 

```

Figure 12. Navigation module. Construction of two-dimensional map

Algorithm 5 (see figure 13), is used to evaluate the map. This module processes the images, extracting salient points and constructing histograms. These histograms are then used to assess the trained neural network. This process helps identify the corresponding neurons. Once the classes are determined, the associated poses are retrieved. The two-dimensional positions on the map are then calculated and returned.

Algorithm 5: Navigation Module. Using the two-dimensional map

Data: I images
Result: $class(I)$ object classes, $Pose$ pose

```

1 keypoints = AKAZE( $I$ )
2  $H(I)$  = BuildHistos(keypoint)
3  $classes(I)$  =  $ANN\_trained$ 
4  $Pose = \frac{1}{n} \sum_{j=1}^n NewPose(I)(classes(i))$ 

```

Figure 13. Navigation module. Using the two-dimensional map

The algorithm operates within certain constraints, including knowing the room's dimensions to calculate the total distance the robot will traverse around it. Additionally, the environment must be free of obstacles, as this work does not incorporate obstacle-avoidance strategies.

Finally, if any elements within the room have been moved, the robot must reconstruct its navigation map to reflect these changes.

3. Results and discussion

The experiments described in this section are divided into two parts: (1) constructing a two-dimensional map and (2) localization within the map. These experiments have been conducted using both virtual and real NAO robots.

3.1. Virtual environment

3.1.1. Map construction

The simulated room depicted in Figure 7, measuring 6×6 meters, was created using Webots. This room was

furnished with various objects, such as chairs, tables, and portraits. A virtual NAO robot was employed to construct the two-dimensional map of the room. The robot initiated its journey from the lower left corner of the room, navigating in a quadrangular closed circuit. The robot turned its head towards the walls throughout its journey to capture images. The walls were numbered from 1 to 4 in a counterclockwise direction to illustrate the results of constructing the two-dimensional map.

The robot completed two counterclockwise circuits around the room, capturing images and recording their spatial relationships. The number of images taken per wall is detailed in Table 1. The term 'lap' refers to the number of circuits the robot completes. 'Images' denotes the total number of images saved during each lap. 'Wall1', 'Wall2', 'Wall3', and 'Wall4' indicate the number of images stored for each wall. In total, 164 images and their associated poses, which were used to construct the two-dimensional map, were recorded.

Table 1. Main parameters of the experiments: Construction of the two-dimensional map

Lap	Images	Wall 1	Wall 2	Wall 3	Wall 4
1	89	20	21	31	17
2	75	18	20	24	13

The parameters corresponding to object recognition are detailed in Table 2. As noted, three iterations of two-dimensional map construction were conducted using 100, 200, and 300 neurons, respectively. The objective was to assess the module's effectiveness in constructing a map accurately reflecting the robot's observations within the room.

Table 2. Parameters of the object recognition module for constructing the two-dimensional map

Experiment	Training	Neurons	Epochs	Time (sec)
1	164	100	100	4,063
2	164	200	200	14,287
3	164	300	300	33,347

After training, two-dimensional maps containing 72, 111, and 132 poses were generated. The points marked on each map in Figure 14 represent a pose associated with a neuron. It is evident that as the number of neurons increases, the distribution of poses becomes more refined. It is important to note that the poses were homogenized across the coordinates and were kept constant during the tour to ensure a precise distribution is displayed.

The distribution in the map constructed with 100 neurons is suboptimal, as it includes some poses within areas where the robot has not traveled, along with clustering of poses in certain sections. The distribution is significantly improved in the map constructed with 200

neurons, although some pose stacking is still evident. The map with 300 neurons exhibits the best distribution, covering more areas comprehensively. While a few erroneous poses are still present, they are minimal.

Thanks to the two-dimensional map, the robot can identify the locations of walls, allowing it to avoid them while executing its tasks.

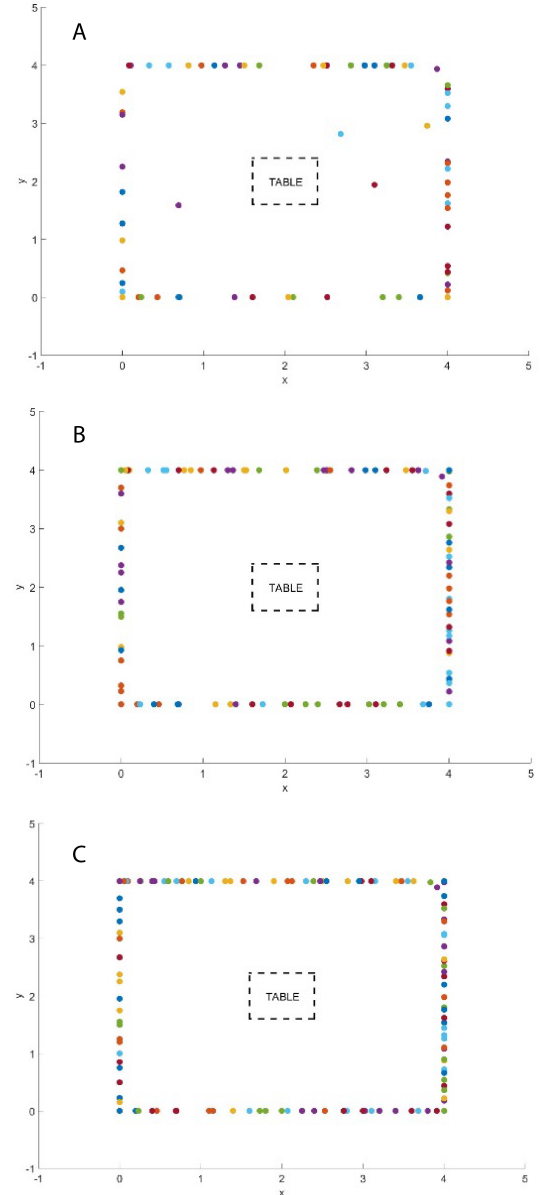


Figure 14. Distribution of neurons by poses in the room of the experiments: (a) 1, (b) 2, and (c) 3

3.1.2. Map location

The purpose of the two-dimensional map is to enable the robot to return to the global position 0 on the map once it has completed its tasks. With the constructed map, the robot can determine its location

within the room using one or two images of the nearest walls. Four experiments were conducted to validate this functionality.

Table 3 lists the parameters, which include the experiment number, the two-dimensional map constructed in the previous section (1, 2, and 3), and the actual position to be calculated (x, y) in meters.

The two-dimensional map construction is evaluated as follows: the virtual robot captures two images from different perspectives at each of the four positions nearest to the walls under assessment. Examples of these captures by the robot are illustrated in Figure 15. At each position, two images of the closest walls are captured.

The first two upper images correspond to the position (0,0), while the subsequent two correspond to the position (4,4) within the room. The results are presented in Table 3, which details five evaluations with two images for each experiment. The module records the individual poses captured in each column for the four experiments, featuring a pair of images per evaluation.

Table 3. Results of the poses evaluations and locations on the map

Nº	Map	(x,y) m	1	2	3	4	5
1	1	(3.5,0.5)	(3.7,1.7)	(3.6,1.6)	(3.7,1.7)	(3.8,1.8)	(3.3,1.7)
2	1	(0,0)	(0.1,0.2)	(0.2,0.2)	(0.3,0.1)	(0.3,0.0)	(0.3,0.2)
3	2	(0.5,3.5)	(0.0,2.0)	(0.0,2.0)	(0.2,2.2)	(0.0,2.0)	(0.2,2.2)
4	3	(4,4)	(4.0,3.8)	(3.9,3.9)	(4,4)	(3.9,3.9)	(3.9,3.9)

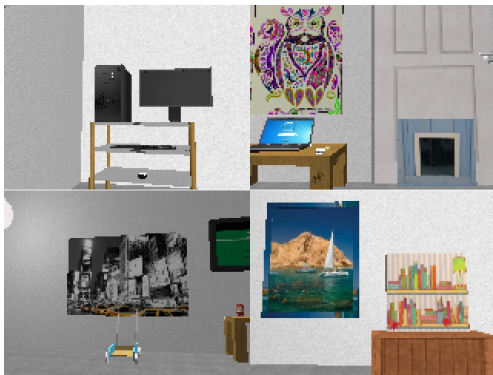


Figure 15. Examples of captures made by the virtual NAO robot

3.2. Real Scenario

3.2.1. Map construction

The two-dimensional map was constructed in a 4×3 meter room, within which the robot developed a 3×3 meter map. The room contains various elements, including posters with diverse information. Figure 16 displays the room's four walls, illustrating the elements

used for learning. Additionally, a 30 cm platform is positioned at the center of the room, as shown in Figure 17. This platform holds 20 objects distributed along the edges, enhancing visibility for the robot and ensuring the objects remain within the work area of the handlers for easy retrieval.

This evaluation completed three circuits to construct a more accurate map. The robot initiated its route from the room's global coordinate (0,0), positioned in the right corner of wall number one.

During the tours, the robot turns its head toward the wall to capture images while advancing and maintaining its relative position (see Figure 18).

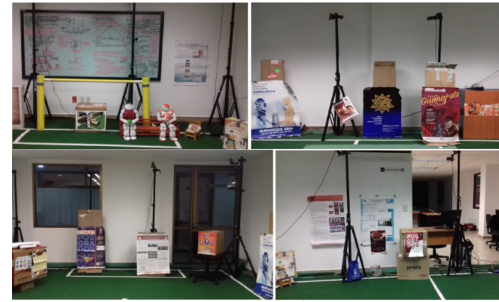


Figure 16. The walls of the real scenario for building the map



Figure 17. Platform with objects placed in the center of the room



Figure 18. The robot makes its path by heading towards the wall to capture images

Table 4 details the images captured during each circuit along the walls. This table specifies the number

of circuits completed, the total images taken, and the images captured corresponding to each wall. A total of sixty-eight images and poses used to construct the two-dimensional map were recorded.

Like the virtual scenario, the captured images are input to the object recognition module, responsible for feature learning and generating the room map.

Table 4. Main parameters of the experiments: Construction of the two-dimensional map

Lap	Images	Wall 1	Wall 2	Wall 3	Wall 4
1	25	7	7	5	6
2	26	5	8	5	8
3	17	5	5	4	3

Table 5 presents the parameters used to generate the room map, including the number of experiments conducted, the images used for training, the number of neurons, and the epochs involved.

Table 5. Parameters for constructing the map

Experiment	Training	Neurons	Times
1	68	400	100
2	68	500	200

After training, the two-dimensional maps contained 27 and 36 poses, respectively. Figure 19 displays these maps, where blue points indicate the poses at which the robot captured images. Figure 19(a) illustrates the ideal map, showing the target poses for image capture during the experiments. The map constructed for experiment 1 corresponds to Figure 19(b), while the map for the second experiment is depicted in Figure 19(c). These maps reflect the distribution of neurons associated with each pose. It is noted that increasing the number of neurons from 400 to 500 slightly improves the distribution. However, the size of the constructed map was reduced from 3×3 meters to 1.5×1.5 meters.

From the analysis above, it can be inferred that the reduction in map size resulted from numerous false positives and the inter-association of poses, which led to their consolidation.

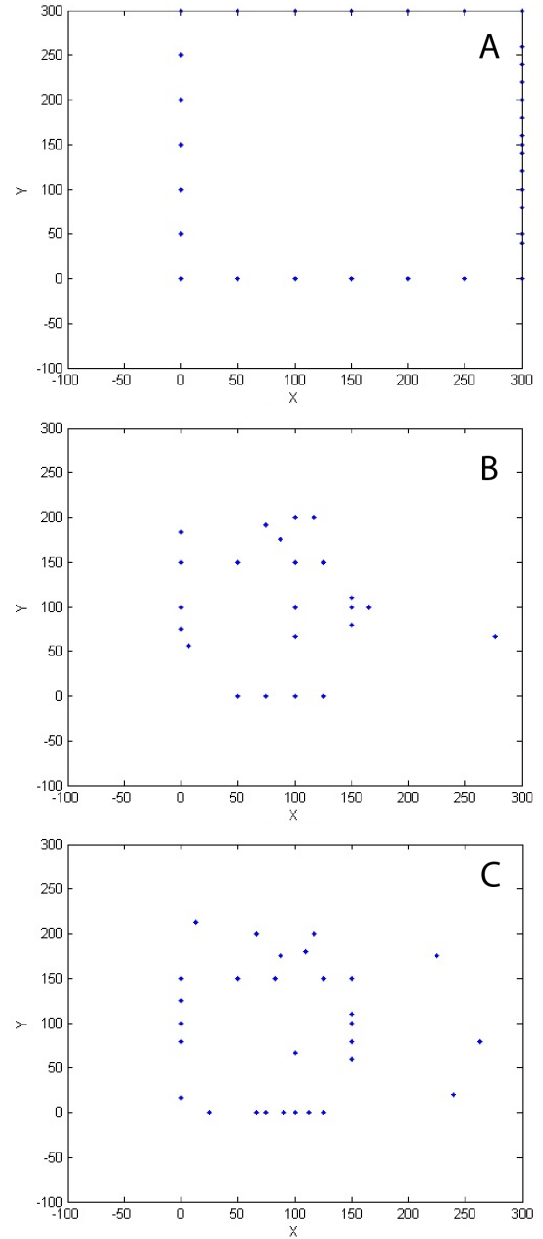


Figure 19. Distribution of neurons by poses in the room

3.2.2. Map localization

The task of localization on the two-dimensional map serves several purposes. One key objective is for the robot to return to the starting point to deliver an object as requested by the user. Additionally, the robot uses the map to locate room walls, which helps avoid them during search tasks for items.

Therefore, with the constructed map, the robot can determine its location within the room using one or two images of the nearest walls. This capability was assessed through ten experiments that were conducted.

Table 6 lists the experiment numbers and the corresponding positions to be calculated (x, y) in meters.

Table 6. Main parameters of experiments for the map location

N°	1	2	3	4	5	6	7	8	9	10
(x,y)m	(0,0)	(0,1)	(0,2)	(0,3)	(1,0)	(2,0)	(3,0)	(3,3)	(1.5,2)	(2,1.5)

The accuracy of the robot's location on the two-dimensional map is determined using two images captured from the closest potential positions of the wall adjacent to that point.

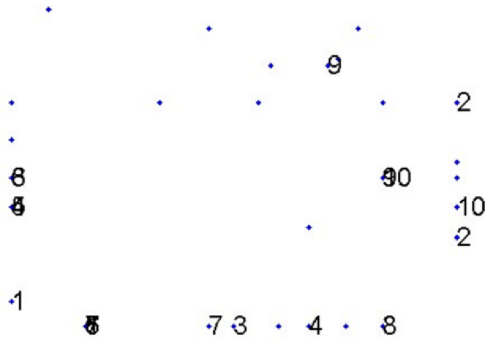
The results are presented in Table 7, where the 10 locations are associated with two poses derived from evaluating the two images taken from each position. Due to inaccuracies in constructing the two-dimensional map, the obtained poses do not closely

match the actual positions.

The highest precision was achieved with pose number (1), showing an accuracy of $\pm (0.25, 0.16)$ close to the expected pose. The next best precision was obtained with pose number (9), showing an accuracy of $\pm (0.34, 0.62)$. The least accurate poses were (2) and (8), with precisions of $\pm (1.50, 0.50)$ and $\pm (1.75, 2.00)$, respectively. Although the constructed map was inaccurate, the evaluation yields favorable results given the trained map. Figure 20 provides a graphical representation of the 10 locations determined using the module on the previously trained two-dimensional map. It is observed that most poses are very close to the trained positions, except for poses 2, 7, and 8, which were significantly misaligned.

Table 7. Results of the evaluations of poses for each experiment

N°	1	2	3	4	5	6	7	8	9	10
1	(0,0.16)	(1.50,1.50)	(0.75,0)	(1.00,0)	(0,0.80)	(0,1.0)	(0.25,0)	(1.25,0)	(1.06,1.75)	(1.50,0.80)
2	(0.25,0)	(1.50,0.60)	(1.25,0)	(0,0.80)	(0.25,0)	(0.25,0)	(0.66,0)	(0,1.00)	(1.25,1.00)	(1.25,1.00)

**Figure 20.** Plot with the 10 locations determined on the trained map

4. Conclusions

This study presents the development of an algorithm for constructing two-dimensional maps using inertial odometry and visual elements. The two-dimensional map is created utilizing an object recognition module based on local features and unsupervised artificial neural networks. This module is employed to learn the room's layout and associate a pose with each neuron in the network, which is trained to represent the two-dimensional map.

Experiments were conducted using (1) a virtual NAO robot and (2) a real NAO robot within an authentic scenario. The results are promising, as it was possible to construct a two-dimensional map of the room and accurately locate the mobile robot with

a precision of up to $\pm (0.06, 0.1)$ in simulation and $\pm (0.25, 0.16)$ in the natural environment. These results can be further improved by enhancing the quality of the images.

1. The approach to generating maps from visual information has several limitations, including the following: The NAO robot's cameras are not optimal for capturing high-quality images, leading to errors in both the learning and recognition phases.
2. The environment must be structured to include sufficient visual references on the room's walls to improve the robot's localization accuracy.
3. This implementation does not account for dynamic elements; therefore, the scene only contains the robot, the table, and the surrounding objects.
4. The robot's path must be straight, necessitating a clear path free of objects to allow proper positioning relative to the wall and its visual markers.
5. The approach relies heavily on visual information, so the absence of such information would cause confusion and significantly hinder the robot's ability to navigate around the room.

4.1. Future work

1. **Enhanced Sensor Fusion:** Future work will focus on improving data integration from inertial

odometry and visual elements. This approach aims to reduce reliance on solely visual features, thereby enhancing the robustness and accuracy of the system.

2. **Evaluation of Neural Network Architectures:** Various neural network architectures will be evaluated to determine the most suitable for the construction map task. The architecture that demonstrates the best performance will be selected for further development and implementation.
3. **Testing Advanced Feature Point Detectors:** To enhance system performance, state-of-the-art feature point detectors will be tested. These detectors are expected to offer significant improvements in the detection and processing of feature points, contributing to overall system efficiency.

References

- [1] IFR. (2024) Homepage. International Federation of Robotics. International Federation of Robotics. [Online]. Available: <https://ifr.org/>
- [2] Y. Omori, T. Furukawa, T. Ishikawa, and M. Inaba, "Humanoid vision design for object detection, localization and mapping in indoor environments," in *2018 IEEE International Symposium on Safety, Security, and Rescue Robotics (SSRR)*, 2018, pp. 1–6. [Online]. Available: <https://doi.org/10.1109/SSRR.2018.8468604>
- [3] X. Cui, M. Wang, B. Fan, and J. Yi, "Target detection based on binocular stereo vision," in *2017 International Conference on Computer Technology, Electronics and Communication (ICCTEC)*, 2017, pp. 1093–1097. [Online]. Available: <https://doi.org/10.1109/ICCTEC.2017.00239>
- [4] R. Scona, S. Nobili, Y. R. Petillot, and M. Fallon, "Direct visual SLAM fusing proprioception for a humanoid robot," in *2017 IEEE/RSJ International Conference on Intelligent Robots and Systems (IROS)*, 2017, pp. 1419–1426. [Online]. Available: <https://doi.org/10.1109/IROS.2017.8205943>
- [5] L. K. Garzón Obregón, L. A. Forero Rincón, and O. M. Duque Suárez, "Diseño e implementación de un sistema de visión artificial usando una técnica de mapeo y localización simultánea (SLAM) sobre una plataforma robótica móvil," *Mundo FESC*, vol. 8, no. 16, pp. 8–17, 2018. [Online]. Available: <https://is.gd/pqjvTy>
- [6] F. Blochiger, M. Fehr, M. Dymczyk, T. Schneider, and R. Siegwart, "Topomap: Topological mapping and navigation based on visual SLAM maps," in *2018 IEEE International Conference on Robotics and Automation (ICRA)*, 2018, pp. 3818–3825. [Online]. Available: <https://doi.org/10.1109/ICRA.2018.8460641>
- [7] E. Ovalle-Magallanes, N. G. Aldana-Murillo, J. G. Avina-Cervantes, J. Ruiz-Pinales, J. Cepeda-Negrete, and S. Ledesma, "Transfer learning for humanoid robot appearance-based localization in a visual map," *IEEE Access*, vol. 9, pp. 6868–6877, 2021. [Online]. Available: <https://doi.org/10.1109/ACCESS.2020.3048936>
- [8] T. Lasguignes, I. Maroger, M. Fallon, M. Ramezani, L. Marchionni, O. Stasse, N. Mansard, and B. Watier, "ICP Localization and Walking Experiments on a TALOS humanoid robot," in *2021 20th International Conference on Advanced Robotics (ICAR)*, 2021, pp. 800–805. [Online]. Available: <https://doi.org/10.1109/ICAR53236.2021.9659474>
- [9] P. Wozniak, H. Afrisal, R. G. Esparza, and B. Kwolek, "Scene recognition for indoor localization of mobile robots using deep CNN," in *Computer Vision and Graphics*, L. J. Chmielewski, R. Kozera, A. Orłowski, K. Wojciechowski, A. M. Bruckstein, and N. Petkov, Eds. Cham: Springer International Publishing, 2018, pp. 137–147. [Online]. Available: https://doi.org/10.1007/978-3-030-00692-1_13
- [10] E. S. Lahemer and A. Rad, "An adaptive augmented vision-based ellipsoidal slam for indoor environments," *Sensors*, vol. 19, no. 12, 2019. [Online]. Available: <https://doi.org/10.3390/s19122795>
- [11] T.-J. Lee, C.-H. Kim, and D.-I. D. Cho, "A monocular vision sensor-based efficient slam method for indoor service robots," *IEEE Transactions on Industrial Electronics*, vol. 66, no. 1, pp. 318–328, 2019. [Online]. Available: <https://doi.org/10.1109/TIE.2018.2826471>
- [12] M. Fourmy, D. Atchuthan, N. Mansard, J. Solà, and T. Flayols, "Absolute humanoid localization and mapping based on IMU Lie group and fiducial markers," in *2019 IEEE-RAS 19th International Conference on Humanoid Robots (Humanoids)*, 2019, pp. 237–243. [Online]. Available: <https://doi.org/10.1109/Humanoids43949.2019.9035005>
- [13] S. J. Dignadice, J. R. Red, A. J. Bautista, A. Perol, A. Ollanda, and R. Santos, "Application of simultaneous localization and mapping in the development of an autonomous robot," in *2022 8th International Conference on Control, Automation and Robotics (ICCAR)*,

- 2022, pp. 77–80. [Online]. Available: <https://doi.org/10.1109/ICCAR55106.2022.9782658>
- [14] S. Wen, M. Sheng, C. Ma, Z. Li, H. K. Lam, Y. Zhao, and J. Ma, “Camera recognition and laser detection based on EKF-SLAM in the autonomous navigation of humanoid robot,” *Journal of Intelligent & Robotic Systems*, vol. 92, no. 2, pp. 265–277, Oct 2018. [Online]. Available: <https://doi.org/10.1007/s10846-017-0712-5>
- [15] X. Deng, Z. Zhang, A. Sintov, J. Huang, and T. Bretl, “Feature-constrained active visual SLAM for mobile robot navigation,” in *2018 IEEE International Conference on Robotics and Automation (ICRA)*, 2018, pp. 7233–7238. [Online]. Available: <https://doi.org/10.1109/ICRA.2018.8460721>
- [16] A. Li, J. Wang, M. Xu, and Z. Chen, “DP-SLAM: A visual SLAM with moving probability towards dynamic environments,” *Information Sciences*, vol. 556, pp. 128–142, 2021. [Online]. Available: <https://doi.org/10.1016/j.ins.2020.12.019>
- [17] N. Krombach, D. Droschel, S. Houben, and S. Behnke, “Feature-based visual odometry prior for real-time semi-dense stereo SLAM,” *Robotics and Autonomous Systems*, vol. 109, pp. 38–58, 2018. [Online]. Available: <https://doi.org/10.1016/j.robot.2018.08.002>
- [18] Y. S. Jiyu Cheng and M. Q.-H. Meng, “Improving monocular visual slam in dynamic environments: an optical-flow-based approach,” *Advanced Robotics*, vol. 33, no. 12, pp. 576–589, 2019. [Online]. Available: <https://doi.org/10.1080/01691864.2019.1610060>
- [19] S. Ganesan and S. K. Natarajan, “A novel directional sampling-based path planning algorithm for ambient intelligence navigation scheme in autonomous mobile robots,” *Journal of Ambient Intelligence and Smart Environments*, vol. 15, pp. 269–284, 2023, 3. [Online]. Available: <https://doi.org/10.3233/AIS-220292>
- [20] K. Zhang, H. Gui, Z. Luo, and D. Li, “Matching for navigation map building for automated guided robot based on laser navigation without a reflector,” *Industrial Robot: the international journal of robotics research and application*, vol. 46, no. 1, pp. 17–30, Jan 2019. [Online]. Available: <https://doi.org/10.1108/IR-05-2018-0096>
- [21] C. Wang, J. Wang, C. Li, D. Ho, J. Cheng, T. Yan, L. Meng, and M. Q.-H. Meng, “Safe and robust mobile robot navigation in uneven indoor environments,” *Sensors*, vol. 19, no. 13, 2019. [Online]. Available: <https://doi.org/10.3390/s19132993>
- [22] A. Roychoudhury, M. Missura, and M. Bennewitz, “3D polygonal mapping for humanoid robot navigation,” in *2022 IEEE-RAS 21st International Conference on Humanoid Robots (Humanoids)*, 2022, pp. 171–177. [Online]. Available: <https://doi.org/10.1109/Humanoids53995.2022.10000101>
- [23] F. Martín, J. Ginés, D. Vargas, F. J. Rodríguez-Lera, and V. Matellán, “Planning topological navigation for complex indoor environments,” in *2018 IEEE/RSJ International Conference on Intelligent Robots and Systems (IROS)*, 2018, pp. 1–9. [Online]. Available: <https://doi.org/10.1109/IROS.2018.8594038>
- [24] Aldebaran. NAO Documentation. Aldebaran NAO Documentation. [Online]. Available: <https://is.gd/eSNPWH>
- [25] MIA. (2023) Mathematical image analysis group. MIA Group. [Online]. Available: <https://is.gd/69mEso>
- [26] P. Fernández Alcantarilla, “Fast explicit diffusion for accelerated features in nonlinear scale spaces,” in *British Machine Vision Conference (BMVC)*, 09 2013. [Online]. Available: <http://dx.doi.org/10.5244/C.27.13>
- [27] H. Schar, *Optimale Operatoren in der Digitalen Bildverarbeitung*. University of Heidelberg, Germany, 2000. [Online]. Available: <https://doi.org/10.11588/heidok.00000962>
- [28] X. Yang and K. Cheng, “LDB: an ultra-fast feature for scalable augmented reality on mobile devices,” *2012 IEEE International Symposium on Mixed and Augmented Reality (ISMAR)*, pp. 49–57, 2012. [Online]. Available: <https://doi.org/10.1109/ISMAR.2012.6402537>
- [29] B. Fritzke, “Growing cell structures—a self-organizing network for unsupervised and supervised learning,” *Neural Networks*, vol. 7, no. 9, pp. 1441–1460, 1994. [Online]. Available: [https://doi.org/10.1016/0893-6080\(94\)90091-4](https://doi.org/10.1016/0893-6080(94)90091-4)
- [30] T. Kohonen, “The self-organizing map,” *Proceedings of the IEEE*, vol. 78, no. 9, pp. 1464–1480, 1990. [Online]. Available: <https://doi.org/10.1109/5.58325>
- [31] Cyberbotics. (2023) Simulating your robots with webots. Cyberbotics - Robotics simulation services. Cyberbotics - Robotics simulation services. [Online]. Available: <https://is.gd/Q31yau>
- [32] K. L. Flores-Rodríguez, F. Trujillo-Romero, and W. Suleiman, “Object recognition modular

system implementation in a service robotics context,” in *2017 International Conference on Electronics, Communications and Computers*

(*CONIELECOMP*), 2017, pp. 1–6. [Online]. Available: <https://doi.org/10.1109/CONIELECOMP.2017.7891833>



OPTIMIZING STRUCTURAL INTEGRITY OF FIGHTER AIRCRAFT WING STATIONS: A FINITE ELEMENT ANALYSIS APPROACH

OPTIMIZACIÓN DE LA INTEGRIDAD ESTRUCTURAL DE LAS ESTACIONES DE ALA DE AERONAVES DE COMBATE: UN ENFOQUE DE ANÁLISIS DE ELEMENTOS FINITOS

Aun Haider Bhutta^{1,*}

Received: 02-05-2024, Received after review: 29-05-2024, Accepted: 13-06-2024, Published: 01-07-2024

Abstract

Modern fighter aircraft are equipped with multiple stations on the fuselage and under the wings to accommodate various external stores, both jettisonable and non-jettisonable. Each configuration undergoes airworthiness certification, including structural analysis of individual stations within the carriage flight envelope. This study focuses on the structural analysis of a fighter aircraft wing station within this specified envelope. To perform this analysis, the wing station is extracted from the comprehensive global wing model, creating a sub-model with equivalent stiffness properties. Utilizing ANSYS Workbench®, Finite Element Analysis (FEA) is conducted for critical load cases to determine the Factor of Safety (FoS). The initial analysis reveals that the wing station has an FoS of 1.2 under the maximum design load. Prestressed modal and buckling analyses indicate a 10% increase in stiffness due to stress-stiffening effects. To further enhance load-carrying capacity, parametric design changes are introduced. Increasing the bolt diameter from 8 mm to 10 mm raises the FoS to 1.33, resulting in an 8% increase in the maximum load-carrying capacity of the wing station. This comprehensive approach, employing FEA, ensures the wing's structural integrity under static load conditions within the carriage envelope. The study's findings support the wing station's enhanced performance and contribute to safer and more efficient aircraft operations.

Keywords: External store; Weapon Carriage; Static Structural Analysis; Sub-modelling; Modal Analysis; Buckling Analysis; Design Optimization

Resumen

Los aviones de combate modernos están equipados con múltiples estaciones en el fuselaje y debajo de las alas para acomodar varios almacenes externos, tanto descartables como no descartables. Cada configuración se somete a una certificación de aeronavegabilidad, incluido un análisis estructural de las estaciones individuales dentro de la envolvente de vuelo del transporte. Este estudio se centra en el análisis estructural de una estación de ala de un avión de combate dentro de esta envolvente especificada. Para realizar este análisis, la estación del ala se extrae del modelo global integral del ala, creando un submodelo con propiedades de rigidez equivalentes. Utilizando ANSYS Workbench®, se realiza un análisis de elementos finitos (FEA) para casos de carga críticos para determinar el factor de seguridad (FoS). El análisis inicial revela que la estación del ala tiene un FoS de 1,2 bajo la carga máxima de diseño. Los análisis modales y de pandeo pretensados indican un aumento del 10 % en la rigidez debido a los efectos de rigidez por tensión. Para mejorar aún más la capacidad de carga, se introducen cambios de diseño paramétrico. El cambio del diámetro del perno de 8 mm a 10 mm incrementa el FoS a 1,33, lo que da como resultado un aumento del 8 % en la capacidad máxima de carga de la estación del ala. Este enfoque integral, que emplea FEA, garantiza la integridad estructural del ala bajo condiciones de carga estática dentro de la envolvente del carro. Los hallazgos del estudio respaldan el rendimiento mejorado de la estación del ala y contribuyen a operaciones de aeronaves más seguras y eficientes.

Palabras clave: Tienda externa, transporte de armas, análisis estructural estático; submodelado, análisis modal, análisis de pandeo, optimización del diseño

^{1,*}Instituto de Aeronáutica y Astronáutica, Universidad Aérea de Islamabad, Pakistán.
 Corresponding author✉: aunbhutta@gmail.com.

1. Introduction

In the last two decades, there has been a notable upswing in the adoption of the finite element method (FEM) for the analysis of complex structures [1]. This numerical technique provides a highly accurate approximate solution for problems that lack closed-form solutions.

In static structural finite element analysis (FEA), constitutive laws describe how materials respond to applied loads and define the relationship between stress and strain. Hooke's Law, presented in Equation (1), is the fundamental constitutive law employed for linear elastic materials. This law provides a linear relationship between the stress (σ_{ij}) and strain tensors (ϵ_{kl}), represented as follows:

$$\sigma_{ij} = C_{ijkl}\epsilon_{kl} \quad (1)$$

C_{ijkl} is the elastic stiffness tensor, which depends on material properties such as Young's modulus E and Poisson's ratio (ν)

In a practical FEA scenario, several variables are known, including material properties (Young's modulus, Poisson's ratio and density), geometry (dimensions and shape of the structure), and boundary conditions (displacements such as fixed supports or prescribed movements, and forces such as applied loads or pressure).

In FEA, unknown quantities include nodal displacements (u_i) at each node in the mesh, as well as strains (ϵ_{ij}) and stresses (σ_{ij}) at each integration point or node. For a linear elastic material in 3D, the stiffness matrix can be expressed using Lamé's constants, λ and G , derived from Young's modulus and Poisson's ratio.

$$\lambda = \frac{E\nu}{(1+\nu)(1-2\nu)}, G = \frac{E}{2(1+\nu)} \quad (2)$$

Equation (3) presents stress-strain relationship in matrix form.

$$\begin{bmatrix} \sigma_{xx} \\ \sigma_{yy} \\ \sigma_{zz} \\ \sigma_{xy} \\ \sigma_{yz} \\ \sigma_{zx} \end{bmatrix} = \begin{bmatrix} \lambda + 2G & \lambda & \lambda & 0 & 0 & 0 \\ \lambda & \lambda + 2G & \lambda & 0 & 0 & 0 \\ \lambda & \lambda & \lambda + 2G & 0 & 0 & 0 \\ 0 & 0 & 0 & G & 0 & 0 \\ 0 & 0 & 0 & 0 & G & 0 \\ 0 & 0 & 0 & 0 & 0 & G \end{bmatrix} \begin{bmatrix} \epsilon_{xx} \\ \epsilon_{yy} \\ \epsilon_{zz} \\ \epsilon_{xy} \\ \epsilon_{yz} \\ \epsilon_{zx} \end{bmatrix} \quad (3)$$

By inputting the known material properties and boundary conditions into the FEA software, the unknowns (displacements, strains, and stresses) can be determined. This process ensures accurate prediction of structural behaviour under applied loads, facilitating the design and assessment of structural integrity.

A review of published research reveals the prevalent use of fixed boundary conditions (BC) in the static structural analysis of members isolated from the global

structure [2]. While commonly employed, it is acknowledged that this boundary condition represents a conservative approximation, which overestimates the maximum stress on the structural member, consequently leading to an underestimation of the Factor of Safety (FOS) [3].

The use of fixed support boundary conditions in the analysis of statically indeterminate structures, such as aircraft wings, presents notable limitations primarily due to the assumptions that fixed supports introduce, which may not accurately reflect real-world conditions [4]. Fixed supports assume no movement or rotation at the support points, which is often unrealistic in practical scenarios. Aircraft wings experience various forces and moments that cause deformations, significantly influencing overall structural behaviour [5]. Additionally, joints and connections in an aircraft are not perfectly rigid; they possess some degree of flexibility which must be considered for a more accurate structural analysis.

Fixed supports can misrepresent actual load paths and stress distributions within the structure. Aircraft wings are engineered to distribute loads efficiently, but fixed supports can alter these distributions, leading to inaccurate analyses [6]. This can result in artificial stress concentrations that do not exist in the structure, potentially leading to erroneous assessments of structural integrity and fatigue life.

Moreover, fixed supports simplify the boundary conditions to a degree that may not accurately capture material non-linearities, such as plastic deformation and creep [7]. Aircraft wings frequently operate under conditions where these material non-linearities are significant, necessitating boundary conditions that can account for such effects. Additionally, large deformations and geometric non-linearities in aircraft wings require boundary conditions that can adapt to changing configurations, a capability that fixed supports cannot provide.

Lastly, results from analyses using fixed supports may not correlate well with experimental data or in-flight measurements. To ensure accurate and reliable analysis, engineers often resort to more realistic boundary conditions that simulate the interaction between different parts of the structure, and flexible supports that incorporate the elasticity of attachments and connections. Hybrid models, combining various boundary conditions, are also employed to better capture the complex interactions within the structure. These advanced boundary conditions facilitate more accurate predictions of structural behaviour under diverse loading conditions, leading to safer and more efficient aircraft designs.

The wing of an aircraft is classified as a statically indeterminate structure [8]. Such structures feature kinematic redundancy, wherein the constraints exceed the minimum necessary to prevent rigid body motion

under applied loads. In statically indeterminate structures, the values of reaction forces and moments at supports are influenced by the stiffness characteristics of the structure [9]. Consequently, the stiffness of the wing plays a crucial role in determining the load distribution on the tulips of the wing station [10].

Rather than imposing a fixed boundary condition on a local model isolated from the global model, an alternative approach involves assigning nodal displacements derived from the solution of the global Finite Element (FE) model [11]. An FE analysis of the isolated structural member, incorporating these nodal displacements and the applied load, is conducted to obtain accurate results. This method requires solutions for both the global and local models for each load case [12].

A third technique involves isolating the local model from the global model using translational and rotational springs. The stiffness of these springs depends on the deformation field of the global model under the applied load [13]. Subsequently, a refined local model is analysed using these springs for each load case. Implementing these springs in ANSYS is accomplished by applying elastic support boundary conditions, with stiffness derived from analysing the global wing model under design load [14].

This examination focuses on a contemporary jet fighter aircraft.

Figure 1 depicts the wing of an aircraft, including four spars: the Front Wall Spar, Front Spar, Main Spar, and Rear Spar [15]. These spars constitute a cohesive framework intricately interconnected through a system of 12 ribs.

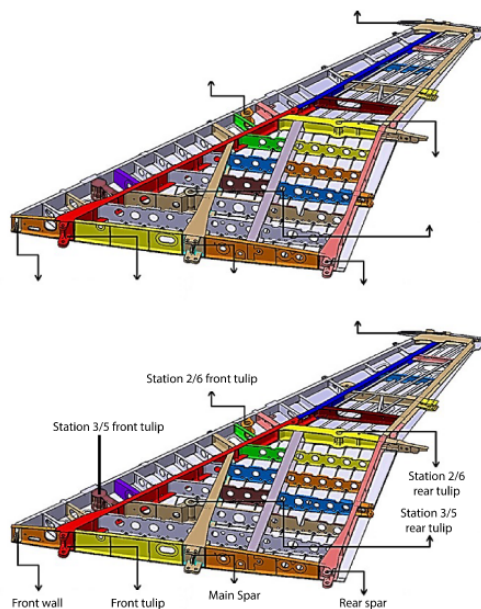


Figure 1. Internal Structure of Aircraft Wing [15]

This study focuses on outboard wing station 2/6,

located on Wing Rib 7, specifically designated for carrying external stores. This station comprises two integral structural components: the Front Tulip (FT) and the Rear Tulip (RT). Considering the limitations of fixed boundary conditions, this study enhances the analysis fidelity by incorporating wing stiffness. The primary aim is to ascertain the maximum load-carrying capacity of wing station 2/6, employing accurate boundary conditions through the sub-modelling technique [16].

This method aims to provide a more accurate portrayal of structural behaviour, enabling precise evaluation of stress levels and FOS for the wing station. Incorporating wing stiffness enhances reliability of structural analysis and provides nuanced insights into wing performance under diverse conditions. Sub-modelling techniques account for the influence of wing stiffness, resulting in improved accuracy and understanding of structural behaviour. Ultimately, integrating wing stiffness enhances structural analysis reliability, offering valuable insights into wing performance across various scenarios.

2. Materials and Methods

The methodology involves extracting the front and rear tulips from the global wing model and introducing wing stiffness via elastic boundary conditions derived from FE analysis under the design load [17]. Critical loads are applied to each wing tulip, and static structural analysis is conducted in ANSYS Workbench version 14.5 to generate deformation and stress field. Utilizing the Factor of Safety (FOS) based on yield strength, the study determines the maximum load-carrying capacity of the wing station. Prestressed modal and buckling analyses [18] are performed to assess the stress-stiffening effect under the maximum design load. The real potential of this study lies in the design optimization, which is implemented through parametric alterations of the bolt holes of the wing tulip. This process enhances the load-carrying capacity of the wing station, facilitating a comprehensive evaluation of structural performance and enhancing the overall capabilities of the fighter aircraft [19]. While this study provides a comprehensive understanding of the wing station's behaviour under static loads, it does not account for cyclic loading conditions. PSD analysis for cyclic loading will be addressed in subsequent studies.

3. Results And Discussion

3.1. Boundary Conditions for Tulips

The FE model of the wing, constructed using line and shell elements, is illustrated in Figure 2. Analysis of this wing model under design load generates a displacement field depicted in Figure 3. The resulting displacement field under applied loads provides

stiffness values for the elastic support imposed as a boundary condition for the analysis of the Front and Rear Tulips.

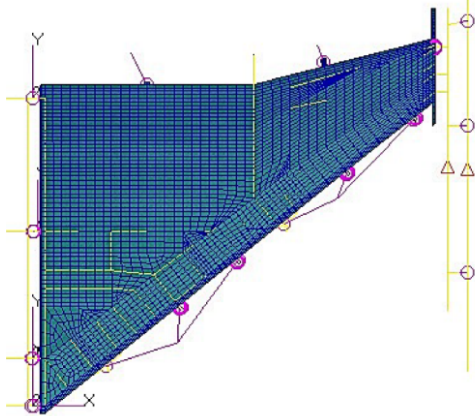


Figure 2. FE Model of the Wing [9]

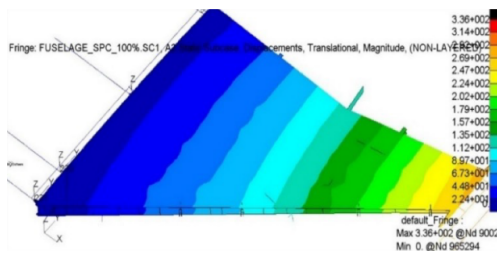


Figure 3. Deformation Field of the Wing

The stiffness values for the respective elastic supports, obtained through ANSYS Workbench version 14.5, are presented. These stiffness values are utilized in the analysis of isolated wing tulips.

Loads applied to the wing are transferred to the fuselage, causing deformation and motion at the aircraft's center of gravity. To eliminate rigid body motion in the analysis, it is necessary to constrain the aircraft's centreline. In the current study, the wing model of the aircraft is constrained to six degrees of freedom (6 DOF) at the aircraft's centreline. This constraint prevents undesired rigid body motions, ensuring an accurate load transfer and structural behaviour simulation. By applying these constraints, the analysis provides stable and realistic boundary conditions for the Finite Element Analysis (FEA).

3.2. FE Models of Tulips

CAD models of the front and rear tulips for wing station 2/6, which have been developed in the ANSYS Design Module®, are illustrated in Figure 4 and Figure 5, respectively. These CAD models serve as templates for developing FE models in ANSYS Workbench®. Material properties assigned to the wing tulips are detailed in the aerodynamic analysis of aircraft with external stores within the carriage envelop of the aircraft, providing provides critical load cases for wing tulips [1]. Table 3 and Table 4 comprehensively outline the load cases exerted on the Front Tulip (FT) and Rear Tulip (RT) during the carriage envelop [1]. These forces and bending moments are applied to both the front and rear tulips of station 2/6.

Table 1. Elastic Boundary Condition for Tulips [9]

Tulip	Linear Stiffness	Rotational Stiffness
Front Tulip	242 kN/m	11173 Nm/rad
Rear Tulip	99 kN/m	50825 Nm/rad

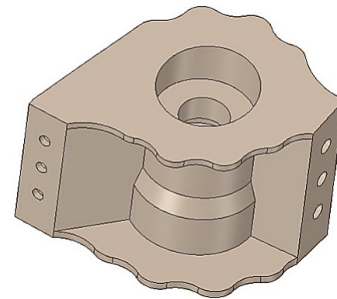


Figure 4. Solid Model of the Front Tulip (FT) [9]

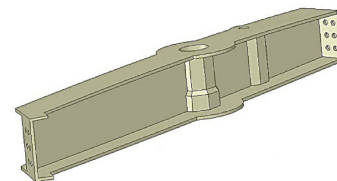


Figure 5. Solid Model of the Rear Tulip

Table 2. Material Properties of Tulips

Component	Material	σ_y (MPa)	E (GPa)	Poisson Ratio ν	Density (g/cm^3)
Front Tulip (FT)	30CrMnSi	835	196	0.3	7.75
Rear Tulip (RT)	7050-	427	70	0.33	2.82

Table 3. Loads Cases (LC) for the Front Tulip (FT) (force in kN and moments in kN.m) [1]

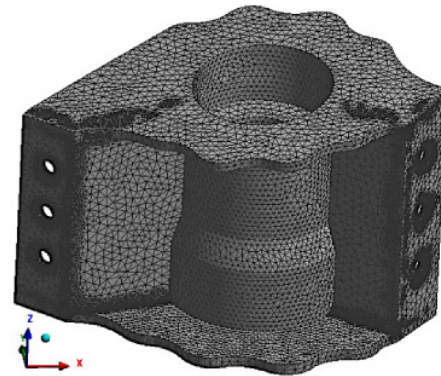
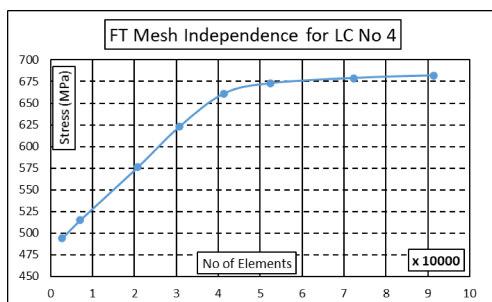
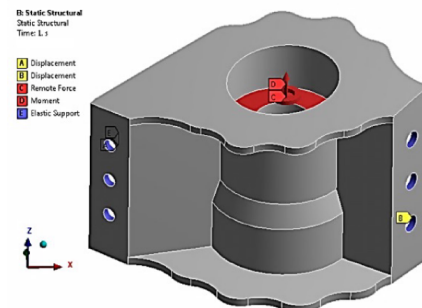
LC	N_Z	F_X	F_Y	F_Z	M_X	M_Y	M_Z
1	5	1.2	-11	-33	0	0	1
2	5	-20	-4	1	2	-78	-3
3	4.5	3.8	-12	-29	-1	40	2
4	4.5	28	4	-37	1	35	1
5	2	-14.8	-9	-11	2	-82	-2
6	2	16.8	-5	-20	-1	-49	1
7	4.5	2.96	-10	-30	0	21	1
8	4.5	30	10	-37	1	37	1
9	2.74	-10	-5	-17	2	-121	-3
10	2.74	14	3	-24	0	11	1
11	2	-16	-6	-10	2	-112	-3
12	2	11	-6	-5	0	-31	1
13	-1	1.4	2	6	0	31	1

Table 4. Load Cases (LC) for the Rear Tulip (RT) (force in kN and moments in kN.m) [1]

LC	N_Z	F_X	F_Y	F_Z	M_X	M_Y	M_Z
14	1	4	2	0	-1	-2	24
15	5	6	7	0	-2	-8	-9
16	5	2	6	2	-3	-7	13
17	2	1	3	1	-1	-4	-13
18	5	6	7	0	-2	-8	-10
19	1	-1	1	1	0	-1	2
20	4.5	-4	7	2	0	-6	-28
21	4.5	-3	3	11	0	0	24
22	2.17	15	6	-5	1	-5	6
23	2.17	-40	6	3	0	0	73

3.3. Analysis of the Front Tulip (FT)

The model has been free-meshed using Tet6 elements, which are tetrahedral-shaped elements with three nodes and a quadratic shape function. To ensure accuracy, the mesh is refined at stress hot spots located at bolt holes. As illustrated in Figure 6, a mesh independence study establishes that the solution becomes independent of mesh refinement at 70,000 elements. Figure 7 displays the meshed model of the Front Tulip (FT), while Figure 8 illustrates the applied boundary conditions and loads on the FT.

**Figure 7.** Free Mesh of the FT [9]**Figure 6.** Grid Independence of the FT**Figure 8.** Loads and Boundary Conditions on the FT

For each load case, deformation and stress plots are generated in ANSYS. The comparison of maximum equivalent (von Mises) stress for each load case on the Front Tulip (FT) is illustrated in Figure 9. Load Case No. 4 is identified as the critical load case for the FT, with a stress value of 674 MPa. The deformation field of the Front Tulip under critical Load Case No 4 is depicted in Figure 10. A maximum deformation of 0.13 mm is observed on the flange of the FT.

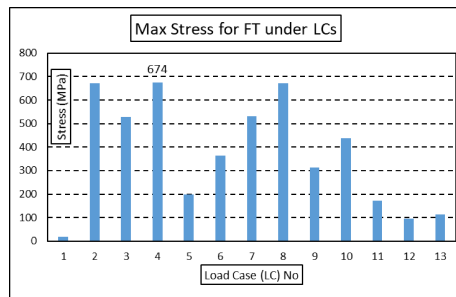


Figure 9. Max Stress for the FT under all LCs

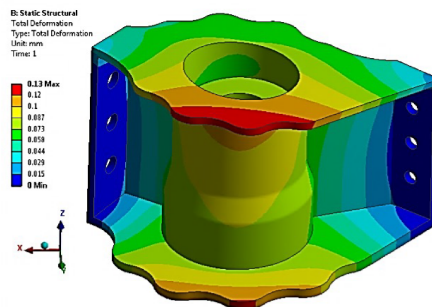


Figure 10. Deformation of the FT under LC No 4

Further insight into the structural response, namely the resultant stress field and Factor of Safety (FOS), is provided in Figure 11 and Figure 12, respectively. The FOS of the Front Tulip (FT) is 1.23 under critical Load Case No. 4, indicating that the FT is safe within the carriage envelop. These analyses contribute to a comprehensive understanding of the structural behaviour, assessing safety margins and identifying potential areas for design optimization.

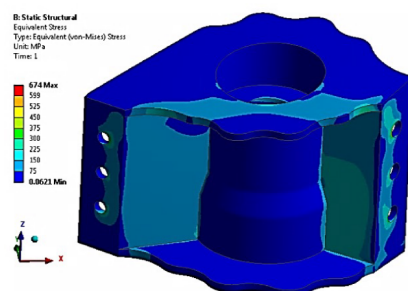


Figure 11. Equivalent Stress of the FT under LC No 4

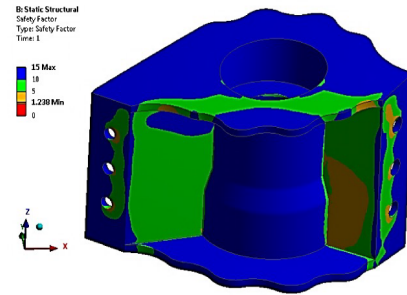


Figure 12. FOS of the FT under LC No 4

3.4. Analysis of the Rear Tulip (RT)

The free meshing of the rear tulip model has been conducted using Tet6 elements, which are tetrahedral-shaped elements with three nodes and a quadratic shape function. Mesh refinement at bolt holes is implemented to capture the large stress gradient at these hot spots. A mesh independence study, as illustrated Figure 13, demonstrated that the solution became independent of mesh refinement at 130,000 elements. Figure 14 illustrates the meshed model of the Rear Tulip (RT). Figure 15 illustrates the boundary conditions and applied loads, represented as forces and moments.

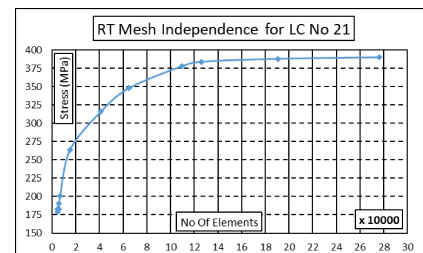


Figure 13. Mesh Independence for the RT

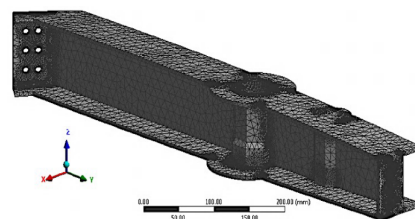


Figure 14. Free Mesh for the RT

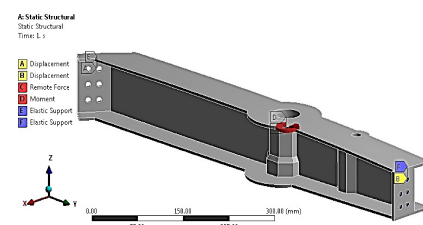


Figure 15. Boundary Condition and Loads for the RT

Through Finite Element (FE) analysis, deformation and stress for each load case were determined. The comparison of maximum equivalent (von Mises) stress for each load case on the Rear Tulip (RT) is presented in Figure 16. The critical load case for RT is identified as Load Case No 21, exhibiting a stress value of 323 MPa. Figure 17 illustrates the deformation field of the Rear Tulip under Load Case No. 21. A maximum deformation of 0.83 mm is observed under this critical LC.

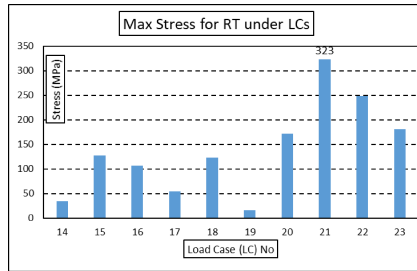


Figure 16. Max Stress for all LCs on the RT

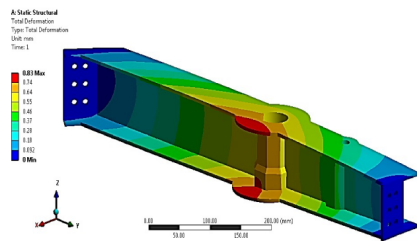


Figure 17. Deformation of RT under LC No 21

Additional insights into resultant stress field and Factor of Safety (FOS) under this specific load case is provided in Figure 18 and Figure 19. FOS of RT is 1.3 under the critical LC NO 21 which indicates that RT is safe within the carriage envelop. These comprehensive analyses contribute to a detailed understanding of the structural behaviour, aiding in assessment of safety margins and potential areas for design optimization of Rear Tulip.

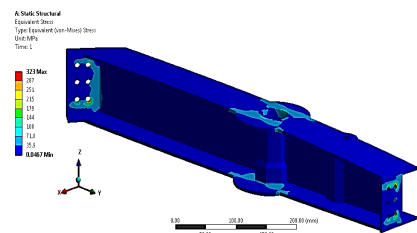


Figure 18. Equivalent Stress of the RT under LC No 21

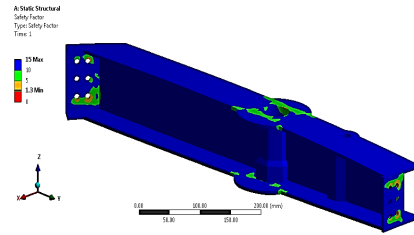


Figure 19. FOS of the RT for under LC No 21

3.5. Modal and Prestressed Modal Analysis

Modal analysis of the Front and Rear Tulips of the wing station has been conducted to explore the dynamic characteristics of free vibrations without external forces [20]. This analysis used free mesh models of the Front and Rear Tulips within the ANSYS Modal Module. The fundamental mode shapes for the Front and Rear Tulips are depicted in Figure 20 and Figure 21, respectively. The fundamental mode frequencies for the Front Tulip (FT) and Rear Tulip (RT) are 286 Hz and 282 Hz, respectively.

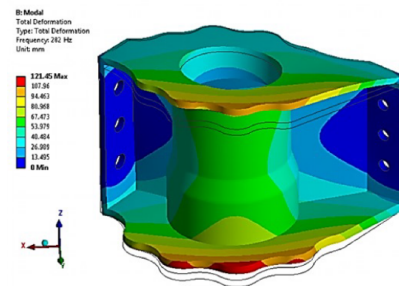


Figure 20. Fundamental Mode Shape for Free Mesh

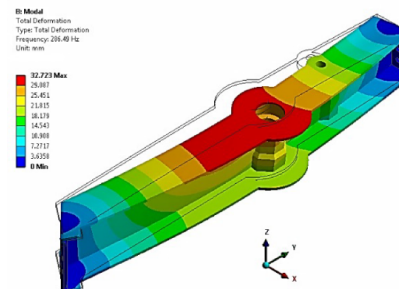


Figure 21. Fundamental Mode Shape of the RT

Additionally, a prestressed modal analysis has been conducted to assess stress-stiffening effects. A comparison between free and prestressed modal frequencies for the Front and Rear Tulips is presented in Figure 22 and Figure 23, respectively. The prestressed modal analysis reveals a minimal decrease in modal frequencies for the Front Tulip (FT). For the Rear Tulip (RT), there is no decrease in modal frequency under applied

stress. Therefore, the stress-stiffening effect for the FT and RT Tulips is insignificant.

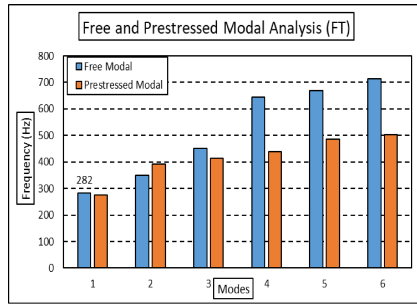


Figure 22. Free and Prestressed Modal Analysis of the FT

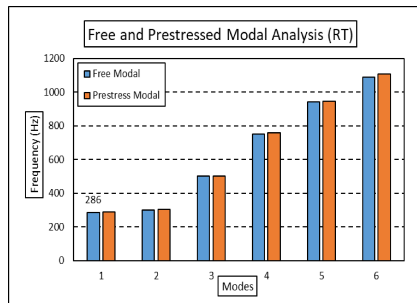


Figure 23. Free and Prestressed Modal Analysis of RT

A comparative analysis offers insights into how prestressed conditions affect the modal behaviour of tulips, shedding light on the structural response under the influence of pre-existing stresses. These findings enhance the comprehensive understanding of the dynamic characteristics of the Front and Rear Tulips.

3.6. Buckling Analysis

Buckling analyses of the Front and Rear Tulips have been conducted to ascertain buckling loads and corresponding buckling mode shapes [21]. The results of these analyses are depicted in Figure 24 and Figure 25, showcasing the first buckling mode for the Front and Rear Tulips, respectively, under their critical load cases.

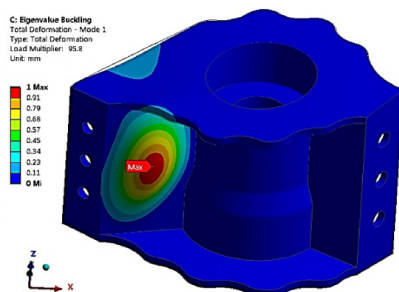


Figure 24. 1st Buckling Mode of the FT

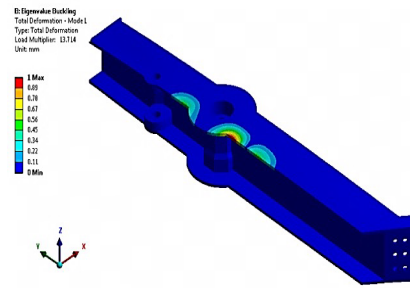


Figure 25. 1st Buckling Mode of RT

The buckling load multipliers for the front and rear tulips are determined to be 95 and 13, respectively, under critical load cases. These high load multipliers suggest buckling is not a likely failure mode for the wing tulips. The mode shapes provide crucial insights into the structural stability of the tulips under specific loading conditions, enhancing the identification of potential failure modes and the determination of safety margins for the wing station components.

3.7. Optimization

The current radius for all bolt holes of the tulips are 4 mm. This study reveals that the maximum stress under a critical load case occurs at the bolt holes. To conduct a stress sensitivity analysis, the diameter of the bolt holes varies from 6 to 10 mm using the ANSYS Optimization Module [22]. Figure 26 and Figure 27 display the stress response surfaces as a function of bolt-hole radii for the Front Tulip and Rear Tulip, respectively. These surfaces visually demonstrate how changes in bolt-hole radii influence the tulips' maximum stress.

Figure 26 indicates that the radii of bolts on the inboard side (P2) have no discernible impact on the maximum stress value of the Front tulip (P3). Conversely, the radii of bolts on the outboard side (P1) significantly influence the maximum stress value of the Front tulip. Initially, increasing the radii of bolt holes on the outboard side from 3 mm results in an increase in the maximum stress value (P3) up to 3.5 mm; beyond this point, further increases lead to a decrease in the maximum stress value.

Figure 27 demonstrates that the radii of bolt holes on both the front (P1) and rear (P2) sides of the Rear Tulip significantly impact the maximum stress value (P3). Initially, as the values of P1 and P2 increase from 3 mm, the maximum stress value decreases, reaching a minimum of 4.5 mm. However, further increases in the radii of the bolt holes increase the maximum stress value.

This sensitivity analysis reveals that the minimum stress for the Front Tulip occurs with a bolt-hole radius of 5 mm, while for the Rear Tulip, a radius of 4.5 mm is optimal. These design parameters reduce the maximum stress to 627 MPa and 286 MPa for the Front

and Rear Tulips, respectively. The larger bolt holes contribute to an increased Factor of Safety (FOS) of 1.33. Consequently, the maximum load-carrying capacity of the wing station increases from 653 kg to 706 kg with this optimized design. This sensitivity analysis is crucial for optimizing the design of bolted connections in tulips, helping to identify the most suitable diameter that minimizes stress concentrations and enhances the overall structural performance of the Front and Rear Tulips.

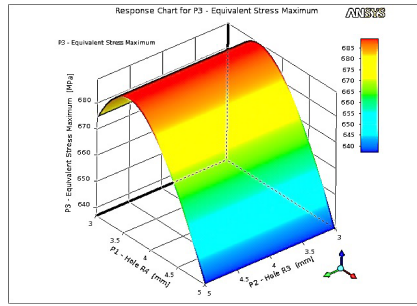


Figure 26. Response Surface for Max Stress FT

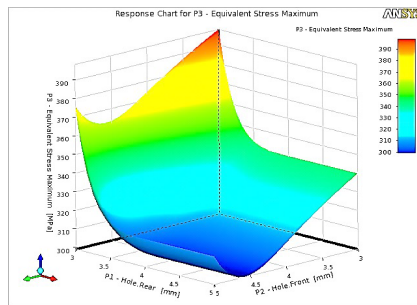


Figure 27. Response Surface for Max Stress RT

4. Conclusions

This study addresses a significant gap in the state-of-the-art application of similar research problems by focusing on the influence of stiffness characteristics on the maximum load-carrying capacity of a fighter aircraft's wing. Although previous studies have explored various factors affecting the structural integrity of aircraft components, few have delved into the role of wing stiffness and its direct impact on load-carrying capacity. This research integrates wing stiffness into the Finite Element (FE) model of isolated tulips, providing an analysis that accurately predicts the structural integrity of the weapon station. Additionally, using sub-modelling as a versatile and computationally efficient technique introduces an innovative methodology, bridging a gap in the existing literature by showcasing its applicability to intricate structural components with minimal computational expense.

Validation of the initial hypothesis through obtained data underscores the significance of wing stiffness in assessing the wing station's maximum load-carrying capacity. Overall, this research enhances the understanding of structural analysis in aerospace engineering by providing novel insights and methodologies to address a critical gap in the field. The key findings of this research are outlined as follows:

Front Tulip:

- Optimal bolt-hole radius: 5 mm
- Reduced maximum stress: 627 MPa

Rear Tulip:

- Optimal bolt-hole radius: 4.5 mm
- Reduced maximum stress: 286 MPa

Factor of Safety (FOS):

- Increased to 1.33 with larger bolt holes

Maximum Load-Carrying Capacity:

- Increased from 653 kg to 706 kg with the optimized design

Identifies critical design parameters for optimizing bolted connections in tulips, helping to determine the most suitable diameter that minimizes stress concentrations and enhances the overall structural performance of both the Front and Rear Tulips.

A notable limitation of this research is the exclusion of fasteners from the analysis, predicated on the assumption of perfect load transfer between the structural elements of the wing and the wing tulips. Consequently, this study does not account for the potential failure modes associated with fasteners.

Future research endeavours should explore the following aspects to enhance the comprehensiveness of structural analyses. Addressing these aspects would significantly contribute to the structural assessments of large assemblies.

Non-linear Effects:

- Implications of non-linear effects on structural integrity.

Mesh Patterns:

- Effects of regular mesh patterns on simulation results.

Cyclic Loading / Power Spectral Density (PSD) Analysis:

- Cyclic loading and PSD analysis to evaluate long-term structural performance.

Author Contributions

The entirety of this research, including literature review, methodology, results and findings represents work of Author.

Acknowledgments

The author acknowledges the support of his department at Air University for providing all the necessary resources for this publication.

Conflict of Interest

The author declared no potential conflicts of interest concerning research, authorship, and publication of this article.

Funding

The author received no financial support for research, authorship, and publication of this article.

Data Availability Statements

The current study is available from the corresponding author upon reasonable request.

References

- [1] K. Sinha, T. Klimmek, M. Schulze, and V. Handoyo, "Loads analysis and structural optimization of a high aspect ratio, composite wing aircraft," *CEAS Aeronautical Journal*, vol. 12, no. 2, pp. 233–243, Apr 2021. [Online]. Available: <https://doi.org/10.1007/s13272-021-00494-x>
- [2] B. D. Upadhyay, S. S. Sonigra, and S. D. Daxini, "Numerical analysis perspective in structural shape optimization: A review post 2000," *Advances in Engineering Software*, vol. 155, p. 102992, 2021. [Online]. Available: <https://doi.org/10.1016/j.advengsoft.2021.102992>
- [3] N. Zimmermann and P. H. Wang, "A review of failure modes and fracture analysis of aircraft composite materials," *Engineering Failure Analysis*, vol. 115, p. 104692, 2020. [Online]. Available: <https://doi.org/10.1016/j.engfailanal.2020.104692>
- [4] R. L. Muhanna and S. Shahi, *Uncertainty in Boundary Conditions—An Interval Finite Element Approach*. Cham: Springer International Publishing, 2020, pp. 157–167. [Online]. Available: https://doi.org/10.1007/978-3-030-40814-5_20
- [5] T. Martins, V. Infante, L. Sousa, A. Fonseca, P. Antunes, A. Moura, and B. Serrano, "Numerical and experimental study of aircraft structural health," *International Journal of Fatigue*, vol. 132, p. 105348, 2020. [Online]. Available: <https://doi.org/10.1016/j.ijfatigue.2019.105348>
- [6] J. Lim, C. You, and I. Dayyani, "Multi-objective topology optimization and structural analysis of periodic spaceframe structures," *Materials & Design*, vol. 190, p. 108552, 2020. [Online]. Available: <https://doi.org/10.1016/j.matdes.2020.108552>
- [7] C. Touzé, A. Vizzaccaro, and O. Thomas, "Model order reduction methods for geometrically nonlinear structures: a review of nonlinear techniques," *Nonlinear Dynamics*, vol. 105, no. 2, pp. 1141–1190, Jul 2021. [Online]. Available: <https://doi.org/10.1007/s11071-021-06693-9>
- [8] C. You, M. Yasaee, S. He, D. Yang, Y. Xu, I. Dayyani, H. Ghasemnejad, S. Guo, P. Webb, J. Jennings, and G. Federico, "Identification of the key design inputs for the FEM-based preliminary sizing and mass estimation of a civil aircraft wing box structure," *Aerospace Science and Technology*, vol. 121, p. 107284, 2022. [Online]. Available: <https://doi.org/10.1016/j.ast.2021.107284>
- [9] A. Haider Bhutta, "Appropriate boundary condition for finite element analysis of structural members isolated from global model," *NED University Journal of Research*, vol. 18, no. 3, pp. 61–75, 2021. [Online]. Available: <https://doi.org/10.35453/NEDJR-STMECH-2021-0001>
- [10] E. Narvydas, N. Puodziuniene, and T. A. Khan, "Application of finite element sub-modeling techniques in structural mechanics," *Mechanika*, vol. 27, no. 6, pp. 459–464, 2021. [Online]. Available: <https://doi.org/10.5755/j02.mech.25962>
- [11] J. Jang and S. Ahn, "Fe modeling methodology for load analysis and preliminary sizing of aircraft wing structure," *International Journal of Aviation, Aeronautics, and Aerospace*, vol. 6, no. 2, 2019. [Online]. Available: <https://doi.org/10.15394/ijaaa.2019.1301>
- [12] A. Mishra, S. Pal, G. Singh Malhi, and P. Singh, "Structural analysis of UAV airframe by using FEM techniques: A review," *International Journal of Advanced Science and Technology*, vol. 29, pp. 195–204, 06 2020. [Online]. Available: <https://is.gd/4NRfx9>
- [13] S. Henclik and A. Maurin, "Determination of the stiffness matrix of flat springs for modeling of the boundary condition at a pipeline support," *Mechanical Systems and Signal Processing*, vol.

- 123, pp. 102–116, 2019. [Online]. Available: <https://doi.org/10.1016/j.ymssp.2018.12.047>
- [14] M. d. C. Alves, F. N. Corrêa, J. R. M. de Sousa, and B. P. Jacob, “A coupled, global/local finite element methodology to evaluate the fatigue life of flexible risers attached to floating platforms for deepwater offshore oil production,” *Mathematics*, vol. 12, no. 8, 2024. [Online]. Available: <https://doi.org/10.3390/math12081231>
- [15] V. Karnozov, “China’s fighter aircraft detailed,” *Defence Review Asia*, vol. 13, no. 1, pp. 42–47, 2019. [Online]. Available: <https://is.gd/dM2DHD>
- [16] A. G. Manca and C. M. Pappalardo, “Topology optimization procedure of aircraft mechanical components based on computer-aided design, multibody dynamics, and finite element analysis,” in *Advances in Design, Simulation and Manufacturing III*, V. Ivanov, I. Pavlenko, O. Liaposhchenko, J. Machado, and M. Edl, Eds. Cham: Springer International Publishing, 2020, pp. 159–168. [Online]. Available: https://doi.org/10.1007/978-3-030-50491-5_16
- [17] A. Aabid, M. A. M. B. M. Zakuan, S. A. Khan, and Y. E. Ibrahim, “Structural analysis of three-dimensional wings using finite element method,” *Aerospace Systems*, vol. 5, no. 1, pp. 47–63, Mar 2022. [Online]. Available: <https://doi.org/10.1007/s42401-021-00114-w>
- [18] P. Wang, Y. Chen, R. Pei, C. Lian, K. Zhang, and Y. Zhou, “Buckling and post-buckling analysis of composite wing box under loads with torsion-bending coupling,” *Thin-Walled Structures*, vol. 193, p. 111266, 2023. [Online]. Available: <https://doi.org/10.1016/j.tws.2023.111266>
- [19] N. Yang, “Methodology of aircraft structural design optimisation,” *International Journal of Computer Applications in Technology (IJCAT)*, vol. 70, no. 3, pp. 145–154, 2022. [Online]. Available: <https://dx.doi.org/10.1504/IJCAT.2022.130874>
- [20] A. Basutkar, K. Baruah, and S. K. Kudari, “Frequency analysis of aircraft wing using FEM,” in *Recent Trends in Mechanical Engineering*, G. S. V. L. Narasimham, A. V. Babu, S. S. Reddy, and R. Dhanasekaran, Eds. Singapore: Springer Singapore, 2020, pp. 527–533. [Online]. Available: https://doi.org/10.1007/978-981-15-1124-0_46
- [21] B. Ravi Kumar, “Investigation on buckling response of the aircraft’s wing using finite-element method,” *Australian Journal of Mechanical Engineering*, vol. 18, no. sup1, pp. S122–S131, 2020. [Online]. Available: <https://doi.org/10.2514/1.C034818>
- [22] S. De, M. Jrad, and R. K. Kapania, “Structural optimization of internal structure of aircraft wings with curvilinear spars and ribs,” *Journal of Aircraft*, vol. 56, no. 2, pp. 707–718, 2019. [Online]. Available: <https://doi.org/10.2514/1.C034818>



STORYTELLING UTILIZING GENERATIVE AI TO FOSTER INCLUSION OF INDIVIDUALS WITH DISABILITIES

CUENTACUENTOS BASADO EN IA GENERATIVA PARA PROMOVER LA INCLUSIÓN DE PERSONAS CON DISCAPACIDADES

Keren Mitsue Ramírez Vergara^{1,*} , Asdrúbal López-Chau¹ ,
 Rafael Rojas Hernández¹

Received: 27-03-2024, Received after review: 05-06-2024, Accepted: 18-06-2024, Published: 01-07-2024

Abstract

This article presents the comprehensive design and evaluation of a digital storytelling system tailored for Latin American children aged 4 to 6, leveraging generative artificial intelligence. Tests were conducted to assess the system's functionality, content diversity, generation times, and voice quality, including intonation, speed, and pronunciation. The results substantiate the system's operational efficacy and user-friendly interface. The stories generated demonstrate substantial diversity, as indicated by Jaccard indices calculations, which reveal a maximum value of 0.2 derived from evaluating 30 distinct stories. As expected, there was a proportional increase in story generation times relative to their length. 'Onyx' from OpenAI's text-to-speech (TTS) was identified as the most appropriate voice for storytelling. Nonetheless, pronunciation inaccuracies were observed across all tested TTS model voices. The analysis demonstrated that the system generates a variety of stories that foster value formation in Spanish-speaking children, thereby promoting the importance of including individuals with disabilities. Notably, all content within the stories was found to be suitable for children, with no inappropriate material detected in any of the narratives.

Keywords: ChatGPT, Storytelling, Disability, AI Generative, Inclusion

Resumen

En este artículo se presenta el diseño completo y la evaluación de un sistema cuentacuentos digital destinado a niños de entre 4 y 6 años en Latinoamérica. Este sistema está basado en inteligencia artificial generativa. Se realizaron pruebas que abarcaron el funcionamiento del sistema, la diversidad de contenidos, los tiempos de generación, la evaluación de voz, entonación, velocidad y calidad de pronunciación. Los resultados confirman que el sistema funciona correctamente y es intuitivo. Las historias generadas muestran un alto grado de diversidad, ya que al calcular los índices de Jaccard, el valor máximo encontrado fue de 0,2 en las evaluaciones de treinta cuentos analizados. Como era de esperarse, los tiempos de generación aumentan conforme se incrementa la longitud de los cuentos. Se identificó que la voz que mejor se adapta para contar los cuentos es Onyx de la TTS de OpenAI. Sin embargo, se observaron errores de pronunciación en todas las voces del modelo TTS. De acuerdo con el análisis realizado, el sistema crea historias diferentes, que promueven valores en los niños de habla hispana, fomentando la importancia de la inclusión de personas con discapacidad. Cabe destacar que en ningún cuento se encontró contenido no apto para niños.

Palabras clave: ChatGPT, cuenta cuentos, discapacidad, IA generativa, inclusión

^{1,*}Centro Universitario UAEM ZUMPANGO, Universidad Autónoma del Estado de México. Zumpango, Estado de México. México. Autor para correspondencia ✉: kramirezv003@alumno.uaemex.mx.

Suggested citation: Ramírez Vergara, K. M.; López-Chau, A. and Rojas Hernández, R. "Storytelling Utilizing Generative AI to Foster Inclusion of Individuals with Disabilities," *Ingenius, Revista de Ciencia y Tecnología*, N.º 32, pp. 101-113, 2024, DOI: <https://doi.org/10.17163/ings.n32.2024.10>.

1. Introduction

Generative Artificial Intelligence (GAI) constitutes a notable breakthrough in artificial intelligence (AI), offering the capability to generate diverse content types, including texts, images, source code for various programming languages, scenario designs, legal arguments, and high-definition videos.

Large Language Models (LLMs) facilitate the automated generation of text, crafting original documents by leveraging extensive textual data harvested from the Internet. This generation is enabled through contemporary reinforcement learning architectures incorporating human feedback and deep learning technologies [1], specifically transformers.

ChatGPT has become a potent tool across multiple domains, including education, marketing, finance, and customer service. In the educational sector, the deployment of generative text-based AI has witnessed a significant global increase in the digital era [2]. This technology assists in elucidating concepts through simplified explanations, facilitates problem-solving by demonstrating diverse methodologies, and aids in developing reading and comprehension skills among early-year students, among other applications.

This innovative technology propels the shift toward an educational paradigm that is more immersive, dynamic, participatory, and inclusive, underscoring the pivotal roles of teachers and students as agents of change [3]. Integrating systems like ChatGPT into educational frameworks is poised to augment human capabilities, contribute to reducing inequalities, and foster the promotion of core values.

One effective method to cultivate these values is through storytelling to children. This approach not only aids in comprehending the world but also stimulates the imagination and facilitates conflict resolution. Storytelling can convey significant messages, expand horizons, and encourage active engagement with the environment. Furthermore, it enhances communication, debate, and interpretation skills essential for holistic development [4].

As an educational tool, storytelling significantly enhances teaching and learning by making knowledge acquisition engaging and enjoyable. Storytelling facilitates reflection and moral consideration and is crucial in stimulating children's cognitive and intellectual development from an early age [4].

Therefore, enriching the storytelling experience with human values early in a child's life is vital. Accordingly, the system proposed in this article is designed for children aged 4 to 6 years, a critical period during which children start to become acquainted with written text.

The system's emphasis on inclusive education aligns with the increasing importance attributed in recent decades to eliminating discrimination against

vulnerable groups. This initiative aims to mitigate such issues, particularly in Mexico, where inclusive educational practices are limited.

According to 2019 OECD reports, Mexico ranks among the countries with the lowest levels of educational inclusion, with only 2.85% of students with disabilities receiving education, despite approximately 15% of the student population having some form of disability [5]. Furthermore, the World Bank noted in 2021 that although there are approximately 85 million people with disabilities in Latin America and the Caribbean [6], progress in enhancing this demographic's employment, education, and healthcare programs has been minimal.

This article outlines the design and implementation of a system that leverages generative artificial intelligence, specifically ChatGPT, among other technologies, for the automatic generation of stories targeted at Spanish-speaking children. The system is driven by two primary objectives: a) to instill values such as respect, tolerance, and empathy towards individuals with disabilities through storytelling, and b) to enhance reading and comprehension skills among Spanish-speaking children.

The principal contributions of this article are summarized as follows:

1. It proposes a novel approach to address the challenge of enhancing the inclusion of people with disabilities in Latin America, utilizing a cutting-edge technological solution.
2. It details the comprehensive design of a generative artificial intelligence (GAI)-based software system specifically tailored to create and narrate stories for Spanish-speaking children.
3. It illustrates the development of a specifically crafted prompt that generates diverse stories, which cultivate values of empathy and respect towards individuals with disabilities.
4. It assesses the system's performance in terms of the stories' diversity and the intonation, speed, and pronunciation quality of the storytelling narratives.
5. It makes the complete source code of the system and supplementary files available for non-commercial use through a GitHub repository. [7].

1.1. Literature Review

A comprehensive literature review was conducted using the IEEE Explore, Science Direct, and Scopus electronic databases. Searches were carried out in both English and Spanish. The inclusion criteria were restricted to journal articles, books, and conference papers published between 2021 and 2024. This specific

date range was chosen because generative text artificial intelligence became globally accessible starting in 2021. 91 documents were collected through the review process, comprising 85 articles, 5 books, and 1 manual.

The searches were conducted using the following keywords and logical operators:

- "*inclusiveness AND AI AND education*",
- "*disability AND AI AND education*",
- "*storytelling AND inclusiveness AND education*",
- "*apps AND inclusiveness AND AI*"

The analysis of sources retrieved from well-established databases indicated that Scopus contributed 18 documents, ACM Digital Library 4, ScienceDirect 47, and IEEE Explore 4 documents. Articles not directly relevant to the current study were excluded, resulting in a focused selection of 23 pertinent articles.

The state-of-the-art review centered on four core categories delineated as the primary research objectives:

- The role of digital storytelling in child development.
- The utilization of artificial intelligence in enhancing creativity.
- The impact of digital storytelling on child development.
- The potential of digital storytelling to promote inclusive education.

1.1.1. Digital Storytelling in Child Development

The significant influence of digital storytelling on child development has been extensively documented by various scholars. Bratitsis *et al.* define a story as a sequence of sentences that narrate events or experiences, typically involving central characters [8].

Through storytelling, themes such as compassion, solidarity, and empathy are prominently featured and explored. Additionally, Juppi observes that a digital story typically integrates elements such as text, music, sound effects, or the author's own recorded voice and recommends that the duration of a digital story should ideally range between 2 and 4 minutes [9]. Juppi further elucidates that digital narratives are often designed to empower individuals by fostering personal growth, enhancing control over their lives, and enabling them to act as informed citizens. This empowerment is facilitated through developing technical and creative skills in expression and communication, which are hallmark

features of digital narratives. Juppi also advocates for educational institutions across various academic levels to leverage digital storytelling to promote inclusive education, empathy, respect, civic engagement, and democratic participation.

The impact of digital storytelling on children has been extensively explored in prior research. Bratitsis and Ziannas investigated the development of social empathy in children over 6 years old through interactive digital storytelling, utilizing the tale "The Sad Little Chick" created in the Scratch programming environment [8]. The study engaged 25 sixth-grade early childhood education students who read the story and engaged in interactive activities designed to elicit their emotional responses. The outcomes were encouraging, demonstrating heightened interest and sensitivity towards the main character and an enhanced understanding of empathy and its practical application in daily situations. This research underscores how digital stories can effectively foster children's comprehension of inclusive values and empathy.

Conversely, Tseng *et al.* developed PlushPal, which utilizes machine-learning techniques to transform plush toys into interactive digital objects. PlushPal enables children to digitalize their stuffed animals, allowing them to recognize gestures and produce personalized sounds [10]. Furthermore, it integrates storytelling techniques to animate the toys, imbuing them with capabilities that foster connections with positive memories and previous experiences.

1.1.2. The utilization of artificial intelligence in enhancing creativity

Creativity is commonly defined as the capacity to generate novel, unique, and valuable ideas or artifacts [11]. This capacity is augmented by GAI systems. For instance, Haase and Hanel suggest that chatbots, equipped with expansive databases, can recombine ideas to produce outputs that exhibit levels comparable to everyday human creativity [11].

Li views AI as an invaluable resource for human writers, facilitating the enhancement and expansion of increasingly complex ideas, thereby fostering a divergent thought process [12]. He anticipates a future where AI and human collaboration will be dynamic, interactive, and participatory. Conversely, Habib *et al.* assess the creativity of GAI systems within educational settings by examining the flexibility, elaboration, and originality of responses via user acceptance tests [1].

Their findings emphasize [13] improvements in divergent thinking and the introduction of varied perspectives. The research underscores the importance of carefully integrating GAI into creative education to promote a symbiotic relationship between human creativity and AI. Additionally, Li supports the notion that the ethical application of ChatGPT could enhance

inclusivity and diversity in educational contexts [12].

1.1.3. Artificial Intelligence in Child Development

In a notable study, Kalantari *et al.* [14] explored the effects of AI on early childhood education. This investigation utilized a qualitative exploratory approach involving children aged 6 to 7 years and their parents to assess a software application named "Kids Story Builder." The findings from this study indicated that the technology not only enhances children's understanding of and connection with themselves and their families but also promotes narrative thinking during the story creation process.

Jiahong and Yang [15] conducted an exploratory review that assesses, synthesizes, and highlights recent literature on the application of AI in early childhood education. However, their study touches only superficially on the specific uses of AI within these contexts.

1.1.4. Artificial Intelligence to Promote Inclusive Education

Artificial intelligence (AI) technologies and emerging technological tools significantly influence society and are progressively being incorporated into educational settings [16].

Consequently, numerous scholars advocate for appropriately integrating these tools within educational frameworks. While the literature reviewed does not reveal specific implementations of Generative AI (GAI) in inclusive education, it does offer guidance, advice, and recommendations designed to ensure a beneficial impact. These technologies can transform education by altering students' experiences within and beyond the classroom [16].

Yu [17] underscores that the core educational value of ChatGPT resides in its ability to facilitate access to knowledge, create content, and promote educational inclusion. He also emphasizes that ethical management, transparency, and accountability represent significant challenges AI introduces in educational contexts. ChatGPT should augment human capabilities and contribute ethically, steering towards a more immersive, dynamic, participatory, and inclusive educational experience.

Li and Lan [18] concur with Salas-Pilco *et al.* [16] and offer a framework for adequately adopting technology, underscoring the importance of promoting social inclusion.

2. Materials and Methods

The GAI-based system designed to generate stories that promote the inclusion of individuals with disabilities was developed using the Kanban methodology.

This approach enhanced continuous task delivery by allowing for the visualization of progress across various sections and tracking pending tasks. The choice of this methodology was informed by its emphasis on continuous delivery, whereby team members work on tasks as they arise without rigidly assigned roles. Any team member could assume new tasks from the list as required. Moreover, a suite of modern technologies was employed to ensure the system's robustness and operational efficiency.

TypeScript was selected as the programming language for its capability to develop robust web applications. It compiles code into JavaScript, enabling it to run across any browser, platform, or operating system [19]. Beyond its technical capabilities, TypeScript is an open-source language that enhances JavaScript syntax, ensuring compatibility with various browsers, servers, and operating systems. The decision to use TypeScript was also supported by its seamless integration with Angular and other libraries, which aids in the development and scalability of the application [20].

Complementing TypeScript, the Angular framework generated the system's user interfaces. Angular is renowned for its efficient Document Object Model (DOM) management and its capability to create scalable web applications in conjunction with TypeScript. Furthermore, Angular is acclaimed for its user-friendly learning curve and capacity to boost development productivity, making it an optimal choice for this project.

ChatGPT was integrated into the application to facilitate the story generation functionality. Its creative collaborator role derives from its capability to ideate dramatic content, develop characters, and craft storylines. ChatGPT has been effectively utilized in interactive storytelling and gaming, enabling users to create dynamic and personalized narrative experiences where the plot adjusts to users' preferences and experiences. Additionally, it can enhance stories or poems with a diverse array of realistic words, emotions, and characters [21]. These attributes render ChatGPT particularly valuable and attractive for generating inclusive content for individuals with disabilities.

The implementation of the application was structured into three distinct phases: developing user interfaces, generating prompts for the model, and integrating the OpenAI API. The overall architecture of the developed system is graphically summarized in Figure 1.

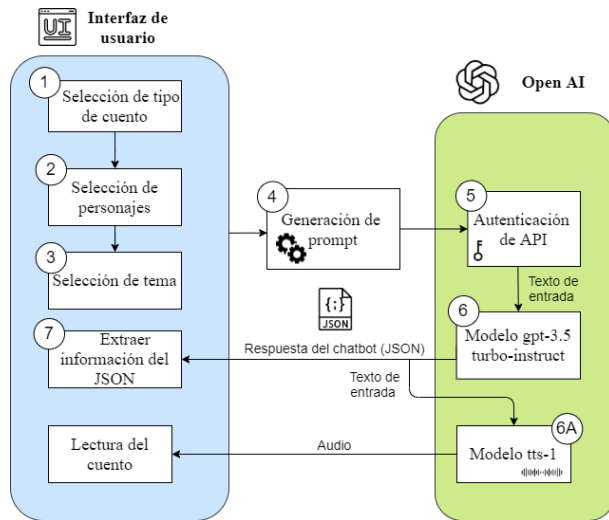


Figure 1. System Architecture

2.1. Prompt Structure Design

Large Language Models (LLM) are trained with an extensive corpus of information, far exceeding what an average individual could read in a lifetime. This vast dataset enables LLM to generate text on virtually any topic requested. However, precise instructions are crucial in the creative process [22], as the quality of ChatGPT's responses heavily depends on the specificity of the prompts provided. Thus, it is incumbent upon users to meticulously craft prompts that elicit valuable content.

During the initial phase of system development, the significance of establishing a general prompt structure to guide the system in generating coherent, relevant, precise, and appropriate results for Spanish-speaking children was recognized. To achieve this, three fundamental elements of this structure were identified, which users can customize to facilitate effective story generation. These elements are as follows:

1. *Type of Story*. This refers to the length of the story, measured by the number of words it contains. According to the classification detailed in [23], children's stories can be categorized into

three types: micro-story, flash story, and short story, consisting of approximately 300, 750, and 2000 words, respectively.

2. *Characters*. This component of the prompt structure encompasses the physical and personality traits of each character in the stories. Initially, these characters were suggested by ChatGPT; subsequently, those aligning with the system's goal of instilling values such as respect, tolerance, and empathy towards people with disabilities in children were selected. Considering the story lengths, it was determined that each story could include up to three characters.
3. *Theme*. This element pertains to the context or overarching theme in which the story unfolds. The selected themes focus on reinforcing ethical and inclusive values, such as respect, tolerance, and environmental stewardship. Given that the system is tailored for children and that the themes can vary with each story generation request, a decision was made to incorporate a maximum of four themes.

In block ④ of Figure 1, the prompt is generated based on parameters the user selects, which directs the model to produce precise and child-appropriate results. The established structure specifies ChatGPT's role in generating the stories and detailed instructions on the format for the returned response. This structure is illustrated in Figure 2.

In this figure, placeholders within braces, such as `{tipo_de_cuento}`, `{numero_de_palabras}`, etc., are substituted with specific values selected by the user (child), corresponding to blocks ①, ② and ③ in the architecture depicted in Figure 1. Furthermore, the characteristics of the stories were defined to achieve the anticipated outcomes. The observations were as follows:

1. *Storyteller Definition*. The model is a storyteller promoting values in individuals with disabilities.
2. *Response Format*. The response must be in JSON format, and its structure must be explicitly defined..

Eres un cuentacuentos creativo que inculca valores en sus cuentos para niños de latinoamérica, los cuentos son divertidos e interesantes, y a veces misteriosos.

La respuesta debe ser en formato JSON con la siguiente estructura:

```
{
  'titulo': string,
  'personajes': [nombre del personaje],
  'contenido': string
}
```

Crea un cuento de {tipo_de_cuento} con {número_de_palabras} palabras sobre el tema {tema_a_tratar}, en el que participen los siguientes personajes:

- {nombre_del_personaje_uno}, un {ocupación_del_personaje_uno} de nacionalidad {nacionalidad_del_personaje_uno} con las siguientes características físicas: {características_físicas_del_personaje_uno}.

La personalidad de {nombre_del_personaje_uno} es {personalidad_del_personaje_uno}.

- {nombre_del_personaje_dos}, un {ocupación_del_personaje_dos} de nacionalidad {nacionalidad_del_personaje_dos} con las siguientes características físicas: {características_físicas_del_personaje_dos}.

La personalidad de {nombre_del_personaje_dos} es {personalidad_del_personaje_dos}.

- {nombre_del_personaje_tres}, un {ocupación_del_personaje_tres} de nacionalidad {nacionalidad_del_personaje_tres} con las siguientes características físicas: {características_físicas_del_personaje_tres}.

La personalidad de {nombre_del_personaje_tres} es {personalidad_del_personaje_tres}.

Consideraciones para el cuento:

- El cuento debe ser original, por favor, esfuérzate en que no se repitan los cuentos.

- Si hay personajes con alguna discapacidad, asegúrate de que sean los protagonistas. Enfoca la atención en ellos para que la trama del cuento resalte el valor de {tema_a_tratar} hacia los personajes con discapacidad.

- Evita colocar en el cuento la descripción física y de personalidad de los personajes, solo menciona implícitamente cual es la discapacidad del personaje, si así la tuvieran.

- El contexto en el que se desarrollan los personajes debe ser ambientado en la nacionalidad del protagonista o los protagonistas, ya sean lugares turísticos, pueblos, costumbres, cultura, ideologías, economía, etc. Debes ser específico en el lugar en el que se encuentran, puedes mencionar nombre de los lugares.

- Puedes elegir el estilo narrativo entre monólogo, narración en segunda persona, narración epistolar, narración como testigo, narración omnisciente, etc. además de cambiar la atmósfera, el ambiente y el simbolismo; la idea es crear un cuento original, creativo y único o inédito que inculque valores a los niños.

- Es importante que los cuentos no sean repetidos en cada una de las iteraciones que se realicen, debe de cambiar el contexto, ambiente, el nombre del cuento, su trama y la forma de narración.

- Es importante que el cuento deje un mensaje o impacto sobre los valores. Este mensaje no debe ser explícito en el cuento, debe ser tratado con una intención didáctica (el niño debe ser capaz de comprender el mensaje o valores a lo largo del desarrollo del cuento).

Figure 2. Prompt for Story Generation

- 3 *Story Creation*. The system is programmed to craft a story utilizing the parameters enclosed in braces, which are to be replaced by values selected by the user.
- 4 *Story Considerations*. This section specifies that the story should be original and center on characters with disabilities who will serve as the protagonists. The narrative aims to portray these individuals' real-life challenges and conflicts and illustrate how they can overcome daily barriers and challenges by embodying values. To ensure the setting is realistic and authentic, it is required that the story's backdrop incorporates elements such as places, ideas, customs, or stories that are characteristic of the characters' nationality, with a specific focus on Latin American and Caribbean contexts.

2.2. Connection with ChatGPT

The third phase of the development process entails integrating the OpenAI API into the system. This API offers a comprehensive suite of services, including natural language processing, speech synthesis, and text generation. However, certain functionalities provided by the API do not apply to the objectives of the proposed system.

Access to OpenAI's services necessitates authentication using an API key supplied by the platform, as depicted in block (5) of Figure 1. It is crucial to acknowledge that usage of this API incurs fees, which vary based on the volume and nature of the requests submitted.

The system employed the GPT-3.5-turbo model for story generation, as indicated in block (6) of the architecture illustrated in Figure 1. The configuration of parameters for this model was as follows:

1. *Message*. This parameter takes an array of message objects, which may function in the roles of system, user, or assistant, each with its specific content [24]. For the system developed, the message structure is detailed in Figure 2.
2. *Model*. The GPT-3.5-turbo-instruct model was utilized.
3. *Number of Tokens*. This parameter establishes the maximum number of tokens the generator can produce in a single request. For this system, the limit was set at 2048 tokens.
4. *Temperature*. This parameter influences the generated text's variability and originality level. A higher temperature setting results in more diverse and creative outputs and increases the likelihood of generating incoherent or irrelevant responses. Consequently, a temperature setting of 0.5 was chosen for optimal performance in this application.

The model outputs the generated content in JSON format. The application then processes this response, which extracts the content and displays it within the user interface (refer to block (7) of the architectural diagram). Consequently, the child views the generated story textually, accompanied by images of the featured characters.

In addition to displaying the story in text form, the developed system is equipped to narrate the generated stories using synthetic voices. This feature was implemented to accommodate the application's primary users: children learning to read. The OpenAI Text To Speech (TTS) API was employed for this purpose, as illustrated in block (6A), Figure 1). This API offers a selection of six integrated voices: alloy, echo, fable, onyx, nova, and shimmer, which support narrations in various languages, including Spanish [25].

2.3. Measuring Story Similarity

One of the principal attributes of the storytelling system is its capability to generate distinct stories with each execution. To quantify this diversity, the Jaccard index was employed.

The Jaccard index is a statistical tool used to assess the similarity and diversity between two sets, calculated according to Equation (1).

$$J(A, B) = \frac{|A \cap B|}{|A \cup B|} \quad (1)$$

Where A and B represent the sets being compared, and the values of the Jaccard index range from 0 to 1. A value of 0 indicates no similarity between the sets, while a value of 1 signifies that the compared sets are identical.

In the analysis of similarity between stories, pre-processing was conducted, comprising the following stages:

- *Text transformation*. All characters were converted to lowercase to ensure uniformity across the dataset.
- *Text cleaning*. All punctuation marks, character names, nationalities, numbers, and any non-alphabetic characters were removed. Additionally, extra spaces were eliminated to ensure text consistency.
- *Lemmatization*. This process involves converting words to their base form, or lemma. Different words with similar meanings can be treated as the same entity, enabling the system to recognize different verb conjugations as the same base

word. The spaCy library was utilized for lemmatization, employing the pre-trained model designated as `es_core_news_md`, tailored explicitly for processing the Spanish language. The lemmatization process was systematically applied to all the words within the document.

3. Results and Discussion

A functionality test was conducted on the system to ensure accurate story generation. Following this, the diversity of the generated content was evaluated, and an analysis of the voices used in story production was undertaken. The test of the storytelling system was executed in a web browser on a computer running the Windows 10 operating system.

3.1. Functionality Tests

The system functionality test entailed inputting parameters selected by a user. For demonstration purposes, the following steps were executed:

1. A micro-story was selected via the interface, as depicted in Figure 3.



Figure 3. Story Type Selection Interface

2. Three characters –Andrés, Fernanda, and Omar– were chosen for the story, as illustrated in Figure 4.

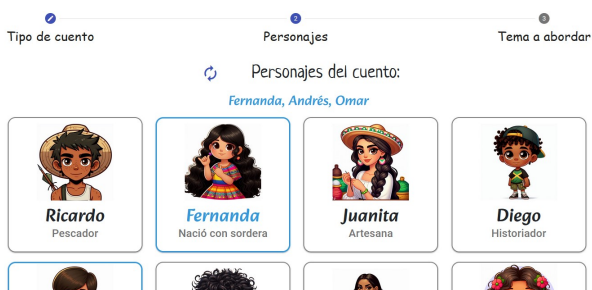


Figure 4. Character Selection Interface

3. The theme of tolerance was selected, as indicated in Figure 5.

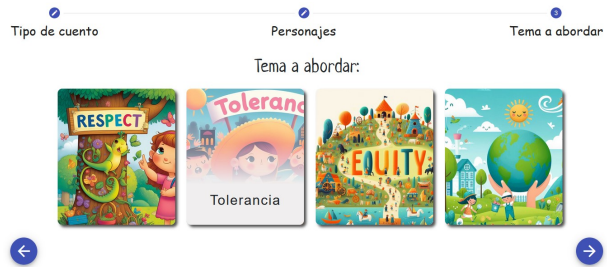


Figure 5. Theme Selection Interface

Once the parameters were set, the story depicted in Figure 6 was generated. This story generation process took approximately 4816 milliseconds.

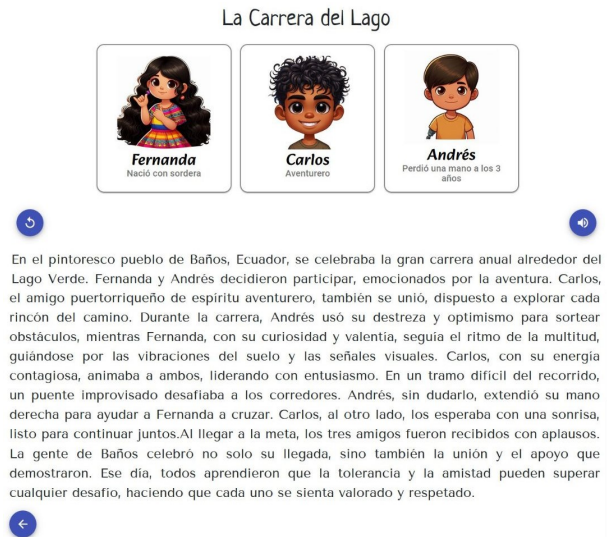


Figure 6. Example of Generated Story

Within the system interface, the user can initiate the playback of the story by selecting the audio button in the upper right corner. The audio, generated by the TTS-1-HD model and narrated using the Alloy voice, lasts 1:01 minutes. The creation process for this audio took 10.79 seconds.

3.2. Diversity of Generated Content

Two experiments were conducted to assess the diversity of content in the generated stories, precisely the extent to which the stories produced by the system differ.

In the first experiment, the characters, themes, and story types were held constant, and the system was tasked with generating stories using these fixed parameters. While the generated stories exhibited similarities,

none of the thirty executions produced identical (repeated) stories. The contents generated in this test are available for public access in the GitHub repository.

Figure 7 summarizes the words frequently used in the titles of the 30 stories generated by the system. Notably, some words not explicitly included in the designed prompts still adhered to the instructions to craft engaging stories.



Figure 7. Word Cloud of the Titles

Conversely, the stories generated by the system prominently feature words that promote tolerance and collaboration, as evidenced by the word cloud in Figure 8, which is derived from the content of the stories.



Figure 8. Word Cloud of the Story Contents

All Jaccard indices between pairs of stories were calculated, and these values are graphically depicted in Figure 9. The analysis reveals minimal similarity among the stories, with the highest Jaccard index value recorded at 0.2137 between micro-stories 23 and 29. These stories are available in the previously mentioned repository.

In the second experiment, stories were generated by randomly selecting characters, themes, and types of stories. After producing more than thirty stories, substantial variety was observed, all by the instructions specified in the designed prompt. Figure 10 graphically displays the Jaccard indices between the stories. The average Jaccard index recorded was 0.0359, with a standard deviation of 0.0427. The highest Jaccard index observed was 0.2.

Upon reviewing the generated stories, it was observed that each narrative incorporates a message that reinforces values and respect towards characters with disabilities.

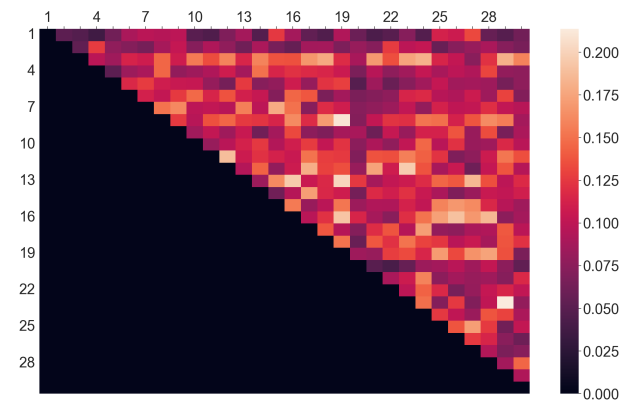


Figure 9. Jaccard Indices Between Stories with Fixed Characters, Type, and Theme

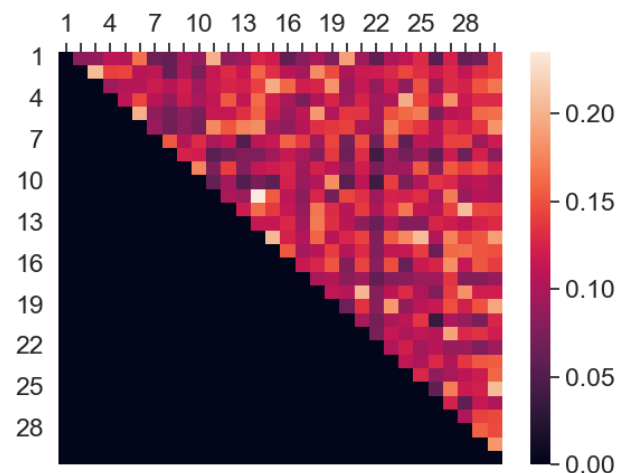


Figure 10. Jaccard Indices Between Stories with Randomly Selected Types, Characters, and Themes

3.3. Analysis of Voices in Story Playback

To evaluate the different voices offered by OpenAI, it was crucial to analyze parameters such as story generation time, voice tone, intonation variation, speech speed, and pronunciation clarity. The primary objective was to identify the most suitable voice to ensure a clear, natural, and emotionally engaging listening experience for children.

3.3.1. Generation Times

The system generated thirty stories, with the type, characters, and themes randomly assigned for each

narrative. The time ChatGPT took for each request to produce the corresponding audio file was meticulously recorded. Eight audio files were generated for micro-stories, eleven for flash fiction, and eleven for short stories. Table 1 summarizes the creation times and durations for each story type.

Table 1. Comparison of Creation Times and Duration of Stories

	Micro-story	Flash fiction	Short story
Creation (average)	9.31 s	11.82 s	12.49 s
Creation(std)	1.03 s	2.41 s	1.82 s
Duration (average)	58 s	66 s	74 s
Duration (std)	13 s	10 s	14 s

As expected, the average time required to create audio files for narration increases with the length of the story. However, the difference in average audio generation times between flash fiction and short stories is less compared to micro-stories. Additionally, it is noted that the generation of audio files for flash fiction exhibits a higher standard deviation compared to the other story types.

It is confirmed that the narration audio duration corresponds with the story type being told. Notably, the duration of the short stories exhibits a larger standard deviation than the other story types.

3.3.2. Voice Tone Evaluation

The tone of voice in a recording plays a crucial role in assessing the end user’s listening experience, as it significantly influences the narratives’ comprehension, empathy, and persuasive power. Upon analyzing the tones in the generated audios, it was observed that three of the six voices, Alloy, Nova, and Shimmer, exhibited a friendly and pleasant tone while narrating the stories, as detailed in Table 2.

Table 2. Comparison of Voice Tones in Story Playback

Voice	Description
Alloy	It projects a friendly tone.
Fable	It is characterized by a serious tone without evoking any specific emotion.
Echo	It exhibits a serious tone with a narrative approach.
Onyx	It exhibits a deep and measured tone, making it ideal for storytelling.
Nova	While possessing a friendly tone, it is perceived as somewhat unnatural.
Shimmer	It features a friendly and natural tone, ideal for storytelling.

Additionally, the voice of Onyx, characterized by its serious tone, was noted to be particularly well-suited for storytelling. This is attributed to its formal quality, which effectively complements this type of narrative.

3.3.3. Intonation Variation

Assessing the variation in intonation within the audio can significantly influence the emotional and persuasive tone of the narrative. In the context of these stories, it plays a crucial role in effectively transmitting the values and messages intended for the children. Table 3 illustrates the intonation variations for the voice types used in OpenAI’s TTS.

Appropriate intonation captures the listener’s attention, elicits emotions, and enhances understanding of the topics discussed. An analysis of this aspect in the audio reveals that while most voices demonstrate consistent intonation variation, the Onyx voice is distinguished by its significant intonation variation. This voice incorporates appropriate pauses, enhancing the narrative of the story. In contrast, the other voices feature very brief pauses. Specifically, the Nova voice demonstrates less effective intonation, resulting in a monotonous and unvaried narration. This factor could potentially diminish children’s interest in listening to the audio.

Table 3. Intonation Variation in Story Playback

Voice	Description
Alloy	It exhibits a constant and precise intonation, closely adhering to punctuation such as commas and periods, thereby contributing to a pleasant and fluid reading experience.
Fable	It maintains a consistent and appropriate intonation in relation to punctuation.
Echo	While the intonation remains consistent and appropriate concerning punctuation, the less noticeable pauses detract from the clarity and narrative flow of the story.
Onyx	It achieves effective intonation through correctly timed pauses, enhancing the story’s narrative.
Nova	The intonation is ineffective, resulting in a monotonous, linear narration.
Shimmer	Despite lacking notable pauses in the narration, it provides good intonation within paragraphs.

3.3.4. Speech Rate

Speech rate is a critical factor that directly impacts story comprehension and the listening experience of child audiences. As detailed in Table 4, the analysis reveals that the Nova voice is inefficient due to its inconsistent rhythm, which complicates comprehension for children. Conversely, the Fable and Echo voices maintain a constant speed, but their narrative styles are overly simplistic and do not align well with the storytelling format. In contrast, the Onyx voice excels with its speech rate, ideally suited for storytelling and offers a more immersive and engaging listening experience.

Table 4. Comparison of Speech Rate in Story Playback

Voice	Description
Alloy	Due to its constant speed, the audio remains clear and understandable.
Fable	It is characterized by a rapid tempo; although pauses are included in the narration, the fast pace diminishes the expressiveness of the audio narrative.
Echo	The speed is consistent, yet it lacks sufficiently long pauses, yielding a presentation more closely resembling plain reading rather than storytelling.
Onyx	The speed is steady and calm, making it arguably the most suitable voice for narrating stories and tales.
Nova	The rhythm varies, featuring periods of quick pronunciation interspersed with slower segments.
Shimmer	It maintains a consistent speed throughout the audio.

3.3.5. Pronunciation Quality

According to OpenAI's documentation, the Text-to-Speech (TTS) model supports voices in various languages, including Spanish. Upon analysis of the thirty audio files, mispronunciations were detected in the narrations. As detailed in Table 5, the Nova voice exhibited notable inefficiencies in word pronunciation and occasionally switched languages, demonstrating instability in maintaining Spanish as the default language. Mispronunciations of character names were observed across all voices. However, despite difficulties pronouncing character names, the Onyx voice exhibited the most accurate pronunciation.

Table 5. Comparison of Pronunciation Clarity in Story Playback

Voice	Description
Alloy	The pronunciation of certain words exhibits a foreign accent, with an elongation of specific sounds. Notably, words such as "Respetar," "perspectiva," and "Ximena" are not articulated correctly in Spanish.
Fable	Pronunciations were detected in several words incorrectly pronounced in Spanish, including "Isabella" and "respeto." Additionally, there were instances where certain words, such as "igualdad," were not wholly articulated.
Echo	Pronunciation errors were noted in several Spanish words, including "hábil," "Ximena," "rumoreaba," "braille," "barrera," and "Sofía." Despite these inaccuracies, this voice exhibits a less foreign accent compared to others.
Onyx	The pronunciation of words is generally clear and precise, yet challenges arise with specific character names, such as "Isabella" and "Ximena."
Nova	The pronunciation lacks precision, exhibiting significant errors, especially in character names. Additionally, in the analysis of five stories narrated with this voice, four exhibited language switches during playback.
Shimmer	This Spanish voice exhibits clear and precise pronunciation, although it struggles with specific character names, such as "Isabella" and "Ximena".

4. Conclusions

AI-based storytelling systems are increasingly recognized as valuable tools in addressing a broad spectrum of challenges. Among these, disability stands out as a significant concern in Latin America and the Caribbean, where it affects over 85 million individuals. These systems offer innovative approaches to inclusivity and accessibility within these communities.

This article proposed designing a storytelling system tailored for Spanish-speaking children, leveraging AI-based generative technologies. This system enables the creation of personalized stories that feature child characters with disabilities, fostering a more inclusive narrative environment.

Including characters with disabilities within the narratives is a critical element that significantly enhances the promotion of diversity and equality from an early age. By leveraging the capabilities of the AI-based generative system, unique stories are generated with each request, even when the same parameters are used. This ensures a diverse and enriching experience with each interaction, underlining the system's effectiveness in fostering inclusivity.

In the various tests conducted on the system, a quantitative comparison of the diversity of the generated stories was performed using the Jaccard index criterion. The results confirmed the low similarity between the analyzed stories, indicating high content variability.

Additionally, the intonation, speed, and pronunciation quality of the synthetic voices were evaluated, highlighting opportunities for improvement in state-of-the-art audio generation technologies for storytelling.

Despite current challenges, such as resource consumption during text-to-speech conversion, lack of natural voice quality, pronunciation errors, and system latency, the proposed system is innovative and holds potential utility for educators seeking to implement inclusive educational tools in their classrooms.

Ongoing efforts are being made to develop additional systems to bridge gaps and enhance accessibility and quality of life for individuals with disabilities. Future research will collaborate with experts from disciplines such as psychology and education to critically assess the content and messages conveyed in the generated stories. Further analysis will also be conducted to determine the suitability and comprehensibility of these stories for children in Latin America.

Acknowledgements

The authors thank the Autonomous University of the State of Mexico for the support provided through project 7018/2024CIB.

References

- [1] J. R. Casar Corredera, “Inteligencia artificial generativa,” *Anales de la Real Academia de Doctores*, vol. 8, no. 3, pp. 475–489, 2023. [Online]. Available: <https://is.gd/3kMGMX>
- [2] J. Sanabria-Navarro, Y. Silveira-Pérez, D. Pérez-Bravo, and M. de Jesús-Cortina-Núñez, “Incidences of artificial intelligence in contemporary education,” *Comunicar*, vol. 77, pp. 97–107, 2023. [Online]. Available: <https://doi.org/10.3916/C77-2023-08>
- [3] S. Droubi, A. Galamba, F. L. Fernandes, A. A. de Mendonça, and R. J. Heffron, “Transforming education for the just transition,” *Energy Research & Social Science*, vol. 100, p. 103090, 2023. [Online]. Available: <https://doi.org/10.1016/j.erss.2023.103090>
- [4] S. Iruri Quispillo and C. A. Villafuerte Álvarez, “Importancia de la narración de cuentos en la educación,” *Comuni@cción: Revista de Investigación en Comunicación y Desarrollo*, vol. 13, no. 3, pp. 233–244, Sep. 2022. [Online]. Available: <https://doi.org/10.33595/2226-1478.13.3.720>
- [5] M. Pozas, C. J. G. Trujillo, and V. Letzel-Alt, “Mexican school students’ perceptions of inclusion: A brief report on students’ social inclusion, emotional well-being, and academic self-concept at school,” *Frontiers in Education*, vol. 8, 2023. [Online]. Available: <https://doi.org/10.3389/feduc.2023.1069193>
- [6] Banco Mundial, “Rompiendo barreras - inclusión de las personas con discapacidad en América Latina y el Caribe.” [Online]. Available: <https://is.gd/diWoks>
- [7] K. Ramírez. (2023) Cuentacuentos. GitHub, Inc. [Online]. Available: <https://n9.cl/pt3ls>
- [8] T. Bratitsis and P. Ziannas, “From early childhood to special education: Interactive digital storytelling as a coaching approach for fostering social empathy,” *Procedia Computer Science*, vol. 67, pp. 231–240, 2015, proceedings of the 6th International Conference on Software Development and Technologies for Enhancing Accessibility and Fighting Info-exclusion. [Online]. Available: <https://doi.org/10.1016/j.procs.2015.09.267>
- [9] P. Juppi, “Engagement and empowerment. Digital storytelling as a participatory media practice,” *Nordicom Review*, vol. 39, 12 2017. [Online]. Available: <https://is.gd/Wo91Bc>
- [10] T. Tseng, Y. Murai, N. Freed, D. Gelosi, T. D. Ta, and Y. Kawahara, “Plushpal: Storytelling with interactive plush toys and machine learning,” in *Proceedings of the 20th Annual ACM Interaction Design and Children Conference*, ser. IDC ’21. New York, NY, USA: Association for Computing Machinery, 2021, pp. 236–245. [Online]. Available: <https://doi.org/10.1145/3459990.3460694>
- [11] J. Haase and P. H. Hanel, “Artificial muses: Generative artificial intelligence chatbots have risen to human-level creativity,” *Journal of Creativity*, vol. 33, no. 3, p. 100066, 2023. [Online]. Available: <https://doi.org/10.1016/j.yjoc.2023.100066>
- [12] R. Li, “A “dance of storytelling”: Dissonances between substance and style in collaborative storytelling with AI,” *Computers and Composition*, vol. 71, p. 102825, 2024. [Online]. Available: <https://doi.org/10.1016/j.compcom.2024.102825>
- [13] S. Habib, T. Vogel, X. Anli, and E. Thorne, “How does generative artificial intelligence impact student creativity?” *Journal of Creativity*, vol. 34, no. 1, p. 100072, 2024. [Online]. Available: <https://doi.org/10.1016/j.yjoc.2023.100072>
- [14] S. Kalantari, E. Rubegni, L. Benton, and A. Vasalou, “When I’m writing a story, I am really good Exploring the use of digital storytelling technology at home,” *International Journal of Child-Computer Interaction*, vol. 38, p. 100613, 2023. [Online]. Available: <https://doi.org/10.1016/j.ijcci.2023.100613>
- [15] J. Su and W. Yang, “Artificial intelligence in early childhood education: A scoping review,” *Computers and Education: Artificial Intelligence*, vol. 3, p. 100049, 2022. [Online]. Available: <https://doi.org/10.1016/j.caeai.2022.100049>
- [16] S. Z. Salas-Pilco, K. Xiao, and J. Os-hima, “Artificial intelligence and new technologies in inclusive education for minority students: A systematic review,” *Sustainability*, vol. 14, no. 20, 2022. [Online]. Available: <https://doi.org/10.3390/su142013572>
- [17] H. Yu, “The application and challenges of chatgpt in educational transformation: New demands for teachers’ roles,” *Heliyon*, vol. 10, no. 2, January 2024. [Online]. Available: <https://doi.org/10.1016/j.heliyon.2024.e24289>
- [18] L. Sijing and W. Lan, “Artificial intelligence education ethical problems and solutions,” in *2018 13th International Conference on Computer Science & Education (ICCSE)*, 2018, pp. 1–5. [Online]. Available: <https://doi.org/10.1109/ICCSE.2018.8468773>

- [19] E. Valverde and P. Hernández, *TypeScript*, 2023. [Online]. Available: <https://is.gd/WICHuR>
- [20] J. Collell and A. Ferry, *CSS3 y Javascript avanzado*. Universitat Oberta de Catalunya, 2023. [Online]. Available: <https://is.gd/JrhbAi>
- [21] A. Nazir and Z. Wang, “A comprehensive survey of ChatGPT: Advancements, applications, prospects, and challenges,” *Meta-Radiology*, vol. 1, no. 2, p. 100022, 2023. [Online]. Available: <https://doi.org/10.1016/j.metrad.2023.100022>
- [22] M. Vicente-Yagüe-Jara, O. López-Martínez, V. Navarro-Navarro, and F. Cuéllar-Santiago, “Writing, creativity, and artificial intelligence. chatgpt in the university context,” *Comunicar*, vol. 77, pp. 47–57, 2023. [Online]. Available: <https://doi.org/10.3916/C77-2023-04>
- [23] J. J. López. ¿Cuántas palabra tiene un cuento o relato corto? [Online]. Available: <https://n9.cl/rdydx>
- [24] OpenAI. (2023) Text generation models. OpenAI Platform. [Online]. Available: <https://is.gd/fkWCFZ>
- [25] ——. (2023) Text to speech. OpenAI Platform. [Online]. Available: <https://is.gd/XskwW5>

GUIDELINES FOR PUBLICATION IN INGENIUS JOURNAL

1. General Information

INGENIUS is a scientific publication of the *Universidad Politécnica Salesiana* of Ecuador, published since January 2007, with a fixed biannual periodicity, specialized in Mechanical Engineering, Electrical Engineering, Electronics, Computer Science and its integration in what is now known as Mechatronics; these lines of action strengthen areas such as automation, control, robotics, among others..

It is a scientific journal, which uses the peer-review system, under double-blind review methodology, according to the publication standards of the Institute of Electrical and Electronics Engineers (IEEE). Compliance with this system allows authors to guarantee an objective, impartial and transparent review process, which facilitates the publication of their inclusion in reference databases, repositories and international indexing.

INGENIUS is indexed in the directory and selective catalog of the Regional Online Information System for Scientific Journals of Latin America, the Caribbean, Spain and Portugal (Latindex), in the Directory of Journals of Open Access DOAJ, In the Information Matrix for the Analysis of Journals, MIAR, In the Ibero-American Network of Innovation and Scientific Knowledge, REDIB and in repositories, libraries and specialized catalogs of Latin America.

The journal is published in a double version: printed (ISSN: 1390-650X) and digital (e-ISSN: 1390-860X), in Spanish, each work being identified with a DOI (Digital Object Identifier System). The articles sent to INGENIUS magazine must comply with the following criteria:

2. Scope and policy

2.1. Theme

Original contributions in Mechanical Engineering, Electrical and Electronic Engineering, Computer Science and its integration in what is now known as Mechatronics, as well as related areas: Automation, Control, Domotics, Robotics in their different fields of action and all those related disciplines with the same central theme.

All the work carried out by national or foreign researchers may be published once they meet the required scientific quality criteria.

2.2. Contributions

INGENIUS Journal preferably publishes articles related to empirical research, and also reports of technological development, proposals for models and innovations, products for the elaboration of graduate and postgraduate thesis that contribute to the field of science and technology, as well as select revisions of literature. (state-of-the-art).

- **Research:** 5,000 to 6,500 words of text, including title, abstracts, descriptors, charts and references.
- **Reports:** 5,000 to 6,500 words of text, including title, abstracts, charts and references.
- **Reviews:** 6,000 to 7,000 words of text, including charts and references. Current, selective and justified references, would be specially valued from among 40 works

The INGENIUS Journal publishes original and unpublished works written in Spanish and English, they may not have been published

through any printed or electronic media, nor be in the process of arbitration or publication.

Every article will be subjected to a rigorous arbitration process; the evaluation of the article will be made according to criteria of originality, relevance, relevance, contributions, scientific rigor and compliance with established editorial guidelines.

Being an arbitrated publication, the Editorial Board approves its publication based on the concept of specialized pairs. The reception of a document does not imply commitment of publication.

It is essential to present a letter of presentation and grant of rights which can be downloaded from: [urlhttps://goo.gl/ZNkMRD](https://goo.gl/ZNkMRD).

Contributions must be exclusively sent and through the OJS (Open Journal System) <https://goo.gl/JF7dWT>. In which all authors must previously register as a user. For any consultation of the procedure you should contact:

revistaingenius@ups.edu.ec,
jcalles@ups.edu.ec ó
mquinde@ups.edu.ec.

To promote diversity in publications, the author(s) may not publish more than one (1) article per issue, nor in consecutive issues. In order for the author(s) to submit their research again to Ingenius, a minimum of 3 published issues must have elapsed.

3. Presentation and structure of the manuscripts

For those works that are empirical investigations, the manuscripts will follow the IMRDC structure (Introduction, Materials and Methods, Results and Discussion and Conclusions), being optional the Notes and Supports. Those papers that, on the contrary, deal with reports, studies, proposals and reviews may be

more flexible in their epigraphs, particularly in material and methods, analysis, results, discussion and conclusions. In all typologies of works, references are mandatory.

Articles may be written on Microsoft Word (.doc or .docx) or L^AT_EX(.tex). The template to be used can be downloaded from the journal's website, a, <https://goo.gl/gtCg6m>, while for L^AT_EX in <https://goo.gl/hrHzzQ>, it is necessary that the file be anonymised in Properties of File, so that the author(s) ID is not displayed.

Figures, Graphs and/or Illustrations, as well as Charts shall be numbered sequentially including an explanatory description for each. The equations included in the article must also be numbered; the figures, charts and equations must be cited in the text.

Use space after point, commas and question marks.

Use “enter” at the end of each paragraph and title heading. Do not use .^{enter}.^anywhere else, let the word processor program automatically break the lines.

Do not center headings or subheadings as they should be aligned to the left.

Charts must be created in the same program used for the document body, but must be stored in a separate file. Use tabs, not spaces, to create columns. Remember that the final size of printed pages will be 21 x 28 cm, so the tables must be designed to fit the final print space.

3.1. Structure of the manuscripts

3.1.1. Presentation and cover letter

1. **Título (español) / Title (inglés):** Concise but informative, in Spanish on the front line and in English on the second, when the article is written in Spanish and vice versa if it is written in English.

2. **Authors and affiliations:** Full name and surname of each author, organized by order of priority and their institutional affiliation with reference to the end of the first sheet, where it must include: Dependency to which belongs within the institution, Institution to which he/she belongs, country, ORCID. A maximum of 5 authors will be accepted, although there may be exceptions justified by the complexity and extent of the topic.
3. **Abstract (Spanish) / Abstract (English):** It will have a maximum extension of 230 words, first in Spanish and then in English. : 1) Justification of the topic; 2) Objectives; 3) Methodology and sample; 4) Main results; 5) Main conclusions.
4. **Keywords (Spanish) / Keywords (English):** 6 descriptors must be presented for each language version directly related to the subject of the work. The use of the key words set out in UNESCO's Thesaurus will be positively valued.
5. **Presentation (Cover Letter):** A statement that the manuscript is an original contribution, not submission or evaluation process in another journal, with the confirmation of the signatory authors, acceptance (if applicable) of formal changes in the manuscript according to the guidelines and partial assignment of rights to the publisher, according to the format established in: <<https://goo.gl/ZNkMRD>>

3.1.2. Manuscript

1. **Título (español) / Title (inglés):** Concise but informative, in Spanish on the front line and in English on the second, when the article is written in Spanish and vice versa if it is written in English.
2. **Authors and affiliations:** Full name and surname of each author, organized by order of priority and their institutional

affiliation with reference to the end of the first sheet, where it must include: Dependency to which belongs within the institution, Institution to which he/she belongs, country, ORCID. A maximum of 5 authors will be accepted, although there may be exceptions justified by the complexity and extent of the topic.

3. **Abstract (Spanish) / Abstract (English):** It will have a maximum extension of 230 words, first in Spanish and then in English. : 1) Justification of the topic; 2) Objectives; 3) Methodology and sample; 4) Main results; 5) Main conclusions.
4. **Keywords (Spanish) / Keywords (English):** 6 descriptors must be presented for each language version directly related to the subject of the work. The use of the key words set out in UNESCO's Thesaurus will be positively valued.
5. **Introduction:** It should include the problem statement, context of the problem, justification, rationale and purpose of the study, using bibliographical citations, as well as the most significant and current literature on the topic at national and international level.
6. **Material and methods:** It must be written so that the reader can easily understand the development of the research. If applicable, it will describe the methodology, the sample and the form of sampling, as well as the type of statistical analysis used. If it is an original methodology, it is necessary to explain the reasons that led to its use and to describe its possible limitations.
7. **Analysis and results:** It will try to highlight the most important observations, describing, without making value judgments, the material and methods used. They will appear in a logical sequence

in the text and the essential charts and figures avoiding the duplication of data.

8. **Discussion and Conclusions:** It will summarize the most important findings, relating the observations themselves to relevant studies, indicating contributions and limitations, without adding data already mentioned in other sections. It should also include deductions and lines for future research.
9. **Supports and acknowledgments (optional):** The Council Science Editors recommends the author (s) to specify the source of funding for the research. Priority will be given to projects supported by national and international competitive projects.
10. **The notes (optional):** will go, only if necessary, at the end of the article (before the references). They must be manually annotated, since the system of footnotes or the end of Word is not recognized by the layout systems. The numbers of notes are placed in superscript, both in the text and in the final note. The numbers of notes are placed in superscript, both in the text and in the final note. No notes are allowed that collect simple bibliographic citations (without comments), as these should go in the references.
11. **References:** Bibliographical citations should be reviewed in the form of references to the text. Under no circumstances should references mentioned in the text not be included. Their number should be sufficient to contextualize the theoretical framework with current and important criteria. They will be presented sequentially in order of appearance, as appropriate following the format of the IEEE.

3.2. Guidelines for Bibliographical references

Journal articles:

- [1] J. Riess, J. J. Abbas, "Adaptive control of cyclic movements as muscles fatigue using functional neuromuscular stimulation". IEEE Trans. Neural Syst. Rehabil. Eng vol. 9, pp.326–330, 2001. [Online]. Available: <https://doi.org/10.1109/7333.948462>

Books:

- [1] G. O. Young, "Synthetic structure of industrial plastics" in *Plastics*, 2nd ed., vol. 3, J. Peters, Ed. New York: McGraw–Hill, 1964, pp. 15–64.

Technical reports:

- [1] M. A. Brusberg and E. N. Clark, "Installation, operation, and data evaluation of an oblique–incidence ionosphere sounder system," in "Radio Propagation Characteristics of the Washington–Honolulu Path," Stanford Res. Inst., Stanford, CA, Contract NOBSR–87615, Final Rep., Feb. 1995, vol. 1

Articles presented in conferences (unpublished):

- [1] Vázquez, Rolando, Presentación curso "Realidad Virtual". National Instruments. Colombia, 2009.

Articles of memories of Conferences (Published):

- [1] L. I. Ruiz, A. García, J. García, G. Taboada. "Criterios para la optimización de sistemas eléctricos en refinerías de la industria petrolera: influencia y análisis en el equipo eléctrico," IEEE CONCAPAN XXVIII, Guatemala 2008.

Thesis:

- [1] L.M. Moreno, "Computación paralela y entornos heterogéneos," Tesis doctoral, Dep. Estadística, Investigación Operativa y Computación, Universidad de La Laguna, La Laguna, 2005.

Guidelines:

- [1] IEEE Guide for Application of Power Apparatus Bushings, IEEE Standard C57.19.100–1995, Aug. 1995.

Patents:

- [1] J. P. Wilkinson, “Nonlinear resonant circuit devices,” U.S. Patent 3 624 125, July 16, 1990.

Manuals:

- [1] Motorola Semiconductor Data Manual, Motorola Semiconductor Products Inc., Phoenix, AZ, 1989.

Internet resources:

- [1] E. H. Miller, “A note on reflector arrays” [Online]. Available. <https://goo.gl/4cJkCF>

3.3. Epigraphs, Figures and Charts

The epigraphs of the body of the article will be numbered in Arabic. They should go without a full box of capital letters, neither underlined nor bold. The numbering must be a maximum of three levels: 1. / 1.1. / 1.1.1. At the end of each numbered epigraph will be given an enter to continue with the corresponding paragraph.

The charts must be included in the text according to order of appearance, numbered in Arabic and subtitled with the description of the content, the subtitle should go at the top of the table justified to the left.

Figures can be linear drawings, maps or black and white halftone or color photographs in 300 dpi resolution. Do not combine photographs and line drawings in the same figure.

Design the figures so that they fit eventually to the final size of the journal 21 x 28 cm. Make sure inscriptions or details, as well as lines, are of appropriate size and thickness so that they are not illegible when they are reduced to their final size (numbers, letters and symbols must be reduced to at least 2.5 mm in height After the illustrations have

been reduced to fit the printed page). Ideally, the linear illustrations should be prepared at about a quarter of their final publication size.

Different elements in the same figure should be spelled a, b, c, etc.

Photographs should be recorded with high contrast and high resolution. Remember that photographs frequently lose contrast in the printing process. Line drawings and maps should be prepared in black.

The text of the figures and maps must be written in easily legible letters.

If the figures have been previously used, it is the responsibility of the author to obtain the corresponding permission to avoid subsequent problems related to copyright.

Each figure must be submitted in a separate file, either as bitmap (.jpg, .bmp, .gif, or .png) or as vector graphics (.ps, .eps, .pdf).

4. Submission process

The manuscript must be sent through the OJS system of the journal, <<https://goo.gl/JF7dWT>>, the manuscript should be uploaded as an original file in .pdf without author data and anonymized according to the above; In complementary files the complete manuscript must be loaded in .doc or .docx (Word file), that is to say with the data of the author (s) and its institutional ascription; Also the numbered figures should be uploaded in independent files according to the corresponding in the manuscript (as bitmap .jpg, .bmp, .gif, or .png or as vector graphics .ps, .eps, .pdf). It is also obligatory to upload the cover letter and grant of rights as an additional file.

All authors must enter the required information on the OJS platform and only one of the authors will be responsible for correspondence.

Once the contribution has been sent the system will automatically send the author for correspondence a confirmation email of receipt

of the contribution.

5. Editorial process

Once the manuscript has been received in OJS, a first check by the editorial team of the following points:

- The topic is in accordance with the criteria of the journal.
- Must have the IMRDC structure.
- Must be in the INGENIUS format.
- Must use the IEEE citation format.
- All references should be cited in the text of the manuscript as well as charts, figures and equations.
- The manuscript is original; for this, software is used to determine plagiarism.

The assessment described above can take up to 4 weeks.

If any of the above is not complete or there is inconsistency, an email will be sent to the author to make the requested corrections.

The author will make the corrections and resend the contribution through an email in response to the notification and will also upload the corrected manuscript into OJS supplementary files.

The editorial team will verify that the requested corrections have been incorporated, if it complies, the manuscript will start the second part of the process that may be followed by the author through OJS, otherwise the author will be notified and the manuscript will be archived.

The second phase of the process consists of the evaluation under the methodology of double-blind review, which includes national and foreign experts considering the following steps:

- The editor assigns two or more reviewers for the article.
- After reviewing the article, the reviewers will submit the evaluation report with one

of the following results.

- Publishable
- Publishable with suggested changes
- Publishable with mandatory changes
- Non publishable
- The editor once received the evaluation by the reviewers will analyze the results and determine if the article is accepted or denied.
- If the article is accepted, the author will be notified to make corrections if required and the corresponding editorial process will be continued.
- If the article is denied, the author will be notified and the manuscript will be archived.
- In the two previous cases the result of the evaluation of the reviewers and their respective recommendations will be sent.

The second phase of the process lasts at least 4 weeks, after which they will be notified to the author giving instructions to continue with the process.

6. Publication

The INGENIUS Journal publishes two issues per year, on January 1st and July 1st, so it is important to consider the dates for sending the articles and their corresponding publication. Articles received until October will be considered for the January publication and those received until April for the July publication.

7. Information on the Use of Artificial Intelligence

Should artificial intelligence be used at any stage of the research presented in the article, authors are required to clearly highlight this in the cover letter associated with the article, specifying the section or sections where artificial intelligence has been used. The purpose

of this requirement is to inform readers about the sections where this technology has been employed, providing greater transparency and understanding of its application in the presented research.

INGENUS, Revista de Ciencia y Tecnología, recognizes the importance of maintaining

high ethical standards in scientific research, particularly in the use of artificial intelligence (AI).

The decision to accept a publication that has utilized artificial intelligence rests at the discretion of the editorial team.

UNIVERSIDAD POLITÉCNICA SALESIANA DEL ECUADOR

Juan Cárdenas Tapia, sdb,
Rector

©Universidad Politécnica Salesiana
Turuhuayco 3-69 y Calle Vieja
Postal code 2074
Cuenca, Ecuador
Teléfono: (+593 7) 205 00 00
Fax: (+593 7) 408 89 58
Email: srector@ups.edu.ec

Exchange

Exchange with other periodicals is accepted.

Address:
Secretaría Técnica de Comunicación
Universidad Politécnica Salesiana
Turuhuayco 3-69 y Calle Vieja
Postal code 2074
Cuenca, Ecuador
Phone: (+593 7) 205 00 00 Ext. 1182
Fax: (+593 7) 408 89 58
Email: rpublicas@ups.edu.ec
www.ups.edu.ec
Cuenca – Ecuador

INGENIUS, Journal Science of Technology,
Issue 32
july/december 2024
John Calle Sigüencia, Editor in chief
revistaingenius@ups.edu.ec

Printed

Centro Gráfico Salesiano: Antonio Vega Muñoz 10-68 y General Torres.
Phone: (+593 7) 283 17 45
Cuenca – Ecuador
Email: centrograficosalesiano@lms.com.ec

OTHER PERIODIC PUBLICATIONS OF THE UNIVERSITY

UNIVERSITAS, Journal of Social and Human Sciences.

LA GRANJA, Journal of the Sciences.

ALTERIDAD, Journal of Education.

RETOS, Journal of Administration Sciences and Economics.

UTOPIA, University Youth Ministry Magazine.

SOPHIA, Collection of Philosophy of Education.

